

1

²A SEARCH FOR LONG-LIVED, CHARGED, SUPERSYMMETRIC PARTICLES
³USING IONIZATION WITH THE ATLAS DETECTOR

⁴BRADLEY AXEN

5



6

September 2016 – Version 0.61

⁸ Bradley Axen: *A Search for Long-Lived, Charged, Supersymmetric Particles using*
⁹ *Ionization with the ATLAS Detector*, Subtitle, © September 2016

¹⁰ The dissertation of Bradley Axen, titled *A Search for Long-Lived, Charged, Super-*
¹¹ *symmetric Particles using Ionization with the ATLAS Detector*, is approved:

¹² _____
¹³ Chair _____ Date

¹⁴ _____
¹⁵ _____ Date

¹⁶ _____
¹⁷ _____ Date

¹⁸ University of California, Berkeley

19

Usually a quotation.

20

Dedicated to.

₂₁ ABSTRACT

₂₂ How to write a good abstract:

₂₃ <https://plg.uwaterloo.ca/~migod/research/beck00PSLA.html>

24 PUBLICATIONS

25 Some ideas and figures have appeared previously in the following publications:

26

27 Put your publications from the thesis here. The packages `multibib` or `bibtopic`
28 etc. can be used to handle multiple different bibliographies in your document.

30 ACKNOWLEDGEMENTS

31 Put your acknowledgements here.

32

33 And potentially a second round.

34

35 CONTENTS

36	1	INTRODUCTION	1
37	I	THEORETICAL CONTEXT	3
38	2	STANDARD MODEL	4
39	2.1	Action and the Lagrangian	4
40	2.2	Gauge Invariance and Forces	5
41	2.2.1	$SU(2) \times U(1)$ and the Electroweak Force	7
42	2.2.2	$SU(3)$ and the Strong Force	7
43	2.3	Noether's Theorem, Charges, and Matter	8
44	2.3.1	Quarks	8
45	2.3.2	Leptons	9
46	2.3.3	Chirality	10
47	2.4	Higgs Mechanism and Mass	10
48	2.5	Phenomenology	12
49	2.5.1	Electroweak Physics	12
50	2.5.2	Strong Physics	12
51	2.5.3	Proton-Proton Collisions	13
52	2.6	Limitations	13
53	2.6.1	Theoretical Concerns	14
54	2.6.2	Cosmological Observations	15
55	3	SUPERSYMMETRY	17
56	3.1	Structure	17
57	3.2	Motivation	19
58	3.3	Simplified Models	20
59	3.4	Long-Lived Particles	21
60	II	EXPERIMENTAL STRUCTURE AND RECONSTRUCTION	23
61	4	THE LARGE HADRON COLLIDER	24
62	4.1	Injection Chain	25
63	4.2	Design	26
64	4.2.1	Layout	26
65	4.2.2	Magnets	27
66	4.2.3	RF Cavities	28
67	4.2.4	Beam	30
68	4.3	Luminosity Parameters	30
69	4.4	Delivered Luminosity	31
70	5	THE ATLAS DETECTOR	34
71	5.1	Coordinate System	36
72	5.2	Magnetic Field	37
73	5.3	Inner Detector	39
74	5.3.1	Pixel Detector	42
75	5.3.2	Semiconductor Tracker	44

76	5.3.3	Transition Radiation Tracker	47
77	5.4	Calorimetry	48
78	5.4.1	Electromagnetic Calorimeter	49
79	5.4.2	Hadronic Calorimeters	50
80	5.5	Muon Spectrometer	52
81	5.5.1	Monitored Drift Tube	54
82	5.5.2	Resistive Plate Chamber	55
83	5.5.3	Cathode Strip Chamber	55
84	5.5.4	Thin Gap Chamber	56
85	5.6	Trigger	57
86	6	EVENT RECONSTRUCTION	61
87	6.1	Charged Particles	61
88	6.1.1	Pixel Neural Network	63
89	6.1.2	Pixel dE/dx	64
90	6.1.3	Vertex Reconstruction	65
91	6.2	Electrons and Photons	65
92	6.2.1	Photon Identification	67
93	6.2.2	Electron Identification	67
94	6.3	Muons	67
95	6.3.1	Muon Identification	68
96	6.4	Jets	68
97	6.4.1	Topological Clustering	68
98	6.4.2	Jet Algorithms	70
99	6.4.3	Jet Energy Scale	70
100	6.5	Missing Transverse Energy	71
101	III	CALORIMETER RESPONSE	74
102	7	RESPONSE MEASUREMENT WITH SINGLE HADRONS	75
103	7.1	Dataset and Simulation	76
104	7.1.1	Data Samples	76
105	7.1.2	Simulated Samples	76
106	7.1.3	Event Selection	76
107	7.2	Inclusive Hadron Response	77
108	7.2.1	E/p Distribution	77
109	7.2.2	Zero Fraction	78
110	7.2.3	Neutral Background Subtraction	80
111	7.2.4	Corrected Response	81
112	7.2.5	Additional Studies	83
113	7.3	Identified Particle Response	86
114	7.3.1	Decay Reconstruction	87
115	7.3.2	Identified Response	88
116	7.3.3	Additional Species in Simulation	90
117	7.4	Summary	90
118	8	JET ENERGY RESPONSE AND UNCERTAINTY	92
119	8.1	Motivation	92
120	8.2	Uncertainty Estimate	92

121	8.3	Summary	95
122	IV	SEARCH FOR LONG-LIVED PARTICLES	98
123	9	LONG-LIVED PARTICLES IN ATLAS	99
124	9.1	Event Topology	99
125	9.1.1	Detector Interactions	100
126	9.1.2	Lifetime Dependence	102
127	9.2	Simulation	104
128	10	EVENT SELECTION	109
129	10.1	Trigger	110
130	10.2	Kinematics and Isolation	111
131	10.3	Particle Species Rejection	115
132	10.4	Ionization	119
133	10.4.1	Mass Estimation	119
134	10.5	Event Selection	121
135	11	BACKGROUND ESTIMATION	123
136	11.1	Background Sources	123
137	11.2	Prediction Method	124
138	11.3	Validation	125
139	11.3.1	Closure in Simulation	125
140	11.3.2	Validation Region in Data	126
141	12	SYSTEMATIC UNCERTAINTIES	128
142	12.1	Background Estimate	128
143	12.1.1	Analytic Description of dE/dx	128
144	12.1.2	Muon Fraction	129
145	12.1.3	IBL Corrections	129
146	12.1.4	Normalization	129
147	12.2	Signal Yield	129
148	12.2.1	initial state radiation (ISR) Modeling	130
149	12.2.2	Pileup Reweighting	130
150	12.2.3	Trigger Efficiency Reweighting	131
151	12.2.4	Missing Transverse Momentum Scale	132
152	12.2.5	Momentum Parametrization	132
153	12.2.6	Ionization Requirement	133
154	12.2.7	Electron and Jet Rejection	133
155	12.2.8	Muon Veto	133
156	12.2.9	Luminosity	135
157	12.2.10	Signal Size	135
158	13	RESULTS	136
159	13.1	Cross Sectional Limits	136
160	13.2	Mass Limits	141
161	13.3	Context for Long-Lived Searches	141
162	14	SUMMARY AND OUTLOOK	144
163	V	APPENDIX	145
164	A	EXPANDED R-HADRON YIELDS AND LIMITS	146

166 LIST OF FIGURES

167	Figure 1	A Feynman diagram representing the interaction of the A field with a generic fermion, f	7
168			
169	Figure 2	The particle content of the SM	9
170	Figure 3	The Feynman diagrams representing the decays of the W and Z bosons to fermions. Here f indicates a generic fermion, \bar{f} its antiparticle, and f' the partner of that fermion in the same generation.	12
171			
172			
173			
174	Figure 4	The parton distribution functions (PDFs) for proton-proton collisions at $Q^2 = 10 \text{ GeV}^2$ and $Q^2 = 10^4 \text{ GeV}^2$. Each shows the fraction of particles which carry a fraction x of the total proton energy at the specified scale [1].	14
175			
176			
177			
178			
179	Figure 5	An approximation of the running of the coupling constants in the Standard Model (SM) up to the Planck scale [2].	15
180			
181			
182	Figure 6	The distribution of velocities of stars as a function of the radius from the center of the galaxy. The contributions to the velocity from the various components of matter in the galaxy are shown [3].	16
183			
184			
185			
186	Figure 7	An approximation of the running of the coupling constants in the Minimal Supersymmetric Model (MSSM) up to the Planck scale [2].	20
187			
188			
189	Figure 8	The decay of a gluino to quarks and an LSP , which precedes through a squark.	21
190			
191	Figure 9	The four collision points and corresponding experiments of the Large Hadron Collider (LHC). The image includes the location of the nearby city of Geneva as well as the border of France and Switzerland.	25
192			
193			
194			
195	Figure 10	The cumulative luminosity over time delivered to the ATLAS experiment from high energy proton-proton collisions since 2011. The energies of the collisions are listed for each of the data-taking periods.	26
196			
197			
198			
199	Figure 11	The accelerator complex that builds up to the full design energies at the LHC . The protons are passed in order to Linac 2, the PSB , the PS , the SPS and then the LHC	27
200			
201			
202			
203	Figure 12	A schematic of the layout of the LHC , not to scale. The arched and straight sections are illustrated at the bottom of the schematic, and all four crossing sites are indicated with their respective experiments.	28
204			
205			
206			

207	Figure 13	A cross section of the the cryodipole magnets which bend the flight path of protons around the circumference of the LHC. The diagram includes both the superconducting coils which produce the magnetic field and the structural elements which keep the magnets precisely aligned.	29
208			
209			
210			
211			
212			
213	Figure 14	The arrangement of four radiofrequency (RF) cavities within a cryomodule.	29
214			
215	Figure 15	The cumulative luminosity versus time delivered to ATLAS (green), recorded by ATLAS (yellow), and certified to be good quality data (blue) during stable beams for pp collisions at 13 TeV in 2015.	32
216			
217			
218			
219	Figure 16	The luminosity-weighted distribution of the mean number of interactions per crossing for the 2015 pp collision data at 13 TeV.	33
220			
221			
222	Figure 17	A cut-away schematic of the layout of the ATLAS detector. Each of the major subsystems is indicated.	35
223			
224	Figure 18	A cross-sectional slice of the ATLAS experiment which illustrates how the various SM particles interact with the detector systems.	35
225			
226			
227	Figure 19	The layout of the four superconducting magnets in the ATLAS detector.	38
228			
229	Figure 20	The arrangement of the subdetectors of the ATLAS inner detector. Each of the subdetectors is labeled in the cut-away view of the system.	40
230			
231			
232	Figure 21	A quarter section of the ATLAS inner detector which shows the layout of each of the subdetectors in detail. The lower panel shows an enlarged view of the pixel detector. Example trajectories for a particle with $\eta = 1.0, 1.5, 2.0, 2.5$ are shown. The Insertible B-Layer (IBL), which was added after the original detector commissioning, is not shown.	40
233			
234			
235			
236			
237			
238			
239	Figure 22	A computer generated three-dimensional view of the inner detector along the line of the beam axis. The subdetectors and their positions are labeled.	41
240			
241			
242	Figure 23	An alternative computer generated three-dimensional view of the inner detector transverse to the beam axis. The subdetectors and their positions are labeled.	41
243			
244			
245	Figure 24	The integrated radiation lengths traversed by a straight track at the exit of the ID envelope, including the services and thermal enclosures. The distribution is shown as a function of $ \eta $ and averaged over ϕ . The breakdown indicates the contributions of individual subdetectors, including services in their active volume.	42
246			
247			
248			
249			
250			
251	Figure 25	A cut away image of the outer three layers of the pixel detector.	45
252			

253	Figure 26	An image of the insertion of the IBL into the current pixel detector.	45
254			
255	Figure 27	A three-dimensional computer-generated image of the geometry of the IBL with a view (a) mostly transverse to the beam pipe (b) mostly parallel to the beam pipe.	46
256			
257			
258	Figure 28	An expanded view of the geometry of the silicon microstrip (SCT) double layers in the barrel region.	47
259			
260	Figure 29	48
261	Figure 30	The depth of (a) the electromagnetic barrel calorimeter in radiation lengths and (b) all calorimeters in interaction lengths as a function of pseudorapidity.	49
262			
263			
264	Figure 31	A schematic of the liquid argon (LAr) calorimeter in the barrel region, highlighting the accordion structure.	50
265			
266	Figure 32	A schematic of a hadronic tile module which shows the alternating layers of steel and plastic scintillator.	51
267			
268	Figure 33	The segmentation in depth and η of the tile-calorimeter modules in the central (left) and extended (right) barrels.	52
269			
270	Figure 34	A cut-away diagram of the muon systems on ATLAS.	53
271	Figure 35	A quarter view of the muon spectrometer which highlights the layout of each of the detecting elements. The BOL, BML, BIL, EOL, EML, and EIL are all Monitored Drift Tube (MDT) elements, where the acronyms encode their positions.	53
272			
273			
274			
275			
276	Figure 36	A schematic of the cross-section of the muon spectrometer in the barrel region.	54
277			
278	Figure 37	A schematic of a single MDT chamber, which shows the multilayers of drift tubes as well as the alignment system.	55
279			
280			
281	Figure 38	A schematic of the Cathode Strip Chamber (CSC) end-cap, showing the overlapping arrangement of the eight large and eight small chambers.	56
282			
283			
284	Figure 39	A schematic of the Thin Gap Chamber (TGC) doublet and triplet layers.	57
285			
286	Figure 40	The L1 Trigger rate broken down into the types of triggers as a function of the luminosity block for the 2015 data collection period.	59
287			
288			
289	Figure 41	The HLT Trigger rate broken down into the types of triggers as a function of the luminosity block for the 2015 data collection period.	60
290			
291			
292	Figure 42	An illustration of the perigee representation of track parameters for an example track. The charge is not directly shown, but is indicated by the direction of curvature of the track [21].	62
293			
294			
295			

296	Figure 43	The x and y locations of the hits generated in a simulated $t\bar{t}$ event in the inner detector. The hits which belong to tracks formed using the inside-out algorithm are highlighted in red, while the hits which belong to tracks formed using the outside-in algorithm are circled in black.	63
302	Figure 44	Examples of the clusters formed in a single layer of the pixel detector for (a) a single isolated particle, (b) two nearly-overlapping particles, and (c) a particle which emits a δ -ray [22].	64
306	Figure 45	The total, fractional jet energy scale (JES) uncertainties estimated for 2015 data as a function of jet p_T	72
308	Figure 46	The E/p distribution and ratio of simulation to data for isolated tracks with (a) $ \eta < 0.6$ and $1.2 < p/\text{GeV} < 1.8$ and (b) $ \eta < 0.6$ and $2.2 < p/\text{GeV} < 2.8$	78
311	Figure 47	The fraction of tracks as a function (a, b) of momentum, (c, d) of interaction lengths with $E \leq 0$ for tracks with positive (on the left) and negative (on the right) charge.	79
315	Figure 48	An illustration (a) of the geometry of energy deposits in the calorimeter. The red energy deposits come from the charged particle targeted for measurement, while the blue energy deposits are from nearby neutral particles and must be subtracted. The same diagram (b) for the neutral-background selection, described in Section 7.2.3.	80
322	Figure 49	$\langle E/p \rangle_{\text{BG}}$ as a function of the track momentum for tracks with (a) $ \eta < 0.6$, (b) $0.6 < \eta < 1.1$, and as a function of the track pseudorapidity for tracks with (c) $1.2 < p/\text{GeV} < 1.8$, (d) $1.8 < p/\text{GeV} < 2.2$	81
326	Figure 50	$\langle E/p \rangle_{\text{COR}}$ as a function of track momentum, for tracks with (a) $ \eta < 0.6$, (b) $0.6 < \eta < 1.1$, (c) $1.8 < \eta < 1.9$, and (d) $1.9 < \eta < 2.3$	82
329	Figure 51	$\langle E/p \rangle_{\text{COR}}$ calculated using LCW-calibrated topological clusters as a function of track momentum for tracks with (a) zero or more associated topological clusters or (b) one or more associated topological clusters.	83
333	Figure 52	Comparison of the $\langle E/p \rangle_{\text{COR}}$ for tracks with (a) less than and (b) greater than 20 hits in the TRT.	84
335	Figure 53	Comparison of the $\langle E/p \rangle_{\text{COR}}$ for (a) positive and (b) negative tracks as a function of track momentum for tracks with $ \eta < 0.6$	85
338	Figure 54	Comparison of the E/p distributions for (a) positive and (b) negative tracks with $0.8 < p/\text{GeV} < 1.2$ and $ \eta < 0.6$, in simulation with the FTFP_BERT and QGSP_BERT physics lists.	85

342	Figure 55	Comparison of the response of the hadronic calorimeter as a function of track momentum (a) at the EM-scale and (b) after the LCW calibration.	86
343			
344			
345	Figure 56	Comparison of the response of the EM calorimeter as a function of track momentum (a) at the EM-scale and (b) with the LCW calibration.	86
346			
347			
348	Figure 57	The reconstructed mass peaks of (a) K_S^0 , (b) Λ , and (c) $\bar{\Lambda}$ candidates.	87
349			
350	Figure 58	The E/p distribution for isolated (a) π^+ , (b) π^- , (c) proton, and (d) anti-proton tracks.	88
351			
352	Figure 59	The fraction of tracks with $E \leq 0$ for identified (a) π^+ and π^- , and (b) proton and anti-proton tracks	89
353			
354	Figure 60	The difference in $\langle E/p \rangle$ between (a) π^+ and π^- (b) p and π^+ , and (c) \bar{p} and π^-	90
355			
356	Figure 61	$\langle E/p \rangle_{\text{COR}}$ as a function of track momentum for (a) π^+ tracks and (b) π^- tracks.	91
357			
358	Figure 62	The ratio of the calorimeter response to single particles of various species to the calorimeter response to π^+ with the physics list FTFP_BERT.	91
359			
360			
361	Figure 63	The spectra of true particles inside anti- k_t , $R = 0.4$ jets with (a) $90 < p_T/\text{GeV} < 100$, (b) $400 < p_T/\text{GeV} < 500$, and (c) $1800 < p_T/\text{GeV} < 2300$	93
362			
363			
364	Figure 64	The JES response uncertainty contributions, as well as the total JES uncertainty, as a function of jet p_T for (a) $ \eta < 0.6$ and (b) $0.6 < \eta < 1.1$	96
365			
366			
367	Figure 65	The correlations between bins of average reconstructed jet momentum as a function of jet p_T and $ \eta $ for jets in the central region of the detector.	97
368			
369			
370	Figure 66	The processes which contribute to gluino pair production in the proton proton collisions, where the quarks and gluons are proton constituents.	100
371			
372			
373	Figure 67	The generated p_T and β distributions for R-Hadrons with $M = 1600 \text{ GeV}$	100
374			
375	Figure 68	A schematic diagram of an R-Hadron event with a lifetime around 0.01 ns. The diagram includes one charged R-Hadron (solid blue), one neutral R-Hadron (dashed blue), Lightest Supersymmetric Particles (LSPs) (dashed green) and charged hadrons (solid orange). The pixel detector, calorimeters, and muon system are illustrated but not to scale.	103
376			
377			
378			
379			
380			
381			

382	Figure 69	Schematic diagram of R-Hadron events with a lifetime around 5 ns, where the masses of the R-Hadron and LSP are (a) nearly degenerate and (b) not degenerate. The diagrams include charged R-Hadrons (solid blue), neutral R-Hadrons (dashed blue), LSPs (dashed green) and charged hadrons (solid orange). The pixel detector, calorimeters, and muon system are illustrated but not to scale.	106
390	Figure 70	A schematic diagram of an R-Hadron event with a lifetime around 20 ns. The diagram includes one charged R-Hadron (solid blue), one neutral R-Hadron (dashed blue), LSPs (dashed green) and charged hadrons (solid orange). The pixel detector, calorimeters, and muon system are illustrated but not to scale.	107
396	Figure 71	A schematic diagram of a very long-lived (VLL) R-Hadron event. The diagram includes one charged R-Hadron (solid blue) and one neutral R-Hadron (dashed blue). The pixel detector, calorimeters, and muon system are illustrated but not to scale.	108
401	Figure 72	The distribution of (a) E_T^{miss} and (b) Calorimeter E_T^{miss} for simulated signal events before the trigger requirement. The final bin includes all events above the axis range.	111
405	Figure 73	The distribution of E_T^{miss} for data and simulated signal events, after the trigger requirement. The final bin includes all events above the axis range.	112
408	Figure 74	The trigger efficiency for the HLT_xe70 trigger requirement as a function of (a) E_T^{miss} and (b) Calorimeter E_T^{miss} for simulated signal events.	113
411	Figure 75	The dependence of dE/dx on N_{split} in data after basic track hit requirements have been applied.	114
413	Figure 76	The distribution of dE/dx with various selections applied in data and simulated signal events. The final bin includes all tracks above the axis range.	114
416	Figure 77	The distribution of track momentum for data and simulated signal events, after previous selection requirements have been applied. The final bin includes all tracks above the axis range.	115
420	Figure 78	The distribution of M_T for data and simulated signal events, after previous selection requirements have been applied. The final bin includes all tracks above the axis range.	116

424	Figure 79	The distribution of summed tracked momentum within a cone of $\Delta R < 0.25$ around the candidate track for data and simulated signal events, after previous selection requirements have been applied. The final bin includes all tracks above the axis range.	117
425			
426			
427			
428			
429	Figure 80	The normalized, two-dimensional distribution of E/p and f_{EM} for simulated (a) 1200 GeV VLL R-Hadron, and (b) 1200 GeV, 10 ns R-Hadron, (c) $Z \rightarrow ee$, and (d) $Z \rightarrow \tau\tau$ events.	118
430			
431			
432			
433	Figure 81	Two-dimensional distribution of dE/dx versus charge signed momentum (qp) for minimum-bias tracks. The fitted distributions of the most probable values for pions, kaons and protons are superimposed.	120
434			
435			
436			
437	Figure 82	The distribution of mass estimated using dE/dx for simulated VLL R-Hadrons with masses between 1000 and 1600 GeV.	120
438			
439			
440	Figure 83	The acceptance \times efficiency as a function of R-Hadron (a) mass and (b) lifetime. (a) shows all of the combinations of mass and lifetime considered in this search, and (b) highlights the lifetime dependence for 1000 GeV and 1600 GeV R-Hadrons.	122
441			
442			
443			
444			
445	Figure 84	The distribution of (a) dE/dx and (b) momentum for tracks in data and simulated signal after requiring the event level selection and the track selection on p_T , hits, and N_{split} . Each sub-figure shows the normalized distributions for tracks classified as hadrons, electrons, and muons in data and R-Hadrons in the simulated signal.	124
446			
447			
448			
449			
450			
451			
452	Figure 85	The distribution of $M_{dE/dx}$ (a) before and (b) after the ionization requirement for tracks in simulated W boson decays and for the randomly generated background estimate.	126
453			
454			
455			
456	Figure 86	The distribution of $M_{dE/dx}$ (a) before and (b) after the ionization requirement for tracks in the validation region and for the randomly generated background estimate.	127
457			
458			
459			
460	Figure 87	The trigger efficiency for the HLT_xe70 trigger requirement as a function of Calorimeter E_T^{miss} for simulated data events with a W boson selection. Simulated signal events and simulated W boson events are also included.	131
461			
462			
463			
464			
465	Figure 88	The efficiency of the muon veto for R-hadrons of two different masses, as a function of $\frac{1}{\beta}$ for simulated R-Hadron tracks.	134
466			
467			

468	Figure 89	The average reconstructed MDT β distribution for $Z \rightarrow \mu\mu$ events in which one of the muons is reconstructed as a slow muon, for both data and simulation. A gaussian fit is superimposed.	134
469			
470			
471			
472	Figure 90	The observed mass distribution of events in data and the generated background distribution in (a) the stable and (b) the metastable signal region. A few example simulated signal distributions are superimposed.	137
473			
474			
475			
476	Figure 91	The observed and expected cross section limits as a function of mass for the stable simulated signal. The predicted cross section values for the corresponding signals are included.	139
477			
478			
479			
480	Figure 92	The observed and expected cross section limits as a function of mass for each generated lifetime. The predicted cross section values for the corresponding signals are included.	140
481			
482			
483			
484	Figure 93	The excluded range of masses as a function of gluino lifetime. The expected lower limit (LL), with its experimental $\pm 1\sigma$ band, is given with respect to the nominal theoretical cross-section. The observed 95% LL obtained at $\sqrt{s} = 8$ TeV [83] is also shown for comparison.	142
485			
486			
487			
488			
489	Figure 94	The constraints on the gluino mass as a function of lifetime for a split-supersymmetry model with the gluino R-Hadrons decaying into a gluon or light quarks and a neutralino with mass of 100 GeV. The solid lines indicate the observed limits, while the dashed lines indicate the expected limits. The area below the curves is excluded. The dots represent results for which the particle is assumed to be prompt or stable.	143
490			
491			
492			
493			
494			
495			
496			

497 LIST OF TABLES

498	Table 1	The particles in the SM and their corresponding superpartners in the MSSM	18
499			
500	Table 2	The design parameters of the LHC beam that determines the energy of collisions and the luminosity, for both the injection of protons and at the nominal circulation.	31
501			
502			
503			
504	Table 3	The performance goals for each of the subsystems of the ATLAS detector. The $ \eta $ coverage specifies the range where the subsystem needs to be able to provide measurements with the specified resolution. The resolutions include a p_T or E dependence that is added in quadrature with a p_T/E independent piece.	36
505			
506			
507			
508			
509			
510	Table 4	A summary of the parameters of each of the three magnet systems on ATLAS.	38
511			
512	Table 5	A summary of the parameters of the inner detector and each of the subdetectors [13].	43
513			
514	Table 6	A summary of the expected performance of the combined inner detector [17]. Included are the reconstruction efficiencies for multiple particle types as well as the momentum and impact parameter (IP) resolution for various momenta.	44
515			
516			
517			
518			
519	Table 7	The trigger menu for the 2015 data collection with $L = 5 \times 10^{33} \text{ cm}^{-2} \text{ s}^{-1}$. Both the L1 and high level trigger (HLT) selection requirements and their trigger rates are shown measured at the specified luminosity are shown. The typical offline selections represent a typical set of offline requirements imposed after the trigger in an analysis.	58
520			
521			
522			
523			
524			
525			
526	Table 8	The dominant sources of corrections and systematic uncertainties in the JES estimation technique, including typical values for the correcting shift (Δ) and the associated uncertainty (σ).	94
527			
528			
529			
530	Table 9	The radial distances of each of the subdetectors and example arrival times for an R-Hadron with $\eta = 0$ and the specified β	101
531			
532			

533	Table 10	The expected number of events at each level of the selection for long-lived (LL) 1600 GeV, 10 ns R-Hadrons, along with the number of events observed in data, for 3.2 fb^{-1} . The simulated yields are shown with statistical uncertainties only. The total efficiency \times acceptance is also shown for the signal and the rejection factor relative to initial track requirement is shown for data. ¹²¹	
534			
535			
536			
537			
538			
539			
540	Table 11	A summary of the sources of systematic uncertainty for the data-driven background in the signal region. If the uncertainty depends on the mass, the maximum values are reported.	128
541			
542			
543			
544	Table 12	A summary of the sources of systematic uncertainty for the simulated signal yield. The uncertainty depends on the mass and lifetime, and the maximum negative and positive values are reported in the table.	130
545			
546			
547			
548	Table 13	Example of the contributing systematic variations to the total systematic for the E_T^{miss} Scale, as measured in a 1200 GeV, Stable R-Hadron signal sample.	132
549			
550			
551	Table 14	The estimated number of background events and the number of observed events in data for the specified selection regions prior to the requirement on mass. The background estimates show statistical and systematic uncertainties.	136
552			
553			
554			
555			
556	Table 15	The left and right extremum of the mass window for each generated mass point with a 10 ns lifetime.	137
557			
558	Table 16	The left and right extremum of the mass window used for each generated stable mass point.	137
559			
560	Table 17	The expected number of signal events, the expected number of background events, and the observed number of events in data with their respective statistical errors within the respective mass window for each generated stable mass point	138
561			
562			
563			
564			
565	Table 18	The expected number of signal events, the expected number of background events, and the observed number of events in data with their respective statistical errors within the respective mass window for each generated mass point with a lifetime of 10 ns.	138
566			
567			
568			
569			
570	Table 19	The observed and expected 95% CL lower limit on mass for gluino R-Hadrons for each considered lifetime.	141
571			
572	Table 20	The left and right extremum of the mass window for each generated mass point with a 50 ns lifetime.	146
573			
574	Table 21	The left and right extremum of the mass window for each generated mass point with a 30 ns lifetime.	146
575			
576	Table 22	The left and right extremum of the mass window for each generated mass point with a 10 ns lifetime.	147
577			

578	Table 23	The left and right extremum of the mass window used for each generated mass point with a lifetime of 3 ns.	147
579			
580	Table 24	The left and right extremum of the mass window used for each mass point with a lifetime of 1 ns.	147
581			
582	Table 25	The left and right extremum of the mass window for each generated mass point with a lifetime of 0.4 ns.	148
583			
584	Table 26	The left and right extremum of the mass window used for each generated stable mass point.	148
585			
586	Table 27	The expected number of signal events, the expected number of background events, and the observed number of events in data with their respective statistical errors within the respective mass window for each generated mass point with a lifetime of 50 ns.	148
587			
588			
589			
590			
591	Table 28	The expected number of signal events, the expected number of background events, and the observed number of events in data with their respective statistical errors within the respective mass window for each generated mass point with a lifetime of 30 ns.	149
592			
593			
594			
595			
596	Table 29	The expected number of signal events, the expected number of background events, and the observed number of events in data with their respective statistical errors within the respective mass window for each generated mass point with a lifetime of 10 ns.	149
597			
598			
599			
600			
601	Table 30	The expected number of signal events, the expected number of background events, and the observed number of events in data with their respective statistical errors within the respective mass window for each generated mass point with a lifetime of 3 ns.	150
602			
603			
604			
605			
606	Table 31	The expected number of signal events, the expected number of background events, and the observed number of events in data with their respective statistical errors within the respective mass window for each generated mass point with a lifetime of 1 ns.	150
607			
608			
609			
610			
611	Table 32	The expected number of signal events, the expected number of background events, and the observed number of events in data with their respective statistical errors within the respective mass window for each generated mass point with a lifetime of p4 ns.	151
612			
613			
614			
615			
616	Table 33	The expected number of signal events, the expected number of background events, and the observed number of events in data with their respective statistical errors within the respective mass window for each generated stable mass point	151
617			
618			
619			
620			

621 LISTINGS

622 ACRONYMS

- 623 SM Standard Model
624 CERN European Organization for Nuclear Research
625 SUSY Supersymmetry
626 MSSM Minimal Supersymmetric Model
627 cMSSM Constrained MSSM
628 pMSSM Phenomenological MSSM
629 LSP Lightest Supersymmetric Particle
630 LHC Large Hadron Collider
631 ATLAS A Toroidal LHC ApparatuS
632 CMS Compact Muon Solenoid
633 ALICE A Large Ion Collider Experiment
634 LHCb Large Hadron Collider beauty experiment
635 LEP the Large Electron Positron collider
636 PS Proton Synchrotron
637 PSB Proton Synchrotron Booster
638 SPS Super Proton Synchrotron
639 SCT silicon microstrip
640 TRT Transition Radiation Tracker
641 LAr liquid argon
642 EM electromagnetic
643 RPC Resistive Plate Chamber
644 TGC Thin Gap Chamber
645 MDT Monitored Drift Tube
646 CSC Cathode Strip Chamber
647 ToT time over threshold
648 RoI Region of Interest

- 649 LCW local cluster weighted
650 MIP minimally ionizing particle
651 IP impact parameter
652 EPJC European Physical Journal C
653 JES jet energy scale
654 LLP Long-Lived Particle
655 LL long-lived
656 VLL very long-lived
657 CR Control Region
658 NLO next-to-leading order
659 NLL next-to-leading logarithmic
660 PDF parton distribution function
661 ISR initial state radiation
662 RMS root mean square
663 IBL Insertible B-Layer
664 CP Combined Performance
665 MDT Monitored Drift Tube
666 RF radiofrequency
667 HLT high level trigger
668 QCD quantum chromodynamics
669 BSM beyond the Standard Model

670

671 INTRODUCTION

672 As of 2012, with the discovery of the Higgs boson, the **SM** provides a complete
673 and validated description of the interactions of fundamental particles. It de-
674 scribes a remarkable range of phenomena given its simple foundation, and has
675 been successful in explaining high energy physics in all experiments yet per-
676 formed. However, it is clear that the picture is incomplete: without a description
677 of gravity or an explanation for dark matter, an extension is necessary to de-
678 scribe new physics at higher energies. These deficiencies motivate a wide range
679 of experiments that search for new physics. The **LHC** provides the highest en-
680 ergy approach, seeking to discover unobserved particles or interactions in high
681 energy proton collisions.

682 The experiments at the **LHC** have searched for a variety of new phenomena
683 in the years since collisions began in 2010. A major focus of these searches has
684 been on Supersymmetry (**SUSY**), an extension to the **SM** which has the potential
685 to ameliorate many of its shortfalls. None of the searches have found evidence of
686 new physics, and between them they have begun to rule out a number of models
687 that would predict new particles at the TeV scale. This motivates searches for
688 more exotic signals that may have been missed, using analysis techniques tuned
689 specifically for those signals.

690 This dissertation presents a search for Long-Lived Particles (**LLPs**) using the
691 13 TeV collisions collected during 2015 at the **LHC**. Charged **LLPs** are predicted
692 to exist in a subset of **SUSY** models, and have dramatically different detector sig-
693 natures than both **SM** processes and other **SUSY** models. This search focuses on
694 isolating that unique signature using ionization in the ATLAS detector.

695 Part I provides the theoretical context and motivation for a search for new
696 physics in high energy collisions. Chapter 2 outlines the basic framework of the
697 **SM** and describes its particles and interactions. It also discusses the limitations of
698 the **SM** that motivate the existence of new physics. Chapter 3 discusses a possible
699 solution to the shortcomings of the **SM**, the theory of Supersymmetry, and the
700 ways that it can generate **LLP**.

701 Part II discusses the structure of the accelerator complex that provides col-
702 lisions as well as the experiment that measures them. Chapter 4 summarizes
703 the design and performance of the **LHC** and the features of the proton-proton
704 collisions it produces. Chapter 5 then discusses the components of the ATLAS
705 detector and how they can be used to measure the particles produced in **LHC**
706 collisions. Chapter 6 describes the algorithms used to reconstruct physics particles
707 and processes from the electronic signals in the detector.

708 Part III presents a measurement of calorimeter response, an important compo-
709 nent of event reconstruction used in many physics analyses. Chapter 7 describes
710 a direct, in situ measurement of calorimeter response using isolated hadrons, and
711 investigates the modeling of that response in simulation. Chapter 8 uses those

712 measurements to construct a correction for the energy of jets in simulation, the
713 **JES**, and to estimate an uncertainty for that correction.

714 Part **IV** details the search for **LLPs**. It begins with a discussion of the simulation
715 of **LLPs** in ATLAS, focusing on the detector signatures and how they vary with
716 the properties of those particles in Chapter **9**. Then Chapter **10** discusses the
717 strategy of the search and the requirements used to select **LLPs** and to reject **SM**
718 backgrounds. Chapter **11** explains a method for predicting the background from
719 **SM** processes, and shows a validation of the technique. Chapter **12** describes the
720 systematic uncertainties on both the selection efficiency for signal events and
721 the background method. The results of the search are presented in Chapter **13**.

722

PART I

723

THEORETICAL CONTEXT

724

You can put some informational part preamble text here.

725

726 STANDARD MODEL

727 The SM of particle physics seeks to explain the symmetries and interactions of
 728 fundamental particles. The SM provides predictions in particle physics for inter-
 729 actions up to the Planck scale (10^{19} GeV). It has been tested by several genera-
 730 tions of experiments and has been remarkably successful; no significant devia-
 731 tions from its predictions have been found.

732 The theory itself is a quantum field theory grown from an underlying sym-
 733 metry, $SU(3) \times SU(2) \times U(1)$, that generates all of the interactions consis-
 734 tent with experimental observations¹. These interactions are referred to as the
 735 Strong, Weak, and Electromagnetic forces. Each postulated symmetry necessi-
 736 tates the existence of an associated conserved charge, which appear as properties
 737 of the observed particles in nature.

738 Although this model has been very predictive, the theory is incomplete; for
 739 example, it is not able to describe gravity or astronomically observed dark mat-
 740 ter. These limitations suggest a need for an extension or new theory to describe
 741 physics at higher energies.

742 2.1 ACTION AND THE LAGRANGIAN

Originally, both action and the Lagrangian were constructed for an integral reformulation of the laws of classical mechanics, which is a purely mathematical step: any differential equation can be re-expressed in terms of an integral equation. The Lagrangian, \mathcal{L} , is classically given by the difference of kinetic energy and potential energy. The Lagrangian is defined this way so that the action, \mathcal{S} , given by

$$\mathcal{S}[\mathbf{q}(t)] = \int_{t_1}^{t_2} \mathcal{L}(\mathbf{q}, \dot{\mathbf{q}}, t) dt \quad (1)$$

743 returns the classical equations of motion when one requires it to be stationary
 744 in the path, $\mathbf{q}(t)$. This formulation of classical mechanics is extremely useful in
 745 calculations, and generalizes beautifully to cover all types of physics.

746 In particular, with the development of quantum mechanics in the twentieth
 747 century, the concepts of action and the Lagrangian were found to generalize to
 748 more complicated physics for which the classical laws do not hold. Quantum
 749 mechanics and quantum field theory can be constructed from the action, using
 750 the path integral formulation, by assuming that a particle undergoes all possible
 751 paths $\mathbf{q}(t)$ with an imaginary phase given by $e^{i\mathcal{S}[\mathbf{q}(t)]/\hbar}$. This reduces to classical
 752 mechanics in the limit as \hbar goes to zero, as all paths for which the action is not
 753 stationary interfere with each other so as to cancel their contributions. Because

¹ excluding gravity

754 the wavefunction of a particle can be completely determined through the action
 755 and the action depends only on the Lagrangian, the Lagrangian itself is sufficient
 756 to describe the physics governing the particle.

757 So, in both classical and quantum mechanics, the Lagrangian of a system con-
 758 tains everything there is to know about the system, apart from initial conditions.
 759 Thus, the most natural way to express that a system has a certain symmetry is to
 760 require that the Lagrangian is invariant under a corresponding symmetry trans-
 761 formation. This makes the Lagrangian the central piece of the discussion of
 762 gauge invariance; the mathematical representation of gauge invariance is that a
 763 gauge transformation on the appropriate components of the Lagrangian returns
 764 an identical Lagrangian. That is,

$$\mathcal{L}(\psi, D^\mu) = \mathcal{L}(U\psi, D'^\mu) \quad (2)$$

765 where ψ is the wavefunction and D^μ is the derivative operator, both of which
 766 may transform under a symmetry operation. There are a number of immedi-
 767 ate and surprisingly powerful consequences of requiring that the Lagrangian is
 768 invariant under a symmetry operation.

769 2.2 GAUGE INVARIANCE AND FORCES

770 The simplest possible relativistic, quantum Lagrangian for matter particles is the
 771 free Dirac Lagrangian, which describes a relativistic fermion in a vacuum.

$$\mathcal{L} = i\bar{\psi}\not{d}\psi - m\bar{\psi}\psi \quad (3)$$

772 A fermion denotes a particle with spin-1/2, and the kinematic term ($i\bar{\psi}\not{d}\psi$) is
 773 chosen to correctly describe the free propagation of a fermionic particle with
 774 mass m . This equation is clearly invariant under a global $U(1)$ transformation,
 775 that is changing ψ by a complex phase has no effect. The derivative operator
 776 commutes with a constant phase factor, and wherever ψ appears its complex
 777 conjugate also appears so as to cancel out the change of phase. However, the
 778 Lagrangian as written is not invariant under the local $U(1)$ symmetry postulated
 779 for the **SM**, which can be written as $U = e^{i\alpha(x)}$. The piece of the Lagrangian
 780 involving a derivative will return an extra term that will break the invariance of
 781 the Lagrangian under this transformation:

$$\begin{aligned} \mathcal{L}' &= i(\bar{\psi}U^\dagger)\not{d}(U\psi) - m(\bar{\psi}U^\dagger)(U\psi) \\ &= i(\bar{\psi}U^\dagger)U(\not{d} - \gamma^\mu\partial_\mu\alpha(x))\psi - m(\bar{\psi}U^\dagger)(U\psi) \\ &= i\bar{\psi}\not{d}\psi - m\bar{\psi}\psi - i\gamma^\mu\partial_\mu\alpha(x)\bar{\psi}\psi \\ &= \mathcal{L} - i\gamma^\mu\partial_\mu\alpha(x)\bar{\psi}\psi \\ &\neq \mathcal{L} \end{aligned}$$

782 So, in order to enforce the required symmetry, the typical approach is to con-
 783 struct a covariant derivative, that is to add a term to the derivative operator

so that the unwanted term in \mathcal{L}' is exactly canceled. A generic form for such a derivative is given by

$$D^\mu = \partial^\mu - iqA^\mu$$

where at this point A^μ is an arbitrary field that transforms under the $U(1)$ operator and q is a scaling factor. Adding this component to the above Lagrangian gives

$$\mathcal{L}' = i(\bar{\psi}U^\dagger)U(\not{d} - \gamma^\mu\partial_\mu\alpha(x) - iq\gamma^\mu A'_\mu)\psi - m(\bar{\psi}U^\dagger)(U\psi) \quad (4)$$

$$\mathcal{L}' = \mathcal{L} + \gamma^\mu(-i\partial_\mu\alpha(x) - iqA'_\mu + iqA_\mu)\bar{\psi}\psi \quad (5)$$

and because the transformation of A^μ is unspecified, $\mathcal{L} = \mathcal{L}'$ whenever

$$A'_\mu = A_\mu - \frac{1}{q}\partial_\mu\alpha(x)$$

The above procedure demonstrated that beginning with the Lagrangian for a free fermion and imposing a local $U(1)$ symmetry required the existence of a vector field A^μ , and specified its transformation under the $U(1)$ gauge group. The additional term in the derivative can be expanded to form a completely separate term in the Lagrangian,

$$\mathcal{L} = i\bar{\psi}\not{d}\psi - m\bar{\psi}\psi - (q\bar{\psi}\gamma^\mu\psi)A^\mu \quad (6)$$

and in this form it is clear that the A^μ term has the exact form of the electromagnetic interaction. That is, this is the Lagrangian which reproduces the relativistic form of Maxwell's equations for a particle interacting with an electromagnetic field. It is natural to also introduce a term to the Lagrangian at this point to describe the free propagation of the vector A field, where the propagation of a vector field has the form of

$$-\frac{1}{16\pi}F^{\mu\nu}F_{\mu\nu} \quad \text{with} \quad F_{\mu\nu} = \partial_\mu A_\nu - \partial_\nu A_\mu \quad (7)$$

This then also describes the electromagnetic interactions in a vacuum and the propagation of a photon. This component of the Lagrangian should also potentially include a mass term, but such a term would not be gauge invariant and so must be excluded. The photon is an example of a gauge boson, a spin-1 particle required to exist by a gauge symmetry of the Lagrangian and one that corresponds to a force. In summary, requiring the $U(1)$ symmetry was enough to recover all of electromagnetism and to predict the existence of a photon in the SM.

The interaction term that was placed into the Lagrangian by this procedure can be conveniently summarized with Feynman diagrams, which diagrammatically represent a transition from an initial state to a final state. The contribution

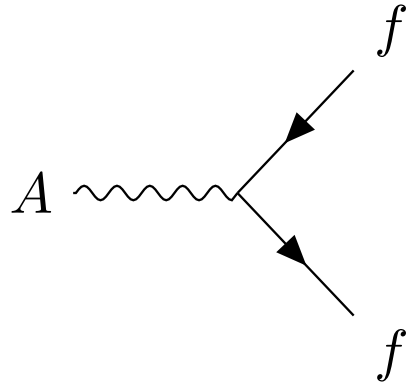


Figure 1: A Feynman diagram representing the interaction of the A field with a generic fermion, f .

of all diagrams that start with the same initial state and end with the same final state must be summed, but more complicated diagrams can be built by linking together the simplest versions. A diagram that corresponds to the above term, $(q\bar{\psi}\gamma^\mu\psi)A^\mu$, is shown in Figure 1, for an interaction with a generic fermion.

2.2.1 $SU(2) \times U(1)$ AND THE ELECTROWEAK FORCE

The full picture of the electroweak section of the SM is more complicated than the simplified explanation of the electromagnetic piece described above. In practice, it is necessary to consider the entire $SU(2) \times U(1)$ symmetry together, but the procedure is the same. Enforcing the symmetry on the Lagrangian requires the introduction of a covariant derivative, this time with four total distinct terms, one for each of the generators of $SU(2) \times U(1)$. The result is a series of terms in the Lagrangian which describe the interaction of a fermion with four vector (spin-1) fields, the W_1 , W_2 , W_3 , and B fields. These fields can mix in the quantum sense, and linear combinations form the W^+ , W^- , Z , and A fields that are considered actual particles in the SM².

2.2.2 $SU(3)$ AND THE STRONG FORCE

The same procedure can be applied starting with the $SU(3)$ symmetry requirement, where eight additional fields must be introduced, one for each of the generators of $SU(3)$. The resulting Lagrangian describes quantum chromodynamics (QCD) and predicts the existence of eight gauge bosons known collectively as gluons. The complexity of the interactions of those eight gluons leads to surprising phenomena, discussed in Section 2.5.2.

² These states are the actual particles because they are mass eigenstates, but the full explanation of this will have to wait for the discussion of the Higgs mechanism.

834 2.3 NOETHER'S THEOREM, CHARGES, AND MATTER

835 Another direct consequence of the symmetries stipulated in the SM are a series
836 of conserved quantities, Noether charges, named after the mathematician and
837 physicist Emmy Noether. The charges arise as a direct consequence of Noether's
838 theorem, which can be informally stated as

839 *For every symmetry of the Lagrangian, there exists a corresponding phys-
840 ical quantity whose value is conserved in time.*

841 Or, stated another way, symmetries of the Lagrangian mathematically require
842 the conservation of specific quantities taken from the Lagrangian. This rela-
843 tionship can also be thought of as operating in the other direction, the exis-
844 tence of a conserved charge can be shown to generate the symmetry in the La-
845 grangian. This theorem is actually quite striking in a somewhat unexpected re-
846 lation between simple geometric symmetries and physically observable conser-
847 vation laws. For example, the theorem connects the translation invariance of
848 the Lagrangian in space to the conservation of momentum and the translation
849 invariance in time to the conservation of energy.

850 In the context of the SM, the required symmetries of $U(1) \times SU(2) \times SU(3)$
851 correspond to the charges that are considered properties of all elementary par-
852 ticles. The most familiar of these properties is the electric charge, Q, which is
853 one of the conserved quantities of $SU(2) \times U(1)$. The remaining pieces of
854 $SU(2) \times U(1)$ correspond to weak isospin, T and T_3 , where T has only non-
855 negative values and T_3 can be positive and negative. The $SU(3)$ symmetry is
856 generated by the three colors of QCD, red, green, and blue, each with a corre-
857 sponding opposite color, anti-red, anti-green, and anti-blue.

858 The matter in the observable universe consists of a collection of particles which
859 carry these charges, in addition to spin and mass. The particles typically thought
860 of as matter are all fermions: particles with spin-1/2. All of the fermions belong
861 to one of two groups, quarks and leptons, and one of three generations. Each
862 of the generations have similar properties but significantly different masses; the
863 particles in consecutive generations have increasing mass. Quarks are distin-
864 guished from leptons in that they carry color charge, in addition to electric charge
865 and weak isospin. The particles in the SM are summarized in Figure 2, and the
866 matter particles are the twelve types of fermions displayed on the left side of the
867 graphic.

868 2.3.1 QUARKS

869 The three generations of quarks each consist of a quark with electric charge +2/3
870 and one with charge -1/3. They are called up and down, charm and strange,
871 and top and bottom respectively, and these are referred to as the quark flavors.
872 Although Figure 2 only shows these six flavors, there is a unique particle for each
873 combination of the three colors and flavor. And each quark has an anti-particle
874 with the opposite electric and color charge values.

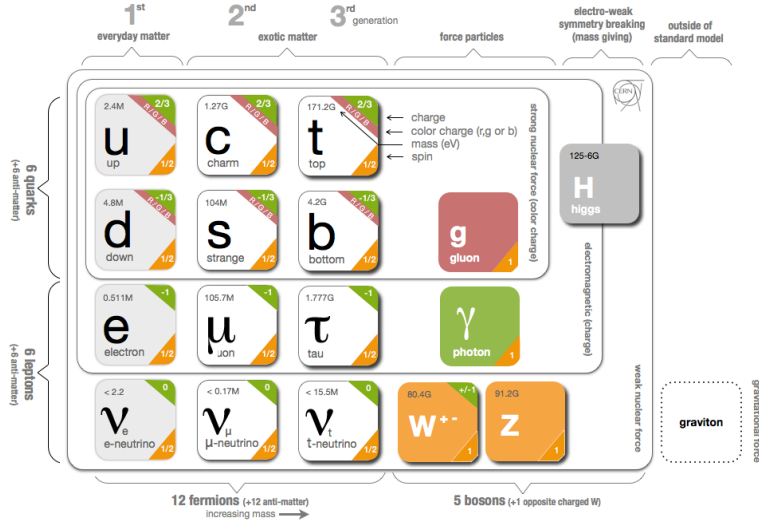


Figure 2: The particle content of the SM.

However, individual quarks are never observed in nature, but instead form color-neutral bound states. This is a consequence of interaction of gluons with color charge called confinement, discussed in Section 2.5.2. One way to form a color neutral combination is a bound state of three quarks with three different color charges, called a baryon. Baryons are the most common type of quark configuration in conventional matter, and include protons and neutrons. The other common configuration is a bound state of a quark and an anti-quark, called a meson, where the two quarks have opposite colors. Although there is no direct conservation law resulting from the symmetries of the SM Lagrangian, an accidental symmetry results in the approximate conservation of baryon number, B , where baryons have $B = 1$ and mesons have $B = 0$. That is, no interactions are present which directly³ alter baryon number

2.3.2 LEPTONS

The remaining fermions, the leptons, do not carry color charge. Each generation contains an electrically charged lepton, the electron, muon, and tau, and an electrically neutral lepton called a neutrino. For the charged leptons, the flavors are mass eigenstates, with the masses listed in Figure 2. The flavors of the neutrinos, on the other hand, are not mass eigenstates: their propagation in quantum superpositions of flavor states leads to oscillations between different flavors. The absolute masses of the neutrinos are not currently known, but the phenomenon of oscillations shows that they have three different mass values. Another accidental symmetry leads to an approximate⁴ conservation of lepton number L , the differ-

³ There are combinations of interactions which can modify either B or L individually, but the combination $B - L$ appears to be conserved in the SM.

⁴ See footnote 3.

ence in the number of leptons and anti-leptons; again there are no interactions present in the SM which directly alter lepton number.

2.3.3 CHIRALITY

All of the fermions described above have two possible values of the magnitude of weak isospin, T , either 0 or 1/2. The fermions with $T = 0$ are called right-handed, while those with $T = 1/2$ are called left-handed. Because T is the charge corresponding to the weak force, right-handed particles do not interact with the weak gauge bosons in the same way that neutral particles do not interact with photons. For left-handed fermions, each of the quark and lepton generations have one particle with $T_3 = -1/2$ and one with $T_3 = +1/2$. The neutrinos have $T_3 = +1/2$, while the charged leptons have $T_3 = -1/2$. Similarly, the positively charged quarks have $T_3 = +1/2$ and the negatively charged quarks have $T_3 = -1/2$. Because the right-handed neutrinos would have no charge of any type, it is not clear if they exist at all.

2.4 HIGGS MECHANISM AND MASS

The description of the electroweak forces above left out an important part of the observed nature of the electroweak force. Many physical experiments observed phenomena corresponding to the interaction of the weak bosons that were best explained if they had significant masses. But as mentioned before, massive bosons would break the gauge invariance of the Lagrangian. A large mass for the W and Z bosons would explain the relative weakness of their interactions compared to the electromagnetic field. The Lagrangian's discussed above did not include a mass term for the gauge bosons, and in fact such a term would not be allowed by the requirement of gauge invariance. This was a significant problem for the SM, and the symmetry of the electroweak sector would have to be broken in order to allow for non zero masses for some of the gauge bosons.

One mechanism to allow for this spontaneous symmetry breaking is the Higgs mechanism, which posits the existence of an additional scalar field. It begins with a $SU(2) \times U(1)$ invariant Lagrangian of the form

$$\mathcal{L} = |D_\mu \phi|^2 - \frac{1}{2}\mu^2\phi^+\phi - \frac{1}{4}\lambda(\phi^+\phi)^2 \quad (8)$$

where ϕ is the new scalar field with two components and, importantly, μ^2 is negative. This leads to a minimum value of the field at a non-zero value of ϕ , specifically where

$$\langle\phi\rangle = \frac{1}{\sqrt{2}} \begin{pmatrix} 0 \\ v \end{pmatrix} \quad \text{with} \quad v = \frac{2\mu^2}{\lambda} \quad (9)$$

929 Expanding the original Lagrangian about its expectation value in terms of the
 930 perturbation H ,

$$\langle \phi \rangle = \frac{1}{\sqrt{2}} \begin{pmatrix} 0 \\ v + H \end{pmatrix} \quad (10)$$

931 gives potential terms in the Lagrangian like

$$\mathcal{L}_H = -\frac{1}{2} m_H^2 H^2 - \sqrt{\frac{\lambda}{2}} m_H H^3 - \frac{1}{4} \lambda H^4 \quad (11)$$

932 where $m_H = \sqrt{2}\mu$. The form of this Lagrangian shows that the non-zero ex-
 933 pectation value of the ϕ field has introduced a massive scalar field H with self
 934 interaction terms. It has an additional important consequence on the description
 935 of the gauge bosons, through the expansion of the term involving the covariant
 936 derivative:

$$|D_\mu \phi|^2 \supset \frac{1}{8} (g^2 (W_{1\mu} W_1^\mu + W_{2\mu} W_2^\mu) + (g' B_\mu - g W_3 \mu)^2) \quad (12)$$

937 where the W_i and B fields are the original $SU(2) \times U(1)$ gauge fields men-
 938 tioned previously. The above equation can be rearranged using linear combi-
 939 nations of the fields to from mass terms for the gauge bosons, and the mass eigen-
 940 states are exactly the W^\pm , Z , and A fields. Only the A field, corresponding to
 941 the photon, results in a zero mass, and the remaining three fields acquire masses.
 942 Because the previously introduced Lagrangian, written in terms of ϕ , was clearly
 943 gauge invariant, this resulting configuration must also be gauge invariant.

944 This is the Higgs mechanism, where the introduction of a gauge invariant
 945 scalar field with a non-zero expectation value can generate masses for the gauge
 946 bosons without violating the underlying symmetries. The particle that is associ-
 947 ated with the perturbations of this field, H , is called the Higgs boson, and is said
 948 to generate the masses of the remaining bosons because the vacuum expectation
 949 value introduces mass-like terms for each of the bosons. The resulting masses
 950 are listed in Figure 2. Because this mechanism was so successful in describing
 951 the observed properties of the W and Z bosons, it has been considered part of
 952 the SM for decades, although the actual Higgs boson was only recently observed
 953 in 2012, confirming the theory.

954 The Higgs mechanism is also responsible for generating the masses of the
 955 fermions. The original mass terms that were listed in the Lagrangian for fermions
 956 are replaced with Yukawa coupling terms, which introduce interactions between
 957 the ϕ field and the fermions. Like with the gauge bosons, the non-zero expec-
 958 tation value of the field yields mass terms, and the expansion about that value
 959 introduces interaction terms between the fermions and the Higgs boson. The
 960 masses are different between each fermion because each has a different Yukawa
 961 coupling, which results in the masses listed in Figure 2.

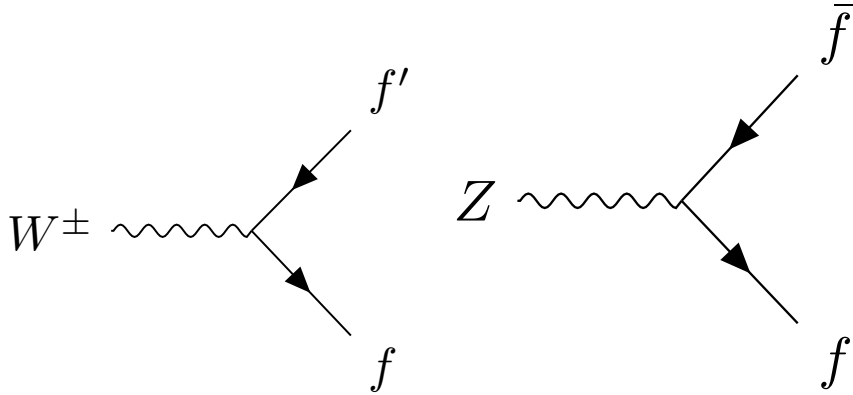


Figure 3: The Feynman diagrams representing the decays of the W and Z bosons to fermions. Here f indicates a generic fermion, \bar{f} its antiparticle, and f' the partner of that fermion in the same generation.

962 2.5 PHENOMENOLOGY

963 The SM Lagrangian described above contains all of the information necessary
 964 to describe particle physics through the path integral formulation. However, a
 965 tremendous amount of complexity emerges from that description because of the
 966 diverse allowed interactions between the ensemble of particles in the SM. A qual-
 967 itative understanding of the phenomenology produced by those interactions is
 968 immensely helpful in understanding the analysis of particle physics.

969 2.5.1 ELECTROWEAK PHYSICS

970 The masses of the W and Z bosons result in significantly different processes
 971 for the weak fields than the electromagnetic field, despite their interactions be-
 972 ing similar before symmetry breaking. The massless photon is stable, and can
 973 propagate in a vacuum, resulting in the familiar long range interactions of elec-
 974 tromagnetism. The W and Z bosons, however, are unstable, as they have large
 975 enough masses to decay to fermions, such as the decays shown in Figure 3. For
 976 this reason, photons can be observed directly, while the other bosons are suffi-
 977 ciently short-lived that they can only be measured from their decay products.

978 Because the electroweak bosons interact with both quarks and leptons, they
 979 are responsible for the production of leptons in proton-proton collisions. Z
 980 bosons and photons produce pairs of opposite sign, same flavor leptons. W
 981 bosons, on the other hand, produce a single lepton and the corresponding neu-
 982 trino.

983 2.5.2 STRONG PHYSICS

984 The phenomenology of the strong sector differs significantly from the weak sec-
 985 tor because the gluons are massless but color charged. Because of this, gluons

986 can interact with each other, and contributions from multiple gluon interactions
 987 lead to a significant growth in the strength of the field at low energies. The depen-
 988 dence of the field strength on the energy scale is described by renormalization,
 989 and in QCD the coupling is only small at high energies. Below approximately 1
 990 GeV, the strength of those interactions results in confinement: the interactions
 991 are so strong that when quark-antiquark pairs separate, the fields between them
 992 generate additional quarks to form color neutral bound states. Above around
 993 the GeV scale, the interactions of quarks become perturbative, similar to the
 994 electroweak fields; this phenomenon is known as asymptotic freedom.

995 At lower energies, however, the strength of the strong interaction is so signif-
 996 icant that the interactions of color-charged particles create additional particles
 997 until they form neutral bound-states. This process is known as hadronization,
 998 and explains why no quarks are observed isolated in nature: they all form bound
 999 states of hadrons like protons, neutrons, and pions. The hadronization process
 1000 can produce a significant number of particles, so that a single energetic quark
 1001 recoiling against another quark can generate a cascade of dozens of hadrons.
 1002 Because of the initial boost of such an energetic configuration, the resulting
 1003 hadrons are collimated, and conical spray of particles often referred to as a jet.

1004 2.5.3 PROTON-PROTON COLLISIONS

1005 Proton-proton collisions are a convenient way to generate high energy interac-
 1006 tions to probe the SM and to search for new physics. At the energies that will be
 1007 discussed in this analysis, the substructure of the protons is very important to the
 1008 description of the resulting interactions. At lowest order, protons are composed
 1009 of two up quarks and one down quark, but this description is incomplete. The
 1010 actual bound state includes a chaotic sea of additional quarks and gluons, each of
 1011 which carries a variable fraction of the proton's energy. When a proton-proton
 1012 collision takes place, it is these constituents that interact with each other, result-
 1013 ing in a highly variable collision energy even when the proton-proton energy is
 1014 consistent.

1015 The fraction of the energy carried by each constituent varies moment to mo-
 1016 ment, but can be modelled probabilistically by PDFs. These are difficult to pre-
 1017 dict theoretically, as the QCD calculations are extremely complex, and instead
 1018 are measured in hard-scattering experiments. They are usually represented by
 1019 how often a given type of particle carries a fraction x of the total proton energy.
 1020 Those fraction change significantly with the scale of the interaction, Q ; the PDFs
 1021 of proton-proton collisions at both $Q^2 = 10 \text{ GeV}^2$ and $Q^2 = 10^4 \text{ GeV}^2$ are
 1022 shown in Figure 4.

1023 2.6 LIMITATIONS

1024 Despite the great success of the relatively simple SM in describing such a broad
 1025 range of emergent phenomena, it is clear that the picture it presents of the in-
 1026 teractions of fundamental particles is incomplete. The SM contains concerning
 1027 coincidences that suggest a more ordered underlying substructure that is not ex-

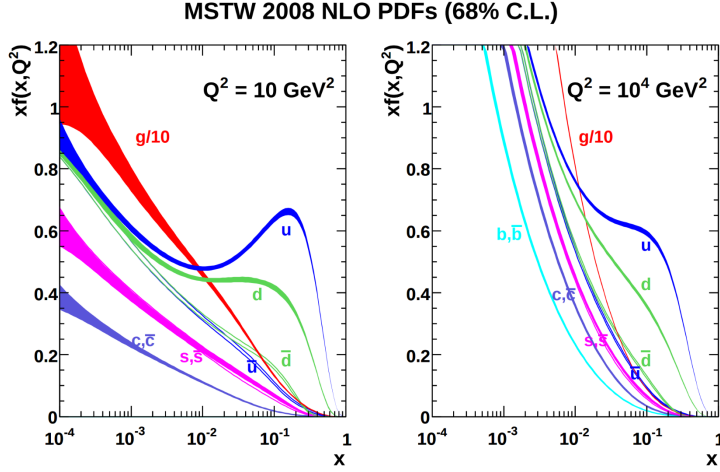


Figure 4: The PDFs for proton-proton collisions at $Q^2 = 10 \text{ GeV}^2$ and $Q^2 = 10^4 \text{ GeV}^2$. Each shows the fraction of particles which carry a fraction x of the total proton energy at the specified scale [1].

1028 pressed in the current form. It also fails to explain a number of cosmological
 1029 measurements of the nature of matter in the universe. These limitations suggest
 1030 the need for new, beyond the Standard Model (BSM) physics that would provide
 1031 a more complete description at higher energies.

1032 2.6.1 THEORETICAL CONCERNS

1033 There have been no successful integrations of the SM's description of the elec-
 1034 troweak and strong forces with the description of gravity, and it is still unclear
 1035 how to account for the effects of gravity at the Planck scale of approximately 10^{19}
 1036 GeV, where its interactions are as strong as the remaining forces. The Planck
 1037 scale is an important cutoff for the SM, as it is clear that the SM must break down
 1038 somewhere between the current highest energy tests of the SM, around 1 TeV,
 1039 and the Planck scale.

1040 One example of this is the Higgs mass, which is determined in the SM by a
 1041 sum of its bare mass and the interactions in the vacuum with all massive parti-
 1042 cles. As there must be new physics at the Planck scale to describe gravity, some
 1043 of those corrections would include contributions at a scale seventeen orders of
 1044 magnitude above the mass of the Higgs. Either the bare mass of the Higgs boson
 1045 precisely cancels those contributions to leave a remainder seventeen orders of
 1046 magnitudes smaller, or a new theory exists at a lower scale the shields the Higgs
 1047 mass from those terms. A theory where such a unlikely cancellation of free pa-
 1048 rameters occurs is called fine-tuned, and one that is free from such cancellations
 1049 is called natural. Theories where the mass of the Higgs is natural are usually pre-
 1050 ferred, as the suggest an underlying, coherent structure. The enormous differ-
 1051 ence in scales between the weak scale (including the Higgs mass), and the Planck
 1052 scale, is often referred to as the hierarchy problem.

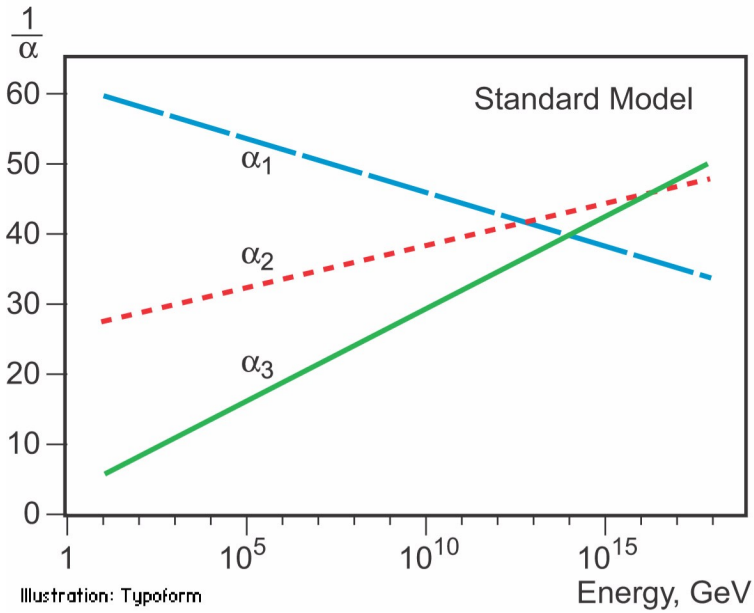


Figure 5: An approximation of the running of the coupling constants in the SM up to the Planck scale [2].

1053 There is also a compelling argument that the $SU(3) \times SU(2) \times U(1)$ gauge
 1054 structure of the SM might originate from a single, unified gauge theory. For ex-
 1055 ample, it is possible to represent that gauge structure as a $SU(5)$ gauge group
 1056 with only a few inconsistencies with the current implementation. This unifica-
 1057 tion is suggested by the scaling of the coupling constants for each of the forces
 1058 under renormalization; they come close to converging to a single value at higher
 1059 energies, as seen in Figure 5. An additional correction to the scaling of the cou-
 1060 pling constants from new physics above the TeV scale could cause them to merge
 1061 into a single value at high energies.

1062 2.6.2 COSMOLOGICAL OBSERVATIONS

1063 The SM contains a symmetry in the description of matter and antimatter that is
 1064 not reflected in cosmological observations. The processes of the standard model
 1065 create or remove matter and antimatter in equal amounts, so a universe that be-
 1066 gins with an equal quantity of each should result in a universe with an approxi-
 1067 mate⁵ balance of matter and antimatter. However, cosmological observations of
 1068 the relative amount of each type clearly show that the directly observable mass
 1069 of the universe is overwhelmingly made of matter. As this difference is largely
 1070 a difference in the generation of baryons and anti-baryons, this discrepancy is
 1071 often referred to as the baryogenesis problem.

1072 A number of astrophysical observations of large scale gravitational interac-
 1073 tions suggest the presence of a significant amount of non-luminous matter that
 1074 interacts with the normal matter only gravitationally. The first evidence of this

⁵There are some processes in the standard model which can result in a small imbalance of matter and antimatter, but not at the scale observed cosmologically.

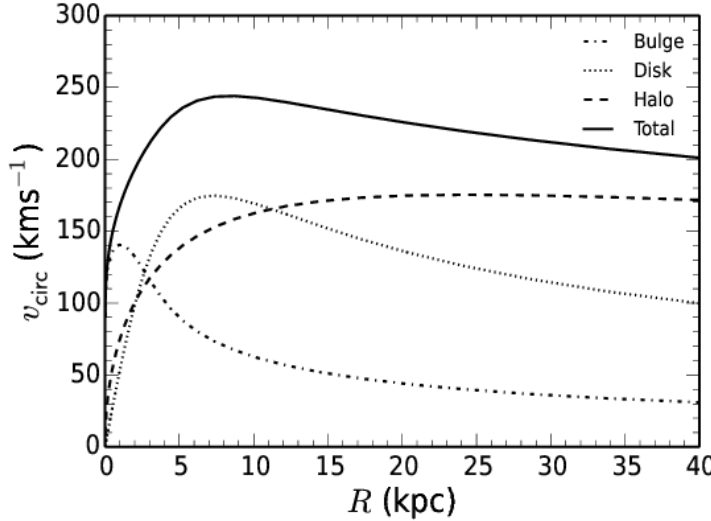


Figure 6: The distribution of velocities of stars as a function of the radius from the center of the galaxy. The contributions to the velocity from the various components of matter in the galaxy are shown [3].

1075 came from the observation of galactic rotation curves, the velocities of stars as
 1076 a function of the radius from the center of a galaxy. These can be directly pre-
 1077 dicted from the amount of matter contained within the sphere up to the radius of
 1078 the star. An estimate of velocity based only on the luminous matter in the galax-
 1079 ies would predict a dependence that falls off with the radius, but the observed
 1080 curves show a mostly constant distribution of velocities [3], as seen in Figure 6.
 1081 The higher velocities than predicted by the luminous matter can be explained by
 1082 a halo of dark matter that extends significantly outside the galactic disk.

1083 This dark matter accounts for a majority of the matter in the universe, and is
 1084 incompatible with the matter particles predicted by the SM. Many observations
 1085 support its existence, but there have been no direct detections of a particle which
 1086 could account for the large quantity of gravitationally interacting dark matter.
 1087 The SM would have to require a significant extension to include the particles
 1088 needed to explain dark matter and the processes needed to explain the observed
 1089 matter-antimatter asymmetry.

1090

1091 SUPERSYMMETRY

1092 The theory of [SUSY](#) presents an extension to the [SM](#) that solves a number of the
1093 outstanding issues. It is based on another proposed symmetry, one which intro-
1094 duces an equality between the fermionic particles and proposed bosonic partners
1095 and also between bosonic particles and their proposed fermionic partners. The
1096 symmetry is defined by extending spacetime into a superspace, which includes
1097 one dimension that describes a particle's spin: a transformation in this space
1098 moves a fermion with spin-1/2 to a boson with spin-0 or vice-versa. Requiring
1099 the [SM](#) to be symmetrical under these transformations requires the existence of a
1100 bosonic partner for every current matter fermion in the [SM](#) and a fermionic part-
1101 ner for every boson. The partners are called superparticles (sparticles), where
1102 quarks partner with squarks and leptons partner with sleptons, and each boson
1103 has a fermionic partner called a gaugino. The superpartners, in the original form
1104 of the theory, should be identical to the original particle in every way except for
1105 spin; that is they would have the same quantum charges and the same mass.

1106 However, the simplest version of the theory, where the symmetry is unbro-
1107 ken, is incompatible with current observations of physics in a number of sys-
1108 tems. The most striking example comes from the electron, as the superpartner
1109 of an electron would introduce a stable, negatively charged, and bosonic parti-
1110 cle. Such a particle would drastically alter atomic properties by providing a way
1111 to create atoms without the valence structure of electrons that results from the
1112 Pauli exclusion principle for fermions. Various high energy physics measure-
1113 ments have also confirmed the spin of the W and Z bosons, for example, and
1114 a fermionic gaugino has never been produced at those masses. The solution to
1115 this incompatibility with observation is to conjecture that the symmetry exists
1116 but is spontaneously broken, where the masses of the supersymmetric particles
1117 are significantly larger than those of the current [SM](#) particles. Like the sponta-
1118 neous symmetry breaking of the electroweak system, this symmetry breaking
1119 can be accomplished by introducing an additional Higgs mechanism.

1120 3.1 STRUCTURE

1121 There are a number of ways to model the particulars of [SUSY](#), but many of the
1122 resulting phenomena are similar, and a discussion of an example is sufficient
1123 to describe the structure and results of the theory. The [MSSM](#) is one example of
1124 a complete description that includes the necessary symmetry breaking to result
1125 in the different masses between particles and sparticles [4]. It is called minimal
1126 because it is designed to use the simplest possible extension to the [SM](#) that incor-
1127 porates [SUSY](#). However even a minimal version includes a remarkable number of
1128 free parameters, over 100, and the [MSSM](#) is often further constrained to include

Sector	Particles	Sparticles
Baryonic Matter	(u, d)	(\tilde{u}, \tilde{d})
	(c, s)	(\tilde{c}, \tilde{s})
	(t, b)	(\tilde{t}, \tilde{b})
Leptonic Matter	(ν_e, e)	$(\tilde{\nu}_e, \tilde{e})$
	(ν_μ, μ)	$(\tilde{\nu}_m u, \tilde{\mu})$
	(ν_τ, τ)	$(\tilde{\nu}_\tau, \tilde{\tau})$
Higgs	(H_u^+, H_u^0)	$(\tilde{H}_u^+, \tilde{H}_u^0)$
	(H_d^0, H_d^-)	$(\tilde{H}_d^0, \tilde{H}_d^-)$
Strong	g	\tilde{g}
Electroweak	(W^\pm, W^0)	$(\tilde{W}^\pm, \tilde{W}^0)$
	B^0	\tilde{B}^0

Table 1: The particles in the SM and their corresponding superpartners in the MSSM.

fewer parameters in models such as the Phenomenological MSSM ([pMSSM](#)) and the Constrained MSSM ([cMSSM](#)) [5].

The theory includes a sparticle partner for every SM particle, which are listed in Table 1. To then provide the different masses for those sparticles, the MSSM introduces a second Higgs interaction. The resulting scalar field, along with the original Higgs field, generates five total particles, h^0 , the original Higgs boson, A^0 , H^0 , and H^\pm , where the last two are electrically charged. These Higgs bosons can mix with the supersymmetric gauginos to form a series of mass eigenstates. These are usually referred to by the order of their masses, where the neutral gauginos (neutralinos) are labeled $\tilde{\chi}_1^0$, $\tilde{\chi}_2^0$, $\tilde{\chi}_3^0$, and $\tilde{\chi}_4^0$. The charged gauginos (charginos) are similarly labeled $\tilde{\chi}_1^\pm$ and $\tilde{\chi}_2^\pm$. Table 1, lists the gauginos which are direct partners of the original gauge bosons in the SM rather than these resulting mass eigenstates.

In addition to the new particle content, the MSSM introduces new interactions for the gauge bosons and gauginos. All interaction terms are added to the Lagrangian which describe the interaction of a gauge boson or gaugino with a particle or sparticle with the appropriate charge. Such terms include a few interactions which would violate the observed $B - L$ symmetry that prevents proton decay. Either the couplings on these terms must be extremely small to match the experimental limits on those decays, or an additional symmetry must be imposed to exclude the terms. The MSSM and several other SUSY models choose to introduce a new symmetry known as R-parity, where the conserved quantity, P_R is defined as

$$P_R = (-1)^{2s+3(B-L)}$$

with s as the spin of the particle. Sparticles are R-parity odd while SM particles are R-parity even. And by requiring that each term in the supersymmetric Lagrangian conserves R-parity, it is enforced that sparticles are produced in pairs.

1145 The conservation of R-parity removes the $B - L$ violating terms from the La-
 1146 grangian. The remaining terms include all of the interactions of the **SM** where
 1147 two of the particles are replaced with their **SUSY** partners, so that R-parity is con-
 1148 served in the interactions. This also has an important significance in making the
 1149 Lightest Supersymmetric Particle (**LSP**), the $\tilde{\chi}_1^0$, stable, as it cannot decay to only
 1150 **SM** particles without violating the conservation of R-parity. The heavier sparti-
 1151 cles then decay in chains, emitting an **SM** particle in each step, and leave behind
 1152 the **LSP** at the end of the chain.

1153 3.2 MOTIVATION

1154 **SUSY** models, including the **MSSM**, ameliorate many of the issues in the **SM** dis-
 1155 cussed in Section 2.6. **SUSY** is particularly well motivated as a natural extension
 1156 to the **SM** because the simple underlying assumption solves three major, seem-
 1157 ingly unrelated concerns. And these benefits all require that at least some of the
 1158 sparticles exist at the TeV scale, within the reach of modern collider experiments.

1159 The first, a solution to the hierarchy problem, comes as a direct consequence
 1160 of the introduction of massive superpartners for each **SM** particle. The contribu-
 1161 tions to the Higgs mass from the much higher energy Planck scale come from a
 1162 series of loop diagrams in the **SM**, where each massive **SM** particle has a loop con-
 1163 tribution. The introduction of superpartners generates a series of corresponding
 1164 diagrams for correction to the Higgs mass, with opposite sign contributions be-
 1165 cause the superpartners have different spins. Those opposite sign contributions
 1166 cancel the divergences from the original loop diagrams at high energies, leaving
 1167 behind a correction to the Higgs mass that is at the same scale as the masses of the
 1168 superpartners. If the superpartners exist at the TeV scale, then the Higgs mass
 1169 of 125 GeV can be explained without significant fine-tuning, and the theory be-
 1170 comes natural.

1171 **SUSY** also has the potential to precisely enable the unification of the coupling
 1172 constants at high energy. Without supersymmetric contributions, the coupling
 1173 constants come close to a single value near the Planck scale suggesting an un-
 1174 derlying trend, as shown in Figure 5, but they do not exactly merge. With the
 1175 addition of the **MSSM**, they can join almost exactly at a single point, enabling a
 1176 unification into a single gauge theory at high energy, as shown in Figure 7. This
 1177 precise unification, like the naturalness argument, also requires that the masses
 1178 of the superpartners be near the TeV scale.

1179 The presence of R-parity in a **SUSY** model also provides an explanation for
 1180 dark matter. The **LSP**, as discussed in Section 3.1, is a massive, neutral, and stable
 1181 particle as long as R-parity is conserved. In the early universe, when the energy
 1182 density was extremely high, **LSPs** could be spontaneously produced just as often
 1183 as other particles like photons, and would result in a thermal equilibrium. Then,
 1184 as the universe cooled, the average energy would be too low to create additional
 1185 **LSPs**, and they would be left behind and only interact with the remaining matter
 1186 gravitationally, a process called freeze out. Since those particles are stable, they
 1187 would remain indefinitely. With the existence of an **LSP** at around the TeV scale,
 1188 this process can explain the observed amount of dark matter in the universe. A

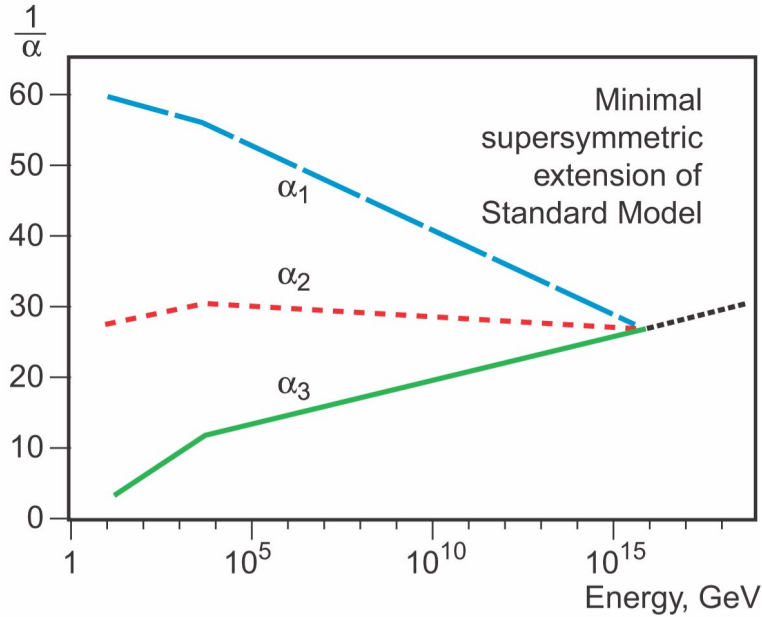


Figure 7: An approximation of the running of the coupling constants in the [MSSM](#) up to the Planck scale [2].

1189 **WIMP!** (**WIMP!**), exactly what is proposed in the [LSP](#), provides the correct interaction
 1190 rate to predict the currently observed ratio of dark matter to baryonic matter.
 1191

1192 Together, this variety of solutions to existing problems provides strong theoretical
 1193 support for the existence of [SUSY](#) near the TeV scale. The [LHC](#) is the first
 1194 collider experiment to be able to probe into TeV scale interactions, providing a
 1195 new opportunity to search for this extension to the [SM](#). A range of models have
 1196 begun to be excluded with masses above 1 TeV [6], leading to a motivation to
 1197 explore a wider variety of models with phenomena that may have been missed
 1198 by the most direct search strategies.

1199 3.3 SIMPLIFIED MODELS

1200 The [MSSM](#) is just one example of a large suite of [SUSY](#) models with similar results.
 1201 Each of those models can have hundreds of individual parameters that ultimately
 1202 determine the masses and interactions of the supersymmetric particles. To avoid
 1203 this complexity in making experimental measurements, the analyses of high en-
 1204 ergy collisions often rely on simplified models. These models focus on a single
 1205 process predicted by a theory, and the observable parameters such as the mass
 1206 of the particles and their lifetimes are controlled directly, rather than tuning the
 1207 hundreds of underlying parameters. This allows straightforward simulation of
 1208 a specific event topology with control over the parameters that most directly
 1209 influence the experimental signatures.

1210 Experimental analyses use these models to search for new physics and to set
 1211 limits on the production rates for a given type of process with working points
 1212 of a few observable parameters. As one example, a simplified model may specify

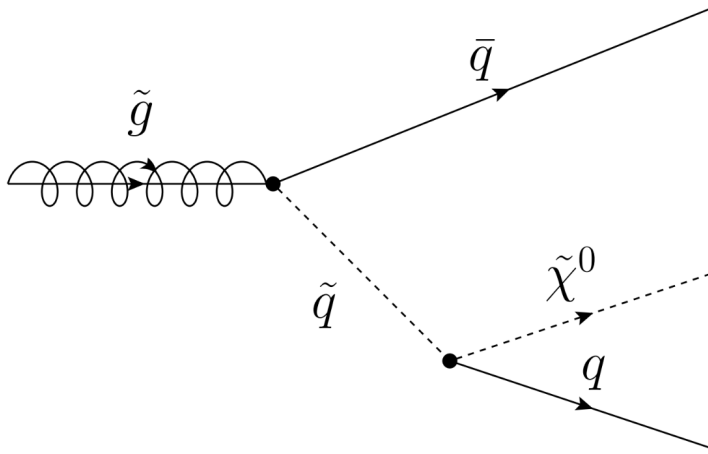


Figure 8: The decay of a gluino to quarks and an LSP, which precedes through a squark.

pair production of gluinos where the free parameters are the mass of the gluino and the types and masses of the particles it can decay into. The small number of parameters allows the phase space to be searched in a grid by simulating events with a few examples for the parameters and interpolating between them. The resulting analysis can set cross sectional limits as a function of the simplified parameters, and this allows for an easy interpretation of the result in a number of SUSY models.

3.4 LONG-LIVED PARTICLES

Some proposed SUSY models can produce LLPs other than just the LSP. The most direct search strategies for SUSY often assume that the various non-stable sparticles decay promptly, rather than propagating through some fraction of the detector. Although the processes involved are very similar, the long-lifetime of the produced particles can lead to very different experimental signatures, and often require separate dedicated searches. It is important to design and execute search strategies for LLPs in order to completely cover possible production of new physics.

There are several ways to generate long lifetimes for the massive SUSY particles, depending on the specific model. In examples like Spread Supersymmetry [7] and Split Supersymmetry [8, 9], the introduction of a split between two mass scales suppresses the decay of gluinos. In these and similar models, the squarks are much heavier than the gluino, where the mass scale of the squarks is roughly 10^6 GeV while the mass scale of the gluinos is roughly 10^3 GeV. The gluino must decay through the production of a virtual squark, as shown in the diagram of Figure 8. The large mass of the squarks in the split models suppresses the decay rate, and can result in lifetimes of the order of 1 ns [7].

Nearly degenerate particles can also result in long lifetimes, again by suppressing decay rates. When a particle must decay to another particle with nearly the same mass, the phase space factor in the decay results in a low decay rate. For

1241 example, a neutron has a lifetime of roughly fifteen minutes because its mass is
1242 so close to the proton. Models which result in a nearly degenerate chargino and
1243 LSP provide a long-lived chargino as well.

1244 Again, because of the wide variety of models which can produce LLPs and the
1245 large number of parameters which determine their masses and lifetimes, the anal-
1246 ysis presented here focuses on simplified models rather than assuming any par-
1247 ticular underlying theory. The models directly specify the decay mode of the
1248 LLPs as well as their masses and lifetimes, using a grid of values. The results of
1249 searches using these simplified models can be interpreted over a very wide range
1250 of models that predict LLPs, even including non-supersymmetric extensions to
1251 the SM.

1252

PART II

1253

EXPERIMENTAL STRUCTURE AND RECONSTRUCTION

1254

You can put some informational part preamble text here.

1255

1256 THE LARGE HADRON COLLIDER

1257 The LHC, a two-ring superconducting hadron accelerator, provides high energy
 1258 proton-proton collisions for several large experiments at European Organiza-
 1259 tion for Nuclear Research (CERN) in Geneva, Switzerland [10, 11]. It is the largest,
 1260 highest-luminosity, and highest-energy proton collider ever built, and was con-
 1261 structed by a collaboration of more than 10,000 scientists from the more than
 1262 100 countries that contribute to CERN. The original design of the LHC focused on
 1263 providing collision energies of up to 14 TeV and generating enough collisions to
 1264 reveal physics beyond the SM which is predicted to exist at higher energy scales.

1265 The LHC was installed in an existing 27 km tunnel at CERN which was orig-
 1266 inally designed to house the Large Electron Positron collider (LEP) [12]. This
 1267 allows the collider to use existing accelerators at the same complex to provide
 1268 the initial acceleration of protons up to 450 GeV before injecting into LHC. The
 1269 injected hadrons are accelerated up to as much as 14 TeV while being focused
 1270 into two beams traveling in opposite directions. During this process the protons
 1271 circulate around the tunnel millions of times, while the beams are intermittently
 1272 crossed at the four locations of the experiments to provide collisions. These col-
 1273 lision points correspond to the four major LHC experiments: ATLAS, Compact
 1274 Muon Solenoid (CMS), Large Hadron Collider beauty experiment (LHCb), and
 1275 A Large Ion Collider Experiment (ALICE), and Figure 9 shows the layout of the
 1276 experiments both on the surface and below. ATLAS and CMS are both general
 1277 purpose, high-luminosity detectors which search for a wide range of new types
 1278 of physics [13, 14]. LHCb studies the interactions of b-hadrons to explore the
 1279 asymmetry between matter and antimatter [15]. ALICE focuses on the collisions
 1280 of lead ions, which the LHC also provides, in order to study the properties of
 1281 quark-gluon plasma [16].

1282 During the first five years of continued operation, after the LHC turned on in
 1283 2010, the LHC has provided four major data collecting periods. In 2010 the LHC
 1284 generated collisions at several energies, starting at 900 GeV. It increased the
 1285 energy from 900 GeV to 2.76 TeV and then subsequently to 7 TeV, with a peak
 1286 luminosity of $2 \times 10^{32} \text{ cm}^{-2}\text{s}^{-1}$, and a total delivered luminosity of 50 pb^{-1} .
 1287 The next run, during 2011, continued the operation at 7 TeV and provided an
 1288 additional 5 fb^{-1} with a peak luminosity of $4 \times 10^{33} \text{ cm}^{-2}\text{s}^{-1}$. The energy was
 1289 then increased to 8 TeV for the data collection during 2012, which provided 23 fb^{-1}
 1290 with a peak luminosity of $7.7 \times 10^{33} \text{ cm}^{-2}\text{s}^{-1}$. After the first long shutdown
 1291 for 2013 and 2014, the LHC resumed operation and increased the energy to 13
 1292 TeV in 2015, where it delivered 4.2 fb^{-1} with a peak luminosity of $5.5 \times 10^{33} \text{ cm}^{-2}\text{s}^{-1}$.
 1293 The LHC is currently providing additional 13 TeV collisions in 2016 with higher
 1294 luminosities than during any previous data collection periods. These running
 1295 periods are summarized in Figure 10, which shows the total delivered

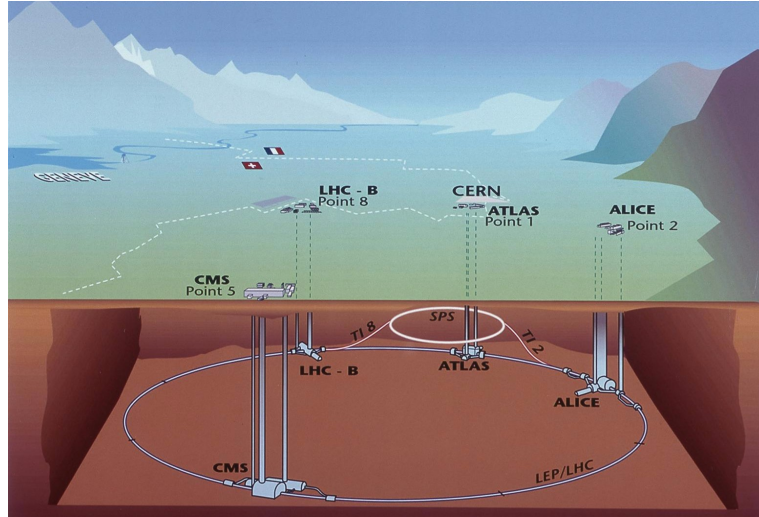


Figure 9: The four collision points and corresponding experiments of the [LHC](#). The image includes the location of the nearby city of Geneva as well as the border of France and Switzerland.

luminosity over time for the ATLAS experiment during each of the four years of data collection since 2011.

4.1 INJECTION CHAIN

The [LHC](#) takes advantage of the presence of previously built accelerators at [CERN](#) to work up to the target energy in consecutive stages. The series of accelerators that feed into the [LHC](#) are known collectively as the injection chain, and together with the [LHC](#) form the accelerator complex. The full complex is illustrated in Figure 11, which details the complex series required to reach collisions of 13 or 14 TeV.

Protons at the [LHC](#) begin as hydrogen atoms in the Linac 2, a linear accelerator which replaced Linac 1 as the primary proton accelerator at [CERN](#) in 1978. In Linac 2, the hydrogen atoms are stripped of their electrons by a strong magnetic field, and the resulting protons are accelerated up to 50 MeV by cylindrical conductors charged by radio frequency cavities. The protons are then transferred to the Proton Synchrotron Booster ([PSB](#)), which uses a stack of four synchrotron rings to accelerate the protons up to 1.4 GeV. Then the protons are injected into the Proton Synchrotron ([PS](#)) which again uses synchrotron rings to bring the energy up to 25 GeV. The intermediate step between Linac 2 and the [PS](#) is not directly necessary, as the [PS](#) can accelerate protons starting from as low as 50 MeV. The inclusion of the [PSB](#) allows the [PS](#) to accept a higher intensity of injection and so increases the deliverable luminosity in the [LHC](#). The penultimate stage of acceleration is provided by the Super Proton Synchrotron ([SPS](#)), a large synchrotron with a 7 km circumference that was commissioned at [CERN](#) in 1976. During this step the protons increase in energy to 450 GeV, after which they can be directly injected into the [LHC](#).

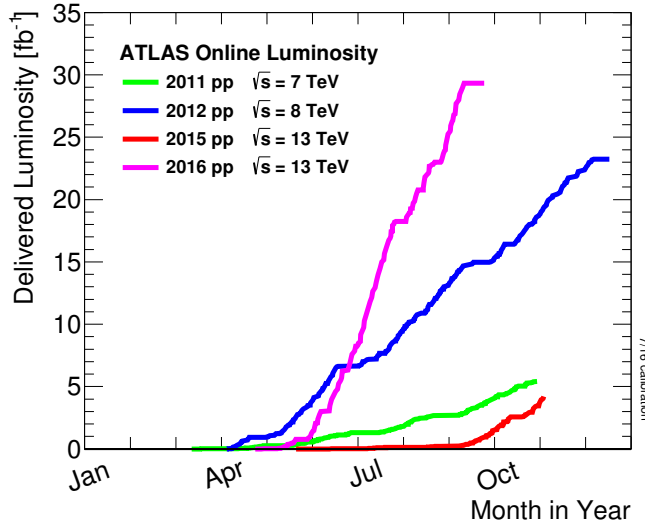


Figure 10: The cumulative luminosity over time delivered to the ATLAS experiment from high energy proton-proton collisions since 2011. The energies of the collisions are listed for each of the data-taking periods.

1321 The final step is the **LHC** itself, which receives protons from the **SPS** into two
 1322 separate beam pipes which circulate in opposite directions. The filling process
 1323 at this steps takes approximately 4 minutes, and the subsequent acceleration to
 1324 the final energy (6.5 TeV during 2015 and up to 7 TeV by design) takes approxi-
 1325 mately half an hour. At this point the protons circulate around the circumference
 1326 tens of thousands of times a second and continue for up to two hours.

1327 4.2 DESIGN

1328 4.2.1 LAYOUT

1329 Many of the aspects of the **LHC** design are driven by the use of the existing **LEP**
 1330 tunnel. This tunnel slopes gradually, with a 1.4% decline, with 90% of its length
 1331 built into molasse rock which is particularly well suited to the application. The
 1332 circumference is composed of eight 2987 meter arcs and eight 528 meter straight
 1333 sections which connect them; this configuration is illustrated in Figure 12. The
 1334 tunnel diameter is 3.7 m throughout its length.

The design energy is directly limited by the size of this tunnel, with its radius of curvature of 2804 m. A significant magnetic field is required to curve the protons around that radius of curvature; the relationship is given by

$$p \simeq 0.3BR \quad (13)$$

1335 where p is the momentum of the particle in GeV, B is the magnetic field in Tesla,
 1336 and R is the radius of curvature in meters. From the target design energy of
 1337 14 TeV, or 7 TeV of momentum for protons in each beam, the required mag-
 1338 netic field is 8.33 Tesla. This is too large a field strength to be practical with
 1339 iron electromagnets, because of the enormous power required and the resulting

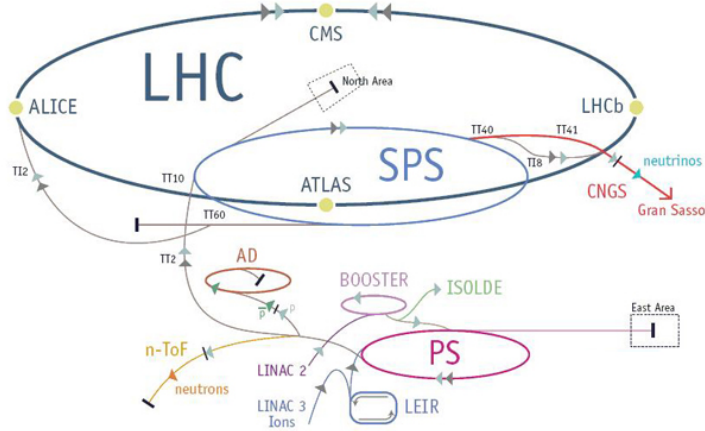


Figure 11: The accelerator complex that builds up to the full design energies at the LHC. The protons are passed in order to Linac 2, the PSB, the PS, the SPS and then the LHC.

1340 requirements for cooling. Because of these constraints, the LHC uses superconducting
 1341 magnets which can maintain that field strength with significantly less power consumption.
 1342

1343 4.2.2 MAGNETS

1344 The magnets chosen were Niobium and Titanium (NbTi) which allow for field
 1345 strengths as high as 10 Tesla when cooled down to 1.9 K. Reaching the target
 1346 temperature of 1.9 K for all of the magnets requires superfluid helium and a large
 1347 cryogenic system along the entire length of the tunnel. During normal operation,
 1348 the LHC uses 120 tonnes of helium within the magnets, and the entire system is
 1349 cooled by eight cryogenic helium refrigerators. The temperature increase that
 1350 occurs during transit from the refrigerator along the beam necessitates that the
 1351 refrigerators cool the helium down to 1.8 K. Any significant increase above this
 1352 temperature range can remove the superconductive properties of the magnets,
 1353 which in turn generates drastically larger heat losses from the current within the
 1354 magnets and causes a rapid rise in temperature called a quench.

1355 There are approximately 8000 superconducting magnets distributed around
 1356 the LHC. The 1232 bending magnets, which keep the protons curving along the
 1357 length of the beam, are twin bore cryodipoles, which allow both proton beams
 1358 to be accommodated by one magnet and all of the associated cooling structure.
 1359 Figure 13 shows the cross section of the design for these dipoles. The magnets
 1360 are very large, 16.5 m long with a diameter of 0.57 meters and a total weight of 28
 1361 tonnes. They are slightly curved, with an angle of 5.1 mrad, in order to carefully
 1362 match the beam path. The twin bore accommodates both magnets inside the
 1363 two 5 cm diameter holes which are surrounded by the superconducting coils.
 1364 The coils require 12 kA of current in order to produce the required magnetic
 1365 field. These coils are comprised of NbTi cable wound in two layers; the wire in

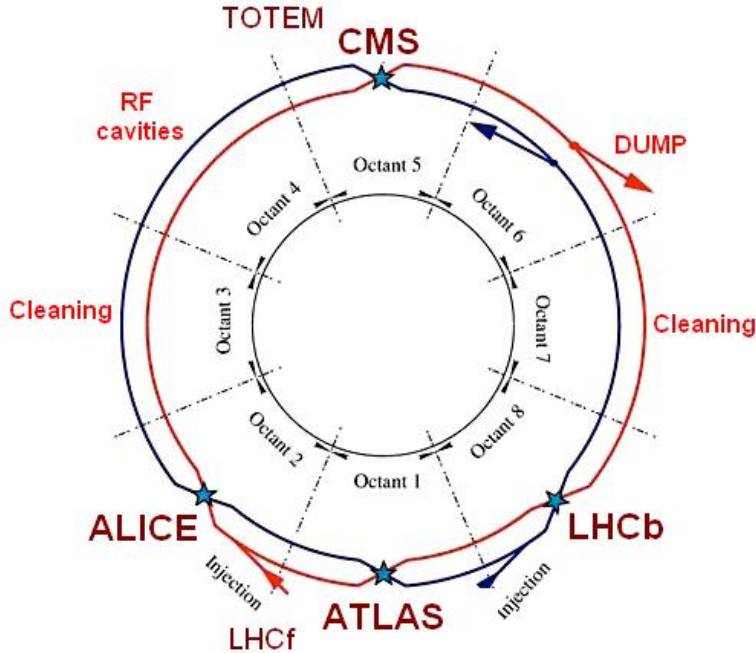


Figure 12: A schematic of the layout of the LHC, not to scale. The arched and straight sections are illustrated at the bottom of the schematic, and all four crossing sites are indicated with their respective experiments.

the inner layer has a diameter of 1.065 mm while the wire in the outer layer has a diameter of 0.825 mm.

The large currents in the wires, along with the magnetic field produced, result in forces on the magnets which would tend to push them apart with over 10,000 Newtons per meter. Constraining the magnets requires a significant amount of structure including non-magnetic stainless steel collars. Both the presence of these electromagnetic forces and the varying thermal contraction coefficient of the pieces of the magnet produce significant forces on the cold mass structure. The cold mass is carefully engineered to so that these stresses do not significantly alter the magnetic field shape, which must be maintained between magnets to a precision of approximately 10^{-4} for successful operation.

The remaining 6800 magnets are a variety of quadrupole, sextapole, octopole, and single bore dipole magnets. These are used to damp oscillations, correct beam trajectories, focus the beams during circulation, and to squeeze the beams before collisions.

4.2.3 RF CAVITIES

Sixteen RF cavities produce the actual acceleration of the proton beam up to the design energy. These RF cavities are tuned to operate at 400 MHz, and are powered by high-powered electron beams modulated at the same frequency, called klystrons. The resonance within the cavity with the oscillating electric field establishes a voltage differential of 2 MV per cavity. The sixteen cavities are split between the two beams, so combined the cavities provide 16 MV per beam,

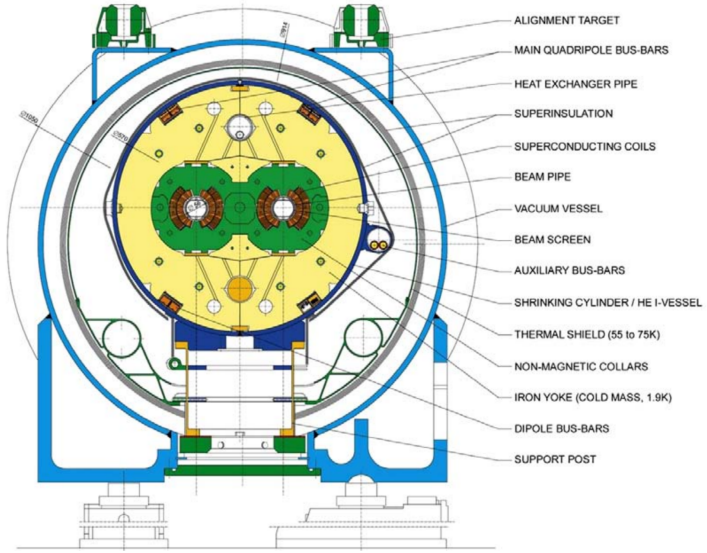


Figure 13: A cross section of the the cryodipole magnets which bend the flight path of protons around the circumference of the LHC. The diagram includes both the superconducting coils which produce the magnetic field and the structural elements which keep the magnets precisely aligned.

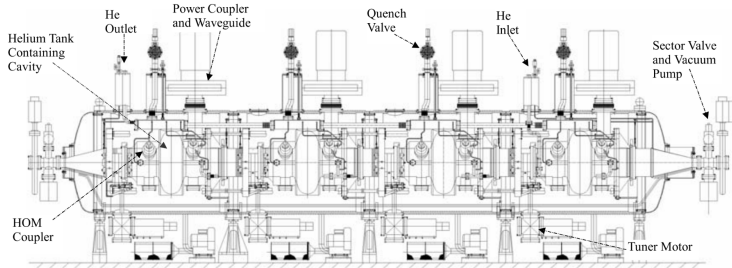


Figure 14: The arrangement of four RF cavities within a cryomodule.

1388 which accelerate the protons on each consecutive pass through the cavity. This
 1389 acceleration is also necessary during circulation even after the target energy has
 1390 been reach in order to compensate for losses from synchrotron radiation.

1391 The cavities are arranged in cryomodules which contain four cavities, with
 1392 two cryomodules per beam; this arrangement is illustrated in Figure 14. These
 1393 cryomodules are necessary to maintain the superconducting state of the cavities,
 1394 which are also constructed from niobium. The RF cavities use niobium along
 1395 with copper to allow for low power losses in the superconductors. The copper
 1396 provides a reduced susceptibility to quenching, as it rapidly conducts away heat
 1397 generated by imperfections in the niobium, as well as natural shielding from the
 1398 earth's magnetic field which can interfere with the RF system.

1399 The nature of the radio frequency oscillations tends to group protons together
 1400 into buckets. A proton traveling exactly in phase with the RF oscillations will not
 1401 be displaced at all during a single circulation, and those slightly ahead or behind
 1402 of that phase will slightly decelerate or accelerate, respectively. This produces

1403 separate clusters of protons which arrive in phase to the cavities every 2.5 ns,
 1404 corresponding to the 400 MHz frequency.

1405 4.2.4 BEAM

1406 The beams of protons circulate within 54 km of 5 cm diameter beam pipe. This
 1407 entire structure is kept under vacuum at 1.9 K to prevent interactions between
 1408 the beam pipe and the magnets as well as to prevent any interactions between the
 1409 circulating protons and gas in the pipe. The vacuum within the pipe establishes
 1410 a pressure as low as 10^{-9} mbar before the protons are introduced.

1411 Because of the very high energies of the circulating protons, synchrotron ra-
 1412 diation is not negligible in the bending regions. The protons are expected to
 1413 radiate 3.9 kW per beam at 14 TeV, with 0.22 W/m, which is enough power to
 1414 heat the liquid helium and cause a quench were it absorbed by the magnets. To
 1415 prevent this, a copper screen is placed within the vacuum tube that absorb the
 1416 emitted photons. This screen is kept between 5 and 20 K by the liquid helium
 1417 cooling system.

1418 4.3 LUMINOSITY PARAMETERS

In addition to the high energy of the collisions, the rate of collisions is extremely important to enabling the discovery of new physics. Many measurements and searches require a large number of events in order to be able to make statistically significant conclusions. The rate of collisions is measured using luminosity, the number of collisions per unit time and unit cross section for the proton-proton collisions. From the beam parameters, luminosity is given by

$$\mathcal{L} = \frac{N_b^2 n_b f_{rev} \gamma}{4\pi \epsilon_n \beta^*} F \quad (14)$$

1419 where N_b is the number of protons per bunch, n_b is the number of bunches per
 1420 beam, f_{rev} is the frequency of revolution, γ is the Lorentz factor for the protons
 1421 at the circulating energy, ϵ_n is the emittance, β^* is the amplitude function at the
 1422 collision point, and F is a geometric factor that accounts for the crossing angle of
 1423 the beams at the collision point. The emittance measures the average spread of
 1424 particles in both position and momentum space, while the amplitude function
 1425 is a beam parameter which measures how much the beam has been squeezed.
 1426 Together ϵ_n and β^* give the size of the beam in the transverse direction, $\sigma =$
 1427 $\sqrt{\epsilon \beta^*}$. β changes over the length of the beam as the accessory magnets shape the
 1428 distribution of protons, but only the value at the point of collisions, β^* , affects
 1429 the luminosity.

1430 The luminosity is maximized to the extent possible by tuning the parameters
 1431 in Equation 14. A number of these are constrained by the design decisions. The
 1432 revolution frequency is determined entirely by the length of the tunnel, as the
 1433 protons travel at very close to the speed of light. The geometric factor F is de-
 1434 termined by the crossing angle of the beams at the collision points, again a com-

Parameter	Unit	Injection	Nominal
Beam Energy	TeV	0.450	7
Peak Instantaneous Luminosity	$\text{cm}^{-2}\text{s}^{-1}$	-	10^{34}
Bunch Spacing	ns	25	25
Number of Filled Bunches	-	2808	2808
Normalized Transverse Emittance	μm	3.75	3.75
Frequency	MHz	400.789	400.790
RF Voltage/Beam	MV	8	16
Stored Energy	MJ	-	362
Magnetic Field	T	0.54	8.33
Operating Temperature	K	1.9	1.9

Table 2: The design parameters of the [LHC](#) beam that determines the energy of collisions and the luminosity, for both the injection of protons and at the nominal circulation.

ponent of the tunnel design; this angle is already very small at $285 \mu\text{rad}$, which helps to maximize the geometric factor.

The major pieces that can be adjusted are the number of protons per bunch, N_b , the number of bunches in the beam, n_b , and the amplitude function β . Increasing either N_b or n_b increases the amount of energy stored in the beam, which presents a danger if control of the beam is lost. At design specifications, the beam stores 362 MJ, which is enough energy to damage the detectors or accelerator if the beam were to wander out of the beam pipe. So, the luminosity is primarily controlled at the [LHC](#) by adjusting β^* , where lowering β^* increases the luminosity. β^* is tuned to provide the various values of luminosity used at the [LHC](#) which can be raised to as much as 10^{34} .

The nominal bunch structure consists of 3654 bunches, each holding 10^{11} protons, which cross a collision point in 25 ns. These are further subdivided into the buckets mentioned in Section 4.2.3 by the clustering properties of the RF cavities. The bunches are further grouped into trains of 72 bunches which are separated by a gap which would otherwise hold 12 bunches. At nominal operation 2808 of the bunches will actually be filled with protons, while the remainder are left empty to form an abort gap that can be used in case the beam needs to be dumped.

The various beam parameters are summarized in Table 2 for the designed operation. In practice, the beam has operated at lower energies and lower luminosities than the design values for the majority of its lifetime, but the [LHC](#) has begun to operate at full design values during Run 2.

4.4 DELIVERED LUMINOSITY

During the data collection of 2015, the [LHC](#) operated at luminosities as large as $5 \times 10^{33} \text{ cm}^{-2}\text{s}^{-1}$. It is convenient to refer to the integrated luminosity, the inte-

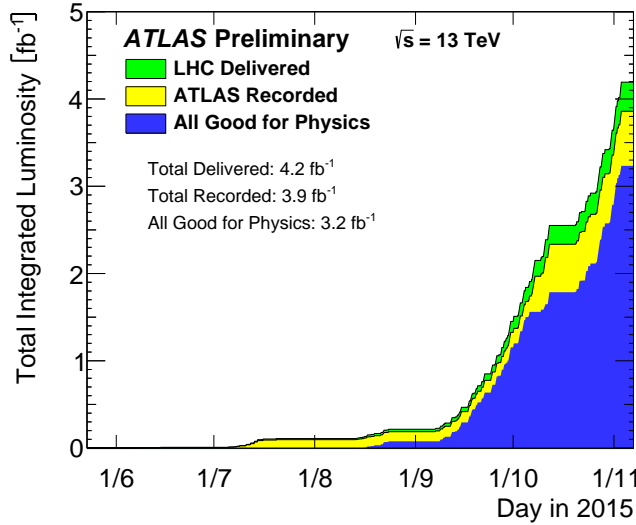


Figure 15: The cumulative luminosity versus time delivered to ATLAS (green), recorded by ATLAS (yellow), and certified to be good quality data (blue) during stable beams for pp collisions at 13 TeV in 2015.

gral of the instantaneous luminosity, which corresponds directly to the number of delivered events for a given process.

$$N = \sigma \times \int \mathcal{L}(t) dt$$

where σ is the cross section for the process of interest. The integrated luminosity over time is shown in Figure 15. This includes the luminosity delivered by the LHC as well as the luminosity that was recorded by ATLAS. ATLAS only records collisions when the LHC reports that the beam conditions are stable, so some of the delivered luminosity is not recorded. The figure also includes the amount of luminosity marked as good for physics, which includes additional requirements on the operation of the detector during data collection that are necessary for precise measurements.

Because the beam circulates and collides bunches of protons, it is possible for a single crossing to produce multiple proton-proton collisions. As the instantaneous luminosity is increased, the average number of collisions generated per bunch crossing increases. An event refers to the entire collection of interactions during a single bunch crossing, while interactions refer to the individual proton-proton collisions. The additional interactions produced during each bunch crossing are referred to as pileup, which can be more precisely defined quantified using the average number of additional proton-proton interactions per crossing, often denoted μ . Figure 16 shows the luminosity-weighted distribution of the mean number of interactions for events collected in 2015. The presence of as many as twenty interactions in a single collision provides a significant challenge in reconstructing events and isolating the targeted physical processes.

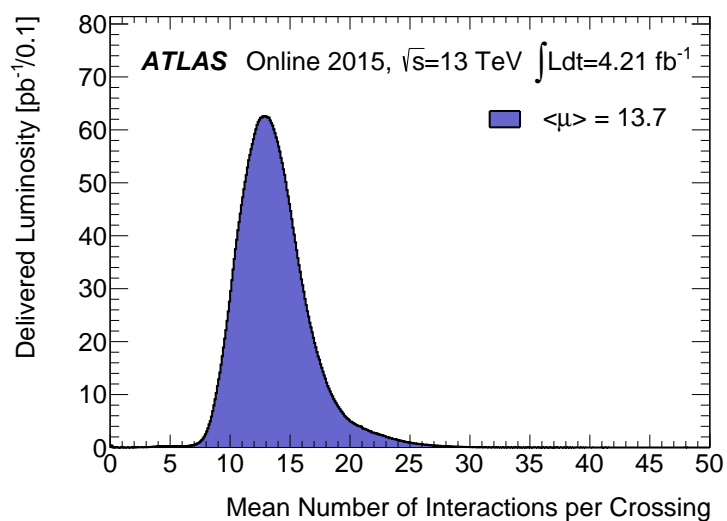


Figure 16: The luminosity-weighted distribution of the mean number of interactions per crossing for the 2015 pp collision data at 13 TeV.

1479

1480 THE ATLAS DETECTOR

1481 The four major LHC experiments at CERN seek to use the never before matched
1482 energies and luminosities of the new collider to explore the boundaries of par-
1483 ticle physics and to gain insight into the fundamental forces of nature. Two of
1484 these experiments, ATLAS and CMS, are general purpose detectors that seek to
1485 measure a variety of processes in the up to 13 TeV proton-proton collisions that
1486 occur as much as 800 million times per second at the LHC at the design lumi-
1487 nosity of $10^{34} \text{ cm}^{-2}\text{s}^{-1}$. ATLAS employs a hermetic detector design, one which
1488 encloses the particle collisions as completely as possible with detecting elements,
1489 that allows it to study a wide range of physics from SM and Higgs measurements
1490 to searches for new physics in models like SUSY [13].

1491 Accommodating this wide variety of goals is a challenge for the design of the
1492 detector. The wide range of energies involved requires high measurement pre-
1493 cision over several orders of magnitude, and the numerous physics processes
1494 require an ability to measure a variety of particle types. At the time of the con-
1495 struction of ATLAS, the Higgs boson had yet to be discovered, but the diphoton
1496 decay mode was (correctly) expected to be important and necessitated a high
1497 resolution photon measurement. The potential for decays of new heavy gauge
1498 bosons, W' and Z' , required a similarly high momentum resolution for leptons
1499 with momentum up to several TeV. Hadronic decay modes of several possible
1500 new high energy particles could result in very energetic jets, again up to several
1501 TeV, and reconstructing the decay resonances would again require good energy
1502 resolution. Several models, such as SUSY or Extra Dimensions, predict the exis-
1503 tence of particles which would not interact with traditional detecting elements.
1504 However these particles can still be observed in a hermetic detector by accurately
1505 measuring the remaining event constituents to observe an imbalance in energy
1506 called missing energy or E_T^{miss} . Measuring E_T^{miss} implicitly requires a good res-
1507 olution on all SM particles that can be produced. And at the lower end of the
1508 energy spectrum, precision SM measurements would require good resolution of
1509 a variety of particle types at energies as low as a few GeV, so the design needs to
1510 accommodate roughly three orders of magnitude.

1511 This broad spectrum of measurements requires a variety of detector systems
1512 working together to form a cohesive picture of each collision. Two large mag-
1513 net systems produce magnetic fields that provide a curvature to the propaga-
1514 tion of charged particles and allows for precision momentum measurements by
1515 other systems. The inner detector uses a combination of tracking technologies
1516 to reconstruct particle trajectories and vertices for charged particles. A variety
1517 of calorimeters measure the energies of hadrons, electrons, and photons over a
1518 large solid angle. A large muon spectrometer identifies muons and uses the sec-
1519 ond magnet system to provide an independent measurement of their momentum

1520 from the inner detector and improve the resolution. The layout of all of these
 1521 systems is shown in Figure 17.

1522 The performance goals needed to achieve the various targeted measurements
 1523 and searches discussed above can be summarized as resolution and coverage re-
 1524 quirements on each of these systems. Those requirements are listed in Table 3.

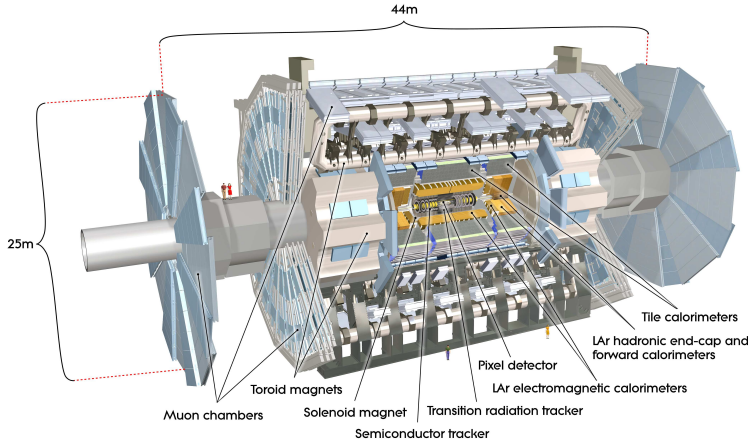


Figure 17: A cut-away schematic of the layout of the ATLAS detector. Each of the major subsystems is indicated.

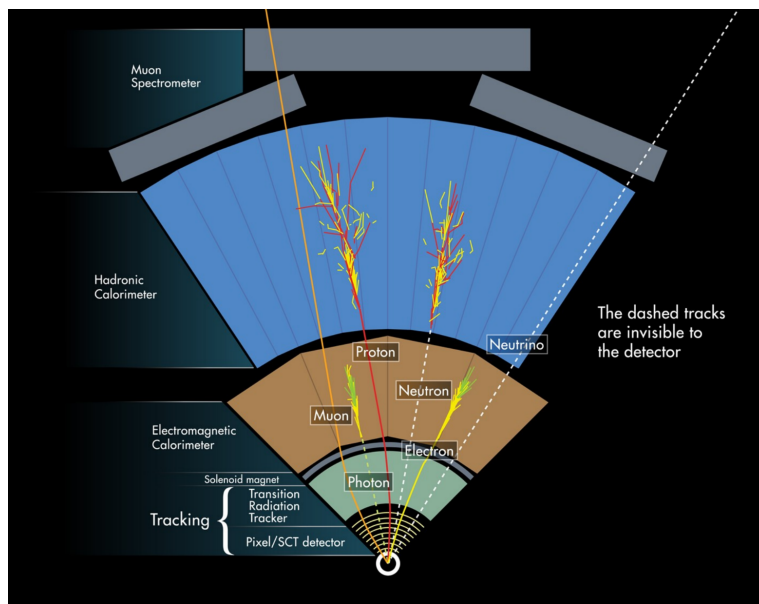


Figure 18: A cross-sectional slice of the ATLAS experiment which illustrates how the various SM particles interact with the detector systems.

1525 Incorporating these various pieces into a single detector is a significant tech-
 1526 nical challenge. The resulting detector has a diameter of 22 m, is 46 m long,
 1527 and weighs 7,000 tons; it is the largest volume particle detector ever constructed.
 1528 The various detector elements need to be constructed and assembled with pre-
 1529 cision as low as micrometers. These systems all need to function well even after
 1530 exposure to the significant radiation dose from the collisions. Designing, con-

Detector Component	Required Resolution	$ \eta $ Coverage	
		Measurement	Trigger
Tracking	$\sigma_{p_T}/p_T = 0.05\% p_T + 1\%$	2.5	-
EM Calorimetry	$\sigma_E/E = 10\%/\sqrt{E} + 0.7\%$	3.2	2.5
Hadronic Calorimetry			
Barrel and Endcap	$\sigma_E/E = 50\%/\sqrt{E} + 3\%$	3.2	3.2
Forward	$\sigma_E/E = 100\%/\sqrt{E} + 10\%$	3.1 – 4.9	3.1 – 4.9
Muon Spectrometer	$\sigma_{p_T}/p_T = 10\% \text{ at } p_T = 1 \text{ TeV}$	2.7	2.4

Table 3: The performance goals for each of the subsystems of the ATLAS detector. The $|\eta|$ coverage specifies the range where the subsystem needs to be able to provide measurements with the specified resolution. The resolutions include a p_T or E dependence that is added in quadrature with a p_T/E independent piece.

1531 structing, and installing the detector took the combined effort of more than 3000
 1532 scientists from 38 countries over almost two decades.

1533 5.1 COORDINATE SYSTEM

1534 The coordinate system defined for the ATLAS detector is used throughout all of
 1535 the sections of this thesis. The system begins with the choice of a z axis along
 1536 the beamline. The positive z side of the detector is commonly referred to
 1537 as the *A*-side, and the negative z side is referred to as the *C*-side. The $x - y$
 1538 plane is then the plane transverse to the beam direction, with the x direction
 1539 defined as pointing from the interaction point to the center of the LHC ring and
 1540 the y direction defined as pointing upwards. The nominal interaction point is
 1541 the origin of this system.

1542 It is more convenient in practice to use a cylindrical coordinate system; this
 1543 choice of coordinate system reflects the cylindrical symmetry of the ATLAS de-
 1544 tector. The distance from the beamline is the radius, r' , and the angle from the
 1545 z -axis is θ . The azimuthal angle uses the usual definition, with ϕ running around
 1546 the z -axis and $\phi = 0$ corresponding to the x -axis. Many aspects of the detector
 1547 are independent of the this coordinate to first order. The θ direction is typically
 1548 specified using rapidity or pseudorapidity, where rapidity is defined as

$$y = \frac{1}{2} \ln \frac{E + p_z}{E - p_z} \quad (15)$$

1549 Rapidity is particularly useful to indicate the component along the z direction
 1550 because differences in rapidity are invariant to boosts along the z -direction. A
 1551 similar quantity which depends only the θ is pseudorapidity,

$$\eta = -\ln \tan \frac{\theta}{2} \quad (16)$$

1552 which is the same as rapidity when the particle is massless and in the limit where
 1553 the energy is much larger than the particle's mass. It is often useful to refer to
 1554 differences in solid angle using the pseudorapidity and the azimuthal angle:

$$\Delta R = \sqrt{\Delta\phi^2 + \Delta\eta^2} \quad (17)$$

1555 The pseudorapidity is also invariant to boosts along the z -axis for high mo-
 1556 mentum particles, and is preferable to rapidity because it does not depend on
 1557 the specific choice of particle. Pseudorapidity is also preferable to θ because par-
 1558 ticle production is roughly uniform in equal-width intervals of η up to about
 1559 $\eta = 5.0$. A particle traveling along the beampipe has $\eta = \text{inf}$ and a particle
 1560 traveling perpendicular to the beampipe has $\eta = 0$. The extent of the tracker,
 1561 $|\eta| < 2.5$, corresponds to approximately $0.05\pi < \theta[\text{rad}] < 0.95\pi$ and the
 1562 extent of the calorimeters, $|\eta| < 4.9$ corresponds to approximately $0.005\pi <$
 1563 $\theta[\text{rad}] < 0.995\pi$. Many detector components are broken into multiple subsys-
 1564 tems to provide coverage at greater $|\eta|$. The lower $|\eta|$ region is referred to as the
 1565 barrel, typically with $|\eta| \lesssim 2$, and the greater $|\eta|$ region is often referred to as the
 1566 endcap.

1567 The initial energy and momentum of a proton-proton collision along the z di-
 1568 rection is unknown in hadron colliders because different energies and momenta
 1569 can be carried by the partons. Along the transverse plane, however, the vector
 1570 sum of momentum will be zero. For this reason, many physical quantities are
 1571 quantified in terms of their projection onto the transverse plan, such as p_T or
 1572 E_T . In addition, p_T alone determines the amount of curvature in the magnetic
 1573 field, and can be measured independently by measuring the curvature of a parti-
 1574 cle's propagation.

1575 5.2 MAGNETIC FIELD

1576 The magnet system used in ATLAS is designed to provide a substantial magnetic
 1577 field in the two regions where the trajectory of particles is measured, the inner
 1578 detector and the muon spectrometer. The magnetic field provides a curvature to
 1579 the trajectory of charged particles and allows the precision tracking elements to
 1580 make high resolutions measurements of p_T . To provide a magnetic field in these
 1581 regions, ATLAS uses a hybrid system with four separate, superconducting mag-
 1582 nets. A single solenoid provides a 2 T axial, uniform magnetic field for the inner
 1583 detector, while a barrel toroid and two endcap toroids produce a non-uniform
 1584 magnetic field of 0.5 and 1 T, respectively, for the muon detectors. This geom-
 1585 etry is illustrated in Figure 19, and the parameters of the three magnet systems
 1586 are summarized in Table 4.

1587 The central solenoid uses a single-layer coil with a current of 7.730 kA to gen-
 1588 erate the 2 T axial field at the center of the magnet. The single-layer coil design
 1589 enables a minimal amount of material to be used in the solenoid's construction,
 1590 which is important because the solenoid is placed between the inner detector
 1591 and the calorimeters. At normal incidence the magnet has only 0.66 radiation
 1592 lengths worth of material, where one radiation length is the mean distance over

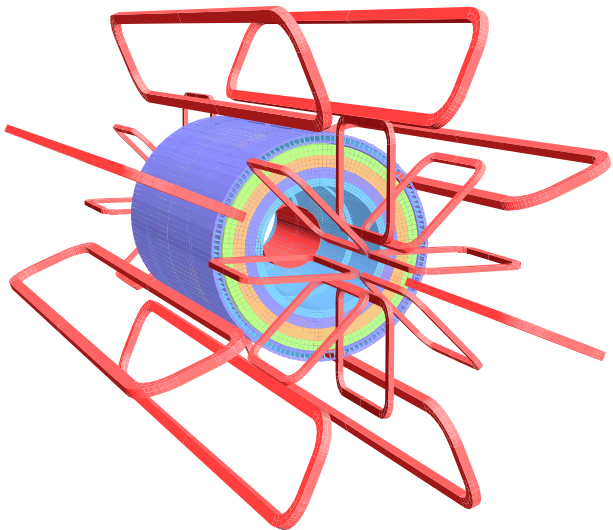


Figure 19: The layout of the four superconducting magnets in the ATLAS detector.

Parameter	Unit	Solenoid	Barrel Toroid	Endcap Toroids
Inner Diameter	m	2.4	9.4	1.7
Outer Diameter	m	2.6	20.1	10.7
Axial Length	m	5.3	25.3	5.0
Weight	tons	5.7	830	239
Conductor Size	mm ²	30×4.25	57×12	41×4.25
Peak Field	T	2.6	3.9	4.1
Heat Load	W	130	990	330
Current	kA	7.7	20.5	20.0
Stored Energy	MJ	38	1080	206

Table 4: A summary of the parameters of each of the three magnet systems on ATLAS.

which a high-energy electron loses all but $1/e$ of its energy through material interactions [6]. The coil is made of a high-strength aluminum stabilized NbTi superconductor which was optimized to achieve a high field with minimal thickness. The axial magnetic field produced by the solenoid bends charged particles in the ϕ direction, following a circular path with a radius specified by Maxwell's equations (see Equation 13).

The barrel toroid consists of eight coils which generate a 0.5 T magnetic field, on average, in the cylindrical region around the calorimeters with an approximately 20 kA current. The coils are separated only by air to reduce the scattering of muons as they propagate through the region. The coils are made of an aluminum stabilized NbTiCu superconductor and each is separately housed in a vacuum and cold chamber. This magnetic configuration produces a field in the ϕ and so curves muons traversing the volume primarily in the η direction.

The endcap toroids follow a similar design to the barrel toroid and produce a 1.0 T magnetic field, on average. Each has eight separate NbTiCu coils, and in this case all eight are housed within a single cold mass. This extra structure is necessary to withstand the Lorentz forces exerted by the magnets. These magnets are rotated 22.5% relative to the barrel toroid to provide a uniform field in the transition between the two systems. The endcap toroids also produce a field in the ϕ direction and curve muons primarily in the η direction.

5.3 INNER DETECTOR

The ATLAS inner detector provides excellent momentum resolution as well as accurate primary and secondary vertex measurements through robust pattern recognition that identifies tracks left by charged particles. These tracks fulfill a number of important roles in the ATLAS measurement system: they measure the momentum of charged particles including electrons and muons, they can identify electrons or photon conversions, they assign various particles and jets to different vertices, and they provide a correction to E_T^{miss} measurements from low energy particles. The system has to be accurate enough to separate tracks from dozens of vertices, to resolve each vertex individually, and to measure the p_T of very high momentum tracks which curve very little even in the large magnetic field. This is accomplished by several independent layers of tracking systems. Closest to the interaction point is the very high granularity Pixel detector, including the newly added Insertible B-Layer, which is followed by the SCT layers. These silicon subdetectors both use discrete space-points to reconstruct track patterns. The final layer, the Transition Radiation Tracker (TRT), uses many layers of straw tube elements interleaved with transition radiation material to provide continuous tracking. The arrangement of these subdetectors is shown in Figure 20. To provide the desired hermetic coverage, the subdetectors are divided into barrel and endcap geometries. Figure 21 shows the layout of the subdetectors in more detail, and illustrates how tracks at various pseudorapidities can traverse the subdetectors; tracks with $\eta > 1.1$ begin to traverse the endcap subdetectors rather than those in the barrel, and tracks with $\eta > 1.7$ use primar-

ily endcap elements. The IBL was not present during the original commissioning of the inner detector and is not shown in this figure.

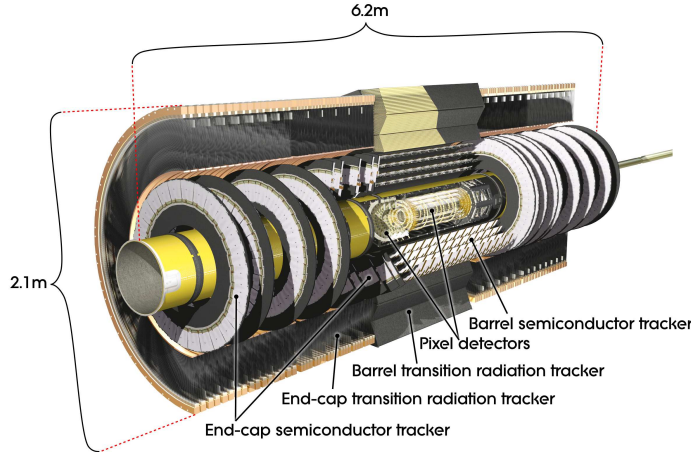


Figure 20: The arrangement of the subdetectors of the ATLAS inner detector. Each of the subdetectors is labeled in the cut-away view of the system.

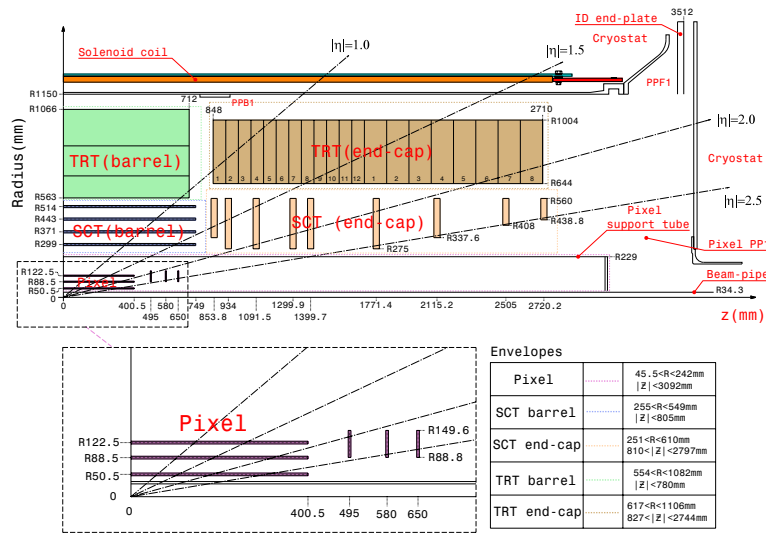


Figure 21: A quarter section of the ATLAS inner detector which shows the layout of each of the subdetectors in detail. The lower panel shows an enlarged view of the pixel detector. Example trajectories for a particle with $\eta = 1.0, 1.5, 2.0, 2.5$ are shown. The IBL, which was added after the original detector commissioning, is not shown.

Figure 22 shows a computer generated three-dimensional view of the inner detector along the beam axis, which emphasizes the straw tube structure of the TRT as well as the overlapping geometry of the SCT. This figure also includes the IBL, which was added during the long shutdown and provides an additional measurement layer in the Pixel detector as of the beginning of Run 2. Figure 23 shows an alternative computer generated three-dimensional view transverse to the beam axis which emphasizes the endcap structures of the SCT and TRT.

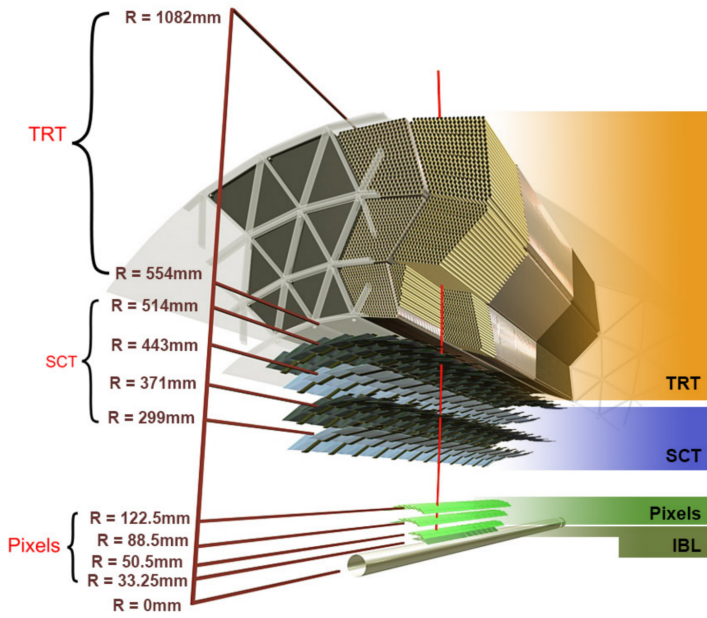


Figure 22: A computer generated three-dimensional view of the inner detector along the line of the beam axis. The subdetectors and their positions are labeled.

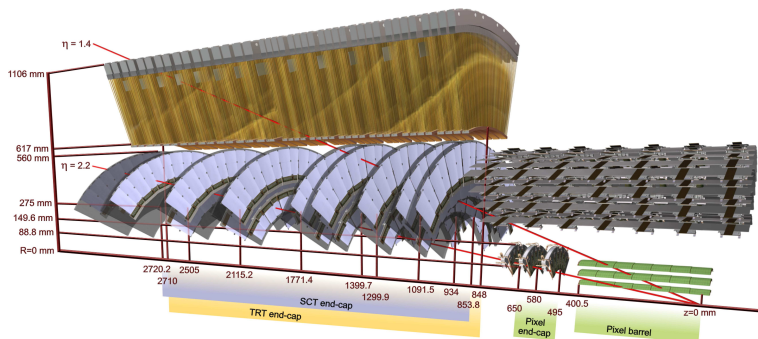


Figure 23: An alternative computer generated three-dimensional view of the inner detector transverse to the beam axis. The subdetectors and their positions are labeled.

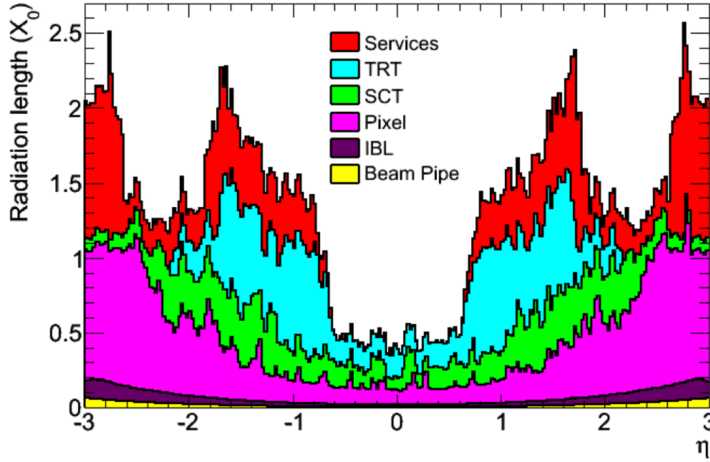


Figure 24: The integrated radiation lengths traversed by a straight track at the exit of the ID envelope, including the services and thermal enclosures. The distribution is shown as a function of $|\eta|$ and averaged over ϕ . The breakdown indicates the contributions of individual sub-detectors, including services in their active volume.

As the closest system to the interaction point, it is crucial for the inner detector to use as little material as possible to avoid scattering of charged particles or photon conversions before they reach the remaining subdetectors. The various components, including the readout electronics, cooling infrastructure, gas volumes, and support structures, were designed to accommodate this need for minimal components. Even with these optimizations, the combination of stringent performance requirements and the harsh radiation environment in the inner detector requires a significant amount of material. This material causes many electrons to lose most of their energy before reaching the electromagnetic calorimeter and approximately 40% of photons convert into an electron-positron pair while traversing the inner detector. Figure 24 shows the integrated radiation lengths traversed by a straight track in the inner detector as a function of η , grouped by subdetector. There is a large increase in the amount of material for support structures around $|\eta| = 1.7$, where the inner detector transitions from barrel to endcap.

The inner detector is designed to work as a cohesive unit to provide complete tracking information for charged particulars, and the subdetectors are complementary. Table 5 summarizes the parameters of each of the subdetectors as well as the parameters of the combined inner detector. Table 6 summarizes the expected performance that can be achieved by the inner detector as a whole.

5.3.1 PIXEL DETECTOR

The Pixel detector is the closest detector to the interaction point and therefore is designed to provide extremely high granularity while simultaneously handling a very large dose of radiation from collisions. It consists of four layers of silicon pixel modules, each of which provides a precision measurement on the trajectory

Parameter	Inner Detector	Pixel	SCT	TRT
Inner Radius	3.1 cm	3.1 cm	30 cm	56 cm
$ \eta $ Coverage	-	2.5	2.5	2.0
Cell Width	-	50 μm	80 μm	4 mm
Cell Length	-	400 μm	12 cm	70 cm
Material at $ \eta = 0.0$	0.3 X/X_0			
Material at $ \eta = 1.7$	1.2 X/X_0			
Material at $ \eta = 2.5$	0.5 X/X_0			
Number of Hits	48	4	8	36
Channels	99 M	92 M	6.3 M	350 k

Table 5: A summary of the parameters of the inner detector and each of the subdetectors [13].

of any charged particle. In the barrel region, the four layers are located at radial distances of 31 mm, 51 mm, 89 mm, and 123 mm. The three outer layers also include endcap elements, illustrated in Figure 21, which are located at 495 mm, 580 mm, and 650 mm away from the interaction point.

The pixel sensor technology uses a p-n junction of n-type bulk that contains both p⁺ and n⁺ impurities. This combination is crucial in maintaining performance after a significant radiation dose, as the n⁺ implants allow the sensor to continue function after the n-type bulk has been converted to a p-type bulk by the accumulation of radiation. In either configuration, when a charged particle passes through the bulk, it ionizes thousands of electron-hole pairs. The electrons and holes are pulled in opposite directions by the electric field established between the anode and cathode of the junction, which then produces a current that can be measured and recorded by readout electronics.

The size of the pixels in the original three layers are 50 μm x 400 μm in the $r - \phi$ and z directions, respectively. Those pixels are bump-bonded to front-end readout chips, the FE-I3, which contains a total of 2880 pixels per chip. In the three original pixel layers, the chips are grouped into modules composed of 16 chips each with 46,080 pixels per module and a total size of 20 mm x 60 mm x 250 μm . The modules are further arranged into long rectangular structures that run parallel to the beamline called staves. By tiling several staves with an offset of 20°, the stave geometry provides full azimuthal coverage in the barrel region while accommodating the readout and cable systems. The endcap regions are instead arranged into petals and then into wheels. This arrangement can be seen in Figure 25 which shows a computer-generated, cut-away image of the outer three layers of the pixel detector. Together these three layers contain 1744 modules between the barrel and two endcap sections.

The innermost layer, the IBL, was added during the long shutdown before Run 2, and provides the fourth track measurement. It was inserted directly into the existing pixel detector by removing the existing beam pipe and replacing it with a significantly smaller version. This insertion can be seen in action in Figure 26,

Parameter	Particle	Value
Reconstruction Efficiency	Muon, $p_T = 1 \text{ GeV}$	96.8%
	Pion, $p_T = 1 \text{ GeV}$	84.0%
	Electron, $p_T = 5 \text{ GeV}$	90.0%
Momentum Resolution	$p_T = 1 \text{ GeV}, \eta \approx 0$	1.3%
	$p_T = 1 \text{ GeV}, \eta \approx 2.5$	2.0%
	$p_T = 100 \text{ GeV}, \eta \approx 0$	3.8%
	$p_T = 100 \text{ GeV}, \eta \approx 2.5$	11%
Transverse IP Resolution	$p_T = 1 \text{ GeV}, \eta \approx 0$	$75 \mu\text{m}$
	$p_T = 1 \text{ GeV}, \eta \approx 2.5$	$200 \mu\text{m}$
	$p_T = 1000 \text{ GeV}, \eta \approx 0$	$11 \mu\text{m}$
	$p_T = 1000 \text{ GeV}, \eta \approx 2.5$	$11 \mu\text{m}$
Longitudinal IP Resolution	$p_T = 1 \text{ GeV}, \eta \approx 0$	$150 \mu\text{m}$
	$p_T = 1 \text{ GeV}, \eta \approx 2.5$	$900 \mu\text{m}$
	$p_T = 1000 \text{ GeV}, \eta \approx 0$	$90 \mu\text{m}$
	$p_T = 1000 \text{ GeV}, \eta \approx 2.5$	$190 \mu\text{m}$

Table 6: A summary of the expected performance of the combined inner detector [17]. Included are the reconstruction efficiencies for multiple particle types as well as the momentum and IP resolution for various momenta.

which emphasizes the extreme precision required to place the the 70 cm long layer with only 2 mm of clearance. The IBL was commissioned to provide continued tracking robustness and high precision in the higher luminosity environment of Run 2 [18]. The proximity of this layer to the collisions necessitated an even higher granularity and better radiation hardness than the other pixel layers. And the strict space requirements to add an active sensing layer so close to the interaction point required a sensor chip with a much higher active area and a larger overall area per chip. These requirements led to the development of a new chip type, the FE-I4 (compared to the FE-I3 chips used in the original pixel detector) with improved radiation hardness and a larger active footprint of 90%. The IBL is comprised of 448 of these individual chips arranged in 14 staves, with 26,880 pixels per chip and a chip size of 18.5 mm x 41.3 mm x 200 μm . The staves, like in the other layers of the pixel detector, are offset by 14° to provide full azimuthal coverage. This arrangement can be seen in Figure 27, which shows two computer-generated images of the IBL geometry and includes the some of the remaining pixel layers.

5.3.2 SEMICONDUCTOR TRACKER

The SCT, the subdetector which immediately surrounds the Pixel detector, provides additional discrete measurements of the trajectory of a charged particle. Because the SCT is further away from the interaction point, the spatial resolution

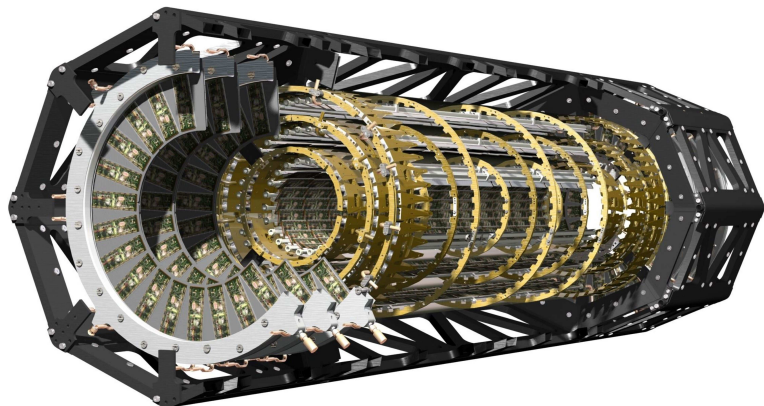


Figure 25: A cut away image of the outer three layers of the pixel detector.

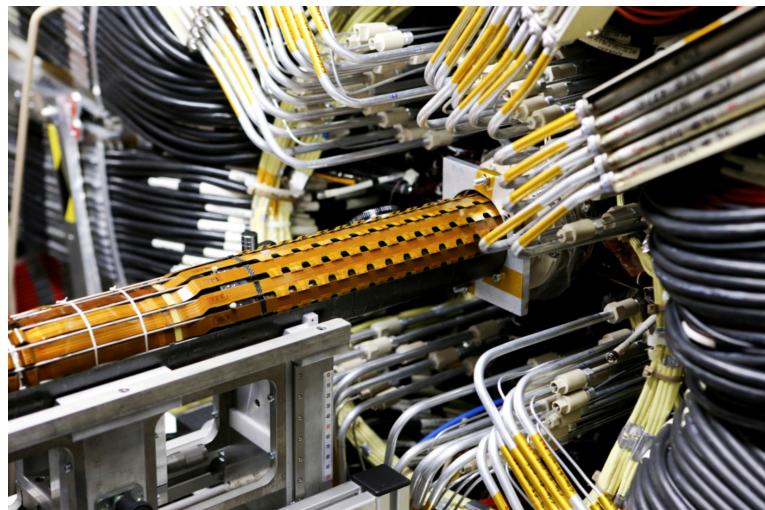


Figure 26: An image of the insertion of the IBL into the current pixel detector.

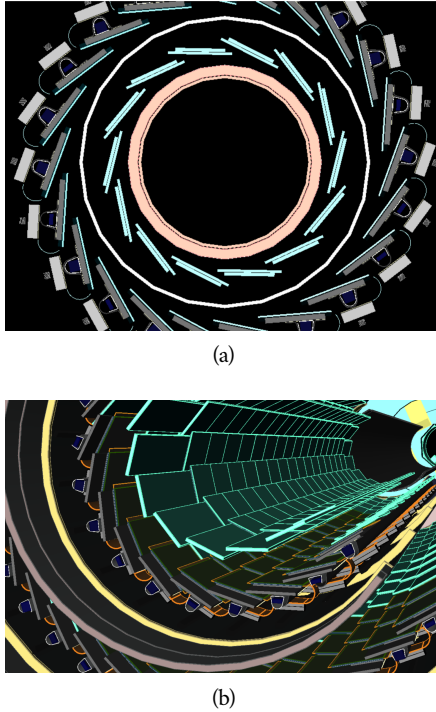


Figure 27: A three-dimensional computer-generated image of the geometry of the **IBL** with a view (a) mostly transverse to the beam pipe (b) mostly parallel to the beam pipe.

1720 does not need to be as high as in the pixel detector, and so the **SCT** uses micro-
 1721 strips instead of pixels. Although pixels provide a more accurate measurement,
 1722 the number of pixels and readout channels required to cover the cylindrical area
 1723 at the radius of the **SCT** layers would be prohibitively complicated and expensive.

1724 Each individual silicon strip sensor contains 768 individual readout strips
 1725 with a total area of $6.36 \text{ cm} \times 6.40 \text{ cm}$ and a pitch of $80 \mu\text{m}$. Pairs of these sen-
 1726 sors are then bonded together to form a combined strip with a length of 12.8 cm.
 1727 Two of these combined strips are then placed back to back with a relative tilt of
 1728 40 mrad. This geometry is illustrated in an expanded view in Figure 28. The pur-
 1729 pose of angular offset of the consecutive layers is to allow the strip sensor areas
 1730 to more accurately measure the position of a particle by comparing the overlap
 1731 of the two strips which were traversed by a track.

1732 Four of these double layers are placed in the barrel region, with radii of 284
 1733 mm, 355 mm, 427 mm, and 498 mm. Together these layers provide eight addi-
 1734 tional measurements for each track that traverses the central $|\eta|$ region. In the
 1735 endcap region, the layers are arranged in wheels, with the double layers simi-
 1736 larly offset to provide improved resolution. With these configurations, the **SCT**
 1737 achieves a spatial resolution of $17 \mu\text{m}$ in the $r - \phi$ direction and $580 \mu\text{m}$ in the
 1738 z direction.

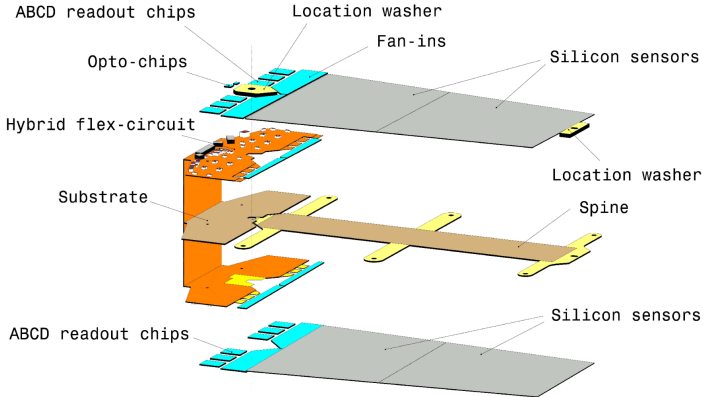


Figure 28: An expanded view of the geometry of the **SCT** double layers in the barrel region.

1739 5.3.3 TRANSITION RADIATION TRACKER

1740 The final component of the inner detector, the **TRT**, provides continuous track-
 1741 ing using straw drift tubes. The tubes are made of Kapton and aluminum with
 1742 a diameter of 4 mm and are filled with a gas mixture of 70% Xe, 27% CO₂, and
 1743 3% O₂. At the center of each tube is a gold-plated anode tungsten wire 30 μm in
 1744 diameter. When a charged particle passes through these tubes, it ionizes the gas
 1745 within. The ions produced drift in the electric field established between the wire
 1746 and the tube wall, and the large electric field near the wire produces avalanche
 1747 multiplication and results in an electric current on the wire that is read out by
 1748 the electronics and provides a track measurement. The time it takes the ioniza-
 1749 tion to drift to the wire can be used to estimate the distance from the wire that
 1750 the particle passed through the tube; this gives a resolution on the distance of ap-
 1751 proximately 130 μm . Combining several such measurements between consecu-
 1752 tive hits in the **TRT** tubes allows the trajectory of the particle to be reconstructed
 1753 with much better resolution than is available in each individual tube.

1754 In addition to the continuous tracking, the detector can use transition radia-
 1755 tion produced when a particle passes between the layers to distinguish between
 1756 electrons and heavier charged particles. The space between the tubes is filled
 1757 with CO₂, and so has a different dielectric constant than the gas within the tubes
 1758 which contains Xe. At the transition between those media, a relativistic par-
 1759 ticle emits radiation proportional to γ , so inversely proportional to mass at a
 1760 fixed momentum. The photons produced in this transition then produce an
 1761 ionization cascade which is significantly larger than the signal for the minimally-
 1762 ionizing charged particles. To distinguish between these two cases, the **TRT** de-
 1763 fines two signal thresholds, a low threshold for the typical signal produced by a
 1764 minimally ionizing particle (**MIP**) and a high threshold for the the signal produced
 1765 by transition radiation. A high momentum electron is expected to produce ap-
 1766 proximately 7 to 10 high threshold hits as it traverses the **TRT**, and thus these hits
 1767 provide a way to distinguish electrons from other charged particles.

1768 The TRT contains 351,000 tubes in total, divided between the barrel and end-
 1769 cap regions. In the barrel region, the tubes are 144 cm long and arranged in 73
 1770 layers parallel to the beampipe. In the endcap region, the tubes are 37 cm long
 1771 and arranged in 160 layers transverse to the beampipe. These configurations
 1772 can be seen in Figure 22 and Figure 23. With this geometry the TRT achieves a
 1773 resolution of 130 μm in the $r - \phi$ direction.

1774

5.4 CALORIMETRY

1775 The combination of calorimeter systems used in ATLAS can measure the energy
 1776 of electrons, photons, hadrons, and hadronic jets with complete coverage up to
 1777 $|\eta| < 4.9$ and across ϕ . Unlike the inner detector, the calorimeters are capable
 1778 of measuring neutral particles. To accomplish precision measurements of these
 1779 particle types, the ATLAS calorimeter system uses four individual calorimeters,
 1780 a LAr electromagnetic calorimeter in the barrel region, a tile hadronic calorime-
 1781 ter in the barrel region, a LAr hadronic endcap calorimeter, and a LAr forward
 1782 calorimeter. Together these provide hermetic coverage for the ATLAS detec-
 1783 tor. The configuration of these calorimeters is illustrated in Figure 29. **Note: I**
 1784 **could make this section much longer. It might be nice to include a more**
 1785 **complete description of showers for example. I will extend this section if**
 1786 **there is space at the end.**

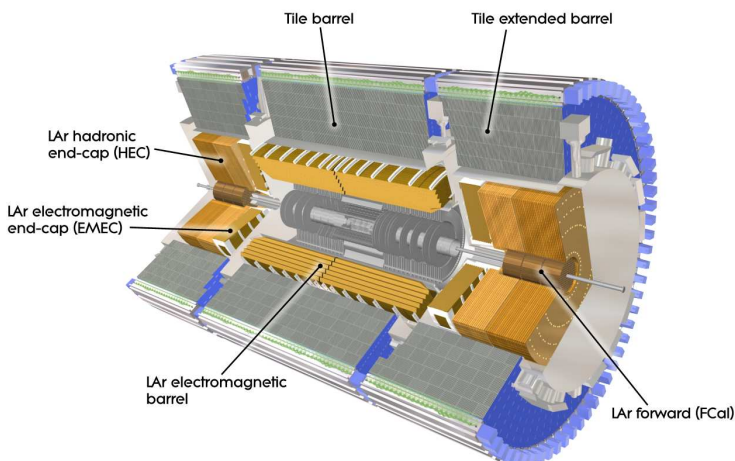


Figure 29

1787 The calorimeters are designed to absorb and measure the energy carried by
 1788 a particle, and completely stop the particle's propagation in the process. This
 1789 requires a significant amount of material to provide interactions. These interac-
 1790 tions then produce secondary particles, which can produce secondary particles
 1791 in turn, and thus form a cascade of particles called an electromagnetic (EM) or
 1792 hadronic shower, depending on the governing mechanism. Electromagnetic and
 1793 hadronic showers have very different properties and require different technolo-
 1794 gies to measure them accurately. All of the calorimeters in the ATLAS calorime-
 1795 ter system are sampling calorimeters: they use alternating layers of absorbing

and active material. The dense absorbing layers initiate the showers while the active layers measure the energy of the produced particles. A fraction of the energy is lost in the inactive layers, so the energy measurement from the active layers has to be corrected to estimate the actual energy of the particle.

The EM calorimeter provides around 20 radiation lengths (X_0) while the hadronic calorimeter provides around 10 interaction lengths (λ_0). As mentioned previously, radiation lengths measure the distance over which an electromagnetically interacting particle loses a characteristic fraction of its energy. Interaction lengths, on the other hand, measure the mean distance traveled by a hadronic particle before undergoing a nuclear interaction [6]. Figure 30 show the radiation lengths in the layers of the EM calorimeter in the barrel region as well as the interaction lengths for all calorimeters.

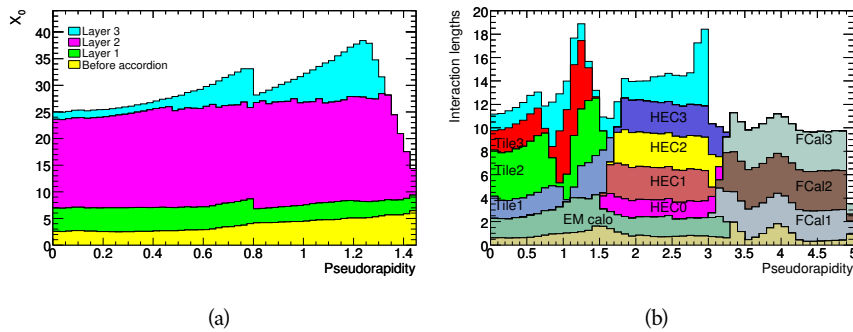


Figure 30: The depth of (a) the electromagnetic barrel calorimeter in radiation lengths and (b) all calorimeters in interaction lengths as a function of pseudorapidity.

5.4.1 ELECTROMAGNETIC CALORIMETER

The electromagnetic calorimeters use alternating layers of liquid argon and lead in an accordion shape. The accordion shape provides complete coverage in the ϕ direction while also providing many alternating layers for the a particle to pass through. The configuration is detailed in Figure 31. When an electron or photon passes through the lead, it produces an electromagnetic shower. The particles produced in those showers then pass into and ionize the liquid argon; the ions produced can then be collected by an electrode in the liquid argon layer to provide the actual energy measurement.

The barrel region is covered by a presampler and three separate sampling layers with decreasing segmentation. The presampler is a thin layer of liquid argon which measures the energy of any electromagnetic showers which are initiated before the particle reaches the calorimeter due to interactions with the detector material. The first layer is the strip layer, which has fine segmentation in η to enhance the identification of shower shapes and to provide a precise η measurement for reconstructing photons and electrons. The strip layer has only 4 radiation lengths worth of material, and has a segmentation of $\Delta\eta = 0.003$ and $\Delta\phi = 0.1$. The second layer is also finely segmented, with a segmentation of $\Delta\eta = 0.025$ and $\Delta\phi = 0.025$, and a thickness of 16 X_0 . This layer is designed

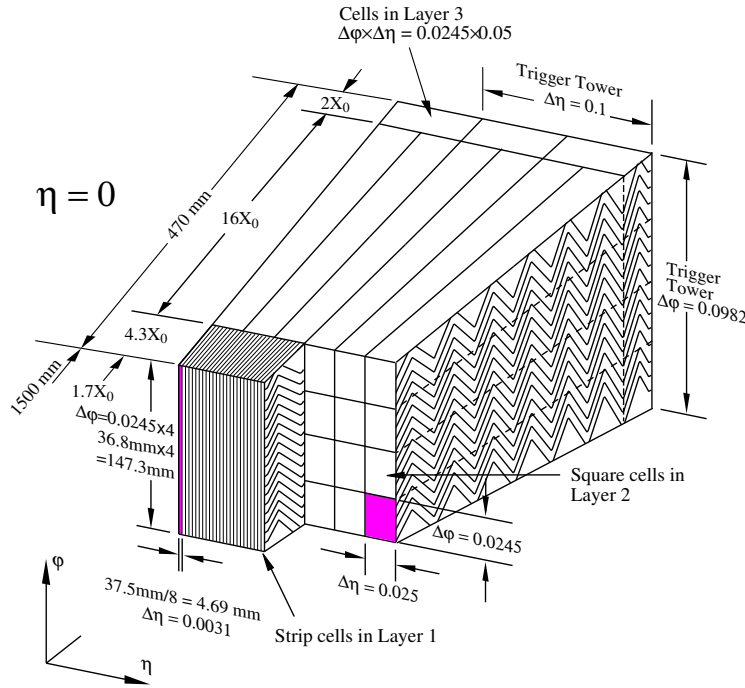


Figure 31: A schematic of the LAr calorimeter in the barrel region, highlighting the accordion structure.

1827 to contain an electromagnetic shower and to measure the majority of the energy
 1828 for photons and electrons. The third layer is only $2 X_0$ thick and measures the
 1829 energy of electromagnetic showers which leak out of the second layer, and helps
 1830 to separate electromagnetic showers from hadronic showers. The structure of
 1831 the LAr endcap calorimeter is similar except that the layers are arranged parallel
 1832 to the beampipe to measure energy deposits from high η particles.

1833 5.4.2 HADRONIC CALORIMETERS

1834 The hadronic calorimeters use a few different technologies to satisfy the resolu-
 1835 tion demands in the different areas of the detector, and together they cover the
 1836 region $|\eta| < 2.7$. In the barrel region, for $|\eta| < 1.7$, the hadronic calorimeters
 1837 are constructed of alternating tiles of steel and plastic scintillator. Like in the
 1838 electromagnetic calorimeter, the dense layer initiates a shower (in this case the
 1839 dense layer is the steel and the shower is hadronic) of particles which pass into
 1840 and ionize the following layer. The ionization in the plastic scintillator instead
 1841 produces a light signal proportional to the amount of ionization produced by the
 1842 shower, and this signal is measured using photomultipliers and provides the ac-
 1843 tual energy measurement. The construction of a tile in the calorimeter is shown
 1844 Figure 32, which highlights the alternating layers of steel and scintillator.

1845 This tile calorimeter, as well as the remaining hadronic calorimeters, have a
 1846 much coarser granularity than the electromagnetic calorimeters. The high gran-
 1847 ularity is not needed for an accurate energy measurement, and the hadronic
 1848 calorimeters are not designed to distinguish particle types like the electromag-

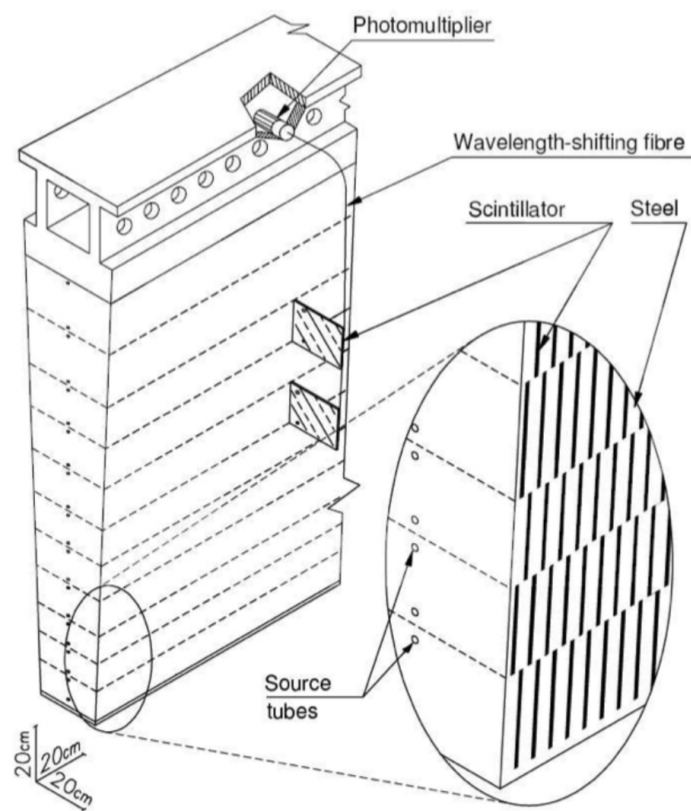


Figure 32: A schematic of a hadronic tile module which shows the alternating layers of steel and plastic scintillator.

netic calorimeters. The tile granularity is approximately $\Delta\eta = 0.1$ and $\Delta\phi = 0.1$, and the segmentation in depth and η is shown in Figure 33.

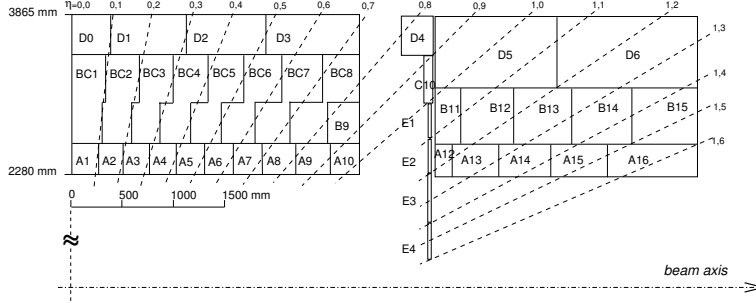


Figure 33: The segmentation in depth and η of the tile-calorimeter modules in the central (left) and extended (right) barrels.

The remaining hadronic calorimeters all use the same alternating sampling structure but with different active and inactive materials. The hadronic endcap calorimeter covers the range of $1.5 < |\eta| < 3.2$ and uses an inactive layer of copper and an active layer of liquid argon. The forward calorimeter covers the range of $3.1 < |\eta| < 4.9$ and uses a dense matrix of copper and tungsten filled with liquid argon.

5.5 MUON SPECTROMETER

Among SM particles, only muons and neutrinos consistently pass through the calorimeters. Because the neutrinos are also electrically neutral, there is no feasible option to measure them directly in ATLAS. The muons, on the other hand, are charged and are thus already measured as a track in the inner detector. The muon spectrometer provides a way to consistently identify muon tracks and also a way to provide an additional measurement of their momentum.

The muon spectrometer contains four subdetectors that cover the barrel and endcap regions. In the barrel region, the muon spectrometer uses a combination of Resistive Plate Chambers (RPCs) and MDTs to provide both a coarse, fast measurement for triggering and a precise momentum measurement for offline event reconstruction. Similarly, in the endcap region, the TGCs, MDTs, and CSCs allow for both triggering and precise measurements. The CSCs are used only in the innermost layer of the endcap region between $2.0 < |\eta| < 2.7$ where the particle flux is too large for the MDTs to provide accurate measurements. The overall layout of the muon systems are shown in the cut-away diagram in Figure 34, and Figure 35 shows a precise schematic of the layout of each of the detecting elements. The geometric arrangement shown provides consistent coverage for muons produced up to $|\eta| < 2.7$, and takes full advantage of the bending of the muons in the toroidal magnetic field, described in Section 5.2, to measure their momentum. Figure 36 shows a cross-section of the arrangement of the muon spectrometer in the barrel; the layers are divided into eight small and eight large chambers that are overlapped to provide complete coverage in ϕ .

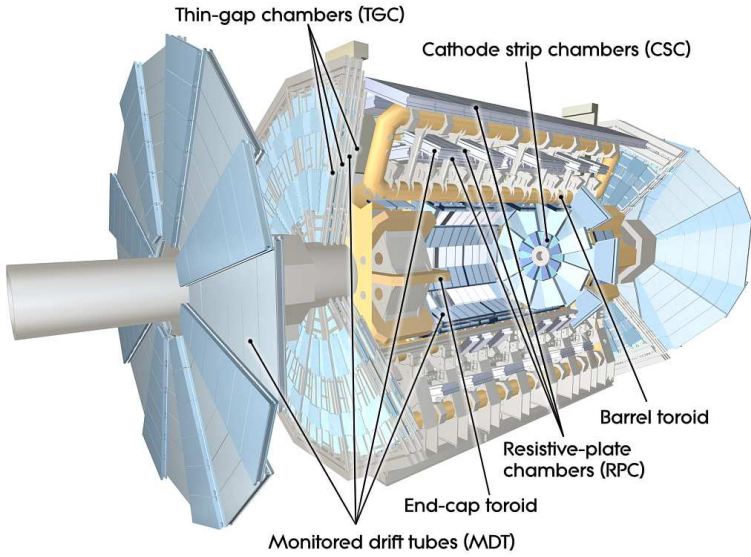


Figure 34: A cut-away diagram of the muon systems on ATLAS.

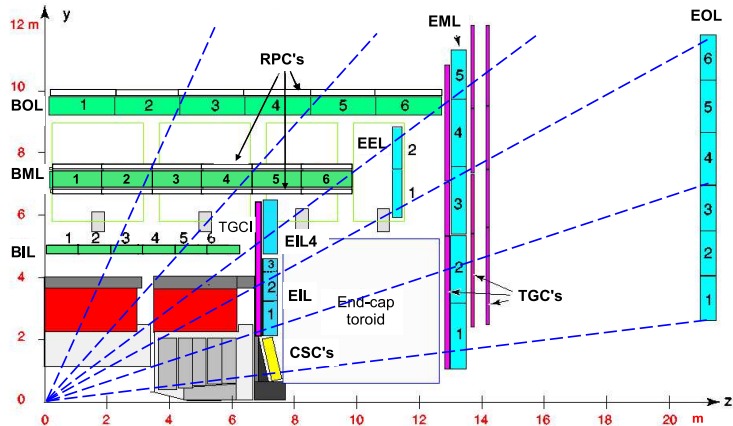


Figure 35: A quarter view of the muon spectrometer which highlights the layout of each of the detecting elements. The BOL, BML, BIL, EML, and EIL are all MDT elements, where the acronyms encode their positions.

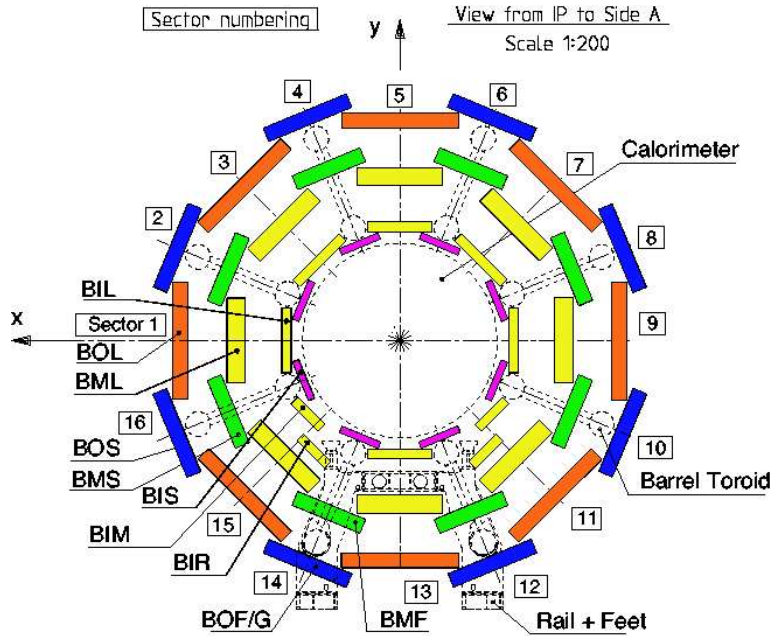


Figure 36: A schematic of the cross-section of the muon spectrometer in the barrel region.

1880 5.5.1 MONITORED DRIFT TUBE

1881 The momentum measurements in the barrel region are provided by three consecutive layers of MDT elements, located at approximately 5 m, 7 m, and 9 m from
 1882 the interaction point. Each of these layers is a composite of two multilayers of
 1883 drift tubes: two layers of three to four layers of tubes, as shown in Figure 37.
 1884 These aluminum tubes are 3 cm in diameter, with lengths between 0.9 and 6.2 m,
 1885 and are filled with a mixture of ArCO₂ kept at 3 bar absolute pressure. A central
 1886 tungsten-rhenium wire with a diameter of 50 μm runs along the length of the
 1887 tube, and is kept at a potential of 3080 V.
 1888

1889 A muon traversing these tubes ionizes the gas, and the ionization electrons
 1890 then drift in the electric field toward the central wire. Close to the wire, the
 1891 electric field is strong enough to cause the original ionization electrons to ionize
 1892 additional electrons, producing an avalanche that can be measured as a current
 1893 along the wire. The time of arrival of that current depends on how far the muon
 1894 entered from the wire, and can be used to achieve a position resolution of 80 μm
 1895 in an individual tube. The combination of the measurements in the consecutive
 1896 layers of tubes improves this position resolution to 35 μm transverse to the tubes,
 1897 with a resolution of 1 m along the tube direction.

1898 To achieve a good resolution over the entire length of a muon track, the rel-
 1899 ative positions of the tubes of the muon spectrometer must be known to an ac-
 1900 curacy of 30 μm . This is achieved by an optical laser alignment system placed in
 1901 each of the individual chambers and throughout the cavern. These monitor any
 1902 changes in position or alignment due to effects like gravitational sag, tem-
 1903 perature shifts, and the magnetic field. The configuration of the alignment system
 1904 within an individual chamber is also shown in Figure 36.

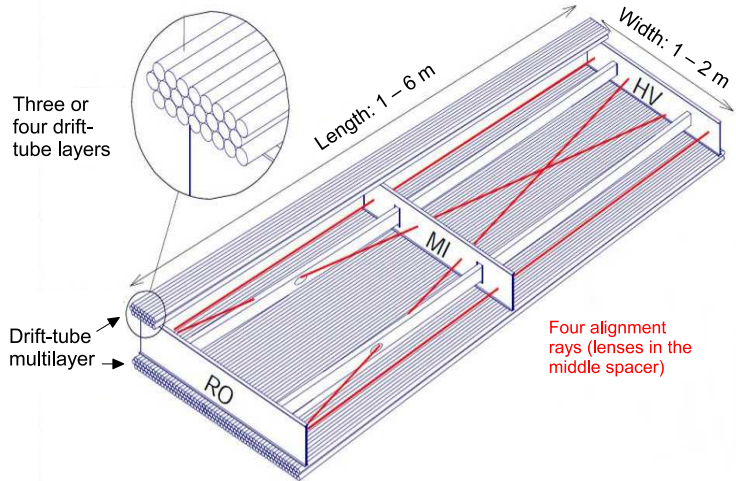


Figure 37: A schematic of a single **MDT** chamber, which shows the multilayers of drift tubes as well as the alignment system.

1905 5.5.2 RESISTIVE PLATE CHAMBER

1906 The **RPC** is the outermost detecting layer in the muon spectrometer in the barrel
 1907 region, and provides a fast measurement of the ϕ position of muons for triggering.
 1908 The speed of the measurement, with a time resolution of just a few tens of
 1909 nanoseconds, requires a poor spatial resolution of approximately 1 cm. There
 1910 are three **RPCs** layers in the muon spectrometer, two located on either side of
 1911 the central **MDT** layer and one located outside the final **MDT** layer, as shown in
 1912 Figure 35. The **RPCs** consist of two layers of parallel plates filled with a gas mix-
 1913 ture of $C_2H_2F_4$. A muon passing through these systems ionizes the gas, like in
 1914 the **MDT**, which causes an avalanche of ionization electrons in the electric field
 1915 maintained between the plates. Metal strips on the outside of the chamber ca-
 1916 pacitively couple to the accumulated charge, and are read out to measure the η
 1917 and ϕ positions of the muon track.

1918 5.5.3 CATHODE STRIP CHAMBER

1919 The majority of the momentum measurements in the endcap region are provided
 1920 by the **MDTs**. In the most forward region of the muon spectrometer, between
 1921 $2.0 < \eta < 2.7$, the particle flux is very high due to contributions from low energy
 1922 photons and neutrons. The **MDT** can only sustain a hit rate of approximately 150
 1923 Hz/cm² because of limitations in the drift times of the gas and the capacity of
 1924 the readout electronics. The **CSCs** were designed to handle higher hit rates, up to
 1925 1000 Hz/cm², and provide the necessary coverage in that high flux region.

1926 The **CSC** consists of several multiwire proportional chambers, where the wires
 1927 are oriented in the radial direction out from the beampipe. There are eight large
 1928 and eight small chambers, arranged to partially overlap in the ϕ direction, as
 1929 shown in Figure 38. Like in the **MDT**, a muon traversing the system produces
 1930 ionization in the gas; here, however, the ionization is collected on a number of

wires. These wires couple to cathodes on the chambers which are segmented into strips in two directions. The relative amount of charge on each of the neighboring strips can be used to interpolate to the position of the muon in both η and ϕ .

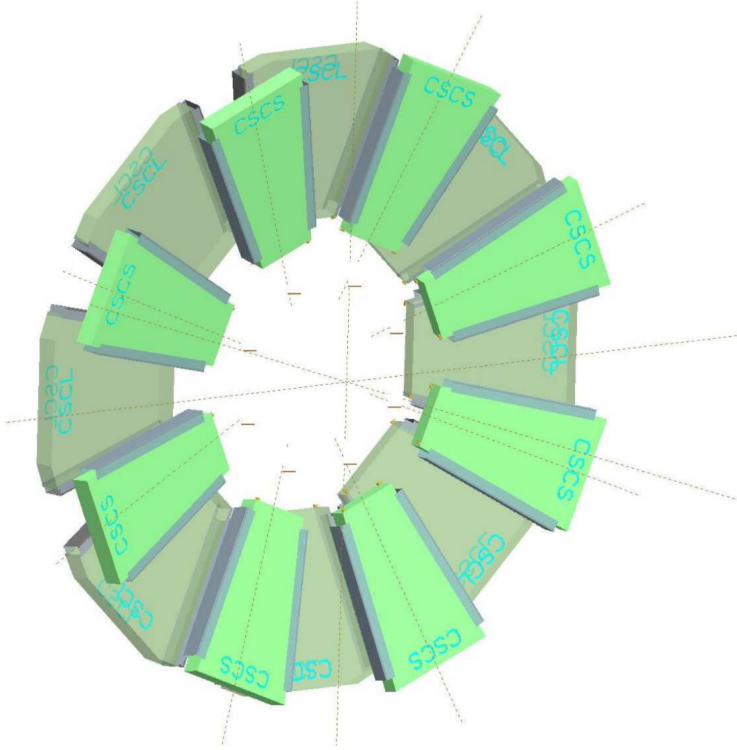


Figure 38: A schematic of the [CSC](#) endcap, showing the overlapping arrangement of the eight large and eight small chambers.

5.5.4 THIN GAP CHAMBER

Like in the barrel region, a separate, fast detector is required to provide position measurements of muons for trigger in the endcap region. This is provided by the [TGC](#) which consists of seven layers in the middle station of the endcap, two doublet layers and one triplet layer, and a single doublet layer in the inner endcap station. Figure 39 shows the arrangement of the triple and doublet layers of the [TGCs](#).

Like the [CSCss](#), the [TGCs](#) are multiwire proportional chambers with a wire-to-cathode distance of 1.4 mm and a wire-to-wire distance of 1.8 mm. Readout strips on the outside of the chambers run perpendicular to the wires, and couple to the charge collected on the wires to provide a position measurement in the η direction. The current induced on the wires is also readout to provide a position measurement in the ϕ direction. The high electric field and small wire-to-wire distance give it the required good time resolution to be used for triggering events.

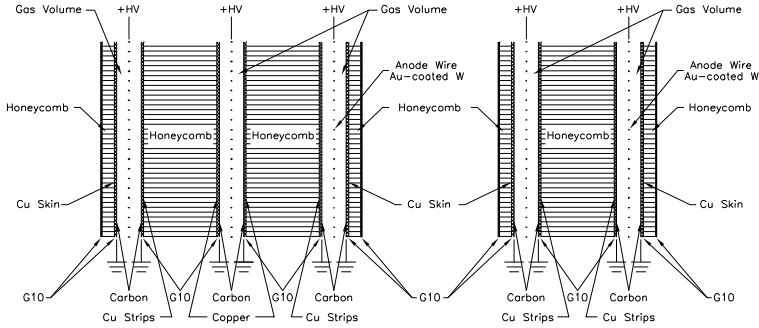


Figure 39: A schematic of the [TGC](#) doublet and triplet layers.

1949 5.6 TRIGGER

1950 It is not possible for the detector and the associated computing systems to record
 1951 the terabytes of data that the 40 MHz event rate produces every second. Instead,
 1952 a small fraction of these events are selected by the trigger system to be recorded
 1953 and later analyzed. Selecting interesting events at such a high rate poses a sig-
 1954 nificant challenge for the both the detector design and the implementation of a
 1955 trigger decision and data acquisition system. The trigger must balance the time
 1956 needed to decide to keep an event, to avoid losing information, with the filtering
 1957 accuracy to consistently select a full menu of physics events that can be used for
 1958 the wide array of searches and measurements targeted by ATLAS.

1959 The ATLAS trigger system, as of Run 2, consists of two levels of decision mak-
 1960 ing. The first level, referred to as L1, is hardware based and uses inputs from
 1961 a subset of the detector elements to narrow the considered event rate from the
 1962 original 40 MHz down to 100 kHz. The 100 kHz rate is the maximal rate that the
 1963 event information can be transferred from the detector. The second, software-
 1964 based level, referred to as the [HLT](#), makes the final decisions on which events to
 1965 keep for analysis and selects a rate of around 1 kHz. The collection of selection
 1966 criteria used to make the L1 decisions feed into subsequent selection criteria in
 1967 the [HLT](#), and the set of these combinations of L1 and [HLT](#) criteria from the trig-
 1968 ger menu which defines exactly what events are recorded on ATLAS. The trigger
 1969 menu used for 2015 data collection is shown in Table 7, which summarizes the
 1970 selection requirements at both levels and additionally shows the peak measured
 1971 rates contributed by each.

1972 At L1, the trigger system uses information primarily from the calorimeters
 1973 and muon spectrometer to select high p_T jets, electrons, photons, and muons.
 1974 The electromagnetic calorimeter uses reduced granularity energy measurements
 1975 as well as isolation requirements to select electrons and photons. The hadronic
 1976 calorimeter also uses a combination of reduced granularity energy measurements
 1977 and isolation to select high momentum jets and hadronically decaying tau lep-
 1978 tons.

1979 The calorimeters are also used to provide triggers based on missing energy:
 1980 the coarse granularity energy measurements are used to calculate a directional
 1981 sum of energies and to trigger on a significant imbalance. Only the [RPCs](#) and

Trigger	Typical offline selection	Trigger Selection		Level-1 Peak Rate (kHz)	HLT Peak Rate (Hz) $L = 5 \times 10^{33} \text{ cm}^{-2}\text{s}^{-1}$
		Level-1 (GeV)	HLT (GeV)		
Single leptons	Single iso μ , $p_T > 21$ GeV	15	20	7	130
	Single e , $p_T > 25$ GeV	20	24	18	139
	Single μ , $p_T > 42$ GeV	20	40	5	33
	Single τ , $p_T > 90$ GeV	60	80	2	41
Two leptons	Two μ 's, each $p_T > 11$ GeV	2×10	2×10	0.8	19
	Two μ 's, $p_T > 19, 10$ GeV	15	18, 8	7	18
	Two loose e 's, each $p_T > 15$ GeV	2×10	2×12	10	5
	One e & one μ , $p_T > 10, 26$ GeV	20 (μ)	7, 24	5	1
	One loose e & one μ , $p_T > 19, 15$ GeV	15, 10	17, 14	0.4	2
	Two τ 's, $p_T > 40, 30$ GeV	20, 12	35, 25	2	22
	One τ , one μ , $p_T > 30, 15$ GeV	12, 10 (+jets)	25, 14	0.5	10
Three leptons	One τ , one e , $p_T > 30, 19$ GeV	12, 15 (+jets)	25, 17	1	3.9
	Three loose e 's, $p_T > 19, 11, 11$ GeV	15, 2×7	17, 2×9	3	< 0.1
	Three μ 's, each $p_T > 8$ GeV	3×6	3×6	< 0.1	4
	Three μ 's, $p_T > 19, 2 \times 6$ GeV	15	18, 2×4	7	2
	Two μ 's & one e , $p_T > 2 \times 11, 14$ GeV	2×10 (μ 's)	$2 \times 10, 12$	0.8	0.2
	Two loose e 's & one μ , $p_T > 2 \times 11, 11$ GeV	$2 \times 8, 10$	$2 \times 12, 10$	0.3	< 0.1
	One photon	one γ , $p_T > 125$ GeV	22	120	8
Two photons	Two loose γ 's, $p_T > 40, 30$ GeV	2×15	35, 25	1.5	12
	Two tight γ 's, $p_T > 25, 25$ GeV	2×15	2×20	1.5	7
Single jet	Jet ($R = 0.4$), $p_T > 400$ GeV	100	360	0.9	18
	Jet ($R = 1.0$), $p_T > 400$ GeV	100	360	0.9	23
E_T^{miss}	$E_T^{\text{miss}} > 180$ GeV	50	70	0.7	55
Multi-jets	Four jets, each $p_T > 95$ GeV	3×40	4×85	0.3	20
	Five jets, each $p_T > 70$ GeV	4×20	5×60	0.4	15
	Six jets, each $p_T > 55$ GeV	4×15	6×45	1.0	12
b -jets	One loose b , $p_T > 235$ GeV	100	225	0.9	35
	Two medium b 's, $p_T > 160, 60$ GeV	100	150, 50	0.9	9
	One b & three jets, each $p_T > 75$ GeV	3×25	4×65	0.9	11
	Two b & two jets, each $p_T > 45$ GeV	3×25	4×35	0.9	9
b -physics	Two μ 's, $p_T > 6, 4$ GeV plus dedicated b -physics selections	6, 4	6, 4	8	52
Total				70	1400

Table 7: The trigger menu for the 2015 data collection with $L = 5 \times 10^{33} \text{ cm}^{-2}\text{s}^{-1}$. Both the L1 and HLT selection requirements and their trigger rates are shown measured at the specified luminosity are shown. The typical offline selections represent a typical set of offline requirements imposed after the trigger in an analysis.

1982 [TGCs](#) muon subdetectors contribute to the decision at L1, and are used to identify
 1983 high momentum muons. The contributions to the triggering rate of the various
 1984 types of L1 triggers are shown in Figure 40. The total rate is indicated in black
 1985 and is lower than the sum of individual rates because their is significant overlap
 1986 between different trigger channels. The majority of the rate comes from lepton
 1987 and photon triggers.

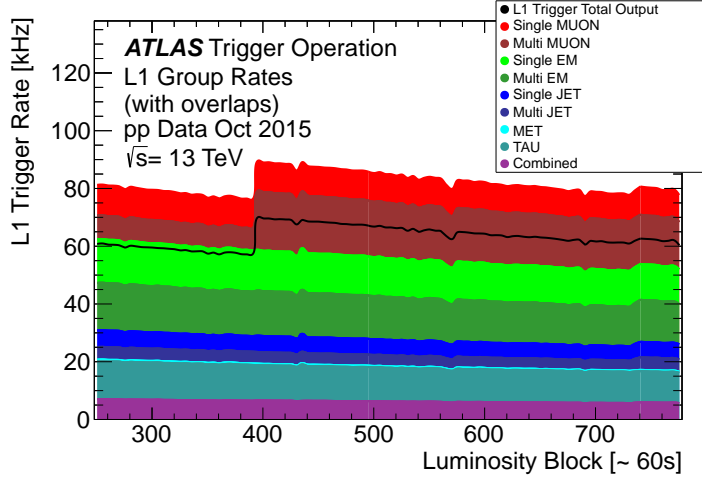


Figure 40: The L1 Trigger rate broken down into the types of triggers as a function of the luminosity block for the 2015 data collection period.

1988 After an event is chosen by the L1 trigger, the detector measurements from the
 1989 bunch crossing which fired the trigger is read out from the front-end electronics
 1990 and stored on read-out boards. This inclusive information is necessary to make
 1991 more the more precise event selections than is possible with the reduced infor-
 1992 mation at L1. The [HLT](#) then uses this information with software algorithms to
 1993 decide whether or not to permanently record the event. The L1 trigger also for-
 1994 wards which decision was made and Region of Interests ([RoIs](#)) to the [HLT](#), which
 1995 allows the [HLT](#) to focus on particular algorithms and particular sections of the
 1996 detector to greatly improve the algorithmic selection speed. The additional in-
 1997 formation available to the [HLT](#) allows it to implement additional trigger targets,
 1998 such as identified jets from the decays of b-hadrons. The contributions to the
 1999 triggering rate of the various types of [HLT](#) triggers are shown in Figure 41.

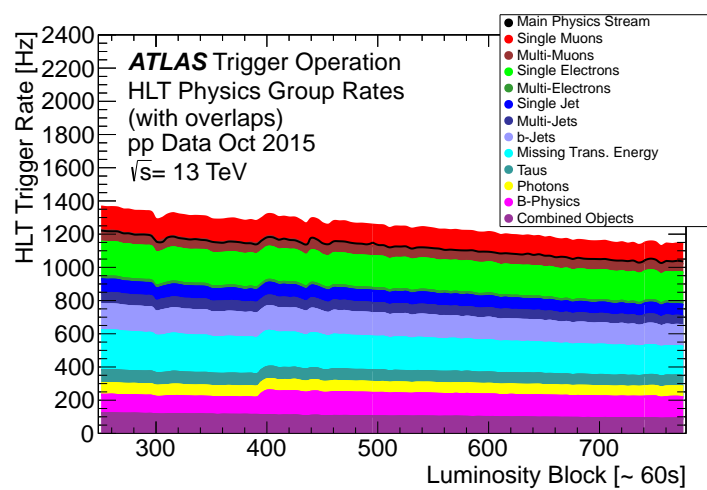


Figure 41: The HLT Trigger rate broken down into the types of triggers as a function of the luminosity block for the 2015 data collection period.

2000

2001 EVENT RECONSTRUCTION

2002 The ATLAS experiment combines measurements in the subdetectors to form a
 2003 cohesive picture of each physics event. The majority of particles that traverse
 2004 the detector leave behind some combination of ionization hits in the tracking
 2005 detectors or energy deposits in the calorimeters, and these measurements can
 2006 be used to reconstruct physical quantities like the particle's energy, momentum,
 2007 or trajectory. Even the type of the particle can be distinguished by comparing
 2008 the various ways that different species of stable particles interact with the sub-
 2009 detectors. Reconstruction is the series of algorithms which take the electronic
 2010 outputs of the detector and assigns them into individual physics objects. The
 2011 physics objects summarize the properties of particles produced by the collision
 2012 or subsequent decays, either for individual isolated particles like leptons, or for
 2013 a collection of the cascade of products produced in the decay of an energetic
 2014 hadron, called a jet. These are the objects and quantities most often used in anal-
 2015 ysis to make measurements of SM processes or to search for new physics.

2016 6.1 CHARGED PARTICLES

2017 As described in Section 5.3, charged particles that traverse the inner detector
 2018 leave behind hits in the subdetectors. Each of these hits translates into a position
 2019 measurement along the trajectory of that particle, with position resolutions de-
 2020 pending on the subdetector that provided the measurement. Track reconstruc-
 2021 tion uses these position measurements to collect hits in consecutive layers of
 2022 the detector into a trajectory consistent with a particle curving in a magnetic
 2023 field [19, 20]. This reconstructed trajectory is called a track. The number of hits
 2024 in the inner detector for each event makes a combinatorial method completely
 2025 infeasible: the algorithms that form tracks must be significantly more intelligent
 2026 so that event reconstruction does not exhaust computing resources.

2027 The first and primary algorithm employed in track reconstruction is called
 2028 the inside-out method, which begins with the assumption that the track orig-
 2029 inated from the interaction point. Its purpose is to identify primary particles,
 2030 those which originate in the proton-proton collisions and with a lifetime long
 2031 enough to reach the inner detector. Combinations of three hits are considered
 2032 from measurements in the Pixel detector and the SCT, and form the seed for a
 2033 track. Specifically, the seeding algorithm looks for a seed using three pixel hits,
 2034 two pixel hits and one SCT hit, or three SCT hits. The seed is then extrapolated
 2035 forwards and backwards into the Pixel and SCT detectors depending on the seed
 2036 location, and hits in each layer are considered to be added to the track using a
 2037 combinatorial Kalman filter [20]. After all of the silicon layers have been consid-
 2038 ered, tracks are filtered to reduce ambiguities from other nearby tracks or from
 2039 combinatorial coincidences. Then the tracks are extended outwards into the TRT

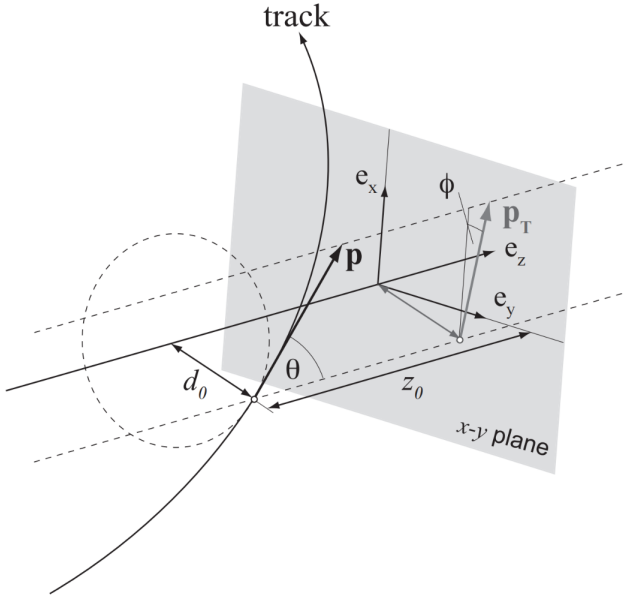


Figure 42: An illustration of the perigee representation of track parameters for an example track. The charge is not directly shown, but is indicated by the direction of curvature of the track [21].

in the same way. This algorithm is how the hits are chosen to be incorporated into a single track. Once the hits are collected, a fitting algorithm calculates the track parameters which best model the locations of the hits and their resolutions. The fitting uses five parameters, $(d_0, z_0, \phi, \theta, q/p)$, to specify a track in a perigee representation: d_0 and z_0 are the transverse and longitudinal impact parameters at the closest approach to the nominal beam axis, ϕ and θ are the usual angular coordinates, and q/p is the charge divided by the momentum. These parameters are illustrated in Figure 42. Those parameters directly determine the direction and momentum of the particle which produced the track.

This inside-out algorithm is complemented by an outside-in algorithm, which is used to find tracks from secondary particles, those produced in the decays or interactions of the primary particles inside the detector. As the name indicates, the outside-in algorithm begins by seeding tracks in the outermost layers of the inner detector, in the TRT. The seed in this case is formed by a segment in the TRT, and the track is propagated backwards into the SCT before being refitted to use all the included points. Some tracks are found with TRT segments only, which can result from interactions with the detector following the SCT. Figure 43 shows an example of the geometry of tracks formed by both algorithms, where the hits belonging to tracks found using the inside-out algorithm are highlighted in red, and the hits belonging to the tracks found using the outside-in algorithm are circled in black. The figure highlights the presence of a large number of both primary and secondary tracks in a single event, as well as the overall large number of hits present in the inner detector.

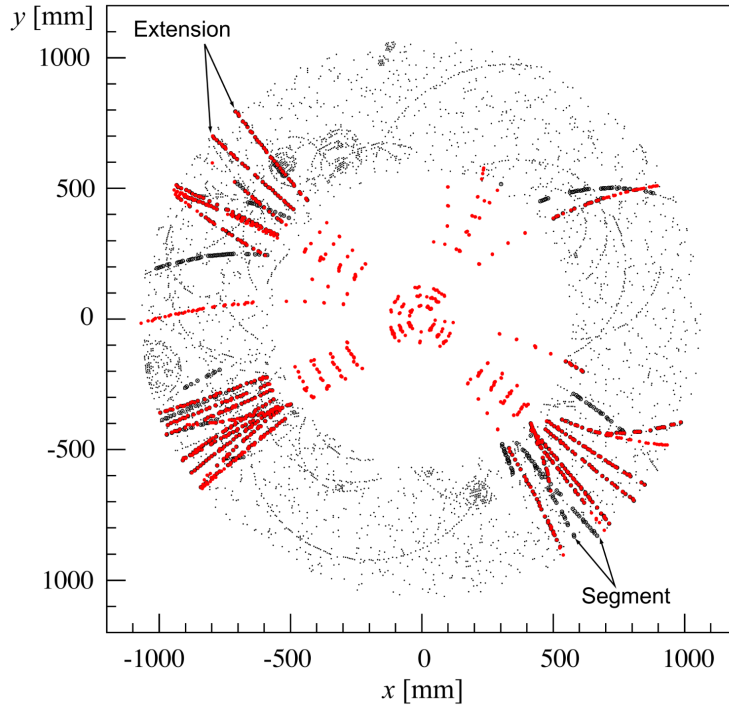


Figure 43: The x and y locations of the hits generated in a simulated $t\bar{t}$ event in the inner detector. The hits which belong to tracks formed using the inside-out algorithm are highlighted in red, while the hits which belong to tracks formed using the outside-in algorithm are circled in black.

2063 The tracks resulting from these algorithms can be contaminated by nearby
 2064 particles confusing the tracking algorithm in a high luminosity environment.
 2065 For example, enough hits present in the inner detector can lead to fake tracks
 2066 from combinations of hits from multiple individual tracks. Therefore, after the
 2067 tracks are formed and fitted, additional quality requirements are imposed in
 2068 order to reduce such backgrounds. Most tracking applications require at least
 2069 seven silicon hits, that is, seven hits between the Pixel detector and **SCT**. Then the
 2070 tracks are required to have at most two holes in the Pixel detector, where holes
 2071 are non-existing but expected measurements in a layer of the subdetector. If the
 2072 missing hit corresponds to an inactive module, however, it is not counted as a
 2073 hole but instead as a hit for tracking as the lack of a measurement is expected in
 2074 that case.

2075 6.1.1 PIXEL NEURAL NETWORK

2076 The hits in the Pixel detector are not typically confined to a single pixel, but
 2077 rather the charge is spread over several pixels per layer which are grouped to-
 2078 gether into clusters. The clustering of these pixels for isolated tracks is relatively
 2079 straightforward, but complications can arise in the high occupancy environment
 2080 where hits from multiple particles can overlap in a single cluster. Figure 44
 2081 shows examples of clusters generated by a single isolated particle, two nearly
 2082 overlapping particles, and a particle which emits a δ -ray. A δ -ray is a secondary

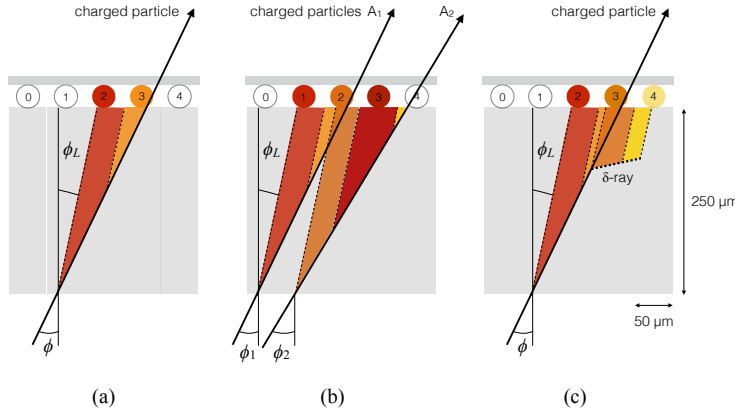


Figure 44: Examples of the clusters formed in a single layer of the pixel detector for (a) a single isolated particle, (b) two nearly-overlapping particles, and (c) a particle which emits a δ -ray [22].

2083 electron which is generated with enough energy to escape a significant distance
2084 away from the original particle and to generate additional ionization.

2085 A series of neural-networks analyzes the shape of the clusters to determine
2086 how many particles produced the cluster and to estimate the positions of each
2087 of the particles within the cluster. These allow for an identification of clusters
2088 caused by more than one particle or by a particle that emits a δ -ray. In a high-
2089 density tracking environment, the multiple position outputs can be used as the
2090 locations of individual hits to allow reconstruction of tracks which almost over-
2091 lap and with a much better separation than is possible without the splitting of
2092 individual clusters.

2093 6.1.2 PIXEL DE/DX

2094 A hit in the Pixel detector corresponds to the voltage generated from ionization
2095 current rising above a threshold value that is tuned to consistently record the
2096 passing of MIPs. A larger amount of charge deposited results in a larger voltage,
2097 and a larger signal remains above the threshold for a longer period of time. The
2098 time over threshold (ToT) is read out of the Pixel detector, and can be used to
2099 provide a measurement of the charge deposited in each pixel. The charge mea-
2100 surements from each of the pixels included in a pixel cluster are summed to form
2101 one charge measurement per layer of the pixel detector. That charge measure-
2102 ment, combined with the angle of incidence of the track and the known sizes of
2103 each detector element, can be converted into a measurement of dE/dx , the ion-
2104 ization energy deposited per unit distance, measured in $\text{MeVg}^{-1}\text{cm}^2$. The IBL
2105 only has sixteen available values (4 bits) of ToT to readout, compared to the 256
2106 available values (8 bits) in the remaining pixel layers. To help alleviate this lack
2107 of range, the IBL also records if it is in overflow: when the ionization is sufficient
2108 to generate a ToT above the largest value that can be recorded in the 4 bits.

2109 The measurements across multiple layers are combined to form an average
 2110 value of dE/dx for the track as a whole. Depending on where a charge particle
 2111 is produced, it will traverse four Pixel layers and create four clusters on average.
 2112 It can produce as few as two clusters in the Pixel detector if it passes through in-
 2113 active modules, and as many as five if it is in a region of the detector where multiple
 2114 modules overlap. To reduce the influence of the typical long Landau tails of the
 2115 distribution of dE/dx deposits [6], the average is calculated as a truncated mean
 2116 of these clusters. The value measured in the IBL is removed if it is in overflow, as
 2117 the measured value is not reliable in that case. If a track has five measurements
 2118 in the pixel detector, the two highest cluster values are removed. If a track has
 2119 two, three, or four measurements in the pixel detector, only the single highest
 2120 cluster value is removed. The remaining values are averaged to form the pixel
 2121 dE/dx .

2122 6.1.3 VERTEX RECONSTRUCTION

2123 A vertex represents the intersection of multiple tracks and corresponds to the
 2124 location of an interaction. If at least two charged particles result from the in-
 2125 teraction, the intersection of their resulting tracks reveals its position with high
 2126 precision. Vertices are divided into two groups, primary vertices which corre-
 2127 spond to the actual proton-proton collisions, and secondary vertices which cor-
 2128 respond to decays of short-lived particles or interactions with the detector. Pri-
 2129 mary vertices are particularly important, as they can provide a precise location
 2130 for the interaction which generated the observed particles. Understanding that
 2131 location is crucial in understanding the geometry of the event.

2132 Primary vertices are reconstructed by iteratively identifying seeds from recon-
 2133 structed tracks [23]. Each track's extrapolated z position at the beamline forms a
 2134 seed, and nearby tracks are fitted using that position as a point along their trajec-
 2135 tory. The goodness of fit with that vertex is considered for each track, measured
 2136 in χ^2 . The final position of the vertex is determined by a fit to all of the con-
 2137 sidered tracks, where the contribution from each track is weighted according to
 2138 the χ^2 compatibility with that vertex. Any tracks from this procedure that are
 2139 displaced by more than 7σ from that vertex are removed from the fit and used
 2140 to seed a new vertex. This procedure is iterated until no additional vertices can
 2141 be found.

2142 This procedure is typically performed twice. The first set of vertices is used
 2143 to fit a profile for the beamspot, which indicates the position of the intersection
 2144 of beams in that particular bunch crossing. The fitted beamspot then provides
 2145 a constraint for the second attempt to locate primary vertices, where both the
 2146 track fitting and seeding of vertices are required to be consistent with interac-
 2147 tions occurring within the beamspot.

2148 6.2 ELECTRONS AND PHOTONS

2149 Electrons are measured as both a charged particle track and energy deposits in
 2150 the electromagnetic calorimeter. Photons, on the other hand, leave energy de-

2151 posits in the electromagnetic calorimeter but do not produce a corresponding
 2152 track. Because the electromagnetic interactions with the calorimeter of both
 2153 photons and electrons produces more photons and electrons, the behavior in the
 2154 calorimeter is very similar and there is significant overlap in the reconstruction
 2155 techniques for each.

2156 The reconstruction of a photon or an electron in the calorimeter is based on
 2157 clustering algorithms which identify groups of energy deposits [24–26]. For this
 2158 purpose, the entire electromagnetic calorimeter is subdivided into a grid of 200
 2159 by 256 towers in the η and ϕ directions, respectively, where the individual grid
 2160 units have a size of $\Delta\eta = 0.025$ and $\Delta\phi = 0.025$. These towers correspond to
 2161 individual cells in the middle, coarsest layer of the EM calorimeter, and in the re-
 2162 maining layers the cells are grouped together cover the same area in $\eta - \phi$ space.
 2163 The clustering begins by finding seeds with a sliding-window algorithm based
 2164 on the towers: a window of 3 by 5 towers is formed and translated until the sum
 2165 of the energy within the window is maximized. If that energy is above 2.5 GeV,
 2166 then that region becomes a seed. The choice of 2.5 GeV was chosen to com-
 2167 promise between maximizing reconstruction efficiency while minimizing fake
 2168 electron seeds from electronic noise or soft hadrons from additional interactions.
 2169 The seeds are rejected if the energy measured in the hadronic calorimeter behind
 2170 the seed is large, as this typically indicates a hadron rather than an electron or
 2171 photon.

2172 Next, the inner detector tracks within a cone of $\Delta R = 0.3$ are compared to
 2173 the location and energy of the seed. Tracks are matched to the cluster if the ex-
 2174 trapolation of the track to the energy-weighted center in the middle layer of the
 2175 EM calorimeter falls within $\Delta\phi < 0.2$ in the direction of the curvature of the
 2176 track or $\Delta\phi < 0.05$ in the direction opposite of the curvature of the track. If the
 2177 seed matches with a track that originated from a primary vertex, the combina-
 2178 tion of track and electromagnetic cluster is reconstructed as an electron. If the
 2179 seed matches with a track that did not originate from a primary vertex, then the
 2180 electromagnetic cluster is reconstructed as a converted photon. And if there is
 2181 no corresponding track in the inner detector, then the cluster is reconstructed
 2182 as a photon.

2183 After classification, the final clustering of the energy in the EM calorimeter
 2184 calorimeter is performed. The classification must be done first, as the expected
 2185 size of the energy deposits in the calorimeter are different for electrons and pho-
 2186 tons. In the barrel region, the final clusters for electrons are formed in rectangles
 2187 of 3 towers in the η -direction and 7 towers in the ϕ -direction. This asymmetric
 2188 window accounts for the curving of the produced charged particles only in the
 2189 ϕ direction. For photons, the size of the rectangle is 3 towers by 5 towers. In the
 2190 endcap region, all object types are clustered in rectangles of 5 towers by 5 tow-
 2191 ers, as the effect of the magnetic field curvature is less pronounced in this region.
 2192 The sum of the energies in these clusters provide the final energy measurement
 2193 for the electron or photon.

2194 6.2.1 PHOTON IDENTIFICATION

2195 The original requirement for constructing a photon cluster, a significant energy
 2196 deposit in the electromagnetic calorimeter without a corresponding track or en-
 2197 ergy deposits in the hadronic calorimeter, is already effective in identifying pho-
 2198 tons. However, there is a significant background for prompt photon production
 2199 from the decays of pions, $\pi^0 \rightarrow \gamma\gamma$. These can be identified using the shape of
 2200 the cluster in the narrow η granularity in the first layer of the EM calorimeter.

2201 6.2.2 ELECTRON IDENTIFICATION

2202 Prompt electrons have a number of backgrounds, such as secondary electrons
 2203 from hadron decays or misidentified hadronic jets, that can be rejected using ad-
 2204 dditional information from the EM calorimeter and the inner detector. The most
 2205 basic level of electron identification, referred to as Loose, makes requirements
 2206 on the shower shapes in the high granularity first layer of the EM calorimeter
 2207 as well as the quality of the inner detector track. It also requires a good match
 2208 between the track and the calorimeter energy deposits and a small fraction of
 2209 energy in the hadronic calorimeter behind the electromagnetic cluster. ATLAS
 2210 defines several additional working points, including Medium and Tight, which
 2211 provide progressively lower background rates for electrons by imposing addi-
 2212 tionally strict requirements on the above variables as well as new requirements
 2213 like the impact parameter of the inner detector track or the comparison of the
 2214 cluster energy to the momentum in the inner detector.

2215 6.3 MUONS

2216 Muons produced in ATLAS first traverse the inner detector and leave behind a
 2217 track as described in Section 6.1. The muon then passes through the calorimeter,
 2218 leaving behind a small, characteristic amount of energy, and then passes through
 2219 the muon spectrometer where it produces hits in the MDTs or CSCs. Muon tracks
 2220 are formed from local segments of hits in each layer of the MDTs or CSCs, and
 2221 then the final muon spectrometer track is formed by combining the two local
 2222 segments [27]. When a track is reconstructed in both the inner detector and
 2223 the muon spectrometer, the track is refitted to include the hits in both the inner
 2224 detector and the muon spectrometer, and forms a combined muon.

2225 In a few regions of the detector, a muon may fail to leave behind both a com-
 2226 plete inner detector and muon system track. For a very small fraction of the
 2227 acceptance of the muon system, there is only one layer of muon chambers and a
 2228 global muon system track is not formed. In this case, as long as the track in the
 2229 inner detector exists and geometrically matches to a segment, a segment-tagged
 2230 muon is formed using momentum measurements from the inner detector. In
 2231 the region where the muon system has coverage but the inner detector does not,
 2232 $2.5 < |\eta| < 2.7$, a stand-alone muon is formed which uses only information
 2233 from the muon system. And for muons produced within one of the few holes in
 2234 the muon system, including $|\eta| < 0.1$, the characteristic energy deposits in the

2235 calorimeter can be used to tag an inner detector track as a calo-tag muon. These
 2236 additional categories are used to achieve high efficiency over a larger range of
 2237 acceptance, but the combined muons are the most reliable.

2238 6.3.1 MUON IDENTIFICATION

2239 The various types of muons are incorporated into three working points: Loose,
 2240 Medium, and Tight, which reflect the increasing muon purity for each of the
 2241 selections definitions. Tight muons include only combined muons with a good
 2242 track fit quality and momentum resolution and at least two hits in a precision
 2243 muon system layer. Medium muons include those in tight as well as combined
 2244 muons with one precision hit and one precision hole, where hole is defined in
 2245 the same way as in Section 6.1. The medium working point also includes stand-
 2246 alone muons with $|\eta| > 2.5$ and at least two hits in precision layers. And finally
 2247 the loose working point includes both medium and tight muons, but additional
 2248 includes segment-tagged and calo-tagged muons in the region $|\eta| < 0.1$.

2249 6.4 JETS

2250 A jet does not directly correspond to a physical particle, unlike all of the recon-
 2251 structed objects described above, but instead tries to capture the conical cascade
 2252 of particles produced in the hadronization of a quark or gluon from the proton-
 2253 proton collision. The hadronization process creates a very large number of col-
 2254 limated particles, with a high enough density that individually reconstructing all
 2255 of the produced particles in the calorimeter is not possible within ATLAS. How-
 2256 ever most analyses are interested only in the kinematics of the particle which
 2257 produced the cascade, rather than the individual products. Therefore, jets are
 2258 a useful tool to measure the combined energy and direction of the ensemble of
 2259 products and thus represents the kinematics of the original. Jet algorithms are
 2260 very generic and can be used to group together a number of types of objects to
 2261 form aggregate representations. For example, truth particles in simulation can
 2262 be grouped in truth jets, or tracks from the inner detector can be grouped to-
 2263 gether to form track jets. This section, however, will focus on calorimeter jets
 2264 which take topoclusters of energy deposits in the calorimeter as inputs and pro-
 2265 duce a combined object which represents the energy measured by the calorime-
 2266 ter and the location where it was deposited.

2267 6.4.1 TOPOLOGICAL CLUSTERING

2268 Hadrons often deposit their energy into multiple individual cells in both the elec-
 2269 tromagnetic and hadronic calorimeters. The purpose of topological clustering is
 2270 to group cells in all three dimensions into clusters that represent a single energy
 2271 deposit. The procedure must be robust enough to reject noise fluctuations in
 2272 the cell energy measurements that can come from both electronic noise and ad-
 2273 dditional low energy particles produced in pileup activity. The background level

of calorimeter noise is called σ_{noise} , and is an important component of the topological clustering.

The topological clusters are formed in a three step process called the 4-2-0 threshold scheme, which uses three energy thresholds to build up a cluster from cells [28]. First, any cells with a measured energy above $4\sigma_{\text{noise}}$ are identified as seed cells. The cells adjacent to the seed cells with a measured energy above $2\sigma_{\text{noise}}$ are called secondary cells. All of the cells which are adjacent to a secondary cell with $E_{\text{cell}} > 2\sigma_{\text{noise}}$ are also labeled secondary cells. Tertiary cells are those immediately adjacent to a seed or secondary cell with a measured energy above zero. Adjacency in this sense is defined in three dimensions, cells are adjacent if they are neighbors within a layer but also if they have the same $\eta - \phi$ coordinates but are in adjacent layers or even in an adjacent layer in another calorimeter.

From these definitions, clusters are built by resolving the seeds in order of significance, the ratio $E_{\text{cell}}/\sigma_{\text{noise}}$. All adjacent secondary cells to the highest significance seed are added to that seed's topocluster, and any of those cells which would also have qualified as seeds are removed from the list of seeds. Once all of the secondary cells have been added, the tertiary cells are then added to that cluster as well. This procedure is then iterated until no seeds remain, forming the first round of topoclusters.

It is also useful to split topoclusters into multiples if local maxima are present within the topocluster, as clusters produced by multiple nearby particles can merge. The splitting process begins by finding local maxima cells in the middle layer of the calorimeters with a minimum energy of 500 MeV and at least four neighboring secondary cells. These requirements reduce the likelihood to split a cluster due to random fluctuations, as the middle layers provide the most reliable energy measurements. Cells between two local maxima can then be shared between two clusters to account for overlapping contributions from two particles. The energy sharing is weighted by the energy of each cluster as well as the distance of the cell to the centroid of that cluster.

The energies of all the cells in the cluster are then summed together to form the energy of that cluster. The energy needs to be corrected for the various losses expected in the calorimeter, as described in Section 5.4. The simplest correction, scaling the measured energy by the sampling fraction, brings the cluster energies to the EM scale. It is called the EM scale because it accurately describes the energy of electromagnetic showers.

Another scale is defined to improve accuracy for hadronic processes, the local cluster weighted (LCW) scale, that helps to correct for the expected variations in hadronic energy deposits. The LCW correction first determines if the shower is hadronic or electromagnetic, based on the depth of the shower and the cluster energy density. For hadronic showers, the energy is corrected for calorimeter non-compensation, an effect which reduces the measured energy of hadronic showers because some of the energy goes into invisible processes like the break up of nuclei. All clusters are then corrected for energy that may be deposited in uninstrumented regions in that cluster's location in the calorimeter, and they are

2319 also corrected with an estimate of how much energy falls outside the extent of
 2320 the cluster based on its shape and the deposit type.

2321 6.4.2 JET ALGORITHMS

2322 Using the topological clusters as inputs, a jet algorithm groups them together
 2323 into a collection of adjacent energy deposits that is intended to correspond to
 2324 a single process [29]. Jet algorithms need a few key characteristics to be usable
 2325 for physics analysis. First, the jets produced by the algorithm should have little
 2326 dependence on the addition of soft particles to the event (infrared safety), as a
 2327 negligible addition of energy should not significantly modify the event topology.
 2328 Similarly, the jets produced by the algorithm should also not significantly depend
 2329 on mostly collinear splitting of an input particle (collinear safety); that is, a single
 2330 quark replaced by two, parallel quarks with half the original's momentum should
 2331 not change the resulting jets, which are intended to capture only the properties
 2332 of the aggregate and not those of individual particles. And finally the algorithm
 2333 needs to be sufficiently simple and fast to be used for the large rate of collected
 2334 proton-proton collisions on ATLAS.

2335 The most commonly used algorithm on ATLAS that satisfies these require-
 2336 ments is called the anti- k_t algorithm, and is discussed in further detail in Refer-
 2337 ence [30]. The anti- k_t , in brief, relies on iteratively combining the input objects
 2338 that are closest together, where closest is defined by a particular distance metric,
 2339 $d_{i,j}$, where the index i represents the combination constructed so far and j is an
 2340 additional object being considered. The combinations stop when the closest re-
 2341 maining object is the beam itself, where the distance to the beam is called $d_{i,B}$.
 2342 An entire class of algorithms follows this procedure with the following distance
 2343 metrics

$$d_{i,j} = \min(k_{ti}^{2p}, k_{tj}^{2p}) \frac{\Delta_{ij}^2}{R^2} \quad (18)$$

$$d_{i,B} = k_{ti}^{2p} \quad (19)$$

2344 where $\Delta_{ij} = (y_i - y_j)^2 + (\phi_i - \phi_j)^2$, k_{ti} is the transverse momentum of the
 2345 object, y is the rapidity, and p is a parameter of the algorithm. Anti- k_t is the
 2346 particular case where $p = -1$, and is a choice that results in an algorithm that is
 2347 both infrared and collinear safe.

2348 The algorithm is repeated until there are no input objects remaining, which
 2349 results in a series of jets. Each jet has a complete four momentum from the com-
 2350 bination of its input clusters, where the combinations assume a mass of zero.
 2351 The jet energies then need to be calibrated to attempt to match the energy of the
 2352 object which produced the jet.

2353 6.4.3 JET ENERGY SCALE

2354 Though the LCW scheme attempts to correct the topoclusters to reflect the true
 2355 deposited energy, the correction does not fully account for energy lost within

2356 the calorimeters. Because of these effects, the original reconstructed jet energy
 2357 does not reflect the true energy of the particle which initiated the jet. Therefore
 2358 it is necessary to additionally correct the reconstructed jet itself, in addition to
 2359 the corrections on the inputs. This correction is referred to as the **JES**, which
 2360 combines several individual steps of calibration [31].

2361 The first calibration step corrections the direction of the jet to ensure that it
 2362 points back to the primary vertex. Next, the energy of the jet is corrected for
 2363 pileup by subtracting the expected contribution from pileup based on the mo-
 2364 mentum, η , and area of the jet as well as the number of reconstructed vertices
 2365 and expected number of interactions per crossing. The largest single correction
 2366 is the absolute η and scale correction, where the jet energy and pseudorapidity
 2367 is corrected to attempt to match the energy and pseudorapidity of the parton
 2368 which produced it. This correction is measured in simulation by comparing the
 2369 reconstructed jet energies to the energy of the truth particle which produced it.
 2370 However the simulation is not relied on alone to estimate this correction, and an
 2371 additional step applies an additional energy correction based on in-situ measure-
 2372 ments in data. These corrections come from various techniques which measure
 2373 jet energies indirectly by balancing them with other, well-measured objects. In
 2374 the central region ($|\eta| < 1.2$), jets are balanced against photons and the leptonic
 2375 decays of Z bosons and high momentum jets ($p_T > 210$ GeV) are also balanced
 2376 against multiple smaller jets in multijet events. Jets at larger pseudorapidities,
 2377 above $|\eta| = 1.2$, are calibrated by balancing with lower pseudorapidity jets.

2378 These steps introduce a number of systematic uncertainties, referred to as
 2379 the **JES** uncertainty. The largest of these comes from the in-situ measurements,
 2380 which are statistically limited in measuring high momentum and high pseudora-
 2381 pidity jets. The total, fractional **JES** uncertainty is shown as a function of p_T in
 2382 Figure 45. The uncertainty falls to a minimum value of just over 1.0% around a
 2383 few hundred GeV, and rises again at high momentum because of the difficulty of
 2384 measuring jet balance in data above 2-3 TeV. The uncertainty is also minimized
 2385 at low $|\eta|$, and grows at large $|\eta|$ again where making in-situ measurements is
 2386 difficult. This technique does not actually provide a measurement of the uncer-
 2387 tainty for the highest energy jets, above 3 TeV, because there are not enough
 2388 measured data events to provide them. An alternative method for deriving the
 2389 **JES** and **JES** uncertainty that can be used even for very high p_T jets will be dis-
 2390 cussed in Chapter 8.

2391 6.5 MISSING TRANSVERSE ENERGY

2392 Among stable **SM** particles, only the neutrino cannot be directly measured in the
 2393 ATLAS detector. Because the neutrino carries neither electric nor color charge,
 2394 it is very unlikely to interact with the tracking detectors or the calorimeters,
 2395 and instead passes through the detector completely unobserved. Some particles
 2396 which have been conjectured to exist, like the **LSP** in many **SUSY** models, would
 2397 also have the same behavior. Therefore, it is important for ATLAS to provide
 2398 some way to assess the momentum carried away by a neutral, colorless parti-
 2399 cle. This can be accomplished through a measurement of missing energy in the

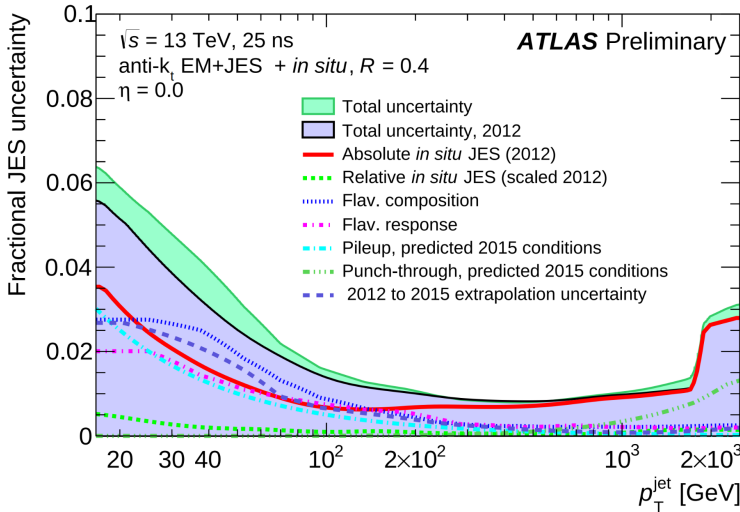


Figure 45: The total, fractional JES uncertainties estimated for 2015 data as a function of jet p_T .

transverse direction, or E_T^{miss} , which quantifies the momentum imbalance of the observed particles. From the conservation of momentum and the lack of the initial momentum in the transverse plane in the proton-proton collisions, any imbalance of momentum can be inferred to be carried away by an unmeasured particle.

E_T^{miss} is more precisely defined as the magnitude of the vector sum of the (p_x, p_y) components of each observed object's momentum. The definition is simple, but there can be significant complexity in defining the inputs. As of Run 2, ATLAS uses a common algorithmic approach to carefully calculate missing energy, but each analysis is free to define its own inputs. For the analysis discussed throughout this thesis, the missing energy inputs consist of the electrons, photons, muons, and jets discussed in the previous sections, in addition to a track-based soft term.

To produce the most precise measurement of E_T^{miss} , it is important to use the best representation of the momentum of each of the input objects, which can often be reconstructed as multiple different types in a single event. For example, an electron can be reconstructed separately as an electron (Section 6.2) and a jet (Section 6.4), but the electron representation has the highest precision for reconstructing the true electron momentum. To ensure no duplications in the E_T^{miss} definition, the inputs are collectively considered for overlap removal. Only the most precise object type is kept for objects that fall within a cone of $\Delta R < 0.2$ for pairs of electrons and jets and a cone of $\Delta R < 0.4$ for other pair types.

The fully reconstructed objects do not include all of the energy within the events, as some clusters do not enter into a jet and some tracks are not classified as electrons or muons. These momentum carried by these objects is accounted for in a soft-term, which tallies all of the energy carried by the particles too soft to form separate objects. The track soft term uses only tracking information to estimate the contribution of soft objects, and does so by vectorially summing the momentum of all well-reconstructed tracks with momentum above 400 MeV.

2429 All of these contributions together give a single E_T^{miss} value for a given event.
2430 The direction of that missing energy is taken as opposite the vector sum of all the
2431 constituents, to correspond to the momentum an invisible particle would have to
2432 have to make the event balanced. Depending on the context, this missing energy
2433 can be considered the energy of a neutrino or an LSP, with a large missing energy
2434 being a common signal criteria for searches for new physics.

2435

PART III

2436

CALORIMETER RESPONSE

2437

You can put some informational part preamble text here.

2438

2439 RESPONSE MEASUREMENT WITH SINGLE HADRONS

2440 As discussed in Section 6.4, colored particles produced in collisions hadronize
 2441 into jets of multiple hadrons. One approach to understanding jet energy mea-
 2442 surements in the ATLAS calorimeters is to evaluate the calorimeter response to
 2443 those individual hadrons; measurements of individual hadrons can be used to
 2444 build up an understanding of the jets that they form. The redundancy of the
 2445 momentum provided by the tracking system and the energy provided by the
 2446 calorimeter provides an opportunity to study calorimeter response using real
 2447 collisions, as described further in Section 7.2.

2448 Calorimeter response includes a number of physical effects that can be ex-
 2449 tracted to provide insight into many aspects of jet modeling. First, many charged
 2450 hadrons interact with the material of the detector prior to reaching the calorime-
 2451 ters and thus do not deposit any energy. Comparing this effect in data and sim-
 2452 ulation is a powerful tool in validating the interactions of particles with the mate-
 2453 rial of the detector and the model of the detector geometry in simulation, see Sec-
 2454 tion 7.2.2. The particles which do reach the calorimeter deposit their energy into
 2455 several adjacent cells, which are then clustered together. The energy of the clus-
 2456 ter is then the total energy deposited by that particle. Comparing the response of
 2457 hadrons in data to that of simulated hadrons provides a direct evaluation of the
 2458 showering of hadronic particles and the energy deposited by particles in matter
 2459 (Section 7.2.4).

2460 The above studies all use an inclusive selection of charged particles, which are
 2461 comprised predominantly of pions, kaons, and (anti)protons. It is also possible to
 2462 measure the response to various identified particle types separately to evaluate
 2463 the simulated interactions of each particle, particularly at low energies where
 2464 differences between species are very relevant. Pions and (anti)protons can be
 2465 identified through decays of long-lived particles, in particular Λ , $\bar{\Lambda}$, and K_S^0 , and
 2466 then used to measure response as described above. This is discussed in detail in
 2467 Section 7.3.

2468 The results in this chapter use data collected at 7 and 8 TeV collected in 2010
 2469 and 2012, respectively. Both are included as the calorimeter was repaired and
 2470 recalibrated between those two data-taking periods. Both sets of data are com-
 2471 pared to an updated simulation that includes new physics models provided by
 2472 Geant4 [32] and improvements in the detector description [33, 34]. The present
 2473 results are published in European Physical Journal C (EPJC) [35] and can be com-
 2474 compared to a similar measurement performed in 2009 and 2010 [36], which used
 2475 the previous version of the simulation framework [37].

2476 7.1 DATASET AND SIMULATION

2477 7.1.1 DATA SAMPLES

2478 The two datasets used in this chapter are taken from dedicated low-pileup runs
 2479 where the fraction of events with multiple interactions was negligible. These
 2480 datasets are used rather than those containing full-pileup events to facilitate mea-
 2481 surement of isolated hadrons. The 2012 dataset at $\sqrt{s} = 8$ TeV contains 8 mil-
 2482 lion events and corresponds to an integrated luminosity of 0.1 nb^{-1} . The 2010
 2483 dataset at $\sqrt{s} = 7$ TeV contains 3 million events and corresponds to an inte-
 2484 grated luminosity of 3.2 nb^{-1} . The latter dataset was also used for the 2010 re-
 2485 sults [36], but it has since been reanalyzed with an updated reconstruction in-
 2486 cluding the final, best understanding of the detector description for the material
 2487 and alignment from Run 1.

2488 7.1.2 SIMULATED SAMPLES

2489 The two datasets above are compared to simulated single-, double-, and non-
 2490 diffractive events generated with Pythia8 [38] using the A2 configuration of
 2491 hadronization [39] and the MSTW 2008 parton-distribution function set [40,
 2492 41]. The admixture of the single-, double-, and non-diffractive events uses the
 2493 default relative contributions from Pythia8. The conditions and energies for
 2494 the two simulations are chosen so that they match those of the corresponding
 2495 dataset.

2496 To evaluate the interaction of hadrons with detector material, the simulation
 2497 uses two different collections of hadronic physics models, called physics lists, in
 2498 Geant4 9.4 [42]. The first, QGSP_BERT, combines the Bertini intra-nuclear
 2499 cascade [43–45] below 9.9 GeV, a parametrized proton inelastic model from 9.5
 2500 to 25 GeV [46], and a quark-gluon string model above 12 GeV [47–51]. The
 2501 second, FTFP_BERT, combines the Bertini intra-nuclear cascade [43–45] below
 2502 5 GeV and the Fritiof model [52–55] above 4 GeV. In either list, Geant4 en-
 2503 forces a smooth transition between models where multiple models overlap.

2504 7.1.3 EVENT SELECTION

2505 The event selection for this study is minimal, as the only requirement is selecting
 2506 good-quality events with an isolated track. Such events are triggered by requir-
 2507 ing at least two hits in the minimum-bias trigger scintillators. After trigger, each
 2508 event is required to have exactly one reconstructed vertex, and that vertex is re-
 2509 quired to have four or more associated tracks.

2510 The particles which are selected for the response measurements are first iden-
 2511 tified as tracks in the inner detector. The tracks are required to have at least 500
 2512 MeV of transverse momentum. To ensure a reliable momentum measurement,
 2513 these tracks are required to have at least one hit in the pixel detector, six hits in
 2514 the SCT, and small longitudinal and transverse impact parameters with respect
 2515 to the primary vertex [36]. For the majority of the measurements in this chapter,

2516 the track is additionally required to have 20 hits in the TRT, which significantly
 2517 reduces the contribution from tracks which undergo nuclear interactions. This
 2518 requirement and its effect is discussed in more detail in Section 7.2.5. In addition,
 2519 tracks are rejected if there is any other reconstructed track which extrapolates
 2520 to the calorimeter within a cone of $\Delta R = \sqrt{(\Delta\phi)^2 + (\Delta\eta)^2} < 0.4$. This require-
 2521 ment guarantees that the contamination of energy from nearby charged particles
 2522 is negligible [36].

2523 7.2 INCLUSIVE HADRON RESPONSE

2524 The calorimeter response is more precisely defined as the ratio of the measured
 2525 calorimeter energy to the true energy carried by the particle, although this true
 2526 energy is unknown. For charged particles, however, the inner detector provides
 2527 a very precise measurement of momentum (with uncertainty less than 1%) that
 2528 can be used as a proxy for true energy. The ratio of the energy deposited by
 2529 the charged particle in the calorimeter, E , to its momentum measured in the
 2530 inner detector p , forms the calorimeter response measure called E/p . Though
 2531 the distribution of E/p contains a number of physical features, this study focuses
 2532 on the trends in two aggregated quantities: $\langle E/p \rangle$, the average of E/p for the
 2533 selected tracks, and the zero fraction, the fraction of tracks with no associated
 2534 energy in the calorimeter for those tracks.

2535 The calorimeter energy assigned to a track is defined using clusters. The clus-
 2536 ters are formed using a 4–2–0 algorithm [56] that begins with seeds requiring
 2537 at least 4 times the average calorimeter cell noise. The neighboring cells with
 2538 at least twice that noise threshold are then added to the cluster, and all bound-
 2539 ing cells are then added with no requirement. This algorithm minimizes noise
 2540 contributions through its seeding process, and including the bounding cells im-
 2541 proves the energy resolution [57]. The clusters are associated to a given track
 2542 if they fall within a cone of $\Delta R = 0.2$ of the extrapolated position of the track,
 2543 which includes about 90% of the energy on average [36].

2544 7.2.1 E/P DISTRIBUTION

2545 The E/p distributions measured in both data and simulation are shown in Fig-
 2546 ure 46 for two example bins of track momentum and for tracks in the central
 2547 region of the detector. These distributions show several important features of
 2548 the E/p observable. The large content in the bin at $E = 0$ comes from tracks that
 2549 have no associated cluster, which occurs due to interactions with detector mate-
 2550 rial prior to reaching the calorimeter or the energy deposit being insuffi-
 2551 ciently large to generate a seed, and are discussed in Section 7.2.2. The small negative
 2552 tail also comes from tracks that do not deposit any energy in the calorimeter but
 2553 are randomly associated to a cluster with an energy below the noise threshold.
 2554 The long positive tail above 1.0 comes from the contribution of neutral parti-
 2555 cles. Nearby neutral particles deposit (sometimes large) additional energy in the
 2556 calorimeter but do not produce tracks in the inner detector, so they cannot be
 2557 rejected by the track isolation requirement. Additionally the peak and mean of

2558 the distribution falls below 1.0 because of the loss of energy not found within
 2559 the cone as well as the non-compensation of the calorimeter.

2560 The data and simulation share the same features, but the high and low tails
 2561 are significantly different. The simulated events tend to overestimate the con-
 2562 tribution of neutral particles to the long tail, an effect which can be isolated and
 2563 removed as discussed in Section 7.2.3. Additionally, the simulated clusters have
 2564 less noise on average, although this is a small effect on the overall response.

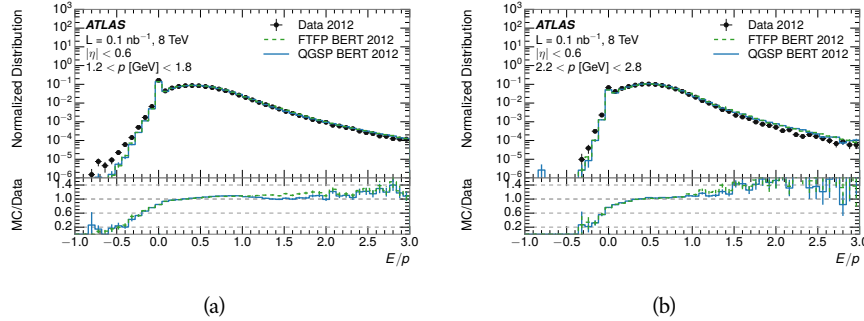


Figure 46: The E/p distribution and ratio of simulation to data for isolated tracks with
 (a) $|\eta| < 0.6$ and $1.2 < p/\text{GeV} < 1.8$ and (b) $|\eta| < 0.6$ and $2.2 < p/\text{GeV} < 2.8$.

2565 7.2.2 ZERO FRACTION

2566 The fraction of particles with no associated clusters, or similarly those with $E \leq$
 2567 0, reflects the modeling of both the detector geometry and hadronic interactions.
 2568 The zero fraction is expected to rise as the amount of material a particle traverses
 2569 increases, while it is expected to decrease as the particle energy increases. This
 2570 dependence can be seen in Figure 47, where the zero fraction in data and simula-
 2571 tion is shown as a function of momentum and the amount of material measured
 2572 in interaction lengths. The trends are similar between 2010 and 2012 and for
 2573 positively and negatively charged particles. The zero fraction decreases with
 2574 energy as expected. The absolute discrepancy in zero fraction between data and
 2575 simulation decreases with momentum from 5% to less than 1%, but this becomes
 2576 more pronounced in the ratio as the zero fraction shrinks quickly with increas-
 2577 ing momentum. The amount of material in the detector increases with η , which
 2578 is used to obtain results for interaction lengths ranging between 0.1 and 0.65 λ .
 2579 As the data and simulation have significant disagreement in the zero fraction
 2580 over a number of interaction lengths, the difference must be primarily from the
 2581 modeling of hadronic interactions with detector material and not just the detec-
 2582 tor geometry. Although two different hadronic interaction models are shown
 2583 in the figure, they have very similar discrepancies to data because both use the
 2584 same description (the BERT model) at low momentum.

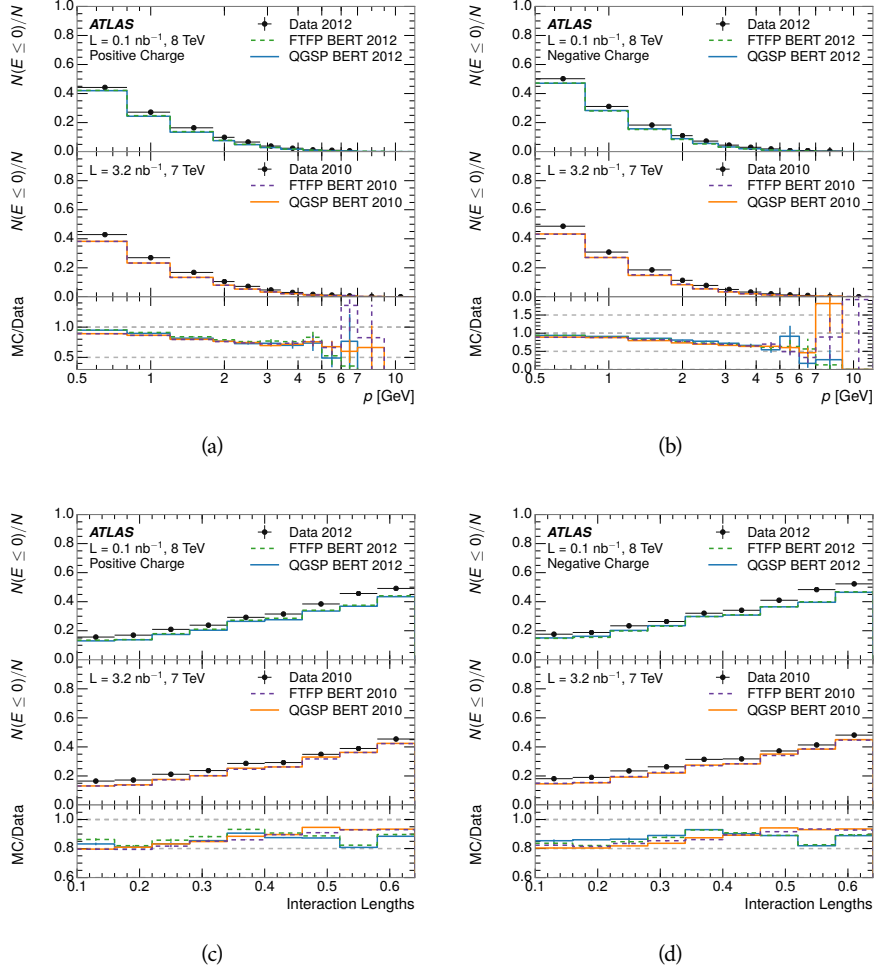


Figure 47: The fraction of tracks as a function (a, b) of momentum, (c, d) of interaction lengths with $E \leq 0$ for tracks with positive (on the left) and negative (on the right) charge.

2585 7.2.3 NEUTRAL BACKGROUND SUBTRACTION

2586 The isolation requirement on hadrons is only effective in removing an energy
 2587 contribution from nearby charged particles. Nearby neutral particles, predomi-
 2588 nantly photons from π^0 decays, also add their energy to the calorimeter clusters,
 2589 but mostly in the electromagnetic calorimeter. The arrangement of energy de-
 2590 posits is shown in Figure 48, which illustrates both energy deposits from the
 2591 hadronic particle and additional deposits from neutral particles. It is possible to
 2592 measure this contribution, on average, using late-showering hadrons that min-
 2593 imally ionize in the electromagnetic calorimeter. Such particles are selected by
 2594 requiring that they deposit less than 1.1 GeV in the EM calorimeter within a
 2595 cone of $\Delta R < 0.1$ around the track. To ensure that these particles are well mea-
 2596 sured, they are additionally required to deposit between 40% and 90% of their
 2597 energy in the hadronic calorimeter within the same cone.

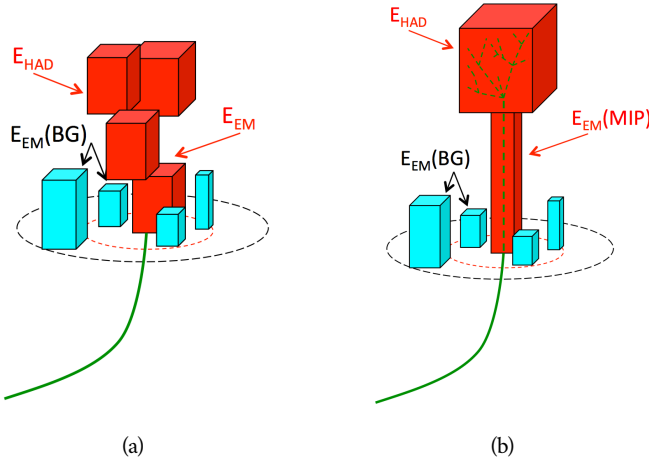


Figure 48: An illustration (a) of the geometry of energy deposits in the calorimeter. The red energy deposits come from the charged particle targeted for measurement, while the blue energy deposits are from nearby neutral particles and must be subtracted. The same diagram (b) for the neutral-background selection, described in Section 7.2.3.

2598 These particles provide a clean sample to measure the nearby neutral back-
 2599 ground because they do not deposit energy in the area immediately surround-
 2600 ing them in the EM calorimeter, as shown in Figure 48. So, the energy deposits in the
 2601 region $0.1 < \Delta R < 0.2$ can be attributed to neutral particles alone. To estimate
 2602 the contribution to the whole cone considered for the response measurement,
 2603 that energy is scaled by a geometric factor of $4/3$. This quantity, $\langle E/p \rangle_{BG}$, mea-
 2604 sured in aggregate over a number of particles, gives the contribution to $\langle E/p \rangle$
 2605 from neutral particles in the EM calorimeter. Similar techniques were used in
 2606 the individual layers of the hadronic calorimeters to show that the background
 2607 from neutrals is negligible in those layers [36].

2608 The distribution of this background estimate is shown in Figure 49 for data
 2609 and simulation with the two different physics lists. The contribution from neu-

tral particles falls from 0.1 at low momentum to around 0.03 for particles above 7 GeV. Although the simulation captures the overall trend, it significantly overestimates the neutral contribution for tracks with momentum between 2 and 8 GeV. This effect was also seen in the tails of the E/p distributions in Figure 46. This difference is likely due to modeling of coherent neutral particle radiation in Pythia8 that overestimates the production of π^0 near the production of the charged particles. The discrepancy does not depend on η and thus is unlikely to be a mismodeling of the detector. This difference can be subtracted to form a corrected average of E/p .

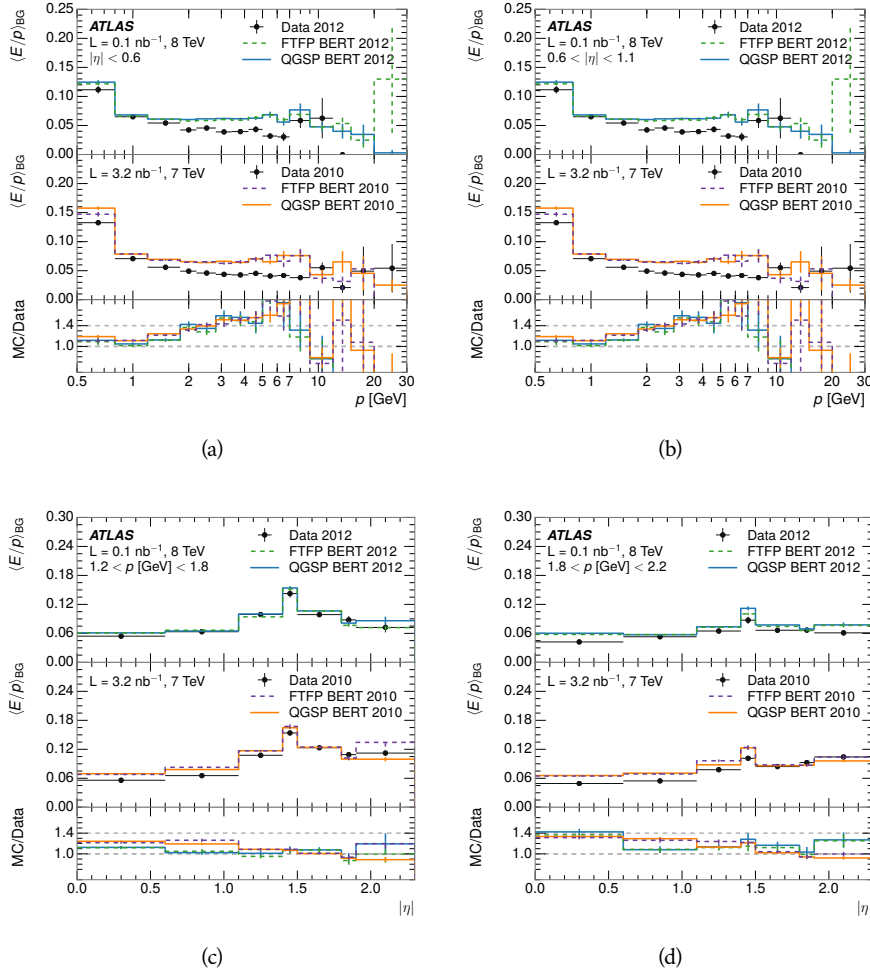


Figure 49: $\langle E/p \rangle_{BG}$ as a function of the track momentum for tracks with (a) $|\eta| < 0.6$, (b) $0.6 < |\eta| < 1.1$, and as a function of the track pseudorapidity for tracks with (c) $1.2 < p/\text{GeV} < 1.8$, (d) $1.8 < p/\text{GeV} < 2.2$.

7.2.4 CORRECTED RESPONSE

Figure 50 shows $\langle E/p \rangle_{COR}$ as a function of momentum for several bins of pseudorapidity. This corrected $\langle E/p \rangle_{COR} \equiv \langle E/p \rangle - \langle E/p \rangle_{BG}$ measures the average calorimeter response without the contamination of neutral particles. It is the

most direct measurement of calorimeter response in that it is the energy measured for fully isolated hadrons. The correction is performed separately in data and simulation, so that the mismodeling of the neutral background in simulation is removed from the comparison of response. The simulation overestimates the response at low momentum by about 5%, an effect that can be mostly attributed to the underestimation of the zero fraction mentioned previously. For $|\eta| < 0.6$, the data-simulation agreement has a larger discrepancy by about 5% for 2010 than 2012, although this is not reproduced in at higher pseudorapidity.

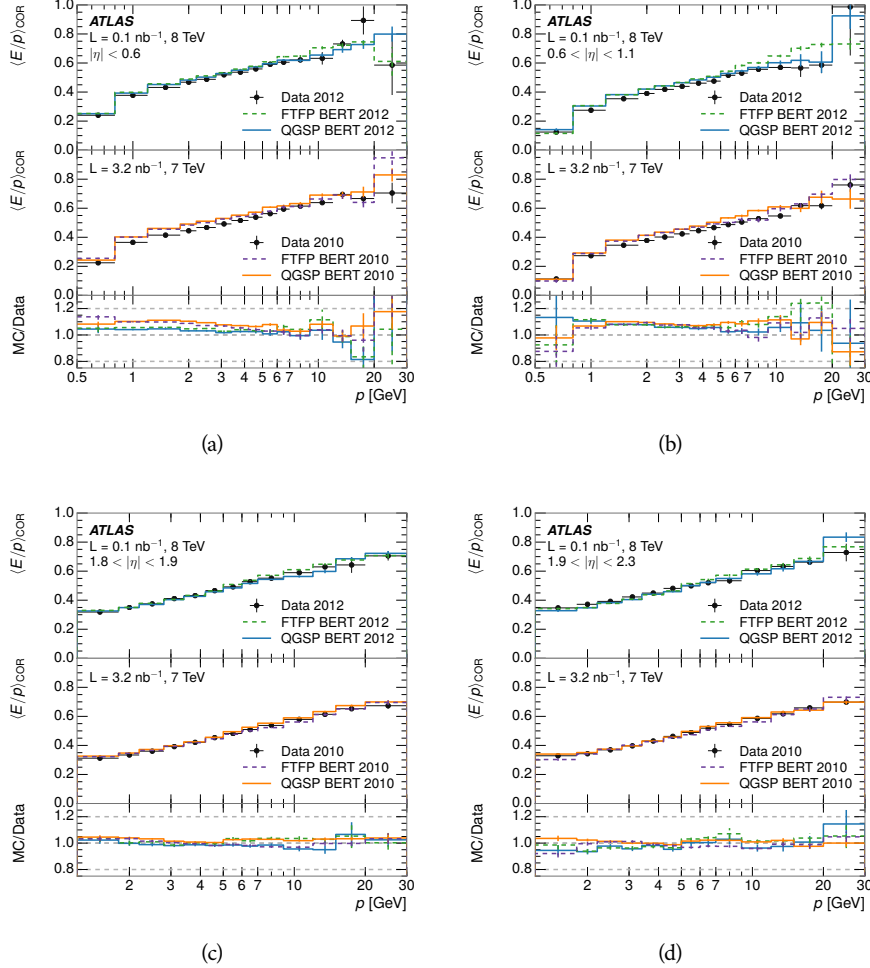


Figure 50: $\langle E/p \rangle_{\text{COR}}$ as a function of track momentum, for tracks with (a) $|\eta| < 0.6$, (b) $0.6 < |\eta| < 1.1$, (c) $1.8 < |\eta| < 1.9$, and (d) $1.9 < |\eta| < 2.3$.

The response measurement above used topological clustering at the EM scale, that is clusters were formed to measure energy but no corrections were applied to correct for expected effects like energy lost outside of the cluster or in uninstrumented material. It is also interesting to measure $\langle E/p \rangle_{\text{COR}}$ using LCW energies, which accounts for those effects by calibrating the energy based on the properties of the cluster such as energy density and depth in the calorimeter. Figure 51 shows these distributions for tracks with zero or more clusters and separately for tracks with one or more clusters. The calibration moves the mean

2639 value of $\langle E/p \rangle_{\text{COR}}$ significantly closer to 1.0 as desired, but the discrepancy be-
 2640 between data and simulation remains in the comparison that includes tracks with
 2641 zero associated clusters. The agreement between data and simulation improves
 2642 noticeably when at least one cluster is required, as this removes the contribution
 2643 from the mismodeling of the zero fraction.

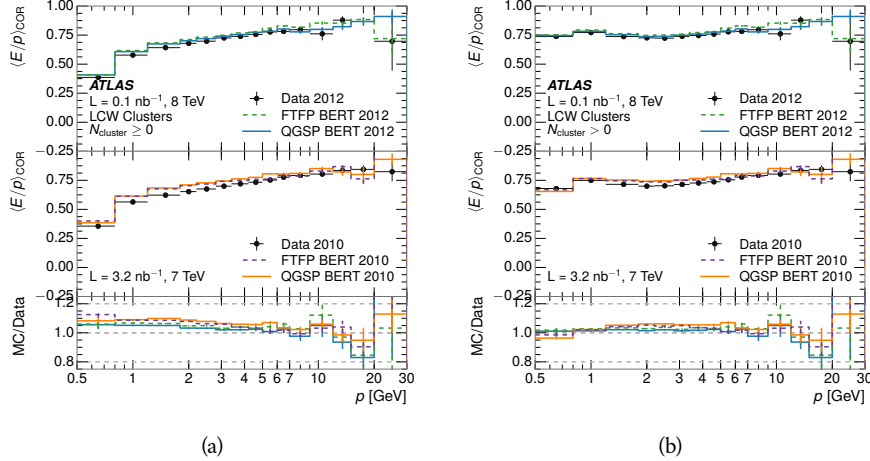


Figure 51: $\langle E/p \rangle_{\text{COR}}$ calculated using LCW-calibrated topological clusters as a function of track momentum for tracks with (a) zero or more associated topological clusters or (b) one or more associated topological clusters.

2644 7.2.5 ADDITIONAL STUDIES

2645 As has been seen in several measurements in previous sections, the simulation
 2646 does not correctly model the chance of a low momentum hadron to reach the
 2647 calorimeter. Because of the consistent discrepancy across pseudorapidity and
 2648 interaction lengths, this can be best explained by incomplete understanding of
 2649 hadronic interactions with the detector [35]. For example, a hadron that scat-
 2650 ters off of a nucleus in the inner detector can be deflected through a significant
 2651 angle and not reach the expected location in the calorimeter. In addition, these
 2652 interactions can produce secondary particles that are difficult to model.

2653 The requirement used throughout the previous sections on the number of
 2654 hits in the TRT reduces these effects by preferentially selecting tracks that do
 2655 not undergo nuclear interactions. It is interesting to check how well the simula-
 2656 tion models tracks with low numbers of TRT hits, which selects tracks that are
 2657 more likely to have undergone a hadronic interaction. Figure 52 compares the
 2658 distributions with $N_{\text{TRT}} < 20$ to $N_{\text{TRT}} > 20$ for real and simulated particles¹.
 2659 As expected, the tracks with fewer hits are poorly modeled in the simulation as
 2660 $\langle E/p \rangle_{\text{COR}}$ differs by as much as 25% at low momentum. They also have signifi-
 2661 cantly lower $\langle E/p \rangle_{\text{COR}}$ on average, because they are much less likely to have an
 2662 associated cluster.

¹The distribution with $N_{\text{TRT}} > 20$ is the same as shown in Figure 50 (a) and is included again here for the comparison.

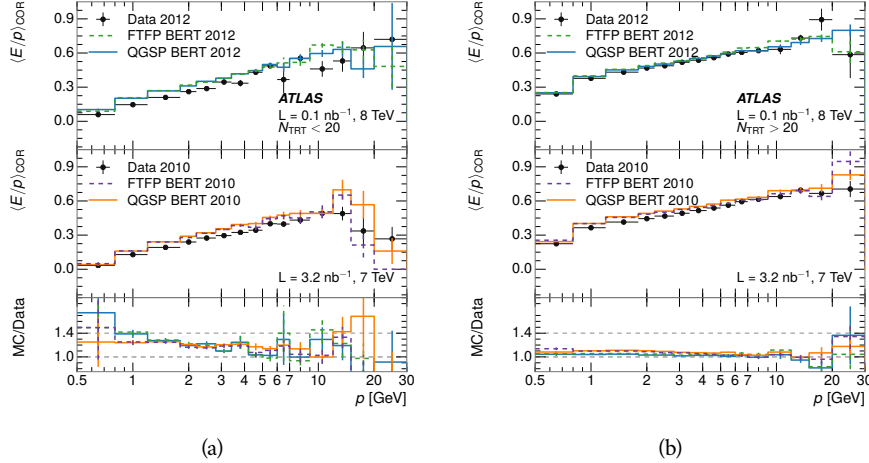


Figure 52: Comparison of the $\langle E/p \rangle_{\text{COR}}$ for tracks with (a) less than and (b) greater than 20 hits in the TRT.

Another interesting aspect of the simulation is the description of antiprotons at low momentum, where QGSP_BERT and FTFP_BERT have significant differences. This can be seen to have an effect in the inclusive response measurement when separated into positive and negative charge. The $\langle E/p \rangle_{\text{COR}}$ distributions for positive and negative particles are shown in Figure 53, where a small difference between QGSP_BERT and FTFP_BERT can be seen in the distribution for negative tracks. The figure also includes data, and the simulation overestimates $\langle E/p \rangle_{\text{COR}}$ mostly due to an underestimation in zero fraction. There is an approximately 5% difference between the 2010 and 2012 simulated events. The difference between positive and negative particles is demonstrated more clearly in Figure 54, which shows the E/p distribution in the two simulations separated by charge. There is a small difference around $E/p > 1.0$, which can be explained by the additional energy deposited by the annihilation of the antiproton in the calorimeter that is modeled well only in FTFP_BERT. This is also explored with data using identified antiprotons in Section 7.3.

The $\langle E/p \rangle$ results in previous sections have considered the electromagnetic and hadronic calorimeters together as a single energy measurement, to emphasize the total energy deposited for a given particle. However, the deposits in each calorimeter are measured separately and $\langle E/p \rangle$ can be constructed for each layer separately. As the layers are composed of different materials and are modeled separately in the detector geometry, confirmation that the simulation matches the data well in each layer adds confidence in both the description of hadronic interactions with the two different materials and also the geometric description of each.

The technique discussed in Section 7.2.3 for selecting MIPs in the electromagnetic calorimeter is also useful in studying deposits in the hadronic calorimeter. The tracks selected with the MIP requirements deposit almost all of their energy exclusively in the hadronic calorimeter. Figure 55 shows $\langle E/p \rangle_{\text{Had}}^{\text{RAW}}$, where RAW indicates that no correction has been applied for neutral backgrounds and

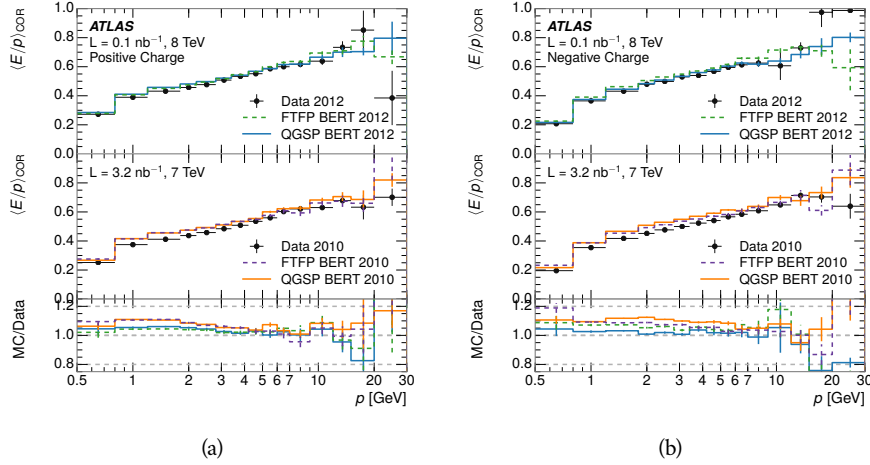


Figure 53: Comparison of the $\langle E/p \rangle_{\text{COR}}$ for (a) positive and (b) negative tracks as a function of track momentum for tracks with $|\eta| < 0.6$.

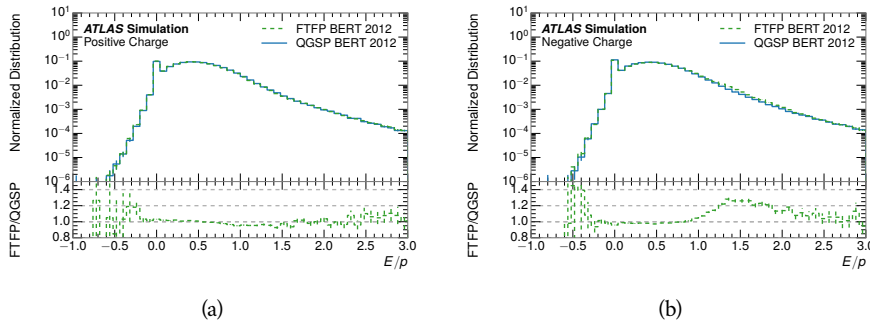


Figure 54: Comparison of the E/p distributions for (a) positive and (b) negative tracks with $0.8 < p/\text{GeV} < 1.2$ and $|\eta| < 0.6$, in simulation with the FTFP_BERT and QGSP_BERT physics lists.

Had indicates that only clusters for the hadronic calorimeter are included². The distributions are shown both for the original EM scale calibration and after LCW calibration. The data and simulation agree very well in this comparison, except in the lowest momentum bin where there is a 5% discrepancy that has already been seen in the measurements in Section 7.2.4.

A similar comparison can be made in the electromagnetic calorimeter by selecting particles which have no associated energy in the hadronic calorimeter. These results are measured in terms of $\langle E/p \rangle_{\text{COR}}^{\text{EM}}$, where EM designates that only clusters in the electromagnetic calorimeter are included and COR designates that the neutral background is subtracted as the neutral background is present in this case. Figure 56 shows the analogous comparisons to Figure 55 in the electromagnetic calorimeter. The $\langle E/p \rangle_{\text{COR}}$ values are lower on average in the EM calorimeter than in the hadronic calorimeter, which is an expected conse-

² The RAW and COR versions of $\langle E/p \rangle$ in this case are the same, as the neutral background is negligible in that calorimeter layer.

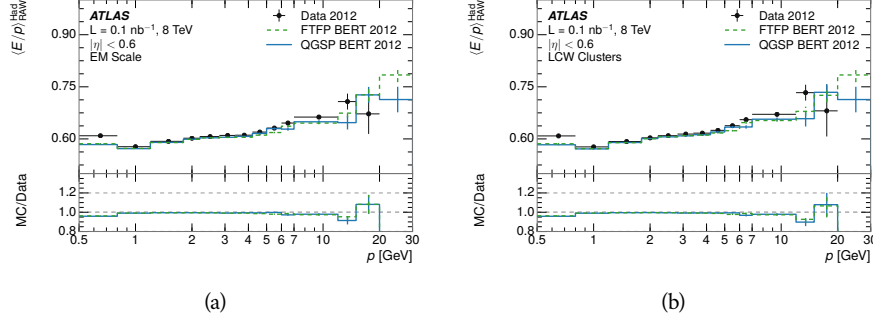


Figure 55: Comparison of the response of the hadronic calorimeter as a function of track momentum (a) at the EM-scale and (b) after the LCW calibration.

quence of their different material types (discussed in Section 5.4). In this case the disagreement between data and simulation is more pronounced, with discrepancies as high as 5% over a larger range of momenta. This level of discrepancy indicates that the description of the electromagnetic calorimeter is actually the dominant source of discrepancy in the combined distributions in Section 7.2.4.

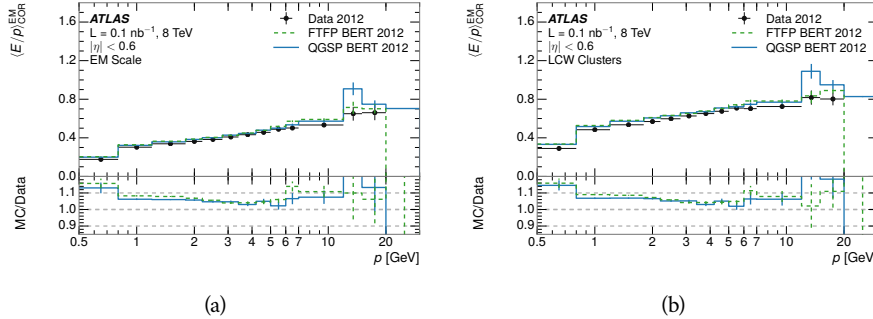


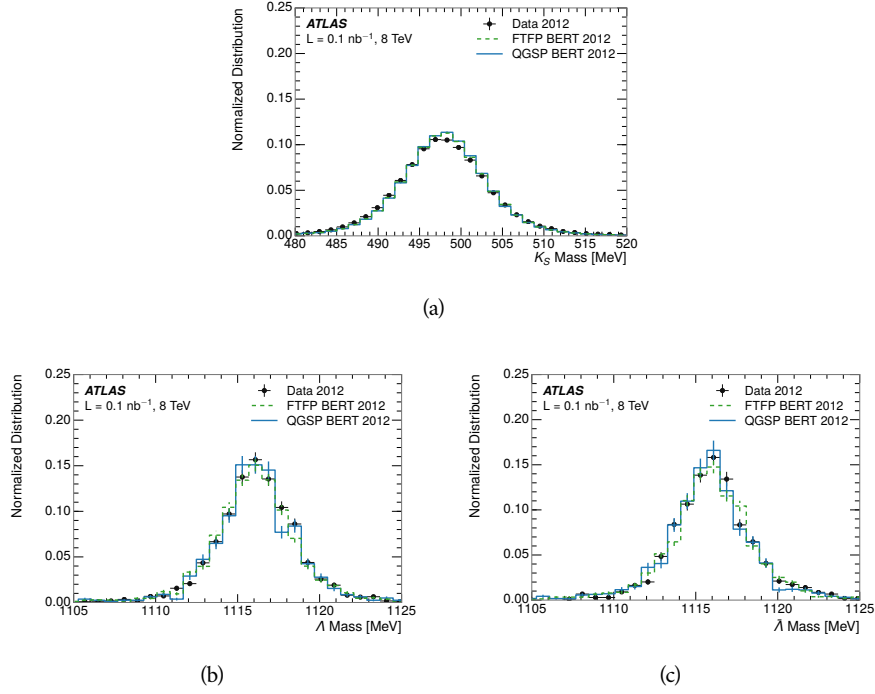
Figure 56: Comparison of the response of the EM calorimeter as a function of track momentum (a) at the EM-scale and (b) with the LCW calibration.

7.3 IDENTIFIED PARTICLE RESPONSE

The inclusive response measurement for hadrons can be augmented by measuring the response for specific particle species. The simulation models each particle type separately, and understanding the properties of each is important in constraining the uncertainty on jets. In order to select and measure specific hadrons, this section relies on the displaced decays of long-lived particles. Such decays can be identified by reconstructing secondary vertices with a requirement on mass. In particular, Λ , $\bar{\Lambda}$, and K_S^0 can be used to select a pure sample of protons, antiprotons, and pions, respectively.

2719 7.3.1 DECAY RECONSTRUCTION

2720 The measurement of the response for identified particles uses the same selection
 2721 as for inclusive particles (Section 7.1.3) with a few additions. Each event used is
 2722 required to have at least one secondary vertex, as described in Section 6.1.3, and
 2723 the tracks are required to match to that vertex rather than the primary vertex.
 2724 Pions are selected from decays of $K_S^0 \rightarrow \pi^+ \pi^-$, which is the dominant decay for
 2725 K_S^0 to charged particles. Protons are selected from decays of $\Lambda \rightarrow \pi^- p$ and an-
 2726 tiprotons from $\bar{\Lambda} \rightarrow \pi^+ \bar{p}$, which are similarly the dominant decays of Λ and $\bar{\Lambda}$
 2727 to charged particles. The species of parent hadron in these decays is determined
 2728 by reconstructing the mass of the tracks associated to the secondary vertex. The
 2729 sign of the higher momentum decay particle can distinguish between Λ and $\bar{\Lambda}$,
 2730 which of course have the same mass, as the proton or antiproton is kinemati-
 2731 cally favored to have higher momentum. The proton or antiproton will carry
 2732 the higher momentum above 95% of the time. Examples of the reconstructed
 2733 masses used to select these decays are shown in Figure 57. The mass peaks in
 2734 data and both simulation models are very similar.



2735 Figure 57: The reconstructed mass peaks of (a) K_S^0 , (b) Λ , and (c) $\bar{\Lambda}$ candidates.
 2736

2737 The dominant backgrounds for the identified particle decays are nuclear in-
 2738 teractions and combinatoric sources. These are suppressed by the kinematic re-
 2739 quirements on the tracks as well as an additional veto which removes candidates
 2740 that are consistent with both a Λ or $\bar{\Lambda}$ and a K_S^0 hypothesis, which is possible
 2741 because of the different assumptions on particle mass in each case [36]. After
 2742 these requirements, the backgrounds are found to be negligible compared to the
 2743 statistical errors on these measurements.

2742 7.3.2 IDENTIFIED RESPONSE

2743 With these techniques the E/p distributions are extracted in data and simulation
 2744 for each particle species and shown in Figure 58. These distributions are shown
 2745 for a particular bin of E_a ($2.2 < E_a/\text{GeV} < 2.8$), rather than p . E_a is the energy
 2746 available to be deposited in the calorimeter: for pions $E_a = \sqrt{p^2 + m_\pi^2}$, for pro-
 2747 tons $E_a = \sqrt{p^2 + m_p^2} - m_p$, and for antiprotons $E_a = \sqrt{p^2 + m_p^2} + m_p$. In the
 2748 pion case, the entire energy of the pion is deposited in the calorimeter, so E_a is
 2749 just the usual energy. For protons, the proton remains after depositing its energy
 2750 in the calorimeter, so its mass is not available and must be subtracted from E_a .
 2751 And for antiprotons, the antiproton constituents annihilate with the quarks in
 2752 the protons and neutrons of the calorimeter material, so it deposits its entire en-
 2753 ergy as well as an the additional energy from the annihilation; this extra energy
 2754 is equal to the mass of the antiproton and is added to the available energy. The
 2755 features of the E/p distributions are similar to the inclusive case, with a peak
 2756 around 0.5 at low momentum. The zero fraction is not as pronounced as in the
 2757 inclusive case. There is a small negative tail from noise and a large fraction of
 2758 tracks with zero energy from particles which do not reach the calorimeter. The
 2759 long positive tail is noticeably more pronounced for antiprotons because of the
 2760 additional energy generated by the annihilation of the antiproton with the mate-
 2761 rial of the detector, and the peak of the distribution is also increased for the same
 2762 reason. The simulation correctly captures these features, and the agreement be-
 2763 tween data and simulation is good to within the available statistical limitations.

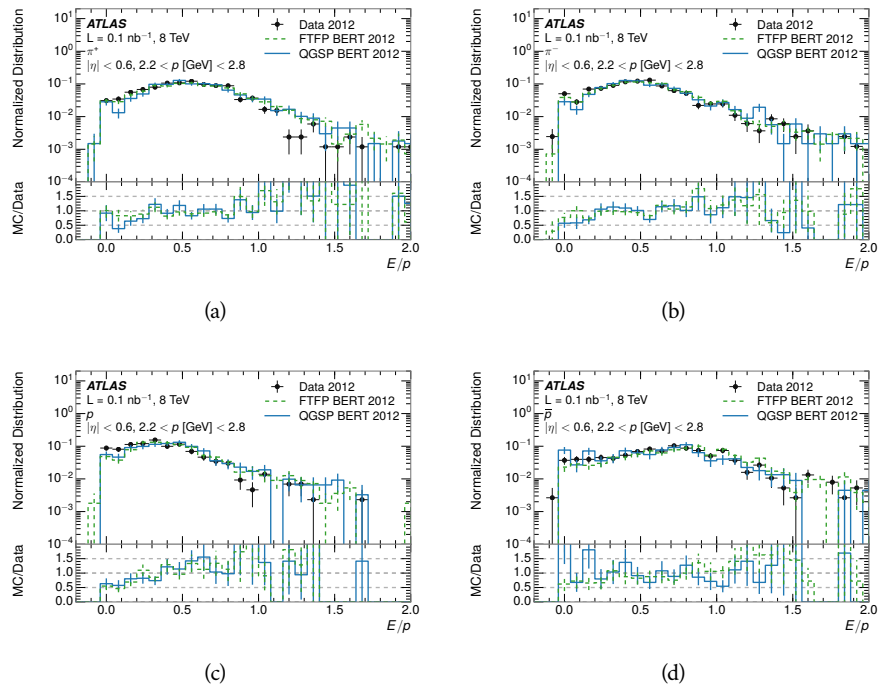


Figure 58: The E/p distribution for isolated (a) π^+ , (b) π^- , (c) proton, and (d) anti-proton tracks.

The zero fraction is further explored in Figure 59 for pions and protons in data and simulation. The simulation consistently underestimates the zero fraction independent of particle species, which implies that this discrepancy is not caused by the model of a particular species but rather a feature common to all. The zero fraction is larger for π^- than π^+ , which is evident in both data and simulation. However there is some suggestion that this increase in zero fraction leads to an even larger discrepancy in the modeling of π^- in simulation.

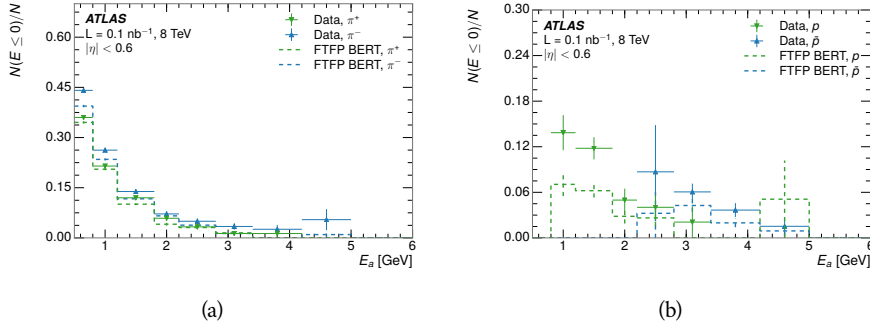


Figure 59: The fraction of tracks with $E \leq 0$ for identified (a) π^+ and π^- , and (b) proton and anti-proton tracks

It is also interesting to compare the response between the different particle species. One approach to do this is to measure the difference in $\langle E/p \rangle$ between two types, which has the advantage of removing the neutral background. These differences are shown in various combinations in Figure 60. The response for π^+ is greater on average than the response to π^- because of a charge-exchange effect which causes the production of additional neutral pions in the showers of π^+ [58]. This effect becomes less significant as the $\langle E/p \rangle$ increases, and the difference approaches zero. Both version of the simulation correctly model this trend. The response for π^+ is also greater on average than the response to p , because a large fraction of the energy of π^+ hadrons is converted to an electromagnetic shower [59, 60]. This effect is again reproduced by both simulations. The \bar{p} response, however, is significantly higher than the response to π^- because of the annihilation of the antiproton, but the difference decreases at higher energies where the additional energy has less relative importance. FTFP_BERT models this effect more accurately than QGSP_BERT because of their different descriptions of \bar{p} interactions with material.

It is also possible to remove the neutral background from these response distributions using the same technique as in Section 7.2.3. The technique is largely independent of the particle species and so can be directly applied to $\langle E/p \rangle$ for pions. The $\langle E/p \rangle_{\text{COR}}$ distributions for pions are shown in Figure 61, which are very similar to the inclusive results. The inclusive hadrons are comprised mostly of pions, so this similarity is not surprising. It is also possible to see the small differences between π^+ and π^- response here, where $\langle E/p \rangle_{\text{COR}}$ is higher on average for π^+ . The agreement between data and simulation is significantly worse for the π^- distributions than for the π^+ , with a discrepancy greater than 10% below 2-3 GeV.

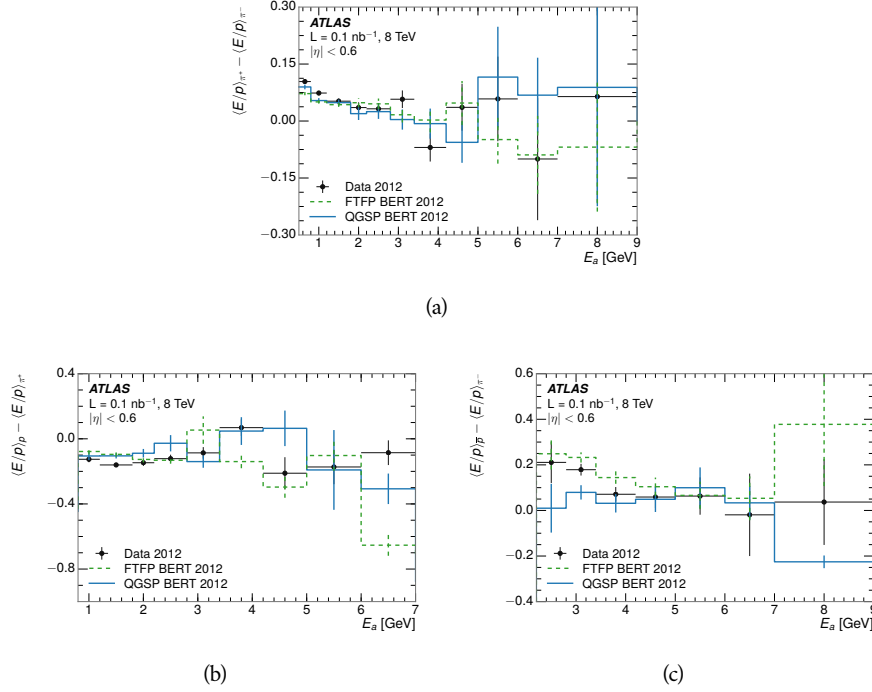


Figure 60: The difference in $\langle E/p \rangle$ between (a) π^+ and π^- (b) p and π^+ , and (c) \bar{p} and π^- .

2797 7.3.3 ADDITIONAL SPECIES IN SIMULATION

2798 The techniques above provide a method to measure the response separately for
 2799 only pions and protons. However the hadrons which forms jets include a number
 2800 of additional species such as kaons and neutrons. The charged kaons are an im-
 2801 portant component of the inclusive charged hadron distribution, which is com-
 2802 prised of roughly 60-70% pions, 15-20% kaons, and 5-15% protons [35]. These
 2803 fractions vary depending on the production mechanism, and the ranges are in-
 2804 dicative of the variations between different events. These are difficult to measure
 2805 in data at the ATLAS detector, as the particles which decay to kaons such as ϕ and
 2806 D mesons have shorter lifetimes and are comparatively rare. These properties
 2807 make it impractical to identify a sufficient number of decays to make statistically
 2808 meaningful measurements. The simulation of these particles includes noticeable
 2809 differences in response between species at low energies, which are shown in Fig-
 2810 ure 62 for FTFP_BERT. The significant differences in response between protons
 2811 and antiprotons below 1 GeV are accounted for above in the definitions of E_a .

2812 7.4 SUMMARY

2813 These various measurements of calorimeter response shown above for data and
 2814 simulation illuminate the accuracy of the simulation of hadronic interactions at
 2815 the ATLAS detector. The results were obtained using 2010 and 2012 data at 7
 2816 and 8 TeV, but reflect the most current understanding of the detector alignment

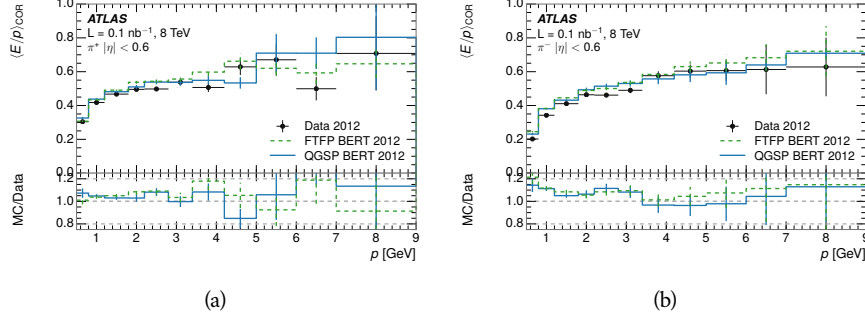


Figure 61: $\langle E/p \rangle_{\text{COR}}$ as a function of track momentum for (a) π^+ tracks and (b) π^- tracks.

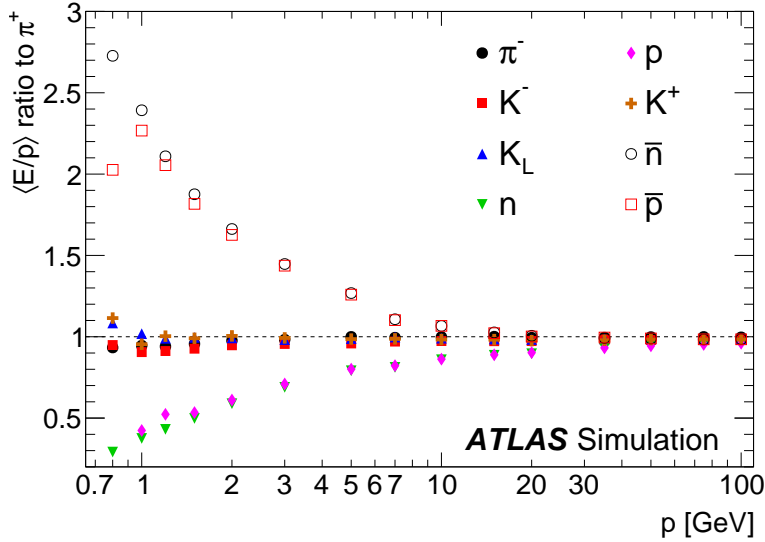


Figure 62: The ratio of the calorimeter response to single particles of various species to the calorimeter response to π^+ with the physics list FTFP_BERT.

and geometry. A number of measurements focusing on a comparison between protons and antiprotons suggest that FTFP_BERT models those interaction more accurately than QGSP_BERT. These measurements, among others, were the motivation to switch the default Geant4 simulation from QGSP_BERT to FTFP_BERT for all ATLAS samples.

Even with these updates, there are a number of approximately 5% discrepancies in response between the data and simulation. The differences result mostly from a difference in the modeling of the zero fraction, which is most significant at low energies. The difference in response without the zero fraction are primarily in the electromagnetic calorimeter, while the modeling of the hadronic calorimeter is accurate. At higher momenta the simulation of hadronic interactions is very consistent with data. Chapter 8 discusses how to use these observed differences to constrain the jet energy scale and its associated uncertainties.

2830

2831 JET ENERGY RESPONSE AND UNCERTAINTY

2832 8.1 MOTIVATION

2833 As jets form a major component of many physics analyses at ATLAS, it is crucial
2834 to carefully calibrate the measurement of jet energies and to derive an uncer-
2835 tainty on that measurement. These uncertainties are often the dominant sys-
2836 tematic uncertainty in high-energy analyses at the LHC. Jet balance techniques,
2837 as discussed in Section 6.4.3, provide a method to constrain the JES and its uncer-
2838 tainty in data, and provide the default values used for ATLAS jet measurements at
2839 most energies [61]. These techniques are limited by their reliance on measuring
2840 jets in data, so they are statistically limited in estimating the jet energy scale at the
2841 highest jet energies. This chapter presents another method for estimating the jet
2842 energy scale and its uncertainty which builds up a jet from its constituents and
2843 thus can be naturally extended to high jet momentum. Throughout this chapter
2844 the jets studied are simulated using Pythia8 with the CT10 parton distribution
2845 set [62] and the AU2 tune [39], and corrections are taken from the studies includ-
2846 ing data and simulation in Chapter 7.

2847 As described in Section 6.4, jets are formed from topological clusters of energy
2848 in the calorimeters using the anti- k_t algorithm. These clusters originate from a
2849 diverse spectrum of particles, in terms of both species and momentum, leading to
2850 significantly varied jet properties and response between jets of similar produced
2851 momentum. Figure 63 shows the momentum and particle distributions of sim-
2852 ultated particles within jets at a few examples energies. Each bin for each distri-
2853 bution shows the fraction of jet constituents of that particle type and that truth
2854 energy for a jet of the specified energy. These show that majority of particles in
2855 jets are charged pions and photons, and the charged pions constituent carry the
2856 highest energies on average. The figure also demonstrates that the majority of
2857 the particles in a jet have much lower momentum than the jet itself; for example
2858 in 90-100 GeV jets less than 1% of particles have energies above 20 GeV. The
2859 E/p measurements provide a thorough understanding of the dominant particle
2860 content of jets, the charged hadrons.

2861 8.2 UNCERTAINTY ESTIMATE

2862 A correct modeling of jets in the data by simulation requires that both the parti-
2863 cle production inside jets as well as the response of the calorimeter to particles
2864 are correctly modeled. Chapter 7 showed that the simulation does not perfectly
2865 model the calorimeter response, and provided measurements that can be used
2866 to correct for discrepancies. To determine the corrections appropriate for jets,
2867 that is to evaluate a jet energy response, the simulated jet energies are compared

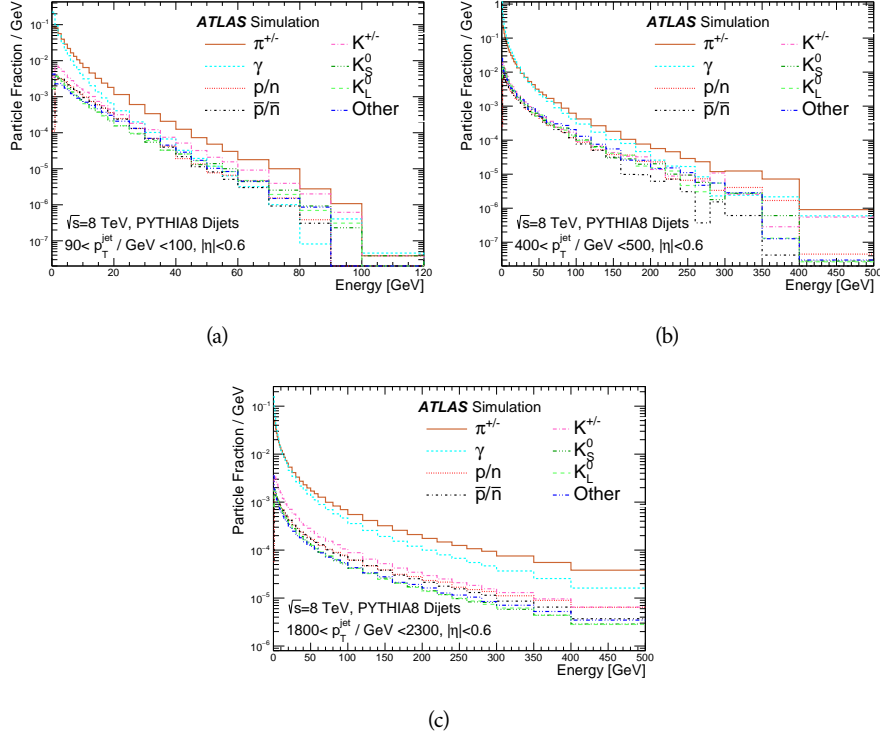


Figure 63: The spectra of true particles inside anti- k_t , $R = 0.4$ jets with (a) $90 < p_T/\text{GeV} < 100$, (b) $400 < p_T/\text{GeV} < 500$, and (c) $1800 < p_T/\text{GeV} < 2300$.

to a corrected jet built up at the particle level. Each cluster in a jet is associated to the truth particle which deposited it, and the energy in that cluster is then corrected for a number of effects based on measurements in data. The primary corrections come from the single hadron response measurements in addition to response measured using the combined test beam which covers higher momentum particles [63]. These corrections include both a shift (Δ), in order to make the simulation match the average response in data, and an uncertainty (σ) associated with the ability to constrain the difference between data and simulation. Some of the dominant sources of uncertainty are itemized in Table 8 with typical values, and the full list considered is described in detail in the associated paper [35]. These uncertainties cover differences between the data and simulation in the modeling of calorimeter response to a given particle. The typical values are listed as ranges to show the variation over momentum and pseudorapidity. For the in situ E/p term, for example, Δ corresponds to the difference between data and simulation for $\langle E/p \rangle_{\text{COR}}$ at the LCW scale (shown in Figure 51 (b)) and σ is the uncertainty on that difference including the statistical uncertainties of both the data and simulated events. No uncertainties are added for the difference between particle composition of jets in data and simulation, as this method focuses on providing a response correction for discrepancies of particle interactions rather than differences in particle composition.

From these terms, the jet energy scale and uncertainty is built up from individual energy deposits in simulation. Each uncertainty term is treated inde-

Abbrev.	Description	Δ (%)	σ (%)
In situ E/p	The comparison of $\langle E/p \rangle_{\text{COR}}$, at the LCW scale, as described in Chapter 7 with statistical uncertainties from 500 MeV to 20 GeV.	0-3	1-5
CTB	The main $\langle E/p \rangle$ comparison uncertainties, binned in p and $ \eta $, as derived from the combined test beam results, from 20 to 350 GeV [63].	0-3	1-5
E/p Zero Fraction	The difference in the zero-fraction between data and MC simulation from 500 MeV to 20 GeV.	5-25	1-5
E/p Threshold	The uncertainty in the EM calorimeter response from the potential mismodeling of threshold effects in topological clustering.	0	0-10
Neutral	The uncertainty in the calorimeter response to neutral hadrons based on studies of physics model variations.	0	5-10
K_L	An additional uncertainty in the response to neutral K_L in the calorimeter based on studies of physics model variations.	0	20
E/p Misalignment	The uncertainty in the p measurement from misalignment of the ID.	0	1
Hadrons, $p > 350$ GeV	An energy independent uncertainty for all particles above the energy range or outside the longitudinal range probed with the combined test beam.	0	10

Table 8: The dominant sources of corrections and systematic uncertainties in the [JES](#) estimation technique, including typical values for the correcting shift (Δ) and the associated uncertainty (σ).

pendently, and is taken to be gaussian distributed. The resulting scale and uncertainty is shown in Figure 64, where the mean response is measured relative to the calibrated energy reported by simulation. The mean response is slightly below one, indicating that the simulation slightly overestimates the calorimeter response on average, and this response is relatively constant as a function of the jet p_T . The dominant uncertainties come from the statistical uncertainties on the E/p measurements at lower energies and the additional uncertainty for out of range measurements at higher energies. Combined the resulting uncertainty ranges from between 1.5% at low momentum and pseudorapidity to as much as 4% at higher momentum and pseudorapidity. The total uncertainty from this method at intermediate jet energies is comparable to other simulation-based methods [64] and is about twice as large as in-situ methods using data [61]. This method is the only one which provides an estimation above 1.8 TeV, however, and so is still a crucial technique in analyses that search for very energetic jets.

These techniques can also be used to measure the correlation between bins of average reconstructed jet momentum across a range of p_T and $|\eta|$, where correlations are expected because of a similarity in particle composition at similar energies. Figure 65 shows these correlations, where the uncertainties on jets in neighboring bins are typically between 30% and 60% correlated. The uncertainty on all jets becomes significantly correlated at high energies and larger pseudorapidities, when the uncertainty becomes dominated by the single term reflecting out of range particles.

8.3 SUMMARY

The technique described above provides a jet energy scale and uncertainty by building up jet corrections from the energy deposits of constituent particles. The E/p measurements are crucial in providing corrections for the majority of particles in the jets. The uncertainty derived this way is between 2 and 5% and is about twice as large at corresponding momentum than jet balance methods. However this is the only uncertainty available for very energetic jets using 2012 data and simulation, and repeating this method with Run 2 data and simulation will be important in providing an uncertainty for the most energetic jets in 13 TeV collisions.

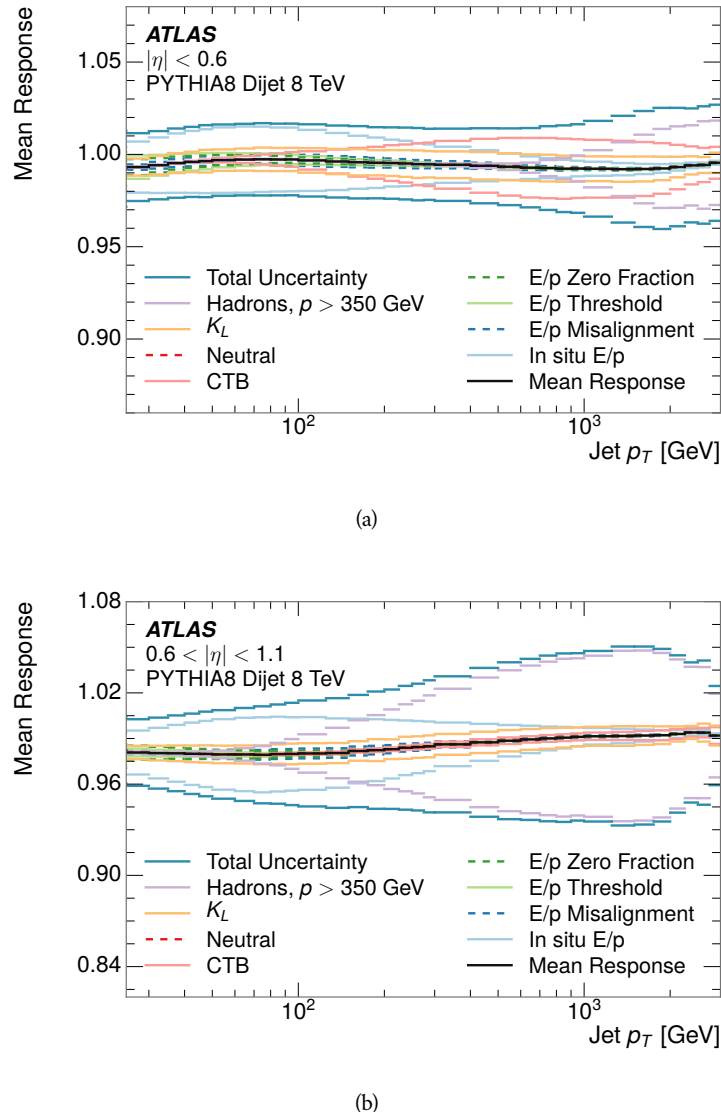


Figure 64: The JES response uncertainty contributions, as well as the total JES uncertainty, as a function of jet p_T for (a) $|\eta| < 0.6$ and (b) $0.6 < |\eta| < 1.1$.

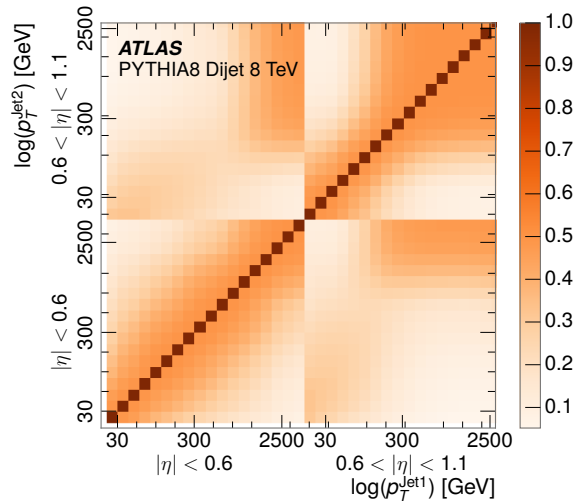


Figure 65: The correlations between bins of average reconstructed jet momentum as a function of jet p_T and $|\eta|$ for jets in the central region of the detector.

2923

PART IV

2924

SEARCH FOR LONG-LIVED PARTICLES

2925

You can put some informational part preamble text here.

2926

2927 LONG-LIVED PARTICLES IN ATLAS

2928 As discussed in Section 2.6, various limitations in the SM suggest a need for new
 2929 particles at the TeV scale. A wide range of extensions to the Standard Model
 2930 predict that these new particles can have lifetimes greater than approximately
 2931 one-hundredth of a nanosecond. These include theories with universal extra-
 2932 dimensions [65, 66], with new fermions [67], and with leptoquarks [68]. As dis-
 2933 cussed in Section 3.4, many SUSY theories also produce these LLPs, in both R-
 2934 Parity violating [69–71] and R-Parity conserving [72–75] formulations. Split su-
 2935 persymmetry [8, 9], for example, predicts long-lived gluinos with O(TeV) masses.
 2936 This search focuses specifically on the SUSY case, but many of the results are
 2937 generic to any model with LLPs.

2938 Long-lived gluinos or squarks carry color-charge and will thus hadronize into
 2939 color neutral bound states called R-Hadrons. These are composit particles like
 2940 the known hadrons but with one supersymmetric constituent, for example $\tilde{g}q\bar{q}$
 2941 and $\tilde{q}\bar{q}$. In this hadronization process, the gluino can acquire an electric charge.
 2942 Gluino pair production, $pp \rightarrow \tilde{g}\tilde{g} + X$, where X denotes the proton remnants,
 2943 has the largest cross sectional increase with the increase in energy to 13 TeV,
 2944 and so this search uses gluino R-Hadrons as its benchmark model. The features,
 2945 techniques, and cross section limits discussed here are all largely independent
 2946 of the model. Planned future updates will extend the case to include additional
 2947 refinements for squark and chargino models, but the current method covers any
 2948 long-lived, charged, massive particle.

2949 9.1 EVENT TOPOLOGY

2950 R-parity conserving SUSY models predict that gluinos will be produced in pairs
 2951 at the LHC, through the processes shown in Figure 66, where the quarks and
 2952 gluons are proton constituents. The gluon-initiated mode dominates for the col-
 2953 lision energy and gluino masses considered for this search. During their produc-
 2954 tion, the long-lived gluinos hadronize into color singlet bound states including
 2955 $\tilde{g}q\bar{q}$ and even $\tilde{g}g$ [76]. The probability to form the gluon-only bound states is
 2956 a free parameter usually taken to be 0.1, and 90% of the remaining R-Hadrons
 2957 form meson states [77]. The charged and neutral states are approximately equally
 2958 likely for mesons, so the R-Hadrons will be charged roughly 50% of the time.

2959 These channels produce R-Hadrons with large p_T , but lower on average than
 2960 their mass, so that they typically propagate with $0.2 < \beta < 0.9$ [77]. Figure 67
 2961 shows the generated p_T and β distributions for a simulated example of R-Hadrons
 2962 with a mass of 1600 GeV. The mean p_T is roughly half of the mass at 800 GeV,
 2963 and so β peaks around 0.5. The fragmentation that produces that hadrons is
 2964 very hard, so the jet structure around the R-Hadron is minimal, with less than 5
 2965 GeV of summed particle momentum expected in a cone of $\Delta R < 0.25$ around

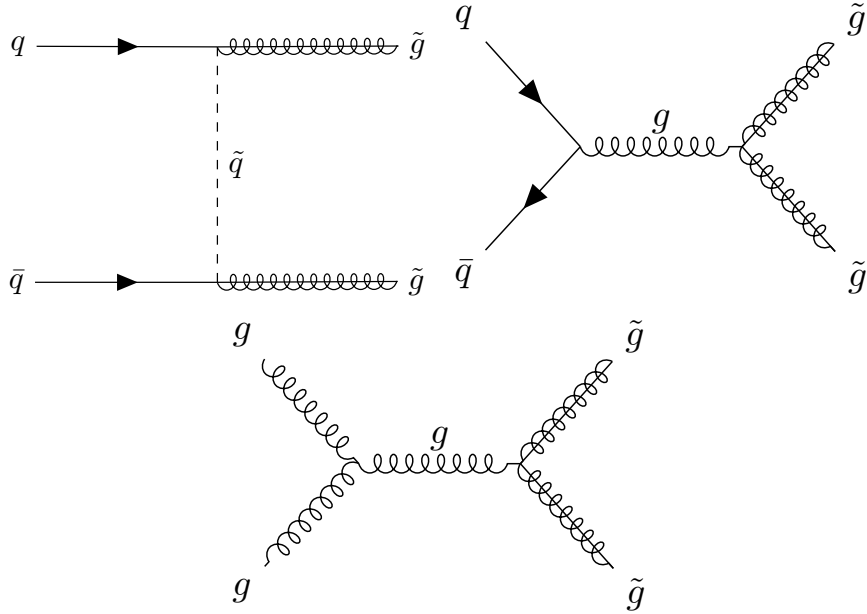


Figure 66: The processes which contribute to gluino pair production in the proton-proton collisions, where the quarks and gluons are proton constituents.

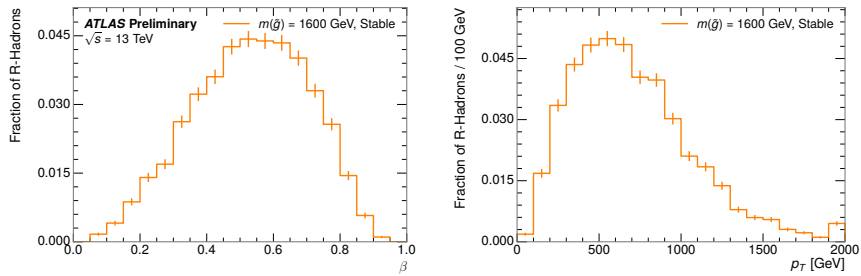


Figure 67: The generated p_T and β distributions for R-Hadrons with $M = 1600$ GeV.

the R-Hadron [77]. After hadronization, depending on the gluino lifetime, the R-Hadrons then decay into hadrons and a LSP [76].

In summary, the expected event for pair-produced long-lived gluinos is very simple: two isolated, high-momentum R-Hadrons that propagate through the detector before decaying to jets. The observable features of such events depend strongly on the interaction of the R-Hadron with the material of the detector and also its lifetime. Section 9.1.1 describes the interactions of R-Hadrons which reach the various detector elements in ATLAS and Section 9.1.2 provides a summary of the observable event descriptions for R-Hadrons of various lifetimes.

9.1.1 DETECTOR INTERACTIONS

Although the distribution of decay times can be parametrized with a single parameter, τ , the time before individual R-Hadrons decay follows an exponential distribution, leading to a range of decay times for any individual lifetime. This is

further confounded by the distribution of β as well as η , so that each R-Hadron propagates at a different velocity and travels a different distance before reaching each detector element. Therefore, the lifetime-dependent event topologies must be discussed as an average, and all times referred to within this section will assume $\beta = 0.5$, an $\eta = 0$, and that the particle decays after a time equal to its lifetime. Table 9 lists the distances of various subdetectors and the time after which a LLP will arrive at that subdetector for a few values of β and with $\eta = 0$.

Subdetector	Distance	τ at $\beta = 0.3$	τ at $\beta = 0.5$	τ at $\beta = 0.7$
Pixel	3.1 cm	0.35 ns	0.20 ns	0.15 ns
Calorimeter	1.5 m	17 ns	10 ns	7.2 ns
Muon System	5 m	56 ns	33 ns	24 ns

Table 9: The radial distances of each of the subdetectors and example arrival times for an R-Hadron with $\eta = 0$ and the specified β .

After approximately 0.2 ns, the R-Hadron reaches the first layer of the pixel detector. If charged, it deposits energy into the material through repeated single collisions that result in ionization of the silicon substrate [6]. Because of its comparatively low β , the ionization energy can be significantly greater than expected for SM particles because the most-probable energy loss grows significantly as β decreases [6]. This large ionization can be measured through the ToT read out from the pixel detector as described in Section 6.1.2. Large ionization in the inner detector is one of the major characteristic features of LLPs. The particle propagates through all four layers of the pixel detector, where each provides a measurement of ionization, and then exits the pixel detector at 0.8 ns.

Throughout the next few nanoseconds, the R-Hadron propagates through the remainder of the inner detector. A charged R-Hadron will provide hits in each of these systems as would any other charged particle, and can be reconstructed as a track. The track reconstruction provides a measurement of its trajectory and thus its p as described in Section 6.1. The large p_T , shown in Figure 67, is another characteristic feature of massive particles produced at the LHC.

As of roughly 10 ns, the R-Hadron enters the calorimeter where it interacts hadronically with the material. Because of its large mass and p , the R-Hadron does not typically stop in the calorimeter, but rather deposits a small fraction of its energy through repeated interactions with nucleons. The probability of interaction between the gluino itself and a nucleon is low because the cross section drops off with the inverse square of its mass, so the interactions are primarily governed by the light constituents [78]. Each of these interactions can potentially change that quark content and thus change the sign of the R-Hadron, so that the charge at exit is typically uncorrelated with the charge at entry [77]. The total energy deposited in the calorimeters during the propagation is small compared to the kinetic energy of the R-Hadron, around 20-40 GeV, so that E/p is typically less than 0.1 [77].

Then, 30 ns after the collision, it reaches the muon system, where it again ionizes in the material if charged and can be reconstructed as a muon track. Because of the charge-flipping interactions in the calorimeter, this track may have

3017 the opposite sign of the track reconstructed in the inner detector, or there may
 3018 be a track present when there was none in the inner detector and vice-versa
 3019 for those which are detected. The propagation time at the typically lower β re-
 3020 sults in a significant delay compared to muons, and a delay over 25 ns causes
 3021 the muon signal to be lost outside the readout window. Between the probabili-
 3022 ty of charge-flip and late arrival, there is a significant chance that an R-Hadron
 3023 which was produced with a charge will not be identified as a muon. When it is
 3024 reconstructed as a muon, that delay can be assessed in terms of a time-of-flight
 3025 measurement, which is another characteristic feature of R-Hadrons.

3026 9.1.2 LIFETIME DEPENDENCE

3027 The above description assumed a lifetime long enough for the R-Hadron to exit
 3028 the detector, which through this search is referred to as **VLL**, as the particle may
 3029 decay after exiting the detector. There are several unique signatures at shorter
 3030 lifetimes where the R-Hadron decays in various parts of the inner detector; these
 3031 lifetimes are referred to as **LL**.

3032 The shortest case where the R-Hadron is considered **LL** is for lifetimes around
 3033 0.01 ns, where the particle decays before reaching any of the detector elements.
 3034 Although the R-Hadrons are produced opposite each other in the transverse
 3035 plane, each R-Hadron decays to a jet and an **LSP**. The two decays are uncorrelated,
 3036 so the two **LSPs** carry different momenta and in different directions. And, since
 3037 the **LSPs** are not measured, the produced jets can be significantly imbalanced in
 3038 the transverse plane which results in large missing energy. That missing energy
 3039 can be used to trigger candidate events, and provides the most efficient trigger
 3040 option for shorter lifetimes. Additionally, the precision of the tracking system
 3041 allows the displaced vertex of the R-Hadron decay to be reconstructed from the
 3042 charged particles in the jet. The distance of that vertex from the interaction point
 3043 can be used to distinguish R-Hadron decays from other processes. Figure 68
 3044 shows a schematic diagram of an example R-Hadron event with such a lifetime.
 3045 The diagram is not to scale, but instead illustrates the detector interactions in the
 3046 pixel detector, calorimeters, and muon system. It includes a representation of a
 3047 charged R-Hadron and a neutral R-Hadron, as well as the **LSPs** and jets (shown as
 3048 charged hadrons) produced in the decay. Neutral hadrons may also be produced
 3049 in the decay but are not depicted. Previous searches on ATLAS have used the
 3050 displaced vertex to target **LLP** decays [79].

3051 The next distinguishable case occurs at lifetimes greater than 0.1 ns, where
 3052 the R-Hadron forms a partial track in the inner detector. This forms a unique
 3053 signature of a disappearing track. Two examples of such an event are illustrated
 3054 in Figure 69, which shows the short track in the inner detector. The decay dis-
 3055 tance must be sufficiently long that it reaches the **SCT**, or else to track will not be
 3056 reconstructed at all. Depending on the mass difference between the R-Hadron
 3057 and the **LSP**, the decay products will either be a single, soft charged hadron and a
 3058 **LSP**, or a jet and a **LSP**. A dedicated search on ATLAS used the disappearing track
 3059 signature in the former case to search for **LLP** in Run 1 [80].

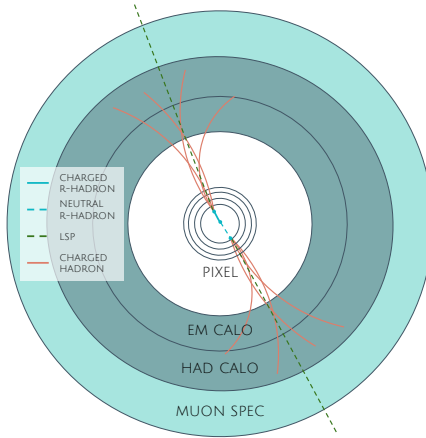


Figure 68: A schematic diagram of an R-Hadron event with a lifetime around 0.01 ns. The diagram includes one charged R-Hadron (solid blue), one neutral R-Hadron (dashed blue), LSPs (dashed green) and charged hadrons (solid orange). The pixel detector, calorimeters, and muon system are illustrated but not to scale.

3060 In the latter case, the decays result in an event-level signature of up to two
 3061 high- p tracks, jets, and significant missing energy. The missing energy has the
 3062 same origin as in the case of 0.01 ns lifetimes, from the decay to unmeasured
 3063 particles, and again can be large. The high- p tracks will also have the charac-
 3064 teristically high-ionization of massive, long-lived particles in the Pixel detector.
 3065 Figure ?? illustrates an example event with one charged R-Hadron which decays
 3066 after approximately 10 ns, and shows how the jets from the decay can still be re-
 3067 constructed in the calorimeter. Several previous searches on ATLAS from Run 1
 3068 have used this signature to search for R-Hadrons [81, 82], including a dedicated
 3069 search for LL particles [83].

3070 If the lifetime is longer than several nanoseconds, in the range of 10-30 ns,
 3071 the R-Hadron decay can occur in or after the calorimeters, but prior to reach-
 3072 ing the muon system. In the case that the decays occur early enough within the
 3073 calorimeters that the decay can be measured, the event topology is very similar
 3074 to the above with jets originating in the inner detector. If the decay occurs after
 3075 the calorimeter, jets may not be reconstructed at all. The events still often have
 3076 large missing energy, although it is generated through different mechanisms, and
 3077 so the same search strategy can be used. The R-Hadrons do not deposit much
 3078 energy in the calorimeters, so a neutral R-Hadron will not enter into the miss-
 3079 ing energy calculation. A charged R-Hadron opposite a neutral R-Hadron will
 3080 thus generate significant missing energy, and close to 50% of pair-produced R-
 3081 Hadron events fall into this category. If both R-Hadrons are neutral then the
 3082 missing energy will be low because neither is detected. Two charged R-Hadrons
 3083 will also result in low missing energy because both are reconstructed as tracks
 3084 and will balance each other in the transverse plane. A small fraction of the time,
 3085 one of the charged R-Hadron tracks may fail quality requirements and thus be ex-
 3086 cluded from the missing energy calculation and again result in significant missing
 3087 energy. Figure 70 illustrates another example event with one charged R-Hadron

3088 which decays after approximately 20 ns, and shows how the jets from the decay
 3089 might not be reconstructed.

3090 The longest lifetimes, the **VLL** case, has all of the features of the 30-50 ns case
 3091 but with the addition of muon tracks for any R-Hadrons that exit the calorimeter
 3092 with a charge. That muon track can provide additional information from time-
 3093 of-flight measurements to help identify **LLPs**. An example of the event topology
 3094 for one charged and one neutral **VLL** R-Hadron is shown in Figure 71. Some
 3095 searches on ATLAS have included this information to improve the search reach
 3096 for **VLL** particles [82, 84].

3097 9.2 SIMULATION

3098 All of the event topologies discussed above are modeled by simulations of R-
 3099 Hadron events in the ATLAS detector. A large number of such samples are
 3100 generated to determine efficiencies, to measure expected yields, and to estimate
 3101 uncertainties. The primary interaction, pair production of gluinos with masses
 3102 between 400 and 3000 GeV, is simulated using **Pythia 6.4.27** [85] with the
 3103 **AUET2B** [86] set of tuned parameters for the underlying event and the **CTEQ6L1** [62]
 3104 **PDF** set. The simulated interactions include a modeling of pileup by adding sec-
 3105 ondary, minimum bias interactions from both the same (in-time pileup) and
 3106 nearby (out-of-time pileup) bunch crossings. This event generation is then aug-
 3107 mented with a dedicated hadronization routine to hadronize the long-lived gluinos
 3108 into final states with R-Hadrons [87], with the probability to form a gluon-gluino
 3109 bound set at 10% [88].

3110 The cross sections used for these processes are calculated at next-to-leading
 3111 order (**NLO**) in the strong coupling constant with a resummation of soft-gluon
 3112 emmission at next-to-leading logarithmic (**NLL**) [89–93]. The nominal predic-
 3113 tions and the uncertainties for each mass point are taken from an envelope of
 3114 cross-section predictions using different **PDF** sets and factorization and renor-
 3115 malization scales [94]. As discussed in Section 2.5.3, the **PDFs** and scales deter-
 3116 mine the cross section by providing the probabilities of the proton constituents
 3117 to interact. Multiple estimates for the **PDF** and scales at 13 TeV can be used to
 3118 provide an average cross section calculation and its uncertainty.

3119 The R-Hadrons then undergo a full detector simulation [37], where the inter-
 3120 actions of the R-Hadrons with the material of the detector are described by ded-
 3121 icated **Geant4** [32] routines. These routines model the interactions described in
 3122 Section 9.1.1, including the ionizing interactions in the silicon modules of the in-
 3123 ner detector and the R-Hadron-nucleon interactions in the calorimeters [95, 96].
 3124 The specific routine chosen to describe the interactions of the R-Hadrons with
 3125 nucleons, the “generic model”, uses a pragmatic approach where the scattering
 3126 cross section is taken to be a constant 12 mb per light quark. In this model the
 3127 gluino itself does not interact at all, although it carries most of the kinetic energy
 3128 of the bound state.

3129 The lifetimes of these R-Hadrons are then simulated at several working points,
 3130 $\tau = 0.1, 1.0, 3.0, 10, 30, 50$ and $> 50\text{ns}$. The actual decay times follow an expo-
 3131 nential distribution, where τ is the characteristic time. Only one decay mode is

3132 simulated for these benchmark samples, $\tilde{g} \rightarrow q\bar{q}\tilde{\chi}_1^0$ with the neutralino mass set
3133 to 100 GeV. The search discussed here is also efficient for heavier neutralinos,
3134 which have very similar topologies but which generate less missing energy.

3135 All of the simulated events are then reconstructed using the same software
3136 used for collision data. The fully reconstructed events are then reweighted to
3137 match the distribution of initial state radiation in an alternative sample of events,
3138 generated with MG5_aMC@NLO [97], which has had a more accurate description
3139 of radiate effects than Pythia6 in previous iterations [83]. MG5_aMC@NLO pre-
3140 dictes a harder distribution of initial state radiation, where 28% more simulated
3141 events generate sufficient missing energy to trigger for [VLL](#) R-Hadrons. This
3142 reweighting provides a more accurate description of the p of the gluino-gluino
3143 system and is important in modeling the efficiency of triggering and offline event
3144 selection.

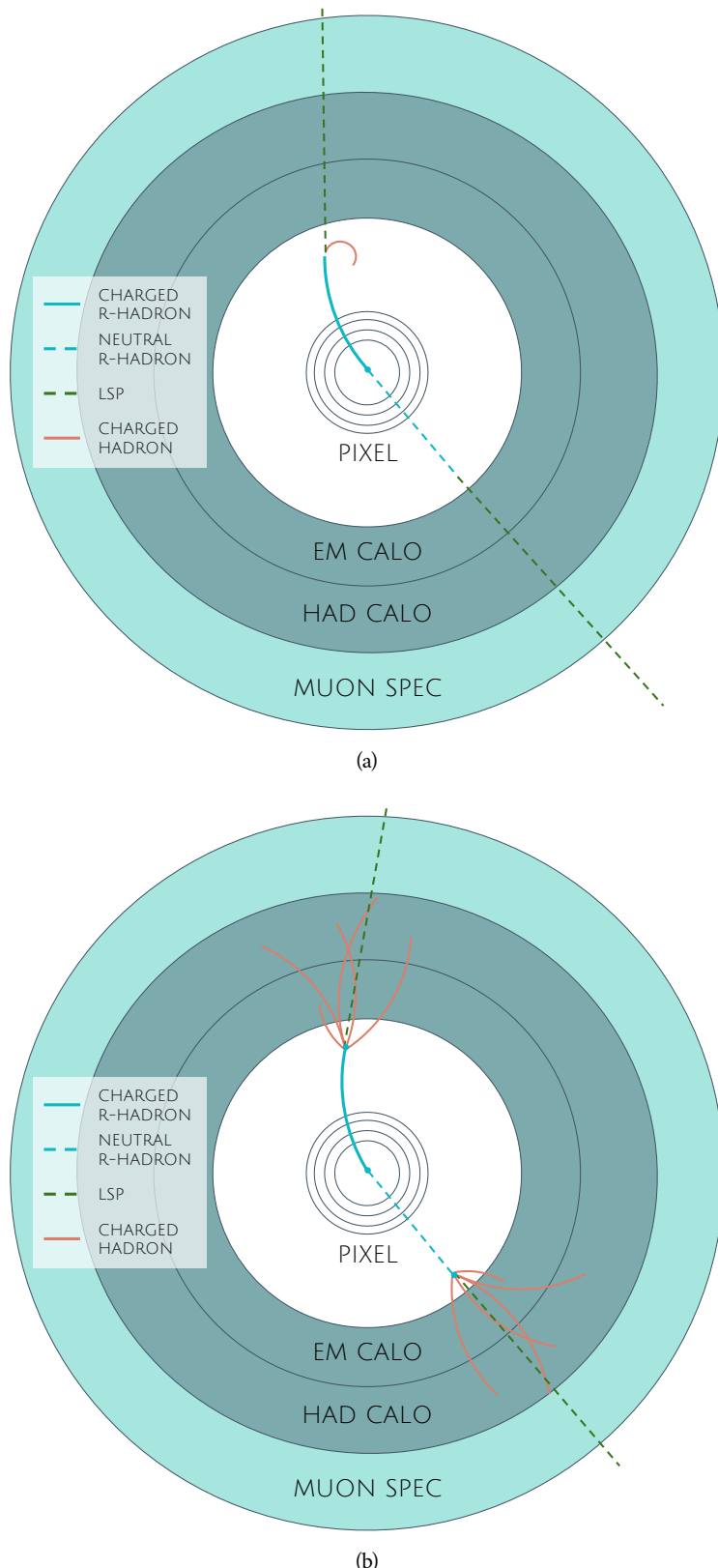


Figure 69: Schematic diagram of R-Hadron events with a lifetime around 5 ns, where the masses of the R-Hadron and LSP are (a) nearly degenerate and (b) not degenerate. The diagrams include charged R-Hadrons (solid blue), neutral R-Hadrons (dashed blue), LSPs (dashed green) and charged hadrons (solid orange). The pixel detector, calorimeters, and muon system are illustrated but not to scale.

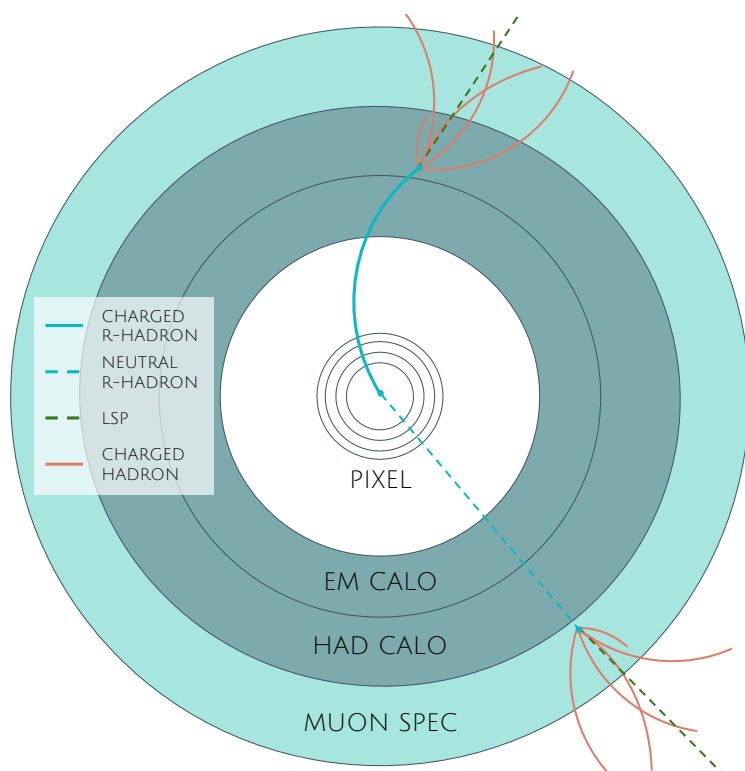


Figure 70: A schematic diagram of an R-Hadron event with a lifetime around 20 ns. The diagram includes one charged R-Hadron (solid blue), one neutral R-Hadron (dashed blue), LSPs (dashed green) and charged hadrons (solid orange). The pixel detector, calorimeters, and muon system are illustrated but not to scale.

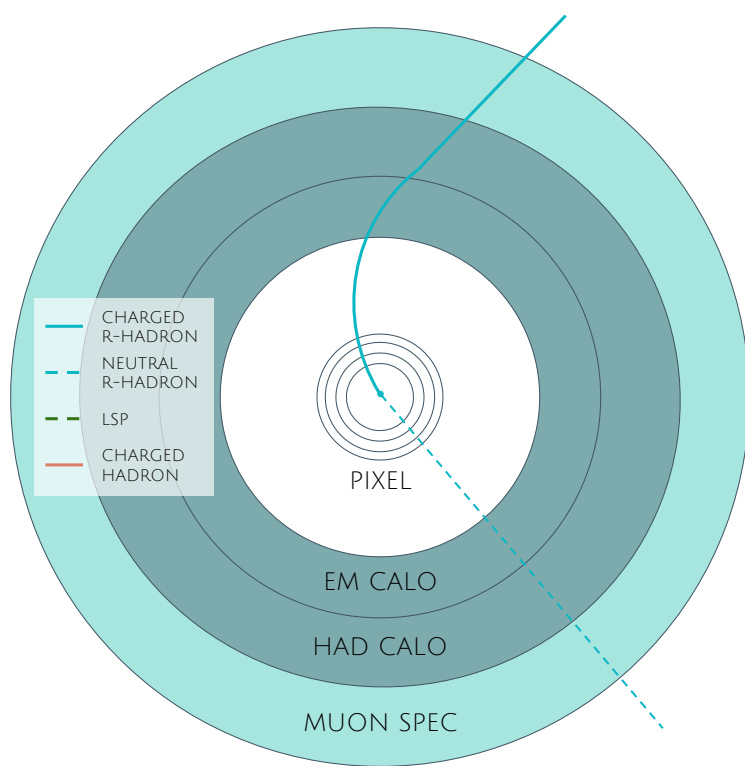


Figure 71: A schematic diagram of a [VLL](#) R-Hadron event. The diagram includes one charged R-Hadron (solid blue) and one neutral R-Hadron (dashed blue). The pixel detector, calorimeters, and muon system are illustrated but not to scale.

3145

3146 EVENT SELECTION

3147 The [LLPs](#) targeted by this search differ in their interactions with the detector from
 3148 [SM](#) particles primarily because of their large mass. When produced at the ener-
 3149 gies available at the [LHC](#), that large mass results in a low β (typically $0.2 < \beta < 0.9$
 3150 as shown in Figure 67). Such slow-moving particles heavily ionize in detector
 3151 material. Each layer of the pixel detector provides a measurement of that ion-
 3152 ization, through [ToT](#), as discussed in Section 6.1.2. The ionization in the pixel
 3153 detector, quantified in terms of dE/dx , provides the major focus for this search
 3154 technique, along with the momentum measured in the entire inner detector. It is
 3155 effective both for its discriminating power and its use in reconstructing a parti-
 3156 cle's mass, and it can be used for a wide range of masses and lifetimes as discussed
 3157 in Section 9.1.2. However dE/dx needs to be augmented with a few additional
 3158 selection requirements to provide a mechanism for triggering and to further re-
 3159 duce backgrounds.

3160 Ionization itself is not currently accessible for triggering, so this search in-
 3161 stead relies on E_T^{miss} to trigger signal events. Although triggering on E_T^{miss} can
 3162 be inefficient, E_T^{miss} is often large for many production mechanisms of [LLPs](#), as
 3163 discussed in Section 9.1.

3164 The use of ionization to reject [SM](#) backgrounds relies on well-measured, high-
 3165 momentum tracks, so some basic requirements on quality and kinematics are
 3166 placed on the tracks considered in this search. A few additional requirements
 3167 are placed on the tracks considered for [LLP](#) candidates that increase background
 3168 rejection by targeting specific types of [SM](#) particles.

3169 The ionization measurement with the Pixel detector can be calibrated to pro-
 3170 vide an estimator of $\beta\gamma$. That estimate, together with the momentum measure-
 3171 ment provided by tracking, can be used to reconstruct a mass for each track
 3172 which traverses the pixel detector,

$$m = \frac{p}{\beta\gamma}$$

3173 That mass variable will be peaked at the [LLP](#) mass for any signal, and provides an
 3174 additional tool to search for an excess. In addition to an explicit requirement on
 3175 ionization, this search constructs a mass-window for each targeted signal mass
 3176 in order to search for an excess of events.

3177 The strategy discussed here is optimized for lifetimes of $O(1) - O(10)$ ns.
 3178 The specific values for each requirement in signal region were optimized con-
 3179 sidering the increase in discovery reach for tightening the requirement on each
 3180 discriminating variable. Pixel ionization is especially useful in this regime as
 3181 particles only need to propagate through the first seven layers of the inner de-
 3182 tector, about 37 cm from the beam axis. The search is still competitive with
 3183 other searches for [LLPs](#) at longer lifetimes, because the primary discriminating

variables are still applicable even for particles that do not decay within the detector [84]. Although the majority of the requirements will be the same for all lifetimes, two signal regions are defined to optimize separately for intermediate and long lifetime particles.

10.1 TRIGGER

Triggering remains a significant difficulty in defining an event selection with high signal efficiency in a search for LLPs. There are no triggers available in the current ATLAS system that can fire directly from a high momentum track with large ionization, as tracking is not available at L1 (Section 5.6). Although in some configurations a charged LLP can fire muon triggers, this requirement introduces significant model dependence on both the allowed lifetimes and the interactions in the calorimeter [77], as discussed in Section 9.1.1.

For a search targeting particles which may decay prior to reaching the muon system, the most efficient available trigger is based on missing energy [77]. As discussed in Section 9.1, signal events can produce significant E_T^{miss} by a few mechanisms. At the trigger level however, the missing energy is only calculated using the calorimeters (Section 5.6) where the R-Hadrons deposit little energy. So, at short lifetimes, E_T^{miss} measured in the calorimeter is generated by an imbalance between the jets and undetected LSPs produced in R-Hadron decays. At longer lifetimes, without the decay products, missing energy is only produced in the calorimeters when the R-Hadrons recoil against an ISR jet.

These features are highlighted in Figure 72, which shows the E_T^{miss} distributions for simulated short lifetime (3 ns) and VLL R-Hadron events. The figure includes both the offline E_T^{miss} , the missing energy calculated with all available information, and Calorimeter E_T^{miss} , the missing energy calculated using only information available at the calorimeter which approximates the missing energy available at the trigger. The short lifetime sample has significantly greater E_T^{miss} and Calorimeter E_T^{miss} than the VLL sample as expected. For the VLL sample, a small fraction of events with very large E_T^{miss} (about 5%) migrate into the bin with very small Calorimeter E_T^{miss} because the E_T^{miss} produced by a charged R-Hadron track opposite a neutral R-Hadron track does not contribute any missing energy in the calorimeters.

So, either case to some extent relies on kinematic degrees of freedom to produce missing energy, as the pair-produced LLPs tend to balance each other in the transverse plain. For long lifetimes in particular, the presence of ISR is important in providing an imbalance in the transverse plane, and is an important aspect of modeling the selection efficiency for R-Hadron events. The missing energy trigger with the lowest threshold available is chosen for this selection in order to maximize the trigger efficiency. The formation of the trigger decision for missing energy was discussed in more detail in Section 5.6. During 2015 data collection this was the HLT_xe70 trigger, which used a 50 GeV threshold on missing energy at L1 and a 70 GeV threshold on missing energy at the HLT which is nearly 100% efficient after the L1 requirement. With these thresholds, the incomplete balance of the LSPs results in a relatively low efficiency for long-

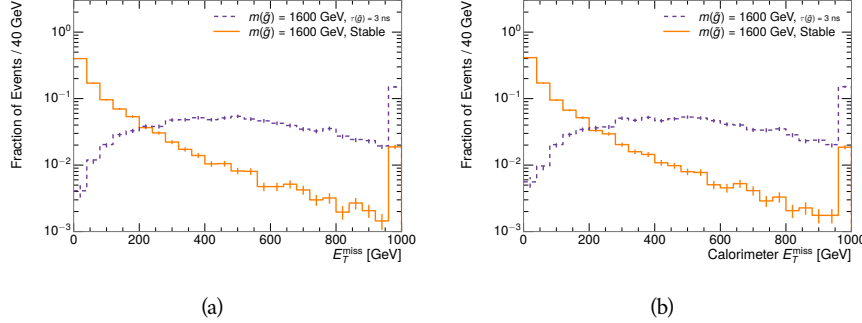


Figure 72: The distribution of (a) E_T^{miss} and (b) Calorimeter E_T^{miss} for simulated signal events before the trigger requirement. The final bin includes all events above the axis range.

3224 lifetime particles, roughly 40%, and efficiencies between 65% and 95% for shorter
 3225 lifetimes depending on both the mass and the lifetime.

3226 10.2 KINEMATICS AND ISOLATION

3227 After the trigger requirement, each event is required to have a primary vertex
 3228 reconstructed from at least two well-measured tracks in the inner detector, each
 3229 with $p_T > 400 \text{ MeV}$. If more than one such vertex exists, the primary vertex is
 3230 taken to be the one with the largest summed p_T^2 for all tracks associated to that
 3231 vertex. The offline reconstructed E_T^{miss} is required to be above 130 GeV to addi-
 3232 tionally reject SM backgrounds. The transverse missing energy is calculated us-
 3233 ing fully reconstructed and calibrated offline objects, as described in Section 6.5.
 3234 In particular the E_T^{miss} definition in this selection uses jets reconstructed with the
 3235 anti- k_t algorithm with radius $R = 0.4$ from clusters of energy in the calorimeter
 3236 (Section 6.4) and with $p_T > 20 \text{ GeV}$, as well as reconstructed muons, electrons,
 3237 and tracks not identified as another object type.

3238 The E_T^{miss} distributions are shown for data and a few simulated signals in Fig-
 3239 ure 73, after the trigger requirement. The data contains some events with E_T^{miss}
 3240 below the nominal trigger threshold of 70 GeV, which can occur because E_T^{miss}
 3241 at trigger level uses only calorimeter information while the full offline E_T^{miss}
 3242 additionally includes tracks and muons which can balance the event. The cut
 3243 placed at 130 GeV is 95% efficient for LL and 90% efficient for VLL particles, after
 3244 the trigger requirement, because of the missing energy generating mechanisms
 3245 discussed previously. The distribution of data in this figure and subsequent fig-
 3246 ures in this section can be interpreted as the distribution of backgrounds, as any
 3247 signal contamination would be negligible if present at these early stages of the
 3248 selection (prior to the final requirement on ionization). The background falls
 3249 rapidly with missing energy, motivating the direct requirement on E_T^{miss} for the
 3250 signal region.

3251 It is typically the practice for searches for new physics on ATLAS to place an
 3252 offline requirement on the triggering variable that is sufficiently tight to guar-

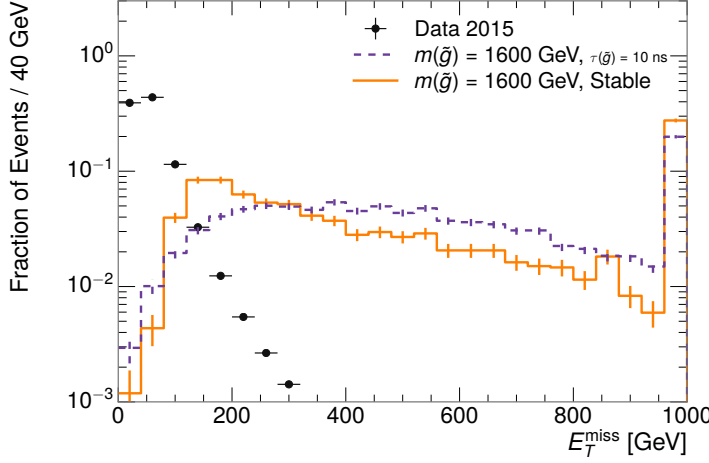


Figure 73: The distribution of E_T^{miss} for data and simulated signal events, after the trigger requirement. The final bin includes all events above the axis range.

3253 antee that the event would pass the trigger. Such a tight requirement makes the
 3254 uncertainty on the trigger efficiency of the simulation negligible, as modeling the
 3255 regime where the trigger is only partially efficient can be difficult. In this analy-
 3256 sis, however, because of the atypical interactions of R-Hadrons with the tracker
 3257 and the calorimeter, the offline requirement on E_T^{miss} is not sufficient to guar-
 3258 antee a 100% trigger efficiency even at large values, as can be seen in Figure 74.
 3259 This figure shows the efficiency for passing the HLT_xe70 trigger as a function
 3260 of the requirement on E_T^{miss} , which plateaus to roughly 85% even at large values.
 3261 This plateau does not reach 100% because events which have large offline miss-
 3262 ing energy from a neutral R-Hadron produced opposite of a charged R-Hadron
 3263 can have low missing energy in the calorimeters. The Calorimeter E_T^{miss} , on the
 3264 other hand, does not have this effect and reaches 100% efficiency at large values
 3265 because it is the quantity that directly corresponds to the trigger threshold. In
 3266 both cases the efficiency of triggering is greater for the short lifetime sample be-
 3267 cause the late decays to hadrons and LSPs produce an imbalance in the calorime-
 3268 ters even though they may not be reconstructed offline as tracks or jets. For this
 3269 reason, the requirement on E_T^{miss} is determined by optimizing the background
 3270 rejection even though it corresponds to a value of trigger efficiency significantly
 3271 below 1.0.

3272 The events are then required to have at least one candidate LLP track. Al-
 3273 though the LLPs are produced in pairs, many models do not consistently yield
 3274 two charged particles, as discussed in Chapter 9. For example, in the R-Hadron
 3275 model highlighted here, only 20% of events have two charged R-Hadrons while
 3276 47% of events have just one. A signal region requiring two charged particle can-
 3277 didates could be a powerful improvement in background rejection for a larger
 3278 dataset, but it is not considered in this version of the analysis as it was found to
 3279 be unnecessary to reject the majority of backgrounds.

3280 For a track to be selected as a candidate, it must have $p_T > 50 \text{ GeV}$ and pass
 3281 basic quality requirements. The track must be associated to the primary vertex.

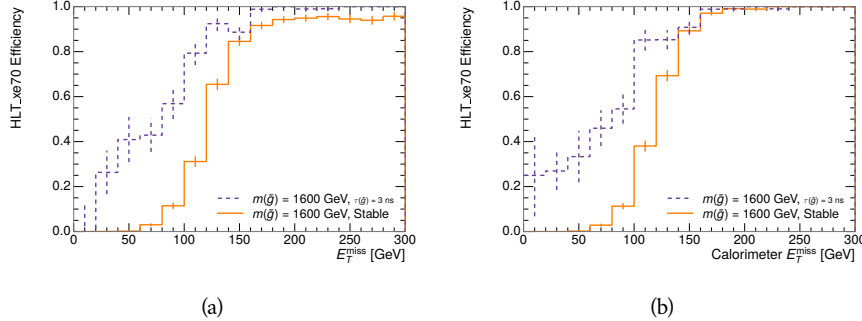


Figure 74: The trigger efficiency for the HLT_xe70 trigger requirement as a function of (a) E_T^{miss} and (b) Calorimeter E_T^{miss} for simulated signal events.

It must also have at least seven clusters in the silicon layers in the inner detector to ensure an accurate measurement of momentum. Those clusters must include one in the innermost layer if the extrapolated track is expected to pass through that layer. And to ensure a reliable measurement of ionization, the track is required to have at least two clusters in the pixel detector that provide a measurement of dE/dx .

At this point in the selection, there is a significant high-ionization background from multiple tracks that significantly overlap in the Pixel detector. Previous versions of this analysis have rejected these overlaps by an explicit overlap rejection between pairs of fully reconstructed tracks, typically by requiring no additional tracks within a cone around the candidate. This technique, however, fails to remove the background from tracks that overlap so precisely that the tracks cannot be separately resolved, which can be produced in very collimated photon conversions.

Another observable, which more directly targets track overlaps, identifies cluster shapes that are likely formed by multiple particles based on a neural network classification algorithm. The number of clusters on a given track that are estimated to have contributions from more than one particle is called N_{split} . As the shape of clusters requires significantly less spatial separation to identify overlaps than it does to reconstruct two fully resolved tracks, this variable is more effective at rejecting backgrounds from overlaps. Figure 75 shows the dependence of ionization on N_{split} ; as N_{split} increases the most probable value of dE/dx grows significantly up to twice the expected value when $N_{\text{split}} = 4$.

A requirement of $N_{\text{split}} = 0$ is very successful in reducing the long positive tail of the dE/dx distributions, as can be seen in Figure 76. Comparing the distribution for “baseline tracks”, tracks with only the above requirements on clusters applied and before the requirement on N_{split} , to the distribution with $N_{\text{split}} = 0$, it is clear that the fraction of tracks with large dE/dx is reduced by several orders of magnitude. The tracks without split hits are very close to the dE/dx distribution of identified muons, which are usually well isolated. Figure 76 also includes the distribution of dE/dx in an example signal simulation to demonstrate how effective dE/dx is as a discriminating variable with this isolation applied. The background falls rapidly for $dE/dx > 1.8 \text{ MeVg}^{-1}\text{cm}^2$ while the majority of

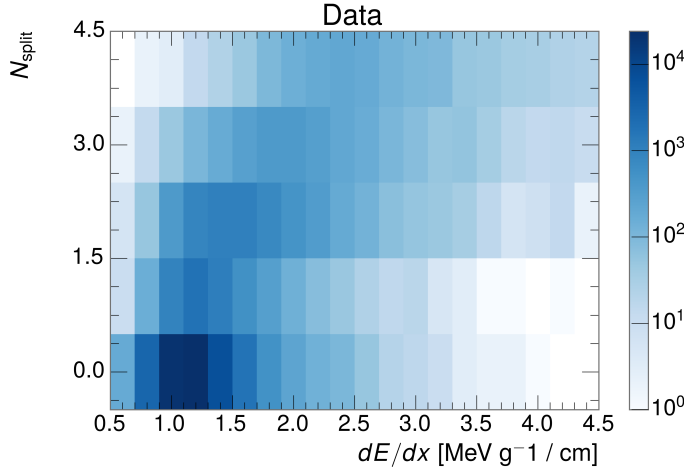


Figure 75: The dependence of dE/dx on N_{split} in data after basic track hit requirements have been applied.

3315 the signal, approximately 90% depending on the mass, falls above that threshold.
 3316 Over 90% of LLP tracks in simulated signal events pass the N_{split} -based isolation
 3317 requirement.

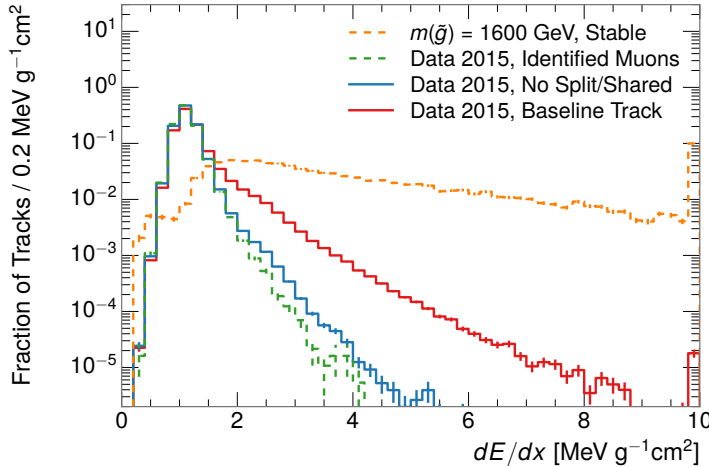


Figure 76: The distribution of dE/dx with various selections applied in data and simulated signal events. The final bin includes all tracks above the axis range.

3318 A few additional kinematic requirements are imposed to help reduce SM back-
 3319 grounds. The momentum of the candidate track must be at least 150 GeV, and
 3320 the uncertainty on that measurement must be less than 50%. The distribution of
 3321 momentum is shown in Figure 77 for tracks in data and simulated signal events
 3322 after the previously discussed requirements on clusters, transverse momentum,
 3323 and isolation have been imposed. The signal particles are much harder on av-

erage than their backgrounds as shown in Figure 67. The transverse mass, M_T , defined as

$$M_T = \sqrt{2p_T E_T^{\text{miss}}(1 - \cos(\Delta\phi(E_T^{\text{miss}}, \text{track})))} \quad (20)$$

estimates the mass of a decay of to a single charged particle and an undetected particle and is required to be greater than 130 GeV to reject contributions from the decay of W bosons. Figure 78 shows the distribution of M_T for data and simulated signal events. The signal is distributed over a wide range of M_T , with about 90% above the threshold value of 130 GeV. The data has a large number of contributions below 100 GeV from W boson decays and an additional peak from a kinematic shaping imposed by the requirements on E_T^{miss} and the track p_T in dijet events.

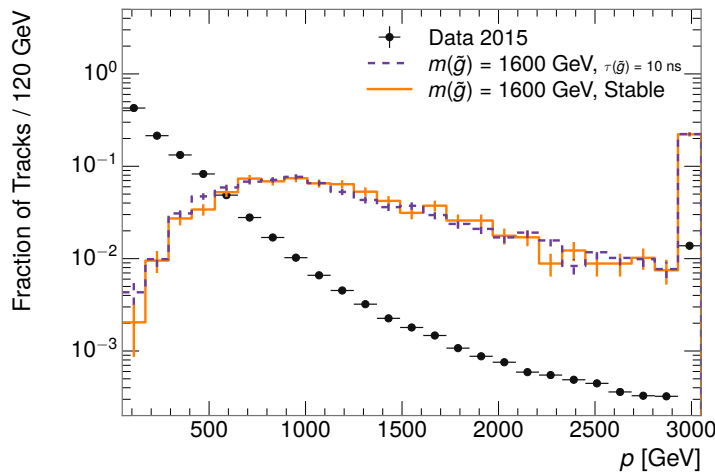


Figure 77: The distribution of track momentum for data and simulated signal events, after previous selection requirements have been applied. The final bin includes all tracks above the axis range.

10.3 PARTICLE SPECIES REJECTION

The amount of ionization deposited by particles with low mass and high momentum has a large positive tail [6], so backgrounds can be formed by a wide variety of SM processes when various charged particles have a few randomly large deposits of energy in the pixel detector. Those backgrounds can be additionally reduced by targeting other interactions with the detector where they are expected to have different behavior than R-Hadrons. The interactions with the detector depend on the types of particles produced rather than the processes which produce them, so this search forms a series of rejections to remove backgrounds from individual particle species. These rejections focus on using additional features of the event, other than the kinematics of the candidate track, as they can provide a powerful source of background rejection with very high signal efficiency. However, the lifetime of an R-Hadron can significantly change

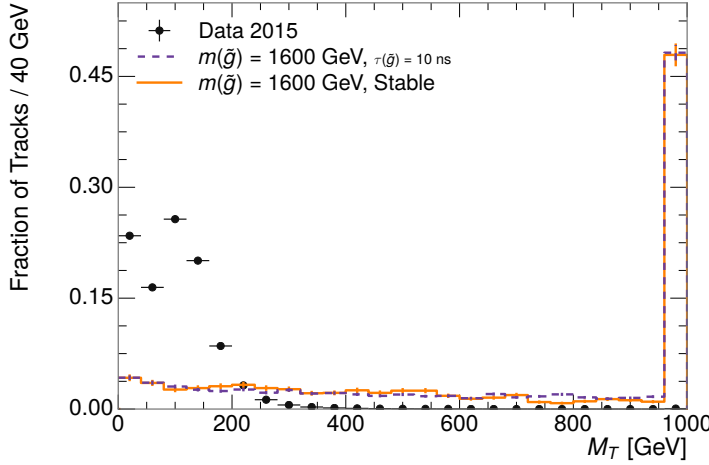


Figure 78: The distribution of M_T for data and simulated signal events, after previous selection requirements have been applied. The final bin includes all tracks above the axis range.

its detector characteristics, as discussed in Section 9.1.2. To accommodate these differences, the **SM** rejections defined in this section are split to form two signal regions, one for long-lifetimes particles, the **VLL** region ($\tau[\text{ns}] \geq 50 \text{ ns}$), and one for intermediate lifetime particles, the **LL** region ($0.4 < \tau[\text{ns}] < 50$).

Jets can contribute high momentum track backgrounds when an individual jet constituent carries large p_T . These tracks can be sufficiently well isolated from the other constituents that they are separately reconstructed and pass the N_{split} requirement. However, jets can be very effectively rejected by considering the larger-scale isolation of the candidate track. In this case the isolation focuses on the production of nearby particles as a jet-veto, rather than the isolation from overlapping tracks based on N_{split} that was used to reduce high-ionization backgrounds. As explained in Section 9.1, the fragmentation process which produces an R-Hadron is very hard and thus is not expected to produce additional particles with a summed momentum of more than 5 GeV. Nearby particles may be produced in the decay of the R-Hadron, but they will be significantly displaced, so the jet-veto only considers tracks associated to the primary vertex. The jet-veto uses the summed momentum of tracks with a cone of $\Delta R < 0.25$, referred to as p_T^{Cone} , which is shown in Figure 79 for data and simulated signal events. In the data this value has a peak at zero from isolated tracks such as leptons, and a long tail from jets which contains as much as 80% of the background above 20 GeV at this stage of the selection. In signal events p_T^{Cone} is strongly peaked at zero and significantly less than 1% of signal events have p_T^{Cone} above 20 GeV. This makes a requirement of $p_T^{\text{Cone}} < 20 \text{ GeV}$ a very effective method to reject background without losing signal efficiency. For the **VLL** signal region, this cut is further tightened to $p_T^{\text{Cone}} < 5 \text{ GeV}$ as it is the most effective variable remaining to extend the search reach for long lifetimes.

Even for fully isolated particles, there are additional methods to reject each type of particle using information in the muon system and calorimeters. Muons

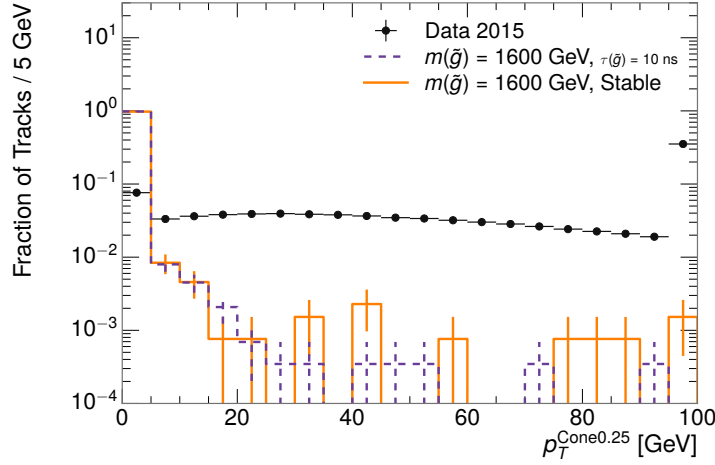


Figure 79: The distribution of summed tracked momentum within a cone of $\Delta R < 0.25$ around the candidate track for data and simulated signal events, after previous selection requirements have been applied. The final bin includes all tracks above the axis range.

can be identified very reliably using the tracks in the muon system, as described in Section 6.3. For intermediate lifetimes ($0.4 < \tau[\text{ns}] < 30$), the LLPs do not survive long enough to reach the muon system, and so muons are vetoed by rejecting tracks that associate to a muon with medium muon identification requirements (Section 6.3). For longer lifetimes ($\tau > 30$ ns), this rejection is not applied because LLPs which reach the muon system can be identified as muons as often as 30% of the time in simulated samples.

Calorimeter-based particle rejection relies on the expected small deposits of energy from LLPs. When the lifetime is long enough to reach the calorimeter, a LLP deposits little of its energy as it traverses the material, as discussed in Section 9.1. Even when the particle does decay before the calorimeter, the majority of its energy is carried away by the LSP and not deposited in the calorimeter. In both cases the energy is expected to be distributed across the layers of the calorimeters and not peaked in just one layer. This can be quantified in terms of E/p , the ratio of calorimeter energy of a nearby jet to the track momentum, and f_{EM} , the fraction of energy in that jet within the electromagnetic calorimeter. When no jets fall within a cone of 0.05 of the particle, E/p and f_{EM} are both defined as zero. E/p is expected to be above 1.0 for electrons and hadrons because of the contributions from other nearby particles. At these momenta there is no significant fraction of tracks with no associated clusters due to interactions with the detector or insufficient energy deposits (see Section 7.2.2). f_{EM} is peaked close to 1.0 for electrons, and distributed between 10% and 90% for hadrons.

These trends can be seen in the two dimensional distribution for signal in Figure 80 for VLL and LL (10 ns) signal events. The majority of R-Hadrons in both samples fall into the bin for $E/p = 0$ and $f_{\text{EM}} = 0$ because the majority of the time there is no associated jet. In the VLL sample, when there is an associated jet, E/p is typically still below 0.1, and the f_{EM} is predominantly less than 0.8.

3402 In the LL sample, on the other hand, E/p is larger on average because of the jets
 3403 produced in the R-Hadron decay. It is still typically below 0.1, however, because
 3404 most of the energy of the R-Hadron is carried by the LSP and not the jet. The
 3405 f_{EM} is much lower on average in this case, below 0.1, because the 10 ns lifetime
 3406 particles rarely decay before passing through the electromagnetic calorimeter.
 3407 Figure 80 also includes simulated Z decays to electrons or tau leptons. From the
 3408 decays to electrons it is clear that the majority of electrons have f_{EM} above 0.9.
 3409 The τ decays include a variety of products. Muons can be seen in the bin where
 3410 $E/p = 0$ and $f_{\text{EM}} = 0$ because they do not have an associated jet. Electrons fall
 3411 into the range where $E/p > 1$ and $f_{\text{EM}} > 0.9$. Hadronic tau decays are the most
 3412 common, and fall in the range of $0.1 < f_{\text{EM}} < 0.9$ and $E/p > 1.0$.

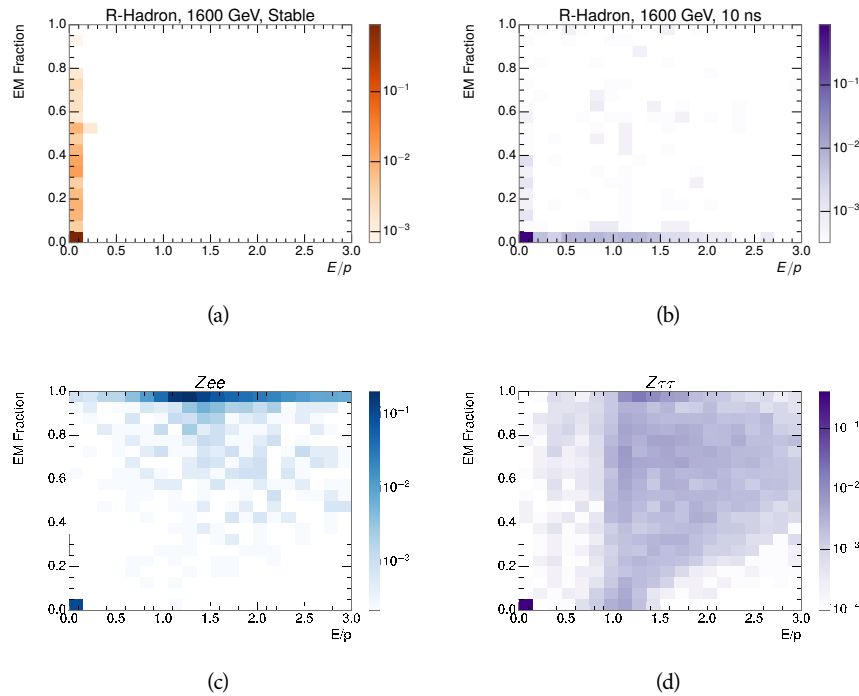


Figure 80: The normalized, two-dimensional distribution of E/p and f_{EM} for simulated
 (a) 1200 GeV VLL R-Hadron, and (b) 1200 GeV, 10 ns R-Hadron, (c) $Z \rightarrow ee$,
 and (d) $Z \rightarrow \tau\tau$ events.

3413 The differences motivate an electron rejection by requiring $f_{\text{EM}} < 0.9$. Simi-
 3414 larly, isolated hadrons are rejected by requiring $E/p < 1.0$. These requirements
 3415 combine to remove the majority of isolated electrons and hadrons but retain over
 3416 95% of the simulated signal across a range of masses and lifetimes. The suite of
 3417 particle species rejection techniques provide a significant analysis improvement
 3418 over previous iterations of ionization-based searches on ATLAS by providing
 3419 additional background rejection with minimal loss in signal efficiency.

3420 10.4 IONIZATION

3421 The final requirement on the candidate track is the primary discriminating vari-
 3422 able, the ionization in the pixel detector. That ionization is measured in terms
 3423 of dE/dx , which was shown for data and simulated signal events in Figure 76.
 3424 dE/dx is dramatically greater for the high mass signal particles than the back-
 3425 grounds, which start to fall immediately after the minimally ionizing peak at 1.1
 3426 MeV g $^{-1}$ cm 2 . The dE/dx for candidate tracks must be greater than a pseudorapidity-
 3427 dependent threshold, specifically $1.80 - 0.11|\eta| + 0.17\eta^2 - 0.05|\eta|^3$ MeV g $^{-1}$ cm $^{-2}$,
 3428 in order to correct for an approximately 5% dependence of the MIP peak position
 3429 on η . The requirement was chosen as part of the signal region optimization, and
 3430 reduces the backgrounds by a factor of 100 while remaining 70-90% efficient for
 3431 simulated signal events depending on the mass.

3432 10.4.1 MASS ESTIMATION

3433 The mean value of ionization in silicon is governed by the Bethe equation and
 3434 the most probable value follows a Landau-Vavilov distribution [6]. Those forms
 3435 inspire a parametric description of dE/dx in terms of $\beta\gamma$,

$$(dE/dx)_{\text{MPV}}(\beta\gamma) = \frac{p_1}{\beta^{p_3}} \ln(1 + [p_2\beta\gamma]^{p_5}) - p_4 \quad (21)$$

3436 which performs well in the range $0.3 < \beta\gamma < 1.5$. This range includes the
 3437 expected range of $\beta\gamma$ for the particles targeted for this search, with $\beta\gamma \approx 2.0$
 3438 for lower mass particles (O(100 GeV)) and $\beta\gamma \approx 0.5$ for higher mass parti-
 3439 cles (O(1000 GeV)). The parameters, p_i , are fit using a 2015 data sample of
 3440 low-momentum pions, kaons, and protons as described in Ref. [98]. Figure 81
 3441 shows the two-dimensional distribution of dE/dx and momentum along with
 3442 the above fitted values for $(dE/dx)_{\text{MPV}}$.

3443 The above equation (21) is then numerically inverted to estimate $\beta\gamma$ and the
 3444 mass for each candidate track. In simulated signal events, the mean of this mass
 3445 value reproduces the generated mass up to around 1800 GeV to within 3%. The
 3446 mass distributions are shown for a few VLL mass points in Figure 82. The large
 3447 widths of these distributions come from the high variability in energy deposits
 3448 in the pixel detector as well as the uncertainty on momentum measurements at
 3449 high momentum, but the means converge to the expected values. A constant
 3450 shift of 3% is observed between the mean of the reconstructed mass distribution
 3451 and the generated mass, which is then corrected by applying a 3% shift in the
 3452 opposite direction.

3453 This analysis evaluates expected yields and the resulting cross sectional limits
 3454 using windows in this mass variable. The windows are formed by fitting mass
 3455 distributions in simulated signal events like those in Figure 82 to Gaussian distri-
 3456 butions and taking all events that fall within $\pm 1.4\sigma$ of the mean. As can be seen
 3457 in Figure 82, typical values for this width are $\sigma \approx 300 - 500$ GeV depending on
 3458 the generated mass.

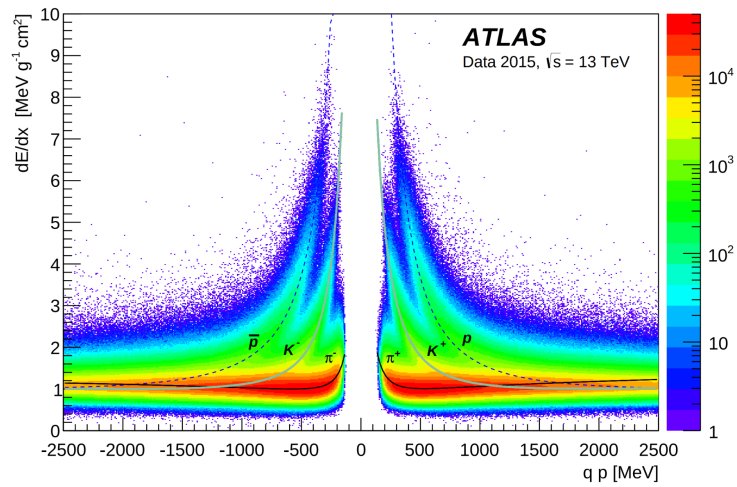


Figure 81: Two-dimensional distribution of dE/dx versus charge signed momentum (qp) for minimum-bias tracks. The fitted distributions of the most probable values for pions, kaons and protons are superimposed.

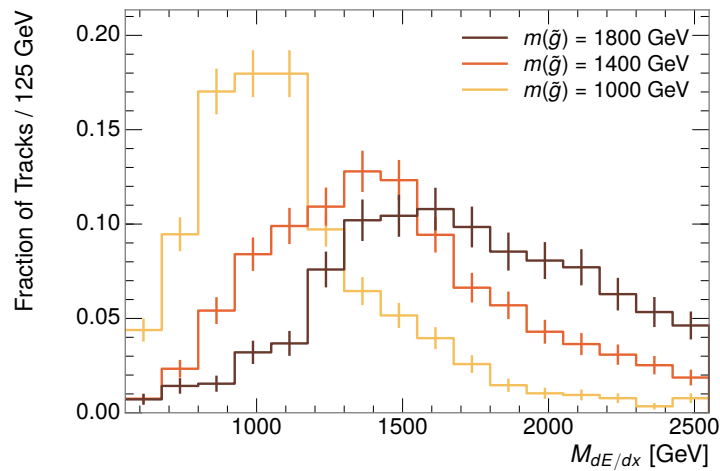


Figure 82: The distribution of mass estimated using dE/dx for simulated VLL R-Hadrons with masses between 1000 and 1600 GeV.

3459 10.5 EVENT SELECTION

3460 The numbers of events passing each requirement are shown in Table 10 for the
 3461 full 2015 dataset and a simulated 1600 GeV, 10 ns lifetime R-Hadron sample.
 3462 The table highlights the overall acceptance \times efficiency for signal events, which
 3463 for this example is 19%. Between SM rejection and ionization, the selection re-
 3464 quirements reduce the background of tracks which pass the kinematic require-
 3465 ments down by an additional factor of almost 2000.

Selection	Exp. Signal Events (Fraction)	Observed Events	Rejection Factor
Generated	26.0 ± 0.3		
E_T^{miss} Trigger	24.8 ± 0.3 (95%)		
$E_T^{\text{miss}} > 130$ GeV	23.9 ± 0.3 (92%)		
Track Quality and $p_T > 50$	10.7 ± 0.2 (41%)	368324	1.0
Isolation Requirement	9.0 ± 0.2 (35%)	108079	3.4
Track $p > 150$ GeV	6.6 ± 0.2 (25%)	47463	7.8
$M_T > 130$ GeV	5.8 ± 0.2 (22%)	18746	20
Electron and Hadron Veto	5.5 ± 0.2 (21%)	3612	100
Muon Veto	5.5 ± 0.2 (21%)	1668	220
Ionization Requirement	5.0 ± 0.1 (19%)	11	33000

Table 10: The expected number of events at each level of the selection for LL 1600 GeV, 10 ns R-Hadrons, along with the number of events observed in data, for 3.2 fb^{-1} . The simulated yields are shown with statistical uncertainties only. The total efficiency \times acceptance is also shown for the signal and the rejection factor relative to initial track requirement is shown for data.

3466 There is a strong dependence of this efficiency on lifetime and mass, with effi-
 3467 ciencies dropping to under 1% at low lifetimes. Figure 83 shows the dependence
 3468 on both mass and lifetime for all signal samples considered in this search. The
 3469 dependence on mass is relatively slight and comes predominantly from the in-
 3470 creasing fraction of R-Hadrons which pass the ionization cut with increasing
 3471 mass. The trigger and E_T^{miss} requirements are most efficient for particles that
 3472 decay before reaching the calorimeters. However, the chance of a particle to be
 3473 reconstructed as a high-quality track decreases significantly at low lifetimes as
 3474 the particle does not propagate sufficiently through the inner detector. These
 3475 effects lead to a maximum in the selection efficiency for lifetimes around 10-30
 3476 ns. The lifetimes up to and including 30 ns are shown with the LL selection and
 3477 the 50 ns and stable points are shown with the VLL selection.

3478 The inefficiency of this signal region at short lifetimes comes almost exclu-
 3479 sively from an acceptance effect, in that the particles do not reach the necessary
 3480 layers of the SCT. This can be seen more clearly by defining a fiducial region
 3481 which includes events with at least one R-Hadron that is produced with non-
 3482 zero charge, $p_T > 50$ GeV, $p > 150$ GeV, $|\eta| < 2.5$, and a decay distance greater
 3483 than 30 cm in the transverse plane. At short (1 ns) lifetimes, the acceptance into

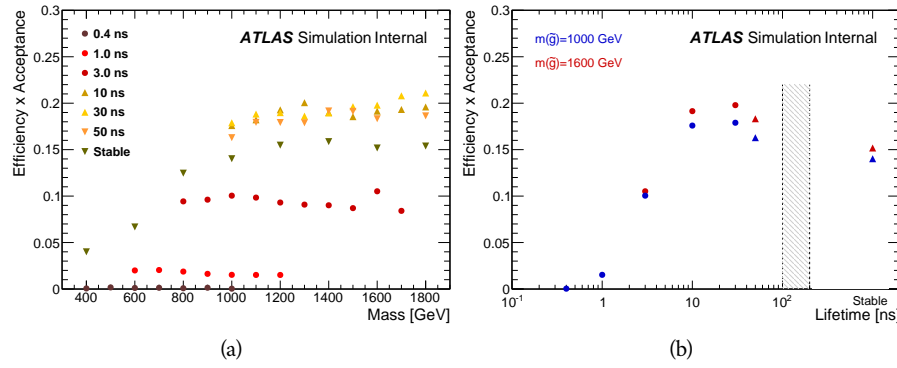


Figure 83: The acceptance \times efficiency as a function of R-Hadron (a) mass and (b) lifetime. (a) shows all of the combinations of mass and lifetime considered in this search, and (b) highlights the lifetime dependence for 1000 GeV and 1600 GeV R-Hadrons.

3484 this region is as low as 4%. Once this acceptance is accounted for, the selection
 3485 efficiency ranges from 25% at lifetimes of 1 ns up to 45% at lifetimes of 10 ns.

3486

3487 BACKGROUND ESTIMATION

3488 The event selection discussed in the previous section focuses on detector sig-
 3489 natures, emphasizing a single high-momentum, highly-ionizing track. That track
 3490 is then required to be in some way inconsistent with the expected properties
 3491 of SM particles, with various requirements designed to reject jets, hadrons, elec-
 3492 trons, and muons (Section 10.3). Therefore the background for this search comes
 3493 entirely from reducible backgrounds that are outliers of various distributions in-
 3494 cluding dE/dx , f_{EM} , and p_T^{Cone} . The simulation can be tuned in various ways to
 3495 do an excellent job of modeling the average properties of each particle type [99],
 3496 but it is not necessarily expected to accurately reproduce outliers. For this rea-
 3497 sons, the background estimation used for this search is estimated entirely using
 3498 data.

3499 11.1 BACKGROUND SOURCES

3500 SM charged particles with lifetimes long enough to form tracks in the inner de-
 3501 tector can be grouped into three major categories based on their detector inter-
 3502 actions: hadrons, electrons, and muons. Every particle that enters into the back-
 3503 ground for this search belongs to one of these types. Relatively pure samples of
 3504 tracks from each of these types can be formed in data by inverting the various
 3505 rejection techniques in Section 10.3. Specifically, muons are selected requiring
 3506 medium muon identification, electrons requiring $E/p > 1.0$ and $f_{EM} > 0.95$,
 3507 and hadrons requiring $E/p > 1.0$ and $f_{EM} < 0.95$.

3508 Figure 84 shows the distributions of momentum and dE/dx for these cate-
 3509 gories in data, after requiring the event level selection as well as the track re-
 3510 quirements on p_T , hits, and N_{split} , as discussed in Section 10.2. Simulated signal
 3511 events are included for reference. These distribution are only illustrative of the
 3512 differences between types, as the rejection requirements could alter their shape.
 3513 This is especially significant for momentum which enters directly into E/p and
 3514 can indirectly affect muon identification. However the various types show clear
 3515 differences in both distributions. The distributions of momentum are not nec-
 3516 cessarily expected to match between the various types because the production
 3517 mechanisms for each type result in different kinematic distributions. dE/dx is
 3518 also different between types because of incomplete isolation; although the re-
 3519 quirement on N_{split} helps to reduce the contribution of nearby particles it does
 3520 not completely remove the effect of overlaps. Muons are better isolated because
 3521 they do not have the additional particle from hadronization present for hadrons
 3522 and they are significantly less likely to interact with the detector and produce
 3523 secondary particles compared to hadrons and electrons. Thus muons have the
 3524 smallest fraction of dE/dx above the threshold of $1.8 \text{ MeVg}^{-1}\text{cm}^2$; hadrons and
 3525 electrons have a larger fraction above this threshold.

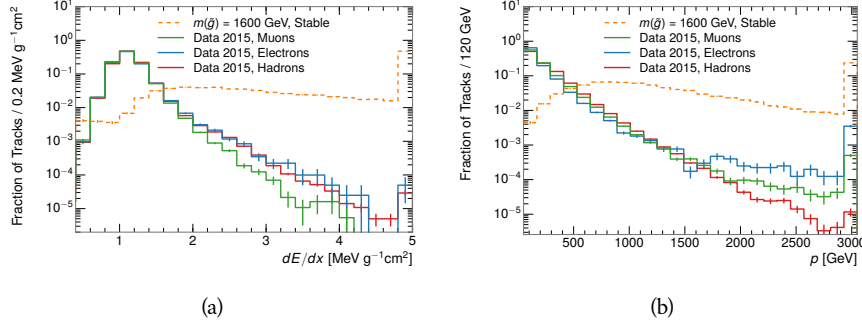


Figure 84: The distribution of (a) dE/dx and (b) momentum for tracks in data and simulated signal after requiring the event level selection and the track selection on p_T , hits, and N_{split} . Each sub-figure shows the normalized distributions for tracks classified as hadrons, electrons, and muons in data and R-Hadrons in the simulated signal.

3526 It is difficult to determine what fraction of each particle type enters into the fi-
3527 nal signal region. The background method will not have significant dependence
3528 on the relative contributions of each species, but it is useful to understand the
3529 differences between each when considering the various tests of the method.

3530 11.2 PREDICTION METHOD

The data-driven background estimation relies on the independence between ionization and other kinematic variables in the event. For standard model particles with momenta above 50 GeV, dE/dx is not correlated with momentum; though there is a slight relativistic rise as momentum increases, the effect is small compared to the width of the distribution of ionization energy deposits.. So, the proposed method to estimate the mass distribution of the signal region is to use momentum from a track with low dE/dx (below the threshold value) and to combine it with a random dE/dx value from a dE/dx template. The resulting track is just as likely as the original, so a number of such random generations provide the expected distributions of momentum and ionization. These are then combined using the parametrization described in Section 10.4.1 to form a distribution of mass for the signal region.

Algorithmically this method is implemented by forming two distinct Control Regions (**CRs**). The first **CR**, CR1, is formed by applying the entire event selection from Chapter 10 up to the dE/dx and mass requirements. The dE/dx requirement is instead inverted for this region. Because of the independence of dE/dx , the tracks in this control region have the same kinematic distribution as the tracks in the signal region, and are used to measure a two-dimensional template of p and η . The second **CR**, CR2, is formed from the event selection through the dE/dx requirement, but with an inverted E_T^{miss} requirement. The tracks in this control region are expected to have similar dE/dx distributions to the signal region before the ionization requirement, and so this region is used to measure a two-dimensional template of dE/dx and η .

3554 The contribution of any signal to the control regions is minimized by the in-
 3555 verted selection requirements. Only less than 10% of simulated signal events
 3556 have either dE/dx or E_T^{miss} below the threshold values in the original signal re-
 3557 gion, while the backgrounds are significantly enhanced by inverting those re-
 3558 quirements. The signal contamination is less than 1% in both control regions
 3559 for all of the simulated masses and lifetimes considered in this analysis.

3560 With those measured templates, the shape of the mass estimation is generated
 3561 by first selecting a random (p , η) combination from CR1. This momentum
 3562 value is combined with a dE/dx value taken from the appropriate distribution
 3563 of dE/dx for the selected η from CR2. The use of η in both random samplings
 3564 controls for any correlation between p , dE/dx , and η . Those values are then
 3565 used to calculate a mass in the same way that is done for regular tracks in data,
 3566 see Section 10.4.1. As this procedure includes all dE/dx values, the cut at 1.8
 3567 MeVg $^{-1}$ cm 2 is then enforced to fully model the signal region. The generated
 3568 mass distribution is then normalized by scaling the background estimate to the
 3569 data in the region $M < 160$ GeV, where signals of this type have already been
 3570 excluded [83]. This normalization uses the distributions of mass generated with-
 3571 out the ionization requirement.

3572 The statistical uncertainties on these background distributions are calculated
 3573 by independently fluctuating each bin of the input templates according to their
 3574 Poisson uncertainties. These fluctuations are repeated a large number of times,
 3575 and the uncertainty on the resulting distribution is taken as the root mean square
 3576 (RMS) deviation of the fluctuations from the average. As the procedure uses one
 3577 million random combinations to generate the distributions, The statistical un-
 3578 certainty from the actual random generations is negligible compared to the un-
 3579 certainty from measuring the templates.

3580 11.3 VALIDATION

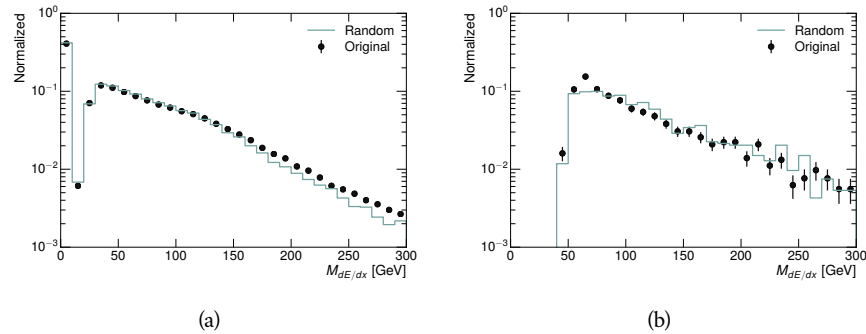
3581 The validity of the background estimation technique can be evaluated in both
 3582 data and simulation. The underlying assumption that random combinations of
 3583 dE/dx and momentum can predict a mass distribution in an orthogonal region
 3584 can be tested using simulated samples where concerns like multiple particle types
 3585 can be controlled. Using the same technique in another set of signal-depleted
 3586 regions in data then extends this confidence to the more complicated case where
 3587 several particle species are inherently included.

3588 11.3.1 CLOSURE IN SIMULATION

3589 The first test of the procedure is done using a simulated sample of $W \rightarrow \mu\nu$
 3590 decays. These types of events provide the ingredients required to test the back-
 3591 ground estimate, E_T^{miss} and isolated tracks, with high statistics. In this example
 3592 there is no signal, so simulated events in the orthogonal CRs are used to estimate
 3593 the shape of the mass distribution of the simulated events in the signal region. To
 3594 reflect the different topology for W boson decays, the CRs use slightly modified
 3595 definitions. In all CRs, the requirement of $p > 150$ GeV and the SM rejection

3596 requirements are removed. Additionally, for the signal region the requirement
 3597 on E_T^{miss} is relaxed to 30 GeV and the corresponding inverted requirement on
 3598 CR2 is also set at 30 GeV.

3599 With these modified selections, the simulated and randomly generated distri-
 3600 butions of $M_{dE/dx}$ are shown in Figure 85. This figure includes the mass distri-
 3601 butions before and after the requirement on dE/dx , which significantly shapes
 3602 the distributions. In both cases the background estimation technique repro-
 3603 duces the shape of $M_{dE/dx}$ in the signal region. There is a small difference in the pos-
 3604 itive tail of the mass distribution prior to the ionization cut, where the random
 3605 events underestimate the fraction of tracks with mass above 150 GeV by about
 3606 20%. After the ionization requirement, however, this discrepancy is not present
 3607 and the two distributions agree to within statistical uncertainties.



3604 Figure 85: The distribution of $M_{dE/dx}$ (a) before and (b) after the ionization requirement
 3605 for tracks in simulated W boson decays and for the randomly generated back-
 3606 ground estimate.

3607 This ability to reproduce the shape of the mass distribution in simulated events
 3608 shows that the technique works as expected. No significant biases are acquired
 3609 in using low dE/dx events to select kinematic templates or in using low E_T^{miss}
 3610 events to select ionization templates, as either would result in a mismodeling of
 3611 the shape of the mass distribution. The simulated events contain only one par-
 3612 ticle type, however, so this test only establishes that the technique works well
 3613 when the the CRs are populated by exactly the same species.

3615 11.3.2 VALIDATION REGION IN DATA

3616 The second test of the background estimate is performed using data in an or-
 3617 thogonal validation region. The validation region, and the corresponding CRs,
 3618 are formed using the same selection requirements as in the nominal method but
 3619 with a modified requirement on momentum, $50 < p[\text{GeV}] < 150$. This allows
 3620 the technique to be checked in a region with very similar properties but where
 3621 the signal is depleted, as the majority of the signal has momentum above 150
 3622 GeV while the backgrounds are enhanced below that threshold. Any biases on
 3623 the particle composition of the CRs for the signal region will be reflected in the
 3624 CRs used to estimate the mass distribution in the validation region.

Figure 86 shows the measured and randomly generated mass distributions for data before and after the ionization requirement. The background estimate does an excellent job of modeling the actual background before the ionization requirement, with good agreement to within the statistical uncertainties out to the limit of the mass distribution. There are very few events in the validation region after the ionization requirement, but the few observed events are consistent with the background prediction. The good agreement in this validation region provides a confirmation that the technique works even in the full-complexity case with multiple particle types entering the distributions. Any bias from changes in particle composition between regions is small compared to statistical uncertainties.

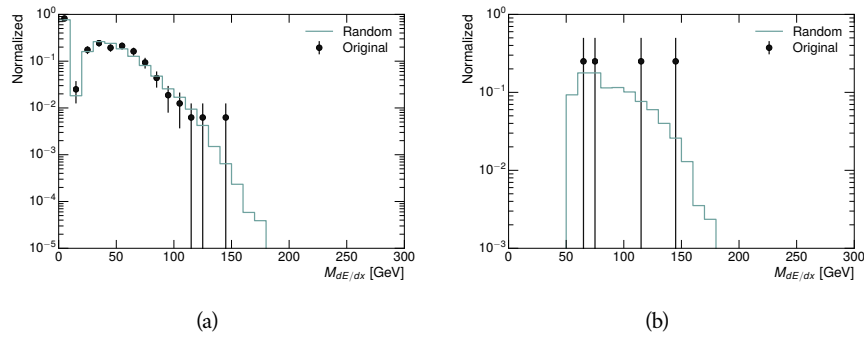


Figure 86: The distribution of $M_{dE/dx}$ (a) before and (b) after the ionization requirement for tracks in the validation region and for the randomly generated background estimate.

3635

3636 SYSTEMATIC UNCERTAINTIES

3637 A number of systematic uncertainties affect the interpretation of the results of
 3638 the search. These uncertainties can be broken down into two major categories,
 3639 those which affect the estimate of the background using data and those which
 3640 affect the measurement of the signal yield estimated with simulated events. The
 3641 total measured systematic uncertainties are 7% for the background estimation
 3642 and approximately 32% for the signal yield depending on lifetime. These system-
 3643 atic uncertainties are expected to be small compared to the statistical fluctuations
 3644 of the measured yields so that measured cross-sectional limits will be dominated
 3645 by statistical uncertainties. The following sections describe each source of sys-
 3646 tematic uncertainty for each of the two types.

3647 12.1 BACKGROUND ESTIMATE

3648 The systematic uncertainties on the background estimate come primarily from
 3649 considering alternative methods for generating the background distributions.
 3650 These uncertainties are small compared to the statistical uncertainties on the
 3651 background estimate which come from the limited statistics in measuring the
 3652 template distributions, as described in Section 11.2. They are summarized in
 3653 Table 11.

Source of Uncertainty:	Value [%]
Analytic Description of dE/dx	4.0
Muon Fraction (Stable Region only)	3.0
IBL Ionization Correction	3.8
Normalization	3.0
Total (Metastable Region):	6.3
Total (Stable Region):	7.0

Table 11: A summary of the sources of systematic uncertainty for the data-driven back-
 ground in the signal region. If the uncertainty depends on the mass, the maxi-
 mum values are reported.

3654 12.1.1 ANALYTIC DESCRIPTION OF DE/DX

3655 The background estimate uses a binned template distribution to estimate the
 3656 dE/dx of tracks in the signal region, as described in Section 11.2. It is also possi-
 3657 ble to fit that measured distribution to a functional form to help smooth the dis-

3658 tribution in the tails of dE/dx where the template is driven by a small number
 3659 of tracks. Both Landau convolved with a Gaussian and Crystal Ball functions
 3660 are considered as the functional form and used to re-estimate the background
 3661 distribution. The deviations compared to the nominal method are found to be
 3662 4%, and this is taken as a systematic uncertainty to cover the inability carefully
 3663 predict the contribution from the long tail of dE/dx where there are few mea-
 3664 surements available in data.

3665 12.1.2 MUON FRACTION

3666 The stable region of the analysis explicitly includes tracks identified as muons,
 3667 which have a known difference in their dE/dx distributions compared to non-
 3668 muon tracks (Section 11.1). To account for a difference in muon fraction be-
 3669 tween the background region and the signal region for this selection, the dE/dx
 3670 templates for muons and non-muons are measured separately and then the rel-
 3671 ative fraction of each is varied in the random generation. The muon fraction
 3672 is varied by its statistical uncertainty and the resulting difference of 3% in back-
 3673 ground yield is taken as the systematic uncertainty.

3674 12.1.3 IBL CORRECTIONS

3675 The IBL, described in Section 5.3.1, received a significant dose of radiation during
 3676 the data collection in 2015. The irradiation can cause a drift in the frontend
 3677 electronics and thus alter the dE/dx measurement which includes the ToT output
 3678 by the IBL. These effects are corrected for in the nominal analysis by scaling the
 3679 dE/dx measurements by a constant factor derived for each run to match the
 3680 average dE/dx value to a reference run where the IBL was known to be stable
 3681 to this effect. However, this corrective factor does not account for inter-run
 3682 variations. To account for this potential drift of dE/dx , the correction procedure
 3683 is repeated by varying the corrections up and down by the maximal run-to-run
 3684 variation from the full data-taking period, which results in an uncertainty of
 3685 3.8%.

3686 12.1.4 NORMALIZATION

3687 As described in Section 11.2, the generated distribution of masses is normalized
 3688 in a shoulder region ($M < 160$ GeV) where signals have been excluded by pre-
 3689 vious analyses. That normalization factor is varied by its statistical uncertainty
 3690 and the resulting fluctuation in the mass distribution of 3% is taken as a system-
 3691 atic uncertainty on the background estimate.

3692 12.2 SIGNAL YIELD

3693 The systematic uncertainties on the signal yield can be divided into three cate-
 3694 gories; those on the simulation process, those on the modeling of the detector

efficiency or calibration, and those affecting the overall signal yield. They are summarized in Table 11. The largest uncertainty comes from the uncertainty on the production cross section for gluinos, which is the dominant systematic uncertainty in this analysis.

Source of Uncertainty	-[%]	+[%]
ISR Modeling (Metastable Region)	1.5	1.5
ISR Modeling (Stable Region)	14	14
Pile-up Reweighting	1.1	1.1
Trigger Efficiency Reweighting	0.9	0.9
E_T^{miss} Scale	1.1	2.2
Ionization Parametrization	7.1	0
Momentum Parametrization	0.3	0.0
Electron Rejection	0.0	0.0
Hadron Rejection	0.0	0.0
μ Identification	4.3	4.3
Luminosity	5	5
Signal size uncertainty	28	28
Total (Metastable Region)	30	29
Total (Stable Region)	33	32

Table 12: A summary of the sources of systematic uncertainty for the simulated signal yield. The uncertainty depends on the mass and lifetime, and the maximum negative and positive values are reported in the table.

12.2.1 ISR MODELING

As discussed in Section 9.2, MadGraph is expected to reproduce the distribution of ISR in signal events more accurately than the nominal Pythia samples. The analysis reweights the distribution of ISR in the simulated signal events to match the distribution found in generated MadGraph samples. This has an effect on the selection efficiency in the signal samples, where ISR contributes to the generation of E_T^{miss} . To account for the potential inaccuracy on the simulation of ISR at high energies, half of the difference between the signal efficiency with the reweighted distribution and the original distribution is taken as a systematic uncertainty.

12.2.2 PILEUP REWEIGHTING

The simulated events were generated prior to data collection with an estimate of the average number of interactions per bunch crossing. This estimate does not match the value of pileup during actual data collection, but a large fraction of the simulated events would be discarded in order to match the distribution in data.

3713 Therefore the simulated signal events are not reweighted for pileup by default
 3714 in the analysis. The effect of the pileup on signal efficiency is not expected to
 3715 depend on the mass or lifetime of the generated signal events, which allows all
 3716 of the generated signal events to be used together to assess the pileup dependence.
 3717 To account for the potential effect of the difference in the number of interactions
 3718 per bunch crossing between data and simulation, the difference in yield between
 3719 the nominal signal events and the reweighted events averaged over all masses
 3720 and lifetimes is taken as a systematic uncertainty on the yield for each mass and
 3721 lifetime (1.1%).

3722 12.2.3 TRIGGER EFFICIENCY REWEIGHTING

3723 As described in Section 10.2, the selection for this analysis does not require a suf-
 3724 ficiently large value of E_T^{miss} to be above the plateau of trigger efficiency. There-
 3725 fore, some signal events which would otherwise pass the event selection can be
 3726 excluded because of the trigger requirement. These effects can be difficult to es-
 3727 timate in simulation, and thus are constrained by comparing data and simulated
 3728 events in an alternative W boson region which uses decays to muons to find a rel-
 3729 atively pure sample of events with missing energy. The trigger efficiency for data
 3730 and simulated W events are shown in Figure 87. The comparison between data
 3731 and MC in this region constrains the simulation of the trigger efficiency. The
 3732 simulated signal events are reweighted by the ratio of data to simulation in the
 3733 W boson decays, while the difference between the data and simulation in those
 3734 decays is taken as a systematic uncertainty. This results in an uncertainty of only
 3735 0.9% as the majority of events are well above the plateau and the disagreement
 3736 between data and simulation is small even below that plateau.

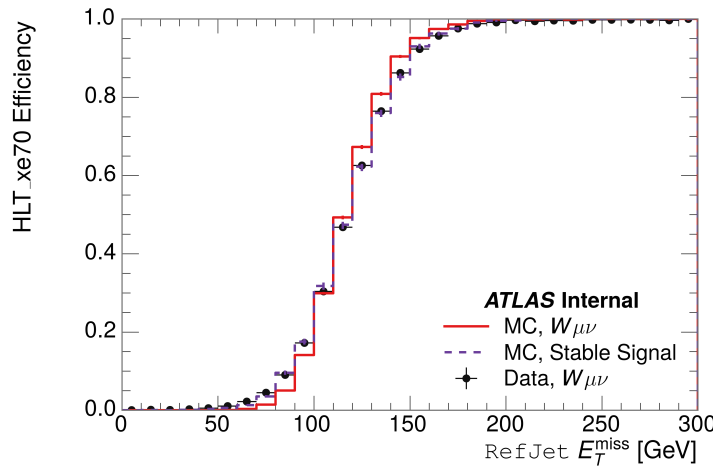


Figure 87: The trigger efficiency for the HLT_xe70 trigger requirement as a function of Calorimeter E_T^{miss} for simulated data events with a W boson selection. Simulated signal events and simulated W boson events are also included.

Systematic Variation	-[%]	+[%]
JET_GroupedNP_1	-0.7	1.3
JET_GroupedNP_2	-0.7	1.2
JET_GroupedNP_3	-0.5	1.3

Table 13: Example of the contributing systematic variations to the total systematic for the E_T^{miss} Scale, as measured in a 1200 GeV, Stable R-Hadron signal sample.

3737 12.2.4 MISSING TRANSVERSE MOMENTUM SCALE

3738 The ATLAS Combined Performance ([CP](#)) group provides a default recommenda-
 3739 tion for systematic variations of jets and missing energy (**note: I'm not quite**
 3740 **sure what to cite for this - I don't see any papers from the jet/met group**
 3741 **after this was implemented**). These variations enter into this analysis only in
 3742 the requirement on E_T^{miss} . The effect of the measured scale of E_T^{miss} is evaluated
 3743 by varying the E_T^{miss} scale according to the one sigma variations provided by all
 3744 [CP](#) recommendations on objects affecting event kinematics in simulated signal
 3745 events. Missing energy is reconstructed from fully reconstructed objects so any
 3746 systematic uncertainties affecting jets, muons, electrons, or the E_T^{miss} soft terms
 3747 are included. The only non-negligible contributions found using this method are
 3748 itemized in Table 13 for an example signal sample (1200 GeV, Stable R-Hadron),
 3749 where the systematic is measured as the relative difference in the final signal ef-
 3750 ficiency after applying the associated variation through the CP tools. The only
 3751 variations that are significant are the grouped jet systematic variations, which
 3752 combine recommended jet systematic uncertainties into linearly independent
 3753 variations.

3754 As the peak of the reconstructed E_T^{miss} distribution in the signal is significantly
 3755 above the current threshold for events which pass the trigger requirement, the
 3756 effect of scale variation is expected to be small, which is consistent with the mea-
 3757 sured systematic of approximately 2%. Events which do not pass the trigger re-
 3758 quirement usually fail because there are no ISR jets in the event to balance the
 3759 R -hadrons' transverse momentum, so the reconstructed E_T^{miss} is low and there-
 3760 fore also expected to be not very sensitive to scale changes.

3761 12.2.5 MOMENTUM PARAMETRIZATION

3762 The uncertainty on the signal efficiency from track momentum is calculated us-
 3763 ing the [CP](#) group recommendations for tracks. In particular, only one recom-
 3764 mended systematic variation affects track momentum, the sagitta bias for q/P .
 3765 This uncertainty is propagated to the final selection efficiency by varying the
 3766 track momentum by the recommended one sigma variation, and the associated
 3767 uncertainty is found to be negligible (0.3%).

3768 12.2.6 IONIZATION REQUIREMENT

3769 The dE/dx distributions in data and simulated events have different most prob-
 3770 able values, which is due in part to radiation effects in the detector that are not
 3771 fully accounted for in the simulation. The difference does not affect the mass
 3772 measurement used in this analysis, as independent calibrations are done in sim-
 3773 ulation and in data. However, it does affect the efficiency of the high dE/dx
 3774 selection requirement. To calculate the size of the effect on the signal efficiency,
 3775 the dE/dx distribution in signal simulation is scaled by a scale factor obtained
 3776 from comparing the dE/dx distribution of inclusive tracks in data and in sim-
 3777 ulation. The difference in efficiency for this sample with a scaled dE/dx dis-
 3778 tribution, relative to the nominal case, is taken as a systematic uncertainty on
 3779 signal efficiency. The uncertainty is as large as 7% for low masses and falls to a
 3780 negligible effect for large masses.

3781 12.2.7 ELECTRON AND JET REJECTION

3782 The systematic uncertainty on the electron rejection is measured by varying the
 3783 EM fraction requirement significantly, from 0.95 to 0.9. This is found to have
 3784 a less than 0.04% effect on signal acceptance, on average, and so is completely
 3785 negligible. Similarly, the uncertainty on jet rejection is measured by tightening
 3786 the E/p requirement from 0.5 to 0.4. This is found to have no effect on signal
 3787 acceptance, so again the systematic is again negligible.

3788 12.2.8 MUON VETO

3789 The metastable signal region requires that the candidate tracks are not identi-
 3790 fied as medium muons because the majority of R-Hadrons in the lifetime range
 3791 included in that region do not reach the muon spectrometers before they de-
 3792 cay. However, the exponential tail of the R-Hadron lifetime distribution results
 3793 in some R-Hadrons traversing the muon spectrometer. These can still fail the
 3794 muon medium identification because they can fail on the requirement on the
 3795 number of precision hits required to pass the loose selection because they ar-
 3796 rive late to the muon spectrometer. This can be seen in Figure 88, which shows
 3797 the efficiency of the muon veto as a function of $1/\beta$, for two simulated stable
 3798 R-Hadron samples.

3799 Thus, the efficiency of the muon veto depends on the timing resolution of
 3800 the spectrometer, so an uncertainty is applied to the signal efficiency to cover
 3801 differences in timing resolution between data and simulation. First, a sample of
 3802 $Z \rightarrow \mu\mu$ events is selected in data in which one of the muons has a late arrival
 3803 time measured in the MDT. Then the reconstructed β distribution is compared
 3804 to the distribution in simulated $Z \rightarrow \mu\mu$ events; the difference between these
 3805 two distributions reflects the difference in timing resolution between data and
 3806 simulation. To emulate this difference in simulated signal events, the magnitude
 3807 of the difference is used to scale and shift the true β distribution of R-Hadrons in
 3808 simulation. Signal events are then reweighted based on this varied β distribution,

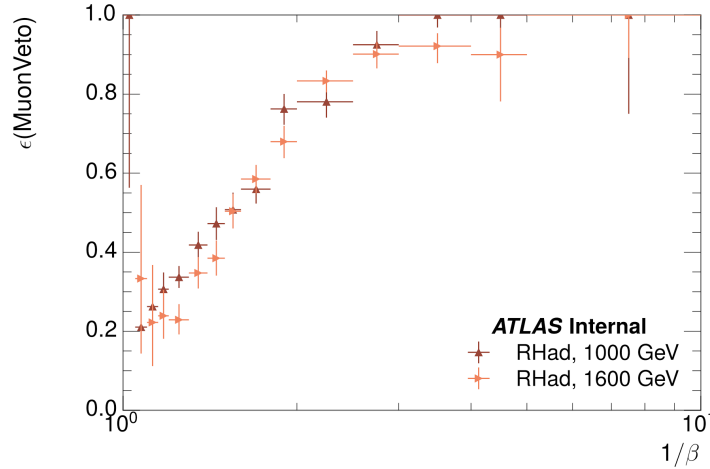


Figure 88: The efficiency of the muon veto for R -hadrons of two different masses, as a function of $\frac{1}{\beta}$ for simulated R-Hadron tracks.

and the difference in the efficiency of the muon veto selection is compared with the nominal and reweighted true β distributions. The difference in muon veto efficiency is taken as a systematic uncertainty of the muon veto.

The comparison of reconstructed β between data and simulation is performed separately in the barrel, transition, and endcap regions of the spectrometer, and the reweighting of the true β distribution in signal is done per region. The comparison of average reconstructed MDT β between data and simulation for the barrel region is shown in Figure 89 for $Z \rightarrow \mu\mu$ events. As expected, The uncertainty is found to be negligible for R -hadrons with short lifetimes, and is only significant for lifetimes above 30 ns.

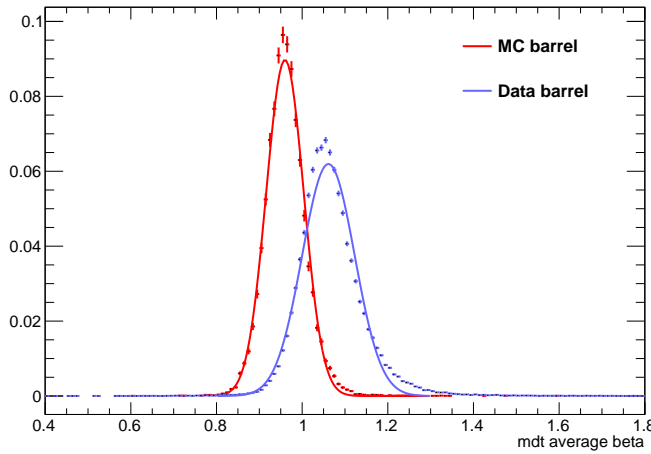


Figure 89: The average reconstructed MDT β distribution for $Z \rightarrow \mu\mu$ events in which one of the muons is reconstructed as a slow muon, for both data and simulation. A gaussian fit is superimposed.

3819 12.2.9 LUMINOSITY

3820 The luminosity uncertainty is provided by a luminosity measurement on ATLAS
3821 and was measured to be 5% at the time of the publication of this analysis.

3822 12.2.10 SIGNAL SIZE

3823 As discussed in Section 9.2, the signal cross sections are calculated at NLO in the
3824 strong coupling constant with a resummation of soft-gluon emission at NLL. The
3825 uncertainties on those cross sections are between 14% to 28% for the R-Hadrons
3826 in the range of 400 to 1800 GeV [95, 96], where the uncertainty increases with
3827 the mass.

3828

3829 RESULTS

3830 This full analysis was performed using the 3.2 fb^{-1} from the 2015 data-taking.
 3831 Using the selections discussed in Chapter 10, sixteen events were observed in
 3832 the stable signal region and eleven events were observed in the metastable signal
 3833 region, prior to requirements on the candidate track mass. The background esti-
 3834 mate discussed in Chapter 11 predicts $17 \pm 2.6(\text{stat}) \pm 1.2(\text{syst})$ events for the
 3835 stable region and $11.1 \pm 1.7(\text{stat}) \pm 0.7(\text{syst})$ events for the metastable region.
 3836 These counts are summarized in Table 14.

3837 The mass estimated using dE/dx (Section 10.4.1) provides the final discrimi-
 3838 nating variable, where the signal would be expected as an excess in the falling ex-
 3839ponential tail of the expected background. The observed distribution of masses
 3840 is shown in Figure 90, along with the predicted distribution from the background
 3841 estimate for each signal region. Both include a few example simulated signal dis-
 3842 tributions, which show the scale of an excess were the R-Hadron signals present.
 3843 There is no statistically significant evidence of an excess in the data over the back-
 3844 ground estimation. From this distribution it is clearly possible to rule out signals
 3845 with lower masses, around 1200 GeV, which have larger cross sections.

3846 13.1 CROSS SECTIONAL LIMITS

3847 Because there is no observed significant excess of events in the signal region, this
 3848 analysis sets upper limits on the allowed cross section for R-Hadron production.
 3849 These limits are set for each mass point by counting the observed events in data,
 3850 along with the expected background and simulated signal events, in windows of
 3851 mass. The mass windows are formed by fitting the distribution of signal events to
 3852 a Gaussian distribution, and the window is then $\pm 1.4\sigma$ around the center of that
 3853 Gaussian. Two examples of the windows formed by this procedure are shown
 3854 in Tables 15-16, for the stable and 10 ns working points. The corresponding
 3855 counts of observed data, expected background, and simulated signal for those
 3856 same working points are shown in Tables 17-18. Appendix A includes the mass
 3857 windows and counts for all of the considered signal points.

Selection Region	Expected Background	Data
Stable	$17.2 \pm 2.6 \pm 1.2$	16
Metastable	$11.1 \pm 1.7 \pm 0.7$	11

Table 14: The estimated number of background events and the number of observed events in data for the specified selection regions prior to the requirement on mass. The background estimates show statistical and systematic uncertainties.

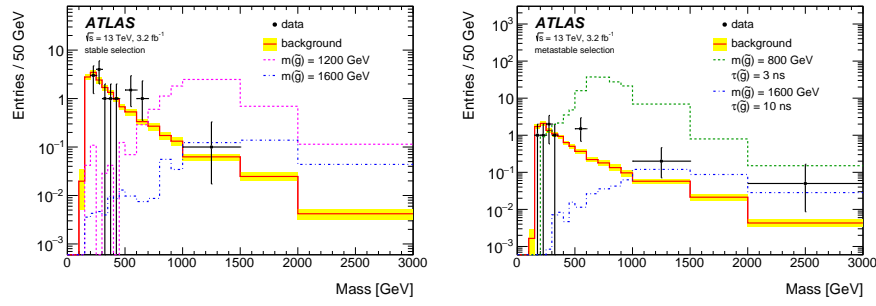


Figure 90: The observed mass distribution of events in data and the generated background distribution in (a) the stable and (b) the metastable signal region. A few example simulated signal distributions are superimposed.

$m(\tilde{g})$ [GeV]	Left Extremum [GeV]	Right Extremum [GeV]
1000	655	1349
1100	734	1455
1200	712	1631
1300	792	1737
1400	717	1926
1500	815	2117
1600	824	2122
1700	900	2274
1800	919	2344

Table 15: The left and right extremum of the mass window for each generated mass point with a 10 ns lifetime.

$m(\tilde{g})$ [GeV]	Left Extremum [GeV]	Right Extremum [GeV]
800	627	1053
1000	726	1277
1200	857	1584
1400	924	1937
1600	993	2308
1800	1004	2554

Table 16: The left and right extremum of the mass window used for each generated stable mass point.

$m(\tilde{g})$ [GeV]	Expected Signal	Expected Background	Observed Data
800	462.83 ± 14.86	1.764 ± 0.080	2.0
1000	108.73 ± 3.38	1.458 ± 0.070	1.0
1200	31.74 ± 0.95	1.137 ± 0.060	1.0
1400	10.22 ± 0.29	1.058 ± 0.058	1.0
1600	3.07 ± 0.09	0.947 ± 0.054	1.0
1800	1.08 ± 0.05	0.940 ± 0.054	1.0

Table 17: The expected number of signal events, the expected number of background events, and the observed number of events in data with their respective statistical errors within the respective mass window for each generated stable mass point

$m(\tilde{g})$ [GeV]	Expected Signal	Expected Background	Observed Data
1000	144.48 ± 5.14	1.499 ± 0.069	2.0
1100	73.19 ± 2.61	1.260 ± 0.060	2.0
1200	41.54 ± 1.41	1.456 ± 0.067	2.0
1300	22.58 ± 0.77	1.201 ± 0.058	2.0
1400	12.70 ± 0.42	1.558 ± 0.071	2.0
1500	6.73 ± 0.24	1.237 ± 0.060	2.0
1600	3.90 ± 0.13	1.201 ± 0.058	2.0
1700	2.27 ± 0.07	1.027 ± 0.052	2.0
1800	1.34 ± 0.04	1.019 ± 0.052	2.0

Table 18: The expected number of signal events, the expected number of background events, and the observed number of events in data with their respective statistical errors within the respective mass window for each generated mass point with a lifetime of 10 ns.

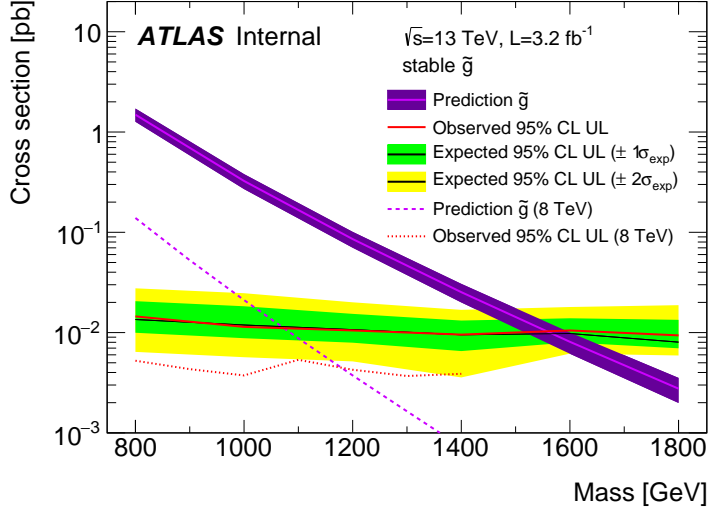


Figure 91: The observed and expected cross section limits as a function of mass for the stable simulated signal. The predicted cross section values for the corresponding signals are included.

3858 The 95% confidence level upper limits on the cross sections for a large grid of
 3859 masses (between 800 and 1800 GeV) and lifetimes (between 0.4 and stable) are
 3860 extracted from these counts with the CL_s method using the profile likelihood
 3861 ratio as a test statistic [100]. For this procedure, the systematic uncertainties esti-
 3862 mated for the signal and background yields are treated as Gaussian-distributed
 3863 nuisance parameters. The uncertainty on the normalization of the expected
 3864 background distribution is included in the expected background events. At this
 3865 point the expected cross section limit is calculated for both the metastable and
 3866 stable signal region for each lifetime point, and the region with the best expected
 3867 limit is selected for each lifetime. Using that procedure, the metastable region is
 3868 used for lifetimes up to and including 30 ns, and the stable region for lifetimes
 3869 above it.

3870 The resulting cross-sectional upper limits are shown as a function of mass in
 3871 Figure 91 and Figure 92 for each lifetime considered. The limits are interpolated
 3872 linearly between each mass point, and the dependence of the limit on the mass
 3873 is small as the efficiency is relatively constant for large R-Hadron masses. There
 3874 is however a strong dependence on lifetime, as discussed in Section 10.5, where
 3875 the probability to form a fully reconstructed track and the kinematic freedom to
 3876 produce E_T^{miss} result in a local maximum in the limit at 10-30 ns. The figures also
 3877 include the expected cross section for pair-produced gluino R-Hadrons for ref-
 3878 erence. For the 10 ns and stable cross section limits, both the observed limit and
 3879 expected cross section for the Run 1, 8 TeV version of this analysis are included.
 3880 There the cross sectional limits are lower because of the increased available lu-
 3881 minosity, while the signal cross sections were also much lower because of the
 3882 lower collision energy.

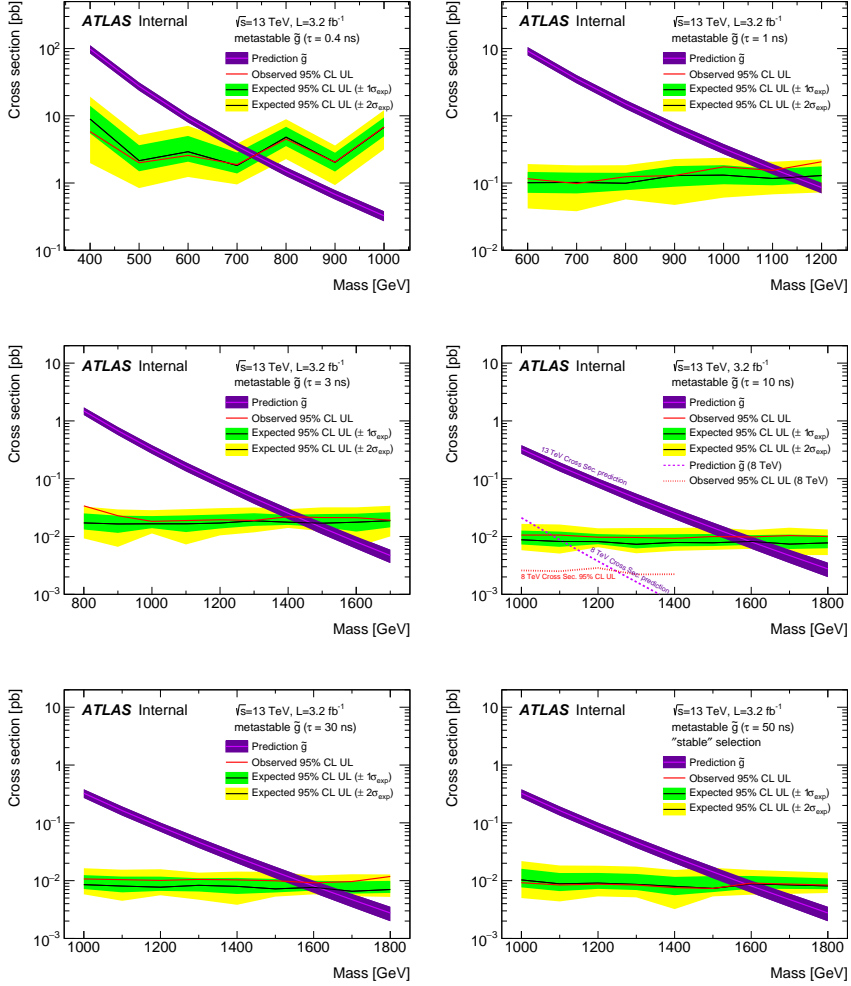


Figure 92: The observed and expected cross section limits as a function of mass for each generated lifetime. The predicted cross section values for the corresponding signals are included.

3883 13.2 MASS LIMITS

3884 The cross-sectional limits can then be used to derive a lower mass limit for gluino
 3885 R-Hadrons by comparing them to the theoretically predicted production cross
 3886 sections. These mass limits range from only 740 GeV at the lowest lifetimes con-
 3887 sidered, where the selection efficiency is very low, to up to 1580 GeV at 30 ns
 3888 where the selection efficiency is maximized. The observed and expected mass
 3889 limits for each lifetime point are detailed in Table 19, which also lists which se-
 3890 lection region was used for each lifetime. These excluded range of masses as a
 3891 function of lifetime is also shown in Figure 93. The Run 1 limits are included for
 3892 comparison; the limits have increased by about 200 GeV on average. The search
 3893 has also improved since the previous incarnation from Run 1 in optimizing the
 3894 region between 30 GeV and detector-stable lifetimes by introducing the second
 3895 signal region. The definition of the stable region prevents the significant drop
 3896 in mass limit that occurred above 30 GeV in the Run 1 analysis.

Selection	τ [ns]	$M_{\text{obs}} > [\text{GeV}]$	$M_{\text{exp}} > [\text{GeV}]$
Metastable	0.4	740	730
"	1.0	1110	1150
"	3.0	1430	1470
"	10	1570	1600
"	30	1580	1620
Stable	50	1590	1590
"	stable	1570	1580

Table 19: The observed and expected 95% CL lower limit on mass for gluino R-Hadrons for each considered lifetime.

3897 13.3 CONTEXT FOR LONG-LIVED SEARCHES

3898 This search plays an important role in the current, combined ATLAS search for
 3899 long lived particles. The mass limits provided by various ATLAS searches for
 3900 long-lived gluino R-Hadrons can be seen in Figure 94. This search provides the
 3901 most competitive limit for lifetimes between 3 ns up through very long lifetimes,
 3902 where it is still competitive with dedicated searches for stable particles. The lim-
 3903 its placed on gluino production are very similar to the limits on promptly decay-
 3904 ing models.

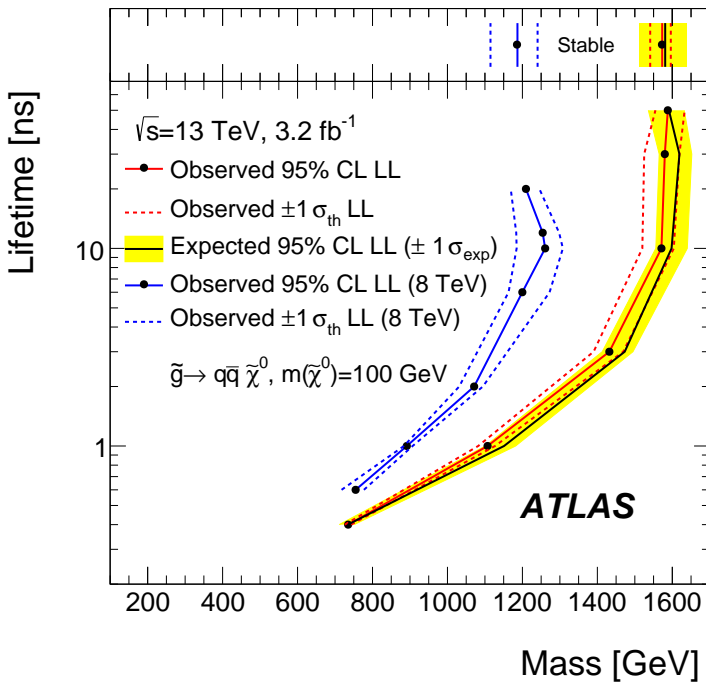


Figure 93: The excluded range of masses as a function of gluino lifetime. The expected lower limit (LL), with its experimental $\pm 1\sigma$ band, is given with respect to the nominal theoretical cross-section. The observed 95% LL obtained at $\sqrt{s} = 8 \text{ TeV}$ [83] is also shown for comparison.

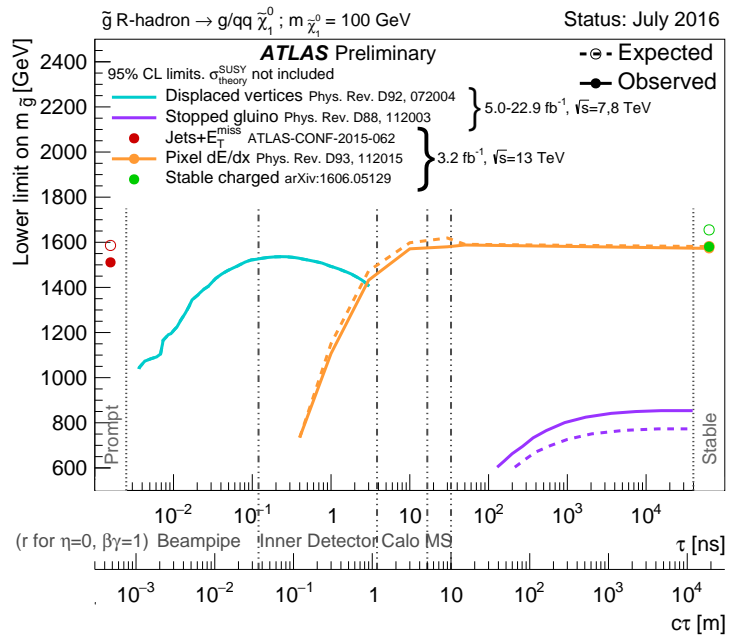


Figure 94: The constraints on the gluino mass as a function of lifetime for a split-supersymmetry model with the gluino R-Hadrons decaying into a gluon or light quarks and a neutralino with mass of 100 GeV. The solid lines indicate the observed limits, while the dashed lines indicate the expected limits. The area below the curves is excluded. The dots represent results for which the particle is assumed to be prompt or stable.

3905

3906 SUMMARY AND OUTLOOK

3907 The search described herein targetted the unique signature of TeV-scale, charged
3908 **LLPs**, which are predicted in a variety of extensions to the **SM** including some
3909 versions of **SUSY**. The dataset of 13 TeV proton-proton collisions was collected
3910 during 2015 by the ATLAS detector at the **LHC**, with an integrated luminosity
3911 of 3.2 fb^{-1} . The specific search strategy focused on identifying massive, charged
3912 particles which propagate through the Pixel detector in ATLAS by their characteristically large ionization.
3913 Recent updates to the strategy also include a number of rejection techniques that significantly reduce **SM** backgrounds compared
3914 to previous iterations. The analysis also provided a data-driven background estimation method that was shown to be effective with validation tests in both
3915 simulation and actual data.

3916 No significant excesses above the background prediction were found in the
3917 data, and so limits were placed on the production of massive, charged, **LLPs**. Using
3918 a benchmark model of simulated R-Hadrons, cross sections above 10-100
3919 fb were excluded at 95% confidence level, depending on the lifetime of the R-
3920 Hadron. Together with the predicted gluino pair-production cross sections, these
3921 lead to mass limits on R-Hadrons up to 1600 GeV where the search is most sensitive.
3922 Though these specific values assume an R-Hadron **LLP**, the search strategy accommodates a number of other species and the limits can be interpreted for
3923 other models. The search provides a significant contribution to the combined
3924 efforts to search for **LLPs** in **SUSY**, as the current version places the largest mass
3925 limits for lifetimes starting at 3 ns and up through very long lifetimes.

3926 These results are expected to be significantly improved in the following years,
3927 primarily because of continuing data collection at 13 TeV at the **LHC**. During
3928 2016, but after the release of this analysis, ATLAS recorded an additional 35.5
3929 fb^{-1} of collisions, and analysis of this data would significantly extend the limits
3930 presented here. The next iteration of the analysis can also provide additional
3931 interpretations of the search, by explicitly including other models like stop R-
3932 Hadrons and charginos in the limit calculations, as has been done in previous
3933 searches [83]. This strategy will continue to provide a competitive approach to
3934 discovering new **LLPs** throughout the lifetime of the **LHC**.

3938

PART V

3939

APPENDIX

3940

$m(\tilde{g})$ [GeV]	Left Extremum [GeV]	Right Extremum [GeV]
1000	682	1387
1100	763	1478
1200	801	1606
1300	809	1841
1400	861	2011
1500	920	2032
1600	952	2173
1800	1017	2422

Table 20: The left and right extremum of the mass window for each generated mass point with a 50 ns lifetime.

$m(\tilde{g})$ [GeV]	Left Extremum [GeV]	Right Extremum [GeV]
1000	689	1321
1100	746	1513
1200	788	1670
1300	860	1734
1400	833	1925
1500	852	2048
1600	833	2283
1700	946	2379
1800	869	2505

Table 21: The left and right extremum of the mass window for each generated mass point with a 30 ns lifetime.

$m(\tilde{g})$ [GeV]	Left Extremum [GeV]	Right Extremum [GeV]
1000	655	1349
1100	734	1455
1200	712	1631
1300	792	1737
1400	717	1926
1500	815	2117
1600	824	2122
1700	900	2274
1800	919	2344

Table 22: The left and right extremum of the mass window for each generated mass point with a 10 ns lifetime.

$m(\tilde{g})$ [GeV]	Left Extremum [GeV]	Right Extremum [GeV]
800	531	1065
900	576	1165
1000	610	1345
1100	635	1432
1200	663	1563
1300	620	1667
1400	742	1727
1500	761	1937
1600	573	2000
1700	621	2182

Table 23: The left and right extremum of the mass window used for each generated mass point with a lifetime of 3 ns.

$m(\tilde{g})$ [GeV]	Left Extremum [GeV]	Right Extremum [GeV]
600	411	758
700	385	876
800	486	970
900	406	987
1000	408	1136
1100	555	1196
1200	516	1378

Table 24: The left and right extremum of the mass window used for each mass point with a lifetime of 1 ns.

$m(\tilde{g})$ [GeV]	Left Extremum [GeV]	Right Extremum [GeV]
400	204	510
500	295	639
600	288	702
700	323	701
800	190	771
900	277	677
1000	249	688

Table 25: The left and right extremum of the mass window for each generated mass point with a lifetime of 0.4 ns.

$m(\tilde{g})$ [GeV]	Left Extremum [GeV]	Right Extremum [GeV]
800	627	1053
1000	726	1277
1200	857	1584
1400	924	1937
1600	993	2308
1800	1004	2554

Table 26: The left and right extremum of the mass window used for each generated stable mass point.

$m(\tilde{g})$ [GeV]	Expected Signal	Expected Background	Observed Data
1000	131.18 ± 6.35	1.803 ± 0.081	1.0 ± 1.0
1100	71.11 ± 3.35	1.409 ± 0.069	1.0 ± 1.0
1200	37.18 ± 1.75	1.310 ± 0.066	1.0 ± 1.0
1300	20.76 ± 0.95	1.431 ± 0.069	1.0 ± 1.0
1400	12.63 ± 0.57	1.273 ± 0.065	1.0 ± 1.0
1500	6.57 ± 0.29	1.115 ± 0.059	1.0 ± 1.0
1600	3.56 ± 0.16	1.041 ± 0.057	1.0 ± 1.0
1800	1.27 ± 0.05	0.918 ± 0.053	1.0 ± 1.0

Table 27: The expected number of signal events, the expected number of background events, and the observed number of events in data with their respective statistical errors within the respective mass window for each generated mass point with a lifetime of 50 ns.

$m(\tilde{g})$ [GeV]	Expected Signal	Expected Background	Observed Data
1000	144.65 ± 6.34	1.328 ± 0.063	2.0 ± 1.4
1100	75.28 ± 3.27	1.255 ± 0.060	2.0 ± 1.4
1200	40.51 ± 1.75	1.193 ± 0.058	2.0 ± 1.4
1300	20.91 ± 0.93	0.997 ± 0.051	2.0 ± 1.4
1400	11.97 ± 0.51	1.131 ± 0.056	2.0 ± 1.4
1500	6.81 ± 0.28	1.111 ± 0.055	2.0 ± 1.4
1600	4.19 ± 0.16	1.193 ± 0.058	2.0 ± 1.4
1700	2.42 ± 0.09	0.963 ± 0.050	2.0 ± 1.4
1800	1.46 ± 0.05	1.138 ± 0.056	3.0 ± 1.7

Table 28: The expected number of signal events, the expected number of background events, and the observed number of events in data with their respective statistical errors within the respective mass window for each generated mass point with a lifetime of 30 ns.

$m(\tilde{g})$ [GeV]	Expected Signal	Expected Background	Observed Data
1000	144.48 ± 5.14	1.499 ± 0.069	2.0 ± 1.4
1100	73.19 ± 2.61	1.260 ± 0.060	2.0 ± 1.4
1200	41.54 ± 1.41	1.456 ± 0.067	2.0 ± 1.4
1300	22.58 ± 0.77	1.201 ± 0.058	2.0 ± 1.4
1400	12.70 ± 0.42	1.558 ± 0.071	2.0 ± 1.4
1500	6.73 ± 0.24	1.237 ± 0.060	2.0 ± 1.4
1600	3.90 ± 0.13	1.201 ± 0.058	2.0 ± 1.4
1700	2.27 ± 0.07	1.027 ± 0.052	2.0 ± 1.4
1800	1.34 ± 0.04	1.019 ± 0.052	2.0 ± 1.4

Table 29: The expected number of signal events, the expected number of background events, and the observed number of events in data with their respective statistical errors within the respective mass window for each generated mass point with a lifetime of 10 ns.

$m(\tilde{g})$ [GeV]	Expected Signal	Expected Background	Observed Data
800	362.97 ± 14.68	1.841 ± 0.080	5.0 ± 2.2
900	169.20 ± 6.69	1.710 ± 0.076	3.0 ± 1.7
1000	84.78 ± 3.23	1.727 ± 0.076	2.0 ± 1.4
1100	40.06 ± 1.60	1.679 ± 0.075	2.0 ± 1.4
1200	20.06 ± 0.81	1.598 ± 0.072	2.0 ± 1.4
1300	10.76 ± 0.43	1.851 ± 0.080	2.0 ± 1.4
1400	5.52 ± 0.22	1.374 ± 0.064	2.0 ± 1.4
1500	3.16 ± 0.13	1.355 ± 0.064	2.0 ± 1.4
1600	2.13 ± 0.11	2.235 ± 0.093	3.0 ± 1.7
1700	1.10 ± 0.06	1.995 ± 0.085	2.0 ± 1.4

Table 30: The expected number of signal events, the expected number of background events, and the observed number of events in data with their respective statistical errors within the respective mass window for each generated mass point with a lifetime of 3 ns.

$m(\tilde{g})$ [GeV]	Expected Signal	Expected Background	Observed Data
600	431.80 ± 36.60	2.418 ± 0.099	3.0 ± 1.7
700	192.77 ± 15.28	3.267 ± 0.126	3.0 ± 1.7
800	69.63 ± 5.90	2.125 ± 0.089	3.0 ± 1.7
900	28.91 ± 2.59	3.114 ± 0.121	3.0 ± 1.7
1000	13.64 ± 1.22	3.359 ± 0.129	5.0 ± 2.2
1100	6.13 ± 0.57	1.879 ± 0.081	3.0 ± 1.7
1200	3.24 ± 0.30	2.387 ± 0.098	5.0 ± 2.2

Table 31: The expected number of signal events, the expected number of background events, and the observed number of events in data with their respective statistical errors within the respective mass window for each generated mass point with a lifetime of 1 ns.

$m(\tilde{g})$ [GeV]	Expected Signal	Expected Background	Observed Data
400	181.71 ± 75.59	6.780 ± 0.238	4.0 ± 2.0
500	103.88 ± 30.05	4.310 ± 0.160	4.0 ± 2.0
600	28.34 ± 9.34	4.868 ± 0.177	4.0 ± 2.0
700	13.62 ± 4.00	3.908 ± 0.147	4.0 ± 2.0
800	2.75 ± 1.15	9.001 ± 0.308	8.0 ± 2.8
900	2.25 ± 0.71	5.045 ± 0.183	5.0 ± 2.2
1000	0.34 ± 0.19	6.026 ± 0.214	6.0 ± 2.4

Table 32: The expected number of signal events, the expected number of background events, and the observed number of events in data with their respective statistical errors within the respective mass window for each generated mass point with a lifetime of p4 ns.

$m(\tilde{g})$ [GeV]	Expected Signal	Expected Background	Observed Data
800	462.83 ± 14.86	1.764 ± 0.080	2.0 ± 1.4
1000	108.73 ± 3.38	1.458 ± 0.070	1.0 ± 1.0
1200	31.74 ± 0.95	1.137 ± 0.060	1.0 ± 1.0
1400	10.22 ± 0.29	1.058 ± 0.058	1.0 ± 1.0
1600	3.07 ± 0.09	0.947 ± 0.054	1.0 ± 1.0
1800	1.08 ± 0.05	0.940 ± 0.054	1.0 ± 1.0

Table 33: The expected number of signal events, the expected number of background events, and the observed number of events in data with their respective statistical errors within the respective mass window for each generated stable mass point

- 3944 [1] A. D. Martin, W. J. Stirling, R. S. Thorne, and G. Watt. “Parton distribu-
3945 tions for the LHC”. In: *Eur. Phys. J.* C63 (2009), pp. 189–285. doi: [10.1140/epjc/s10052-009-1072-5](https://doi.org/10.1140/epjc/s10052-009-1072-5). arXiv: [0901.0002](https://arxiv.org/abs/0901.0002) [hep-ph].
- 3946 [2] Nobelprize.org. “The 2004 Nobel Prize in Physics - Popular Information”.
3947 2014. URL: <https://cds.cern.ch/record/1165534>.
- 3948 [3] Prajwal Raj Kafle, Sanjib Sharma, Geraint F. Lewis, and Joss Bland-Hawthorn.
3949 “On the Shoulders of Giants: Properties of the Stellar Halo and the Milky
3950 Way Mass Distribution”. In: *Astrophys. J.* 794.1 (2014), p. 59. doi: [10.1088/0004-637X/794/1/59](https://doi.org/10.1088/0004-637X/794/1/59). arXiv: [1408.1787](https://arxiv.org/abs/1408.1787) [astro-ph.GA].
- 3951 [4] Savas Dimopoulos and Howard Georgi. “Softly broken supersymmetry
3952 and SU(5)”. In: *Nuclear Physics B* 193.1 (1981), pp. 150 – 162. ISSN: 0550-
3953 3213. doi: [http://dx.doi.org/10.1016/0550-3213\(81\)90522-8](https://dx.doi.org/10.1016/0550-3213(81)90522-8).
- 3954 [5] A. Djouadi et al. “The Minimal supersymmetric standard model: Group
3955 summary report”. In: *GDR (Groupement De Recherche) - Supersymetrie Mont-
3956 pellier, France, April 15-17, 1998*. 1998. arXiv: [hep-ph/9901246](https://arxiv.org/abs/hep-ph/9901246) [hep-ph].
3957 URL: https://inspirehep.net/record/481987/files/arXiv:hep-ph_9901246.pdf.
- 3958 [6] K. A. Olive et al. “Review of Particle Physics”. In: *Chin. Phys.* C38 (2014),
3959 p. 090001. doi: [10.1088/1674-1137/38/9/090001](https://doi.org/10.1088/1674-1137/38/9/090001).
- 3960 [7] Lawrence J. Hall, Yasunori Nomura, and Satoshi Shirai. “Spread Super-
3961 symmetry with Wino LSP: Gluino and Dark Matter Signals”. In: *JHEP* 01
3962 (2013), p. 036. doi: [10.1007/JHEP01\(2013\)036](https://doi.org/10.1007/JHEP01(2013)036). arXiv: [1210.2395](https://arxiv.org/abs/1210.2395)
3963 [hep-ph].
- 3964 [8] G. F. Giudice and A. Romanino. “Split supersymmetry”. In: *Nucl. Phys. B*
3965 699 (2004), p. 65. doi: [10.1016/j.nuclphysb.2004.11.048](https://doi.org/10.1016/j.nuclphysb.2004.11.048). arXiv:
3966 [hep-ph/0406088](https://arxiv.org/abs/hep-ph/0406088).
- 3967 [9] N. Arkani-Hamed, S. Dimopoulos, G. F. Giudice, and A. Romanino. “As-
3968 pects of split supersymmetry”. In: *Nucl. Phys. B* 709 (2005), p. 3. doi: [10.1016/j.nuclphysb.2004.12.026](https://doi.org/10.1016/j.nuclphysb.2004.12.026). arXiv: [hep-ph/0409232](https://arxiv.org/abs/hep-ph/0409232).
- 3969 [10] Lyndon Evans and Philip Bryant. “LHC Machine”. In: *JINST* 3 (2008),
3970 S08001. doi: [10.1088/1748-0221/3/08/S08001](https://doi.org/10.1088/1748-0221/3/08/S08001).
- 3971 [11] C Lefevre. “LHC: the guide (English version). Guide du LHC (version
3972 anglaise)”. 2009. URL: <https://cds.cern.ch/record/1165534>.
- 3973 [12] “LEP Design Report Vol.1”. In: (1983).
- 3974 [13] ATLAS Collaboration. “The ATLAS Experiment at the CERN Large Hadron
3975 Collider”. In: *JINST* 3 (2008), S08003. doi: [10.1088/1748-0221/3/08/S08003](https://doi.org/10.1088/1748-0221/3/08/S08003).

- 3982 [14] S. Chatrchyan et al. “The CMS experiment at the CERN LHC”. In: *JINST*
 3983 3 (2008), S08004. doi: [10.1088/1748-0221/3/08/S08004](https://doi.org/10.1088/1748-0221/3/08/S08004).
- 3984 [15] A. Augusto Alves Jr. et al. “The LHCb Detector at the LHC”. In: *JINST* 3
 3985 (2008), S08005. doi: [10.1088/1748-0221/3/08/S08005](https://doi.org/10.1088/1748-0221/3/08/S08005).
- 3986 [16] K. Aamodt et al. “The ALICE experiment at the CERN LHC”. In: *JINST*
 3987 3 (2008), S08002. doi: [10.1088/1748-0221/3/08/S08002](https://doi.org/10.1088/1748-0221/3/08/S08002).
- 3988 [17] Daniel Froidevaux and Paris Sphicas. “General-Purpose Detectors for
 3989 the Large Hadron Collider”. In: *Annual Review of Nuclear and Particle Sci-
 3990 ence* 56.1 (2006), pp. 375–440. doi: [10.1146/annurev.nucl.54.
 3991 070103.181209](https://doi.org/10.1146/annurev.nucl.54.070103.181209). url: <http://dx.doi.org/10.1146/annurev.nucl.54.070103.181209>.
- 3993 [18] M Capeans, G Darbo, K Einsweiller, M Elsing, T Flick, M Garcia-Sciveres,
 3994 C Gemme, H Pernegger, O Rohne, and R Vuillermet. *ATLAS Insertable B-
 3995 Layer Technical Design Report*. Tech. rep. CERN-LHCC-2010-013. ATLAS-
 3996 TDR-19. 2010. url: <https://cds.cern.ch/record/1291633>.
- 3997 [19] T. Cornelissen, M. Elsing, S. Fleischmann, W. Liebig, and E. Moyse. “Con-
 3998 cepts, Design and Implementation of the ATLAS New Tracking (NEWT)”.
 3999 In: (2007). Ed. by A. Salzburger.
- 4000 [20] “Performance of the ATLAS Inner Detector Track and Vertex Reconstruc-
 4001 tion in the High Pile-Up LHC Environment”. In: (2012).
- 4002 [21] A. Salzburger. “The ATLAS Track Extrapolation Package”. In: (2007).
- 4003 [22] ATLAS Collaboration. “A neural network clustering algorithm for the
 4004 ATLAS silicon pixel detector”. In: *JINST* 9 (2014), P09009. doi: [10.1088/1748-0221/9/09/P09009](https://doi.org/10.1088/1748-0221/9/09/P09009). arXiv: [1406.7690 \[hep-ex\]](https://arxiv.org/abs/1406.7690).
- 4006 [23] ATLAS Collaboration. *Performance of primary vertex reconstruction in proton-
 4007 proton collisions at $\sqrt{s} = 7 \text{ TeV}$ in the ATLAS experiment*. ATLAS-CONF-
 4008 2010-069. 2010. url: <https://cds.cern.ch/record/1281344>.
- 4009 [24] ATLAS Collaboration. “Electron reconstruction and identification effi-
 4010 ciency measurements with the ATLAS detector using the 2011 LHC proton-
 4011 proton collision data”. In: *Eur. Phys. J. C* 74 (2014), p. 2941. doi: [10.1140/epjc/s10052-014-2941-0](https://doi.org/10.1140/epjc/s10052-014-2941-0). arXiv: [1404.2240 \[hep-ex\]](https://arxiv.org/abs/1404.2240).
 4012 PERF-2013-03.
- 4014 [25] ATLAS Collaboration. *Electron efficiency measurements with the ATLAS
 4015 detector using the 2012 LHC proton-proton collision data*. ATLAS-CONF-
 4016 2014-032. 2014. url: <https://cds.cern.ch/record/1706245>.
- 4017 [26] ATLAS Collaboration. *Measurements of the photon identification efficiency
 4018 with the ATLAS detector using 4.9 fb^{-1} of pp collision data collected in 2011*.
 4019 ATLAS-CONF-2012-123. 2012. url: <https://cds.cern.ch/record/1473426>.
- 4021 [27] ATLAS Collaboration. “Muon reconstruction performance of the ATLAS
 4022 detector in proton-proton collision data at $\sqrt{s} = 13 \text{ TeV}$ ”. In: (2016).
 4023 arXiv: [1603.05598 \[hep-ex\]](https://arxiv.org/abs/1603.05598). PERF-2015-10.

- 4024 [28] ATLAS Collaboration. “Topological cell clustering in the ATLAS calorimeters and its performance in LHC Run 1”. In: (2016). arXiv: [1603.02934](https://arxiv.org/abs/1603.02934) [hep-ex]. PERF-2014-07.
- 4025
4026
4027 [29] ATLAS Collaboration. *Properties of jets and inputs to jet reconstruction and calibration with the ATLAS detector using proton–proton collisions at $\sqrt{s} = 13$ TeV*. ATL-PHYS-PUB-2015-036. 2015. URL: <https://cds.cern.ch/record/2044564>.
- 4028
4029
4030
4031 [30] Matteo Cacciari, Gavin P. Salam, and Gregory Soyez. “The anti- k_t jet clustering algorithm”. In: *JHEP* 04 (2008), p. 063. doi: [10.1088/1126-6708/2008/04/063](https://doi.org/10.1088/1126-6708/2008/04/063). arXiv: [0802.1189](https://arxiv.org/abs/0802.1189) [hep-ph].
- 4032
4033
4034 [31] ATLAS Collaboration. *Jet global sequential corrections with the ATLAS detector in proton–proton collisions at $\sqrt{s} = 8$ TeV*. ATLAS-CONF-2015-002. 2015. URL: <https://cds.cern.ch/record/2001682>.
- 4035
4036
4037 [32] S. Agostinelli et al. “GEANT4: A simulation toolkit”. In: *Nucl. Instrum. Meth. A* 506 (2003), pp. 250–303. doi: [10.1016/S0168-9002\(03\)01368-8](https://doi.org/10.1016/S0168-9002(03)01368-8).
- 4038
4039
4040 [33] ATLAS Collaboration. “A study of the material in the ATLAS inner detector using secondary hadronic interactions”. In: *JINST* 7 (2012), P01013. doi: [10.1088/1748-0221/7/01/P01013](https://doi.org/10.1088/1748-0221/7/01/P01013). arXiv: [1110.6191](https://arxiv.org/abs/1110.6191) [hep-ex]. PERF-2011-08.
- 4041
4042
4043
4044 [34] ATLAS Collaboration. “Electron and photon energy calibration with the ATLAS detector using LHC Run 1 data”. In: *Eur. Phys. J. C* 74 (2014), p. 3071. doi: [10.1140/epjc/s10052-014-3071-4](https://doi.org/10.1140/epjc/s10052-014-3071-4). arXiv: [1407.5063](https://arxiv.org/abs/1407.5063) [hep-ex]. PERF-2013-05.
- 4045
4046
4047
4048 [35] ATLAS Collaboration. “A measurement of the calorimeter response to single hadrons and determination of the jet energy scale uncertainty using LHC Run-1 pp -collision data with the ATLAS detector”. In: (2016). arXiv: [1607.08842](https://arxiv.org/abs/1607.08842) [hep-ex]. PERF-2015-05.
- 4049
4050
4051
4052 [36] ATLAS Collaboration. “Single hadron response measurement and calorimeter jet energy scale uncertainty with the ATLAS detector at the LHC”. In: *Eur. Phys. J. C* 73 (2013), p. 2305. doi: [10.1140/epjc/s10052-013-2305-1](https://doi.org/10.1140/epjc/s10052-013-2305-1). arXiv: [1203.1302](https://arxiv.org/abs/1203.1302) [hep-ex]. PERF-2011-05.
- 4053
4054
4055
4056 [37] ATLAS Collaboration. “The ATLAS Simulation Infrastructure”. In: *Eur. Phys. J. C* 70 (2010), p. 823. doi: [10.1140/epjc/s10052-010-1429-9](https://doi.org/10.1140/epjc/s10052-010-1429-9). arXiv: [1005.4568](https://arxiv.org/abs/1005.4568) [hep-ex]. SOFT-2010-01.
- 4057
4058
4059
4060 [38] T. Sjöstrand, S. Mrenna, and P. Skands. “A Brief Introduction to PYTHIA 8.1”. In: *Comput. Phys. Commun.* 178 (2008), pp. 852–867. doi: [10.1016/j.cpc.2008.01.036](https://doi.org/10.1016/j.cpc.2008.01.036). arXiv: [0710.3820](https://arxiv.org/abs/0710.3820).
- 4061
4062
4063 [39] ATLAS Collaboration. *Summary of ATLAS Pythia 8 tunes*. ATL-PHYS-PUB-2012-003. 2012. URL: [http://cds.cern.ch/record/1474107](https://cds.cern.ch/record/1474107).

- 4064 [40] A.D. Martin, W.J. Stirling, R.S. Thorne, and G. Watt. “Parton distributions
 4065 for the LHC”. In: *Eur. Phys. J. C* 63 (2009). Figures from the [MSTW Website](#), pp. 189–285. doi: [10.1140/epjc/s10052-009-1072-5](https://doi.org/10.1140/epjc/s10052-009-1072-5). arXiv:
 4066 [0901.0002](https://arxiv.org/abs/0901.0002).
- 4068 [41] A. Sherstnev and R.S. Thorne. “Parton Distributions for LO Generators”.
 4069 In: *Eur. Phys. J. C* 55 (2008), pp. 553–575. doi: [10.1140/epjc/s10052-008-0610-x](https://doi.org/10.1140/epjc/s10052-008-0610-x). arXiv: [0711.2473](https://arxiv.org/abs/0711.2473).
- 4071 [42] A. Ribon et al. *Status of Geant4 hadronic physics for the simulation of LHC*
 4072 *experiments at the start of LHC physics program*. CERN-LCGAPP-2010-02.
 4073 2010. URL: <http://lcgapp.cern.ch/project/docs/noteStatusHadronic2010.pdf>.
- 4074 [43] M. P. Guthrie, R. G. Alsmiller, and H. W. Bertini. “Calculation of the
 4075 capture of negative pions in light elements and comparison with exper-
 4076 iments pertaining to cancer radiotherapy”. In: *Nucl. Instrum. Meth.* 66
 4077 (1968), pp. 29–36. doi: [10.1016/0029-554X\(68\)90054-2](https://doi.org/10.1016/0029-554X(68)90054-2).
- 4079 [44] H. W. Bertini and P. Guthrie. “News item results from medium-energy
 4080 intranuclear-cascade calculation”. In: *Nucl. Instr. and Meth. A* 169 (1971),
 4081 p. 670. doi: [10.1016/0375-9474\(71\)90710-X](https://doi.org/10.1016/0375-9474(71)90710-X).
- 4082 [45] V.A. Karmanov. “Light Front Wave Function of Relativistic Composite
 4083 System in Explicitly Solvable Model”. In: *Nucl. Phys. B* 166 (1980), p. 378.
 4084 doi: [10.1016/0550-3213\(80\)90204-7](https://doi.org/10.1016/0550-3213(80)90204-7).
- 4085 [46] H. S. Fesefeldt. *GHEISHA program*. Pitha-85-02, Aachen. 1985.
- 4086 [47] G. Folger and J.P. Wellisch. “String parton models in Geant4”. In: (2003).
 4087 arXiv: [nucl-th/0306007](https://arxiv.org/abs/nucl-th/0306007).
- 4088 [48] N. S. Amelin et al. “Transverse flow and collectivity in ultrarelativistic
 4089 heavy-ion collisions”. In: *Phys. Rev. Lett.* 67 (1991), p. 1523. doi: [10.1103/PhysRevLett.67.1523](https://doi.org/10.1103/PhysRevLett.67.1523).
- 4091 [49] N. S. Amelin et al. “Collectivity in ultrarelativistic heavy ion collisions”.
 4092 In: *Nucl. Phys. A* 544 (1992), p. 463. doi: [10.1016/0375-9474\(92\)90598-E](https://doi.org/10.1016/0375-9474(92)90598-E).
- 4094 [50] L. V. Bravina et al. “Fluid dynamics and Quark Gluon string model - What
 4095 we can expect for Au+Au collisions at 11.6 AGeV/c”. In: *Nucl. Phys. A* 566
 4096 (1994), p. 461. doi: [10.1016/0375-9474\(94\)90669-6](https://doi.org/10.1016/0375-9474(94)90669-6).
- 4097 [51] L. V. Bravin et al. “Scaling violation of transverse flow in heavy ion colli-
 4098 sions at AGS energies”. In: *Phys. Lett. B* 344 (1995), p. 49. doi: [10.1016/0370-2693\(94\)01560-Y](https://doi.org/10.1016/0370-2693(94)01560-Y).
- 4100 [52] B. Andersson et al. “A model for low-pT hadronic reactions with gen-
 4101 eralizations to hadron-nucleus and nucleus-nucleus collisions”. In: *Nucl.*
 4102 *Phys. B* 281 (1987), p. 289. doi: [10.1016/0550-3213\(87\)90257-4](https://doi.org/10.1016/0550-3213(87)90257-4).
- 4103 [53] B. Andersson, A. Tai, and B.-H. Sa. “Final state interactions in the (nu-
 4104 clear) FRITIOF string interaction scenario”. In: *Z. Phys. C* 70 (1996), pp. 499–
 4105 506. doi: [10.1007/s002880050127](https://doi.org/10.1007/s002880050127).

- 4106 [54] B. Nilsson-Almqvist and E. Stenlund. “Interactions Between Hadrons
 4107 and Nuclei: The Lund Monte Carlo, Fritiof Version 1.6”. In: *Comput. Phys.*
 4108 *Commun.* 43 (1987), p. 387. doi: [10.1016/0010-4655\(87\)90056-7](https://doi.org/10.1016/0010-4655(87)90056-7).
- 4109 [55] B. Ganhuyag and V. Uzhinsky. “Modified FRITIOF code: Negative charged
 4110 particle production in high energy nucleus nucleus interactions”. In: *Czech.*
 4111 *J. Phys.* 47 (1997), pp. 913–918. doi: [10.1023/A:1021296114786](https://doi.org/10.1023/A:1021296114786).
- 4112 [56] ATLAS Collaboration. “Topological cell clustering in the ATLAS calorime-
 4113 ters and its performance in LHC Run 1”. In: (2016). arXiv: [1603.02934](https://arxiv.org/abs/1603.02934)
 4114 [[hep-ex](#)].
- 4115 [57] Peter Speckmayer. “Energy Measurement of Hadrons with the CERN
 4116 ATLAS Calorimeter”. Presented on 18 Jun 2008. PhD thesis. Vienna: Vi-
 4117 enna, Tech. U., 2008. URL: <http://cds.cern.ch/record/1112036>.
- 4118 [58] CMS Collaboration. “The CMS barrel calorimeter response to particle
 4119 beams from 2 to 350 GeV/c”. In: *Eur. Phys. J. C* 60.3 (2009). doi: [10.1140/epjc/s10052-009-0959-5](https://doi.org/10.1140/epjc/s10052-009-0959-5).
- 4120 [59] J. Beringer et al. (Particle Data Group). “Review of Particle Physics”. In:
 4121 *Chin. Phys. C* 38 (2014), p. 090001. URL: <http://pdg.lbl.gov>.
- 4122 [60] P. Adragna et al. “Measurement of Pion and Proton Response and Lon-
 4123 gitudinal Shower Profiles up to 20 Nuclear Interaction Lengths with the
 4124 ATLAS Tile Calorimeter”. In: *Nucl. Instrum. Meth. A* 615 (2010), pp. 158–
 4125 181. doi: [10.1016/j.nima.2010.01.037](https://doi.org/10.1016/j.nima.2010.01.037).
- 4126 [61] ATLAS Collaboration. “Jet energy measurement and its systematic un-
 4127 certainty in proton–proton collisions at $\sqrt{s} = 7$ TeV with the ATLAS de-
 4128 tector”. In: *Eur. Phys. J. C* 75 (2015), p. 17. doi: [10.1140/epjc/s10052-014-3190-y](https://doi.org/10.1140/epjc/s10052-014-3190-y). arXiv: [1406.0076](https://arxiv.org/abs/1406.0076) [[hep-ex](#)]. PERF-2012-01.
- 4129 [62] Hung-Liang Lai, Marco Guzzi, Joey Huston, Zhao Li, Pavel M. Nadolsky,
 4130 et al. “New parton distributions for collider physics”. In: *Phys. Rev. D* 82
 4131 (2010), p. 074024. doi: [10.1103/PhysRevD.82.074024](https://doi.org/10.1103/PhysRevD.82.074024). arXiv: [1007.2241](https://arxiv.org/abs/1007.2241) [[hep-ph](#)].
- 4132 [63] E. Abat et al. “Study of energy response and resolution of the ATLAS
 4133 barrel calorimeter to hadrons of energies from 20 to 350 GeV”. In: *Nucl.*
 4134 *Instrum. Meth. A* 621.1-3 (2010), pp. 134 –150. doi: <http://dx.doi.org/10.1016/j.nima.2010.04.054>.
- 4135 [64] ATLAS Collaboration. “Jet energy measurement with the ATLAS detec-
 4136 tor in proton–proton collisions at $\sqrt{s} = 7$ TeV”. In: *Eur. Phys. J. C* 73
 4137 (2013), p. 2304. doi: [10.1140/epjc/s10052-013-2304-2](https://doi.org/10.1140/epjc/s10052-013-2304-2). arXiv:
 4138 [1112.6426](https://arxiv.org/abs/1112.6426) [[hep-ex](#)]. PERF-2011-03.
- 4139 [65] Nausheen R. Shah and Carlos E. M. Wagner. “Gravitons and dark mat-
 4140 ter in universal extra dimensions”. In: *Phys. Rev. D* 74 (2006), p. 104008.
 4141 doi: [10.1103/PhysRevD.74.104008](https://doi.org/10.1103/PhysRevD.74.104008). arXiv: [hep-ph/0608140](https://arxiv.org/abs/hep-ph/0608140)
 4142 [[hep-ph](#)].
- 4143 [66] S. S. Adler and S. H. Adler. “A note on the renormalization of the graviton
 4144 propagator”. In: *Phys. Rev. D* 2.1 (1970), p. 247. doi: [10.1103/PhysRevD.2.247](https://doi.org/10.1103/PhysRevD.2.247). arXiv:
 4145 [1106.4442](https://arxiv.org/abs/1106.4442) [[hep-th](#)].

- 4147 [66] Jonathan L. Feng, Arvind Rajaraman, and Fumihiro Takayama. “Graviton cosmology in universal extra dimensions”. In: *Phys. Rev.* D68 (2003),
 4148 p. 085018. doi: [10.1103/PhysRevD.68.085018](https://doi.org/10.1103/PhysRevD.68.085018). arXiv: [hep-ph/0307375](https://arxiv.org/abs/hep-ph/0307375) [hep-ph].
- 4151 [67] Paul H. Frampton and Pham Quang Hung. “Long-lived quarks?” In: *Phys.
 4152 Rev. D* 58 (5 1998), p. 057704. doi: [10.1103/PhysRevD.58.057704](https://doi.org/10.1103/PhysRevD.58.057704).
 4153 url: <http://link.aps.org/doi/10.1103/PhysRevD.58.057704>.
- 4155 [68] C. Friberg, E. Norrbin, and T. Sjostrand. “QCD aspects of leptoquark
 4156 production at HERA”. In: *Phys. Lett.* B403 (1997), pp. 329–334. doi: [10.1016/S0370-2693\(97\)00543-1](https://doi.org/10.1016/S0370-2693(97)00543-1). arXiv: [hep-ph/9704214](https://arxiv.org/abs/hep-ph/9704214) [hep-ph].
- 4158 [69] Herbert K. Dreiner. “An introduction to explicit R-parity violation”. In:
 4159 (1997). arXiv: [hep-ph/9707435](https://arxiv.org/abs/hep-ph/9707435).
- 4160 [70] Edmond L. Berger and Zack Sullivan. “Lower limits on R-parity-violating
 4161 couplings in supersymmetry”. In: *Phys. Rev. Lett.* 92 (2004), p. 201801. doi:
 4162 [10.1103/PhysRevLett.92.201801](https://doi.org/10.1103/PhysRevLett.92.201801). arXiv: [hep-ph/0310001](https://arxiv.org/abs/hep-ph/0310001).
- 4163 [71] R. Barbieri, C. Berat, M. Besancon, M. Chemtob, A. Deandrea, et al. “R-
 4164 parity violating supersymmetry”. In: *Phys. Rept.* 420 (2005), p. 1. doi: [10.1016/j.physrep.2005.08.006](https://doi.org/10.1016/j.physrep.2005.08.006). arXiv: [hep-ph/0406039](https://arxiv.org/abs/hep-ph/0406039).
- 4166 [72] M. Fairbairn et al. “Stable massive particles at colliders”. In: *Phys. Rept.*
 4167 438 (2007), p. 1. doi: [10.1016/j.physrep.2006.10.002](https://doi.org/10.1016/j.physrep.2006.10.002). arXiv:
 4168 [hep-ph/0611040](https://arxiv.org/abs/hep-ph/0611040).
- 4169 [73] Christopher F. Kolda. “Gauge-mediated supersymmetry breaking: Intro-
 4170 duction, review and update”. In: *Nucl. Phys. Proc. Suppl.* 62 (1998), p. 266.
 4171 doi: [10.1016/S0920-5632\(97\)00667-1](https://doi.org/10.1016/S0920-5632(97)00667-1). arXiv: [hep-ph/9707450](https://arxiv.org/abs/hep-ph/9707450).
- 4172 [74] Howard Baer, Kingman Cheung, and John F. Gunion. “A Heavy gluino as
 4173 the lightest supersymmetric particle”. In: *Phys. Rev. D* 59 (1999), p. 075002.
 4174 doi: [10.1103/PhysRevD.59.075002](https://doi.org/10.1103/PhysRevD.59.075002). arXiv: [hep-ph/9806361](https://arxiv.org/abs/hep-ph/9806361).
- 4175 [75] S. James Gates Jr. and Oleg Lebedev. “Searching for supersymmetry in
 4176 hadrons”. In: *Phys. Lett. B* 477 (2000), p. 216. doi: [10.1016/S0370-2693\(00\)00172-6](https://doi.org/10.1016/S0370-2693(00)00172-6). arXiv: [hep-ph/9912362](https://arxiv.org/abs/hep-ph/9912362).
- 4178 [76] Glennys R. Farrar and Pierre Fayet. “Phenomenology of the Production,
 4179 Decay, and Detection of New Hadronic States Associated with Super-
 4180 symmetry”. In: *Phys. Lett.* B76 (1978), pp. 575–579. doi: [10.1016/0370-2693\(78\)90858-4](https://doi.org/10.1016/0370-2693(78)90858-4).
- 4182 [77] A. C. Kraan, J. B. Hansen, and P. Nevski. “Discovery potential of R-hadrons
 4183 with the ATLAS detector”. In: *Eur. Phys. J.* C49 (2007), pp. 623–640. doi:
 4184 [10.1140/epjc/s10052-006-0162-x](https://doi.org/10.1140/epjc/s10052-006-0162-x). arXiv: [hep-ex/0511014](https://arxiv.org/abs/hep-ex/0511014)
 4185 [hep-ex].
- 4186 [78] Rasmus Mackeprang and David Milstead. “An Updated Description of
 4187 Heavy-Hadron Interactions in GEANT-4”. In: *Eur. Phys. J.* C66 (2010),
 4188 pp. 493–501. doi: [10.1140/epjc/s10052-010-1262-1](https://doi.org/10.1140/epjc/s10052-010-1262-1). arXiv:
 4189 [0908.1868](https://arxiv.org/abs/0908.1868) [hep-ph].

- 4190 [79] ATLAS Collaboration. “Search for massive, long-lived particles using mul-
 4191 titrack displaced vertices or displaced lepton pairs in pp collisions at
 4192 $\sqrt{s} = 8$ TeV with the ATLAS detector”. In: *Phys. Rev. D* 92 (2015), p. 072004.
 4193 doi: [10.1103/PhysRevD.92.072004](https://doi.org/10.1103/PhysRevD.92.072004). arXiv: [1504.05162 \[hep-ex\]](https://arxiv.org/abs/1504.05162).
 4194 SUSY-2014-02.
- 4195 [80] ATLAS Collaboration. “Search for charginos nearly mass degenerate with
 4196 the lightest neutralino based on a disappearing-track signature in pp
 4197 collisions at $\sqrt{s} = 8$ TeV with the ATLAS detector”. In: *Phys. Rev. D*
 4198 88 (2013), p. 112006. doi: [10.1103/PhysRevD.88.112006](https://doi.org/10.1103/PhysRevD.88.112006). arXiv:
 4199 [1310.3675 \[hep-ex\]](https://arxiv.org/abs/1310.3675). SUSY-2013-01.
- 4200 [81] ATLAS Collaboration. “Searches for heavy long-lived sleptons and R-
 4201 Hadrons with the ATLAS detector in pp collisions at $\sqrt{s} = 7$ TeV”. In:
 4202 *Phys. Lett. B* 720 (2013), p. 277. doi: [10.1016/j.physletb.2013.02.015](https://doi.org/10.1016/j.physletb.2013.02.015). arXiv: [1211.1597 \[hep-ex\]](https://arxiv.org/abs/1211.1597). SUSY-2012-01.
- 4204 [82] ATLAS Collaboration. “Searches for heavy long-lived charged particles
 4205 with the ATLAS detector in proton–proton collisions at $\sqrt{s} = 8$ TeV”. In:
 4206 *JHEP* 01 (2015), p. 068. doi: [10.1007/JHEP01\(2015\)068](https://doi.org/10.1007/JHEP01(2015)068). arXiv:
 4207 [1411.6795 \[hep-ex\]](https://arxiv.org/abs/1411.6795). SUSY-2013-22.
- 4208 [83] ATLAS Collaboration. “Search for metastable heavy charged particles
 4209 with large ionisation energy loss in pp collisions at $\sqrt{s} = 8$ TeV using the
 4210 ATLAS experiment”. In: *Eur. Phys. J. C* 75 (2015), p. 407. doi: [10.1140/epjc/s10052-015-3609-0](https://doi.org/10.1140/epjc/s10052-015-3609-0). arXiv: [1506.05332 \[hep-ex\]](https://arxiv.org/abs/1506.05332). SUSY-
 4211 2014-09.
- 4213 [84] ATLAS Collaboration. “Search for heavy long-lived charged R -hadrons
 4214 with the ATLAS detector in 3.2 fb^{-1} of proton–proton collision data at
 4215 $\sqrt{s} = 13$ TeV”. In: *Phys. Lett. B* 760 (2016), pp. 647–665. doi: [10.1016/j.physletb.2016.07.042](https://doi.org/10.1016/j.physletb.2016.07.042). arXiv: [1606.05129 \[hep-ex\]](https://arxiv.org/abs/1606.05129).
- 4217 [85] Torbjorn Sjöstrand, Stephen Mrenna, and Peter Skands. “PYTHIA 6.4
 4218 Physics and Manual”. In: *JHEP* 0605 (2006), p. 026. doi: [10.1088/1126-6708/2006/05/026](https://doi.org/10.1088/1126-6708/2006/05/026). arXiv: [hep-ph/0603175](https://arxiv.org/abs/hep-ph/0603175).
- 4220 [86] ATLAS Collaboration. *Further ATLAS tunes of PYTHIA 6 and Pythia 8*. ATL-
 4221 PHYS-PUB-2011-014. 2011. url: <https://cds.cern.ch/record/1400677>.
- 4223 [87] Aafke Christine Kraan. “Interactions of heavy stable hadronizing parti-
 4224 cles”. In: *Eur. Phys. J. C* 37 (2004), pp. 91–104. doi: [10.1140/epjc/s2004-01946-6](https://doi.org/10.1140/epjc/s2004-01946-6). arXiv: [hep-ex/0404001 \[hep-ex\]](https://arxiv.org/abs/hep-ex/0404001).
- 4226 [88] M. Fairbairn et al. “Stable massive particles at colliders”. In: *Phys. Rept.*
 4227 438 (2007), p. 1. doi: [10.1016/j.physrep.2006.10.002](https://doi.org/10.1016/j.physrep.2006.10.002). arXiv:
 4228 [hep-ph/0611040](https://arxiv.org/abs/hep-ph/0611040).
- 4229 [89] W. Beenakker, R. Hopker, M. Spira, and P. M. Zerwas. “Squark and gluino
 4230 production at hadron colliders”. In: *Nucl. Phys. B* 492 (1997), p. 51. doi:
 4231 [10.1016/S0550-3213\(97\)00084-9](https://doi.org/10.1016/S0550-3213(97)00084-9). arXiv: [hep-ph/9610490](https://arxiv.org/abs/hep-ph/9610490).

- 4232 [90] A. Kulesza and L. Motyka. “Threshold resummation for squark-antisquark
 4233 and gluino-pair production at the LHC”. In: *Phys. Rev. Lett.* 102 (2009),
 4234 p. 111802. doi: [10.1103/PhysRevLett.102.111802](https://doi.org/10.1103/PhysRevLett.102.111802). arXiv: [0807.2405 \[hep-ph\]](https://arxiv.org/abs/0807.2405).
- 4236 [91] A. Kulesza and L. Motyka. “Soft gluon resummation for the production
 4237 of gluino-gluino and squark-antisquark pairs at the LHC”. In: *Phys. Rev.*
 4238 *D* 80 (2009), p. 095004. doi: [10.1103/PhysRevD.80.095004](https://doi.org/10.1103/PhysRevD.80.095004). arXiv:
 4239 [0905.4749 \[hep-ph\]](https://arxiv.org/abs/0905.4749).
- 4240 [92] Wim Beenakker, Silja Brensing, Michael Kramer, Anna Kulesza, Eric Lae-
 4241 nen, et al. “Soft-gluon resummation for squark and gluino hadroproduc-
 4242 tion”. In: *JHEP* 0912 (2009), p. 041. doi: [10.1088/1126-6708/2009/12/041](https://doi.org/10.1088/1126-6708/2009/12/041). arXiv: [0909.4418 \[hep-ph\]](https://arxiv.org/abs/0909.4418).
- 4244 [93] W. Beenakker, S. Brensing, M.n Kramer, A. Kulesza, E. Laenen, et al. “Squark
 4245 and Gluino Hadroproduction”. In: *Int. J. Mod. Phys. A* 26 (2011), p. 2637.
 4246 doi: [10.1142/S0217751X11053560](https://doi.org/10.1142/S0217751X11053560). arXiv: [1105.1110 \[hep-ph\]](https://arxiv.org/abs/1105.1110).
- 4247 [94] Michael Krämer et al. *Supersymmetry production cross sections in pp colli-*
 4248 *sions at $\sqrt{s} = 7 \text{ TeV}$* . 2012. arXiv: [1206.2892 \[hep-ph\]](https://arxiv.org/abs/1206.2892).
- 4249 [95] Rasmus Mackeprang and Andrea Rizzi. “Interactions of Coloured Heavy
 4250 Stable Particles in Matter”. In: *Eur. Phys. J. C*50 (2007), pp. 353–362. doi:
 4251 [10.1140/epjc/s10052-007-0252-4](https://doi.org/10.1140/epjc/s10052-007-0252-4). arXiv: [hep-ph/0612161 \[hep-ph\]](https://arxiv.org/abs/hep-ph/0612161).
- 4253 [96] Rasmus Mackeprang and David Milstead. “An Updated Description of
 4254 Heavy-Hadron Interactions in GEANT-4”. In: *Eur. Phys. J. C*66 (2010),
 4255 pp. 493–501. doi: [10.1140/epjc/s10052-010-1262-1](https://doi.org/10.1140/epjc/s10052-010-1262-1). arXiv:
 4256 [0908.1868 \[hep-ph\]](https://arxiv.org/abs/0908.1868).
- 4258 [97] J. Alwall, R. Frederix, S. Frixione, V. Hirschi, F. Maltoni, O. Mattelaer, H. S.
 4259 Shao, T. Stelzer, P. Torrielli, and M. Zaro. “The automated computation
 4260 of tree-level and next-to-leading order differential cross sections, and
 4261 their matching to parton shower simulations”. In: *JHEP* 07 (2014), p. 079.
 4262 doi: [10.1007/JHEP07\(2014\)079](https://doi.org/10.1007/JHEP07(2014)079). arXiv: [1405.0301 \[hep-ph\]](https://arxiv.org/abs/1405.0301).
- 4263 [98] “dE/dx measurement in the ATLAS Pixel Detector and its use for particle
 4264 identification”. In: (2011).
- 4265 [99] ATLAS Collaboration. “The ATLAS Simulation Infrastructure”. In: *Eur.*
 4266 *Phys. J. C*70 (2010), pp. 823–874. doi: [10.1140/epjc/s10052-010-1429-9](https://doi.org/10.1140/epjc/s10052-010-1429-9). arXiv: [1005.4568 \[physics.ins-det\]](https://arxiv.org/abs/1005.4568).
- 4267 [100] Alexander L. Read. “Presentation of search results: The CL(s) technique”.
 4268 In: *J. Phys. G*28 (2002). [,11(2002)], pp. 2693–2704. doi: [10.1088/0954-3899/28/10/313](https://doi.org/10.1088/0954-3899/28/10/313).